2024 NSF/REU
Research Experience for Undergraduates
in
Physics and Astronomy

Student Research Papers
Volume 35

UNIVERSITY OF NOTRE DAME
College of Science

REU Director
Umesh Garg, Ph.D.

REU Student Research Papers – Summer 2024
University of Notre Dame – Department of Physics & Astronomy

Upgrades People, Upgrades: Ushering a new level of sensitivity for Accelerator Mass Spectrometry at the University of Notre Dame

CALVIN M. BACALL

2024 NSF/REU Program
Department of Physics and Astronomy
University of Notre Dame

ADVISOR(S): Prof. Philippe Collon

Abstract

Accelerator Mass Spectrometry (AMS) is the leading technique to measure ultra-low isotopic ratios of long-lived radioisotopes. Within the University of Notre Dame's nuclear science laboratory, an FN tandem accelerator is used with a Browne-Buechner spectrograph operated as a gas filled magnet to separate these isotopes from isobaric interferences. As isobars travel through the gas they coalesce around separate mean charge states, dependent on their nuclear charge. Along with this, a position-sensitive ΔE/E detector is used for particle identification. Two such ionization chambers, MONICA and FASMA, make use of diagonally split anodes to determine each ion's position while sampling multiple ranges of energy deposition. This summer, I reviewed several papers on ionization chambers to understand the housing, electronics, and design principles necessary for our project. During the REU program, I researched, planned, and began constructing a new ionization chamber modeled after the FASMA detector used at the Australian National University (ANU) and MONICA used at Argonne National Lab (ANL). The AMS program at Notre Dame decided to construct its own version to be used for future measurements at the NSL, increasing the current capabilities and lowering the detection limits attainable with its current PGAG-IC detector. This detector will primarily be used for long-lived medium-mass radionuclides such as ^{53}Mn, ^{60}Fe, ^{26}Al, ^{41}Ca, ^{93}Zr, and ^{36}Cl. The detector is currently being assembled at the NSL and first tests are planned for september. Progress toward the commissioning of the detector will be presented alongside plans for its first experiment with ^{53}Mn in Fall 2024.

1 Introduction

Accelerator Mass Spectrometry (AMS) is a powerful research method that possesses applications in several fields stretching from carbon dating to biomedical analysis to climate studies. Accelerator Mass Spectrometry is able to measure rare isotopes in a sample with high precision and sensitivity. AMS combines aspects of both mass spectrometry and particle accelerators to achieve its unique capabilities. The process begins with the sample material being converted into a form suitable for ionization, often a gas or a solid target. This material is then ionized to produce a beam of charged particles.

The ionized particles are then accelerated to high velocities using a particle accelerator. This acceleration imparts high kinetic energy to the ions, which helps in separating isotopes based on their mass-to-charge ratio. The accelerated ions pass through magnetic and electric fields that act as

filters, ensuring that only ions of specific masses reach the detector. This step is crucial as it helps in removing any interfering particles and background noise, leading to more accurate measurements.

One of the key advantages of AMS is its ability to detect isotopes at extremely low concentrations, with sensitivity spanning down to 10^{-16}. [4].

1.1 AMS Applications

AMS possesses applications in numerous scientific fields due to its high sensitivity and precision in detecting rare isotopes. In archaeology, it is essential for radiocarbon dating, which helps determine the age of ancient artifacts and remains by measuring the ^{14}C content. This technique has greatly enhanced our understanding of historical timelines and human activity over millennia.

In environmental science, AMS can to track isotopes like ^{10}Be and ^{14}C in ice cores, sediment layers, and tree rings, providing valuable data on past climate changes and aiding in climate modeling. Additionally, AMS is employed in hydrology to study groundwater movement and contamination by tracing isotopes such as ^{36}Cl.

Biomedical research benefits from AMS by using it to trace metabolic pathways and study drug interactions at very low concentrations, enabling researchers to understand complex biological processes without invasive sampling. In geology, AMS helps date geological formations and volcanic events through the analysis of isotopes like ^{26}Al.

AMS also plays a crucial role in nuclear physics by measuring isotopic ratios as a result of cosmic rays, supernovae, or other astrophysical phenomena. Its ability to work with small sample sizes and detect minute quantities of isotopes makes AMS an invaluable tool across these diverse fields.

1.2 AMS at Notre Dame

At the University of Notre Dame, a large emphasis is placed on developing new techniques within AMS, with a current focus on ^{53}Mn, ^{129}I, and ^{236}U. With the University of Notre Dame's current scope, analysis of medium-mass radionuclides is possible; however, it can be greatly im-

proved by implementing a FASMA (Flexible Anti-Scattering Multi-Anode) style detector. This would allow better experimentation with ^{53}Mn as minimizing ^{53}Cr exists at the limits of our current capabilities. This improved experimentation means that detecting ^{53}Mn at lower levels will be possible. [5]In the future, experimentation with ^{60}Fe, ^{26}Al, ^{41}Ca, ^{93}Zr, and ^{36}Cl will also be possible with this new multi-anode detector.

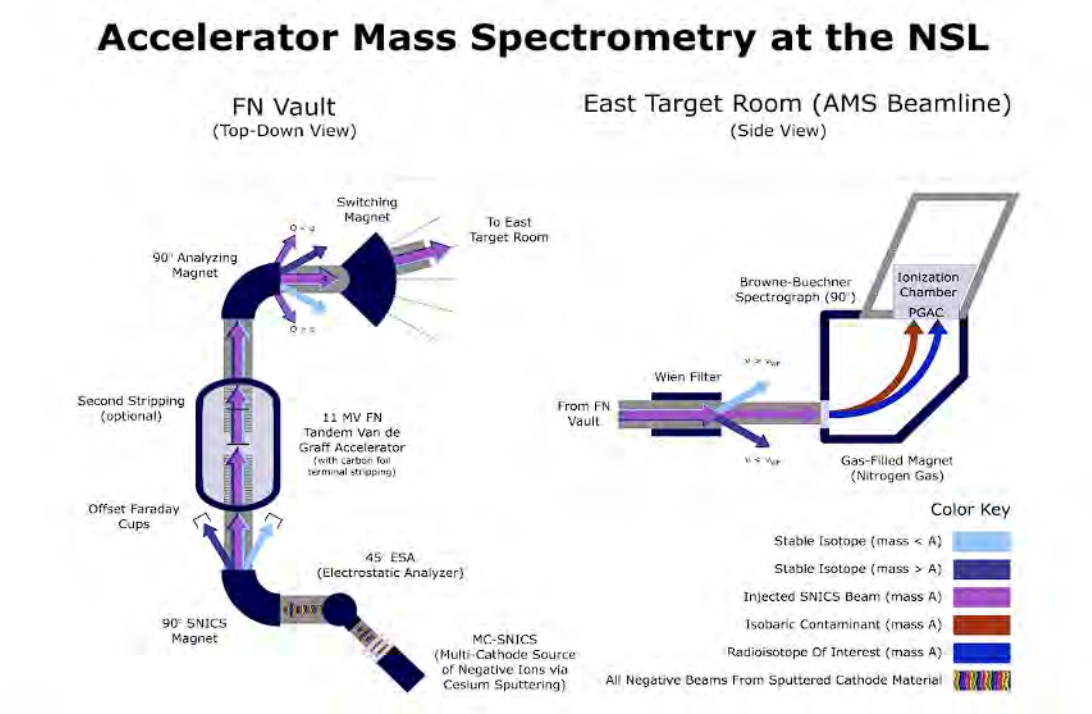

Figure 1: Beam line used by AMS group at the University of Notre Dame

Figure 1, pictured above, shows the different components of the beam line at Notre Dame's Nuclear Science Lab. The process begins with the first filter, which is an m/q filter, known as the Electrostatic Analyzer. Following this, the second filter used is the bouncing Magnet. Following this stage, electrons are stripped and molecules are dissociated within the FN Tandem Accelerator. The accelerator greatly accelerates the beam, allowing for more sensitive measurements by the Analyzing magnet, a p/q filter. The particle accelerator is what differentiates our methods from other mass spectrometry methods. The high velocities are necessary to achieve the 10^{-17} ratio measurements. To further refine the selection, a Wien Filter is used to separate particles based on their velocity, effectively removing p/q contaminants. Finally, the Brown-Buechner Spectrograph

provides isobaric discrimination, ensuring that only the intended isotope remains.

2 Background

The AMS group at the University of Notre Dame is in need of a position-sensitive ΔE/E detector specifically designed for medium-mass radionuclides. This detector will be used for elements such as ^{53}Mn, ^{60}Fe, ^{26}Al, ^{41}Ca, ^{93}Zr, and ^{36}Cl. Examples of ionization chambers of this type include MONICA at Argonne National Laboratory and FASMA at the Australian National University. These detectors utilize diagonally split anodes to determine ion positions while simultaneously sampling multiple energy deposition ranges. Introducing a new detector of this kind will enhance our current capabilities and surpass the detection limits currently achievable with our PGAC-IC.

This new detector will follow key design principles from each of its parent detectors. To begin, the anode plate will have the same trapezoidal shape, as seen in Figure 2. [5]This shape will better match the shape of the beam just before it enters the detector. Along with this, it will protect anodes from disruptions in the electric field and work to eliminate noise and interference.

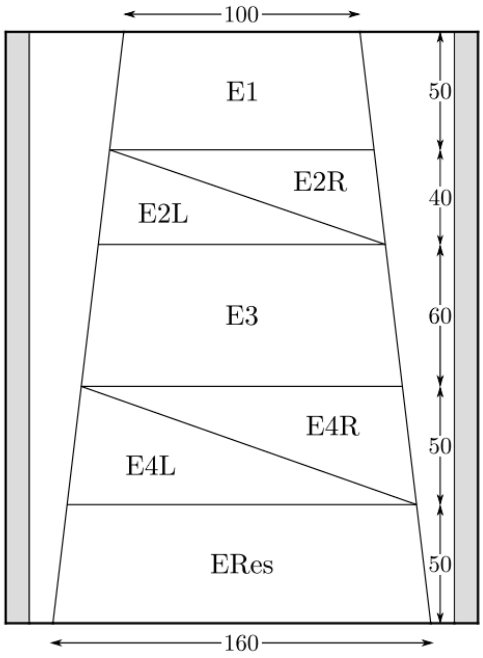

Figure 2: Anode Configuration of FASMA, currently at Australian National University

From MONICA, the new detector will utilize the split anode design, visible in Figure 3.[3] This is essential in determining each ion's position while sampling multiple ranges of energy deposition

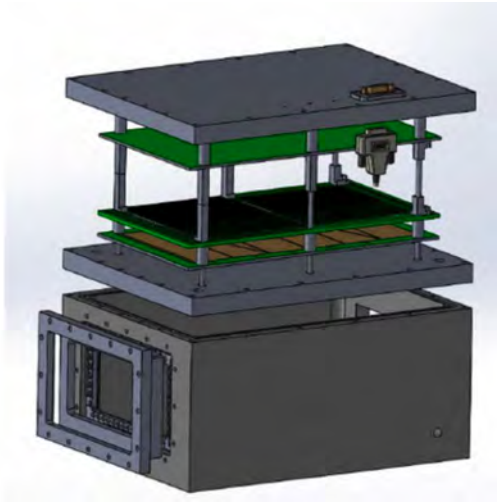

Figure 3: Model of MONICA detector, currently at Argonne National Lab

Because anodes are split, multiple runs can be taken, then the ideal accelerator and filter settings can be found to discriminate the desired isotope. For example, if we use settings that are too high, then too low, we can split this difference to find ideal settings.

2.1 Bragg Curves

In order to better understand the necessity of a multi-anode design, we can use Bragg Curves. Bragg Curves are derived from the Bethe-Bloch formula and can show how energy changes with respect to position, specifically as a beam passes through an ionization chamber. As seen in Figure4. Within the figure, we can see that Mn starts above Cr; however, falls and eventually reaches a point where it is below. Based on this information, we can conclude where Mn will be in earlier anode regions, knowing that this will change as we go further into the detector.

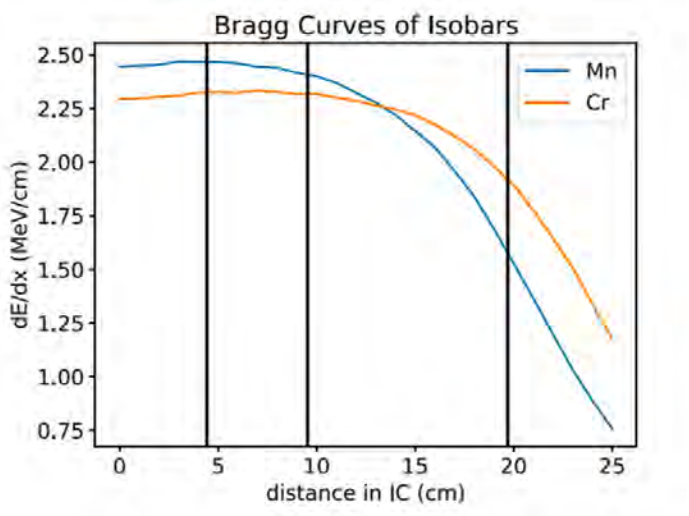

Figure 4: Bragg Curve Diagram Example of Mn and Cr

3 Methods

As for what my tasks consisted of this summer, I conducted extensive research on ionization chambers to gain a thorough understanding. With this, I was much more comfortable moving forward with my project. After creating a detailed plan with the necessary tasks and objectives, I began designing the necessary plates on ExpressPCB, with progress on the anode plate pictured in Figure 5. I also used CAD software to ensure my plates would fit within the housing I was provided. Additionally, I requested quotes for the preamplifier circuit, as these will be a necessary component later on. Finally, I participated in AMS experiments using a different detector, gaining valuable hands-on experience and a deeper understanding of AMS experimentation.

4 Results

Currently, there exists a completed housing, visible in Figure 6. and cathode plate schematic. The anode plate schematic is mostly completed with just the wiring left to be completed. After requesting quotes for the preamplifier circuit necessary, I spoke to a few individuals within the NSL to decide which components would be best to move forward with. As for my understanding of running the FN accelerator, it has greatly deepened, and I am confident I will soon be able to

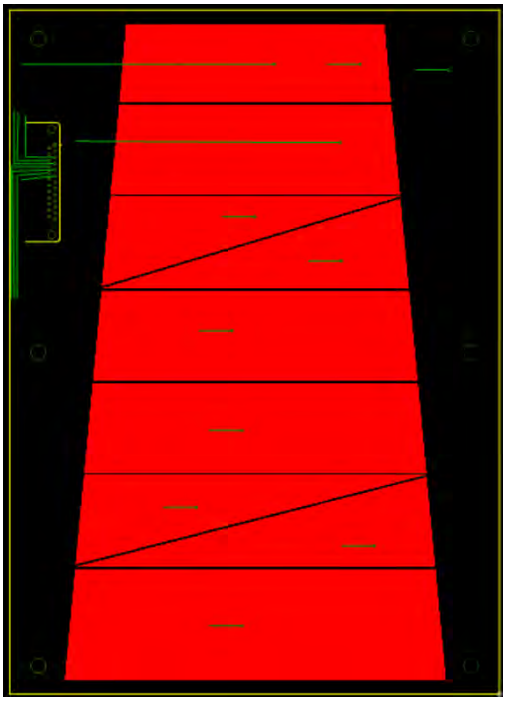

Figure 5: Screenshot of Anode Plate Design within ExpressPCB. The Necessary regions have been drawn with only the necessary wiring to complete.

manage many parts of this process on my own. This will prove to be a useful asset to my group as there are occasionally members from outside the group assisting with experiments. As they may not understand full functionality, they will be able to supervise me as I work on the collection of data necessary for the experiment at hand.

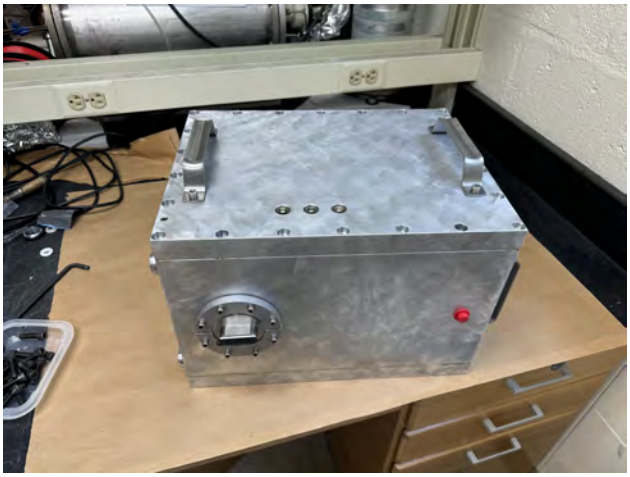

Figure 6: The Aluminum Housing for the new detector. This was created before I took on the commissioning of the new detector.

5 Conclusion

One advantage of being a student at the University of Notre Dame, and not just an REU participant, is that I can continue this project into the academic year. Because 10 weeks is not nearly enough time to plan, commission, and complete the building of an ionization chamber, I will continue to work on my project until it is completed and ready for use in experiments. As for a timeline, I expect to complete the design of the Anode and Cathode plates in ExpressPCB by the end of August, with hopes of beginning vacuum testing of the empty chamber in September. Assuming all necessary internals are received by October, we will be able to move into vacuum testing with an occupied housing, testing all electronics, and preparing for experimentation in November. Along with working on the detector, I will continue participating in my group's beam time in order to become better acquainted with the accelerator and grow as a researcher.

References

[1] T. Bailey, *Development towards 53MN accelerator mass spectrometry capabilities at the University of Notre Dame.* , Nuclear Instruments and Methods in Physics Research Section B: Beam Interactions with Materials and Atoms, Volume 536, 2023.

[2] L. Callahan, *Accelerator Mass Spectrometry with the MONICA Detector at the Argonne Gas-Filled Analyzer and Ultra-Sensitive Detection of 39,42Ar*, University of Notre Dame, 2023.

[3] R. Hellborg, *Accelerator Mass Spectrometry*, Department of Physics, Lund University, 2007.

[4] W. Kutschera , *Atom counting with accelerator mass spectrometry* , Reviews of Modern Physics, Volume 95, 2023.

[5] G. Leckenby , *Remodelling a multi-anode ionisation chamber detector for accelerator mass spectrometry of 53Mn*, Australian National University, 2017.

Producing and Moderating Neutrons for Radioactive Nuclei Neutron Captures

ISAAC BOS

2024 NSF/REU Program
Department of Physics and Astronomy
University of Notre Dame

ADVISOR(S): Prof. Ed Stech, Prof. James DeBoer

Abstract

Neutron captures by radioactive nuclei are an important mechanism for the stellar production of heavier isotopes. This project works towards replicating such reactions in a laboratory setting through a test setup which produces neutrons inside a cube of graphite moderator. Gold wires are used to detect where the neutrons would hit a radioactive ion beam. From four activation runs, each with different energy proton beams producing neutrons and different moderator arrangements, we found that yield increases with proton beam energy and decreases when only half the moderator cube is used. Combined with future work comparing this data to simulations these results allow continued development of a full apparatus for replicating radioactive nuclei neutron captures.

1 Introduction

Neutron capture reactions play a central role in the stellar production of heavier isotopes. In a neutron capture, a parent nucleus absorbs a neutron to become a new, heavier isotope. Most isotopes heavier than iron-56 are produced through processes involving a series of neutron captures. However, our understanding of these processes is limited because many relevant reactions have yet to be replicated in a laboratory setting. This is because many isotopes in stellar neutron capture reactions are radioactive and so the reactions differ from typical nuclear physics experiments. In a typical nuclear experiment, a stationary target is prepared in advance and placed in front of an accelerator which accelerates a beam of charged particles onto the target. However, a target of radioactive parent nuclei will decay before it can be used. Furthermore, neutrons cannot be accelerated onto such a target since they are uncharged.

Reifarth *et. al.* have proposed a setup which overcomes these challenges using a radioactive ion beam instead of a traditional target [1]. Radioactive nuclei can be created, ionized, accelerated, and quickly reacted with neutrons. The neutrons are produced with a second beam of protons which reacts with a lithium-7 target in a ^{7}Li(p,n)^{7}Be reaction. When they are initially emitted the neutrons are moving at high speeds in all directions, so a graphite moderator is used to slow the neutrons and bounce them towards the beam. If it can be implemented, this method should address some challenges associated with neutron beams and radioactive targets by using a radioactive ion beam

and a sort of neutron target.

This work assesses the feasibility of this method by testing the use of the ^{7}Li(p,n)^{7}Be reaction and graphite moderator to produce neutrons. Our setup replaces the radioactive ion beam with gold wires. By counting the number of neutrons the gold absorbs we can confirm that it is possible to create the neutrons required to replicate stellar neutron capture reactions in a laboratory setting.

2 Methods

2.1 Setup

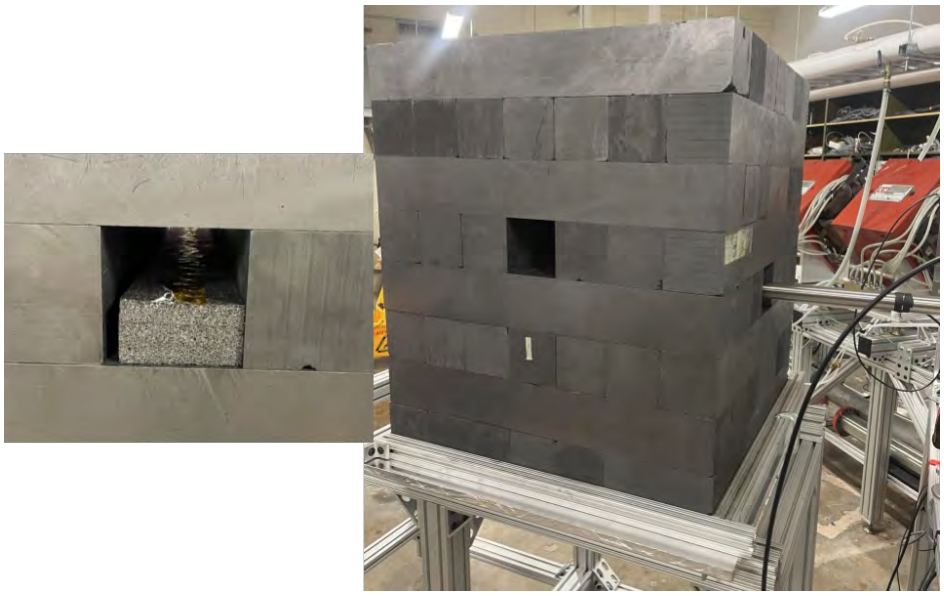

Figure 1: Main image is of the graphite moderator cube. Proton beam line is visible on the left. The hole for the radioactive ion beam or gold wires is on the right, with a closeup of the hole with gold in place in the small right image.

To perform preliminary experiments proposed by Reifarth *et. al.* [1] a test setup was constructed on the beam line of the 5U accelerator at the University of Notre Dame Nuclear Science Laboratory. The setup had three main components: the proton beam line from the 5U accelerator with a lithium-7 target for producing neutrons, a large graphite cube to moderate the neutrons, and small gold wires to absorb the neutrons. The moderating cube was constructed from 4.25 by 4.25 by 29.75-inch

graphite blocks stacked in eight layers with seven blocks in each. The center block was removed from the fourth and fifth layers (see Figure 1).

The hole in the fourth layer was for the proton beam which protruded halfway into the graphite cube. The remaining space was plugged with two 23.75 inch blocks. The cube was mounted on slides parallel to the proton beam line. By sliding the cube, we could access the end of the beam line where the target was mounted. We used a water-cooled target with copper backing and sufficient lithium-7 evaporated on it so that the target can fully stop the beam.

Gold wires were placed in the hole in the fifth layer. Gold only has one stable isotope, gold-197, which absorbs neutrons to form gold-198. Gold-198 has a short, 2.6 day half life and decays with a simple, easy to detect gamma spectrum with just one 411 keV peak, so it is idea for this experiment. Thirty-eight gold wires were used, each weighing about twenty milligrams. They were taped at two centimeter intervals to a two-inch-thick foam block to place them at the same height as a future radioactive beam.

2.2 Measurements

Four accelerator runs were conducted, two with the full graphite cube and two with only the lower four layers. Proton beams where run at either 1950 keV oe 2500 keV. Runs with the full cube where done for 2 hours, while half cube runs where done for longer so the gold activity would be just as detectable. The runs are summarized in Table 1.

Run number	Cube setup	Beam energy (keV)	Run time (hrs)	Total charge (C)
1	Full	1950	2	0.08
2	Full	2500	2	0.08
3	Half	1950	6	0.36
4	Half	2500	4	0.22

Table 1: Summary of each activation run performed on our apparatus.

After each run the activated gold wires were removed from the cube and individually counted using a high-purity germanium (HPGe) detector. The detector is shielded by copper and lead on all

but one side, where samples were placed. Using the program Maestro we recorded the spectrum of each wire. Maestro is able to subtract the background in a selected region of interest to give the net counts in a given peak. Total counts for peaks were found using this method, with runs lasting at least long enough for these counts to reach around five hundred.

We used the net counts of gamma decays at 411 keV to calculate the yield of gold-198 atoms produced by each accelerator run. Eqn. 1 gives the number of radioactive nuclei in a sample at time t in terms of the initial yield of radioactive nuclei N_0 and the decay constant λ. This is applied to the time between the end of activation runs and the beginning of counting t_{wait} and the time spent counting t_{count} in Eqn. 2. The difference between the number of nuclei before and after the start of counting times the efficiency of the detector setup ϵ gives the recorded counts C. Combined with Eqn. 2 this gives Eqn. 3. By solving for N_0 and rewriting in terms of half-life $T_{\frac{1}{2}}$ we get Eqn. 4 which gives the number of Au-198 atoms from the counts measured under a 411 keV peak.

$$N(t) = N_0 e^{-\lambda t} \tag{1}$$

$$N(t_{wait}) = N_0 e^{-\lambda t_{wait}}, N(t_{count}) = N(t_{wait}) e^{-\lambda t_{count}} \tag{2}$$

$$C = \epsilon[N(t_{wait}) - N(t_{count})] = \epsilon N_0 [e^{-\lambda t_{wait}}(1 - e^{-\lambda t_{count}})] \tag{3}$$

$$N_0 = \frac{C}{\epsilon}[2^{-t_{wait}/T_{1/2}}(1 - 2^{-t_{count}/T_{\frac{1}{2}}})]^{-1} \tag{4}$$

Additionally an adjustment to account for dead time of the detector setup and normalization for the number of initial gold-197 atoms in the wire and the number of protons which hit the lithium target is added to the data before it is plotted. When we reuse wires from previous runs residual activity is also subtracted out.

Additionally activity of the graphite blocks was measured using the same HPGe detector. Blocks

were measured before and after the experiment to determine if any new radioactive isotopes were created in them. Blocks were chosen which would have high exposure to neutrons.

3 Results

3.1 Graphite Activity

From spectrum taken of the graphite blocks before activation runs, we identified radioactive europium-152. The gamma spectrum of europium-152 has many peaks, but the most visible peaks for occur at 344 keV and 1408 keV (see dotted lines in Figure 2). The net count rates of both peaks were recorded using Maestro.

The radioactivity of the graphite blocks changed little during our experiment. Table 2 gives the count rates before and after the experiments. Block one and two are the short plugs placed in front of the lithium target for full cube runs; block one was nearest to the target and block two was behind block one. Block three was a full length block placed below the target for all runs. Since the counts at these two measured peaks did not change significantly from our experiments, we can conclude that our experiments did not increase the activity of the Europium in the blocks.

Block	344 keV Before	344 keV After	1408 keV Before	1408 keV After
1	1.348 ± 0.003	1.340 ± 0.005	0.642 ± 0.002	0.660 ± 0.003
2	26.47 ± 0.05	26.00 ± 0.02	12.93 ± 0.03	12.85 ± 0.02
3	0.079 ± 0.003	0.076 ± 0.002	0.0482 ± 0.0001	0.0484 ± 0.0001

Table 2: Europium-152 activity from graphite blocks before and after being using in the moderating cube. All values are reported in counts per second. Values for block 3 are an average of multiple counting runs. Uncertainties are from uncertainty in the Maestro fits for counts in each peak.

Spectrum taken before and after our experiments also show that no new radioactive isotopes where created in the blocks (see Figure 2 for the spectrum from block three). If new radioactive isotopes were present, they would appear as new peaks in the spectrum taken after the experiment that were not present before. We found no significant new peaks. While there are many peaks from both background and europium-152, the peaks are present at similar heights in both spectrum.

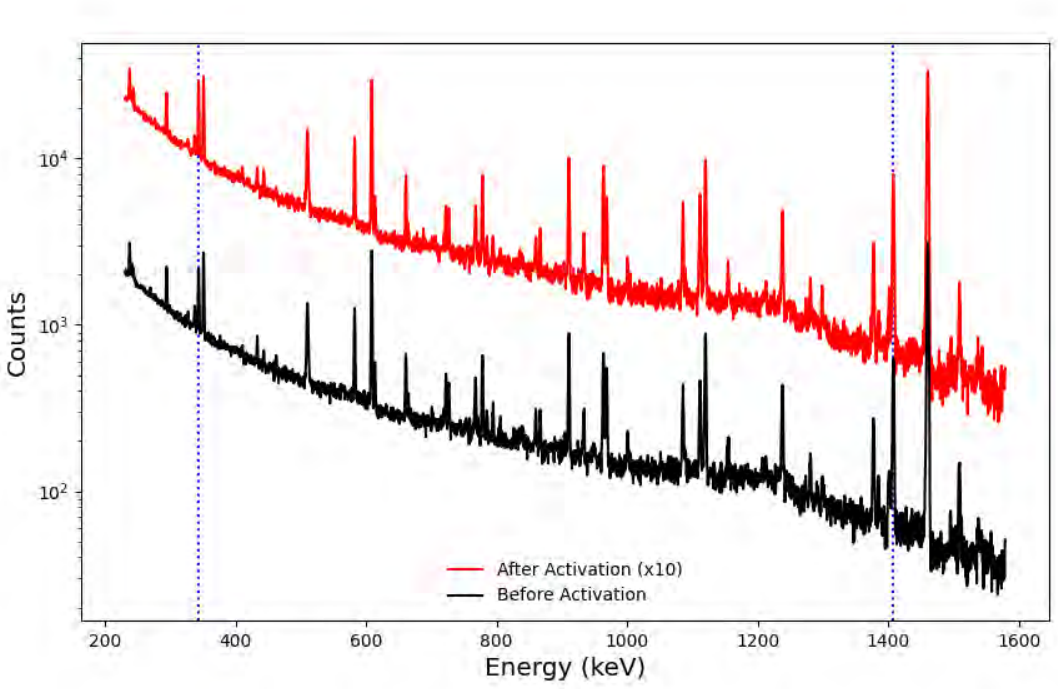

Figure 2: Partial spectrum from a HPGe detector for a graphite block both before (lower line) and after (upper line, scaled by a factor of 10) our experiments. Dotted lines at 344 keV and 1408 keV mark the largest peaks from Eu-152 decays. The lack of new peaks or significant increases in existing peak in the after activation spectrum suggests little new radioactive material was created.

3.2 Gold Activations

Figures 3-6 shows how the number of neutrons reacting with the gold wires varies across the graphite cube for each run. Position is defined with the beam right side of the cube as zero. Gold-198 yield is calculated using Eqn. 4 as described previously.

We see significant differences in the yields of the runs with the same cube but different energies. The 2500 keV runs have about ten times the yield as the corresponding 1950 keV runs. The cross section for the ^{7}Li(p,n)^{7}Be reaction is similar at both energies, so similar amounts of neutrons are produced. However, neutrons produced in the 2500 keV runs will have more energy than those from 1950 keV runs so they can bounce more times in the moderator are therefore more likely to hit the gold wires. Comparing the runs with different cube setups, we see that the full cube produced much higher yield. Full cube runs have about twenty times the energy as half cube runs with the same

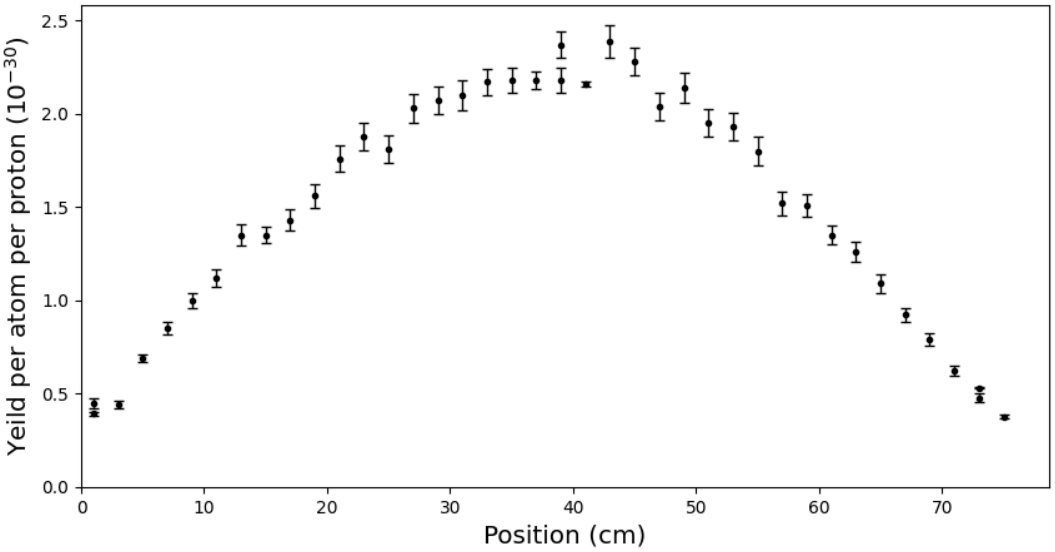

Figure 3: Au-198 yield per Au-197 atom per proton v. position for gold wires from a run with 1950 keV proton beam and full cube (see run 1 in Table 1). Uncertainty in adsorption is from uncertainty in the number of counts recorded.

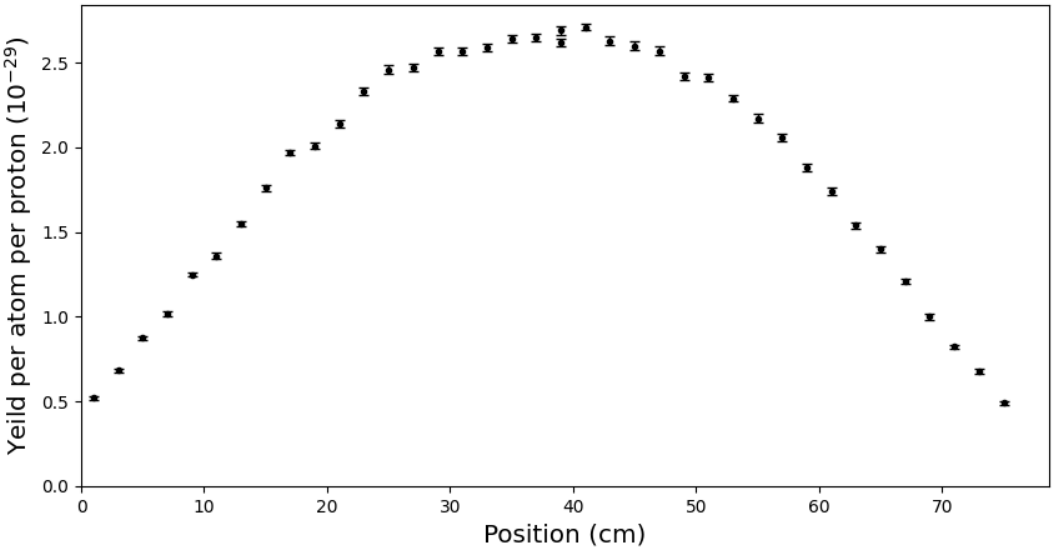

Figure 4: Au-198 yield per Au-197 atom per proton v. position for gold wires from a run with 2500 keV proton beam and full cube (see run 2 in Table 1). Uncertainty in adsorption is from uncertainty in the number of counts recorded.

energy. Without the top part of the cube, neutrons which are emitted upward from the lithium target are not bounced back to the gold and neutrons bounced upward out of the remaining graphite are

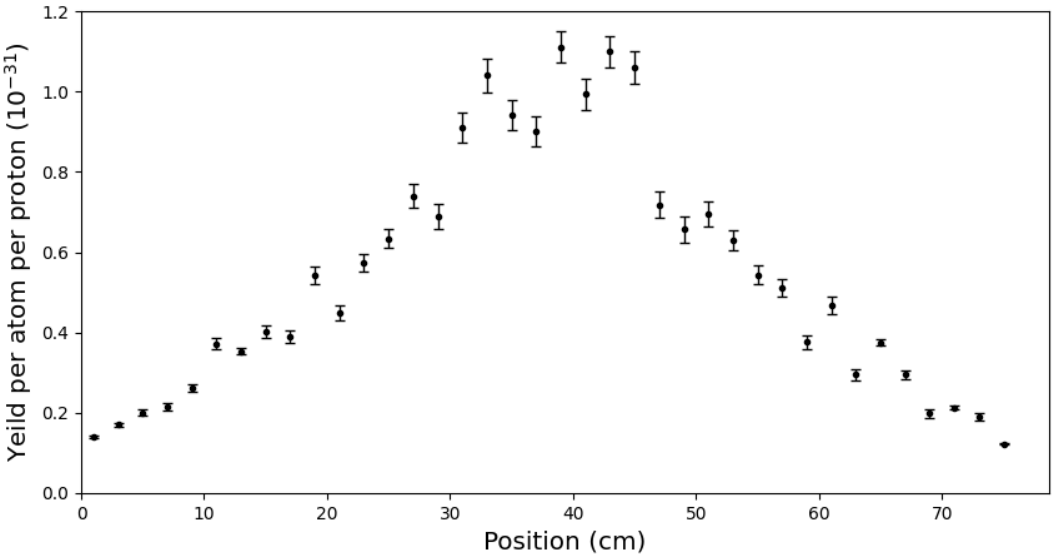

Figure 5: Au-198 yield per target atom per Au-197 v. position for gold wires from a run with 1950 keV proton beam and half cube (see run 3 in Table 1). Uncertainty in adsorption is from uncertainty in the number of counts recorded.

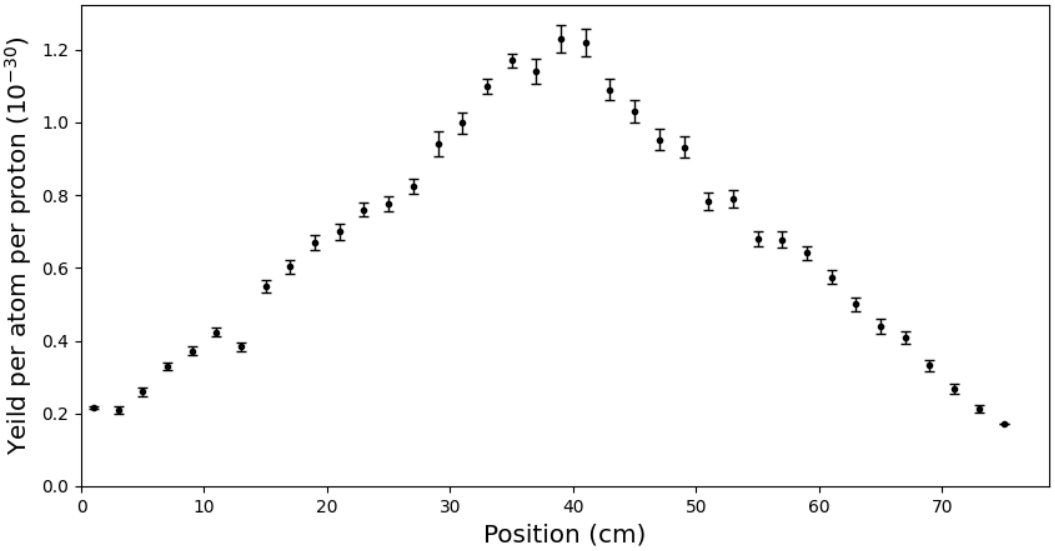

Figure 6: Au-198 yield per Au-197 atom per proton v. position for gold wires from a run with 2500 keV proton beam and half cube (see run 4 in Table 1). Uncertainty in adsorption is from uncertainty in the number of counts recorded.

also lost. This accounts for the lower yields with the half cube. Additionally note how the sharply peaked shape of the half cube runs compares to the more rounded shape with the full cube. Yeild

begins to drop quicker with the half cube. This suggests that the edges of the cube relies more on neutrons which are bounced back by the graphite while neutrons can reach the center with less bouncing.

4 Conclusion

This experiment was able to successfully create a test setup for radioactive neutron capture reactions. Our experiment confirmed that our graphite cube moderates and deflects neutrons so that they can be used in reactions. In particular, our results show that yield will increase with higher energy proton beams and that a half cube of moderator will create lower yield than the full cube, particularly on the edges. We also showed that activation runs do not create significant radioactivity in the moderator.

Future work by collaborators will compare the yield data presented here to simulations of the setup so we will have accurate simulations for future use. An additional test run is also planned with higher energy spallation neutrons at Los Alamos. Eventually this work will lead to the construction at Los Alamos of radioactive ion beam for this setup which can be used to replicate and measure radioactive nuclei neutron captures such as those which occur in stellar environments.

5 Acknowledgements

Thanks to the following collaborators: Rene Reifarth, Andrew Cooper, Aaron Couture, and Olivia Cantrell from Los Alamos National Laboratory, Ed Stech, James deBoer, Daniel Robertson, Khachatur Manukyan, and Miriam Matney from the University of Notre Dame, and Caroline Harrington from the Air Force Institute of Technology for their contributions to this project.

References

[1] R. Reifarth, A. L. Cooper, A. J. Couture, and S. M. Mosby 10.2172/2229692.

The Effect of Low-Temperature Atmospheric Pressure Plasma Jet Parameters on Hydroxyl Radical Production

EMILY CLARK

2024 NSF/REU Program
Department of Physics and Astronomy
University of Notre Dame

ADVISOR(S): Dr. Sylwia Ptasinska

Abstract

In order to further develop applications of plasma irradiation, it is crucial to investigate the effect of plasma parameters on hydroxyl radical production. Hydroxyl radicals damage and kill cancer cells. Due to the short lifetime of hydroxyl radicals, we utilize an indirect quantification technique. We calculate the concentration of 7-hydroxycoumarin in irradiated coumarin samples as a way to measure hydroxyl radical production at various plasma voltages and frequencies. We find that hydroxyl radical production overall increases with an increase in voltage and frequency. Understanding the trends that arise from varying plasma parameters allows us to further explore the impacts of plasma-generated reactive species on biological material.

1 Introduction

The antitumor effects of low temperature plasmas at atmospheric pressures has been well established by many previous studies, which is particularly interesting for the field of clinical medicine, especially in the areas of cancer treatment and wound healing [1]. Atmospheric pressure plasmas have been shown to selectively damage and kill cancerous cells while healthy cells remain alive [2]. This eliminates the downsides of modern cancer treatments such as chemotherapy, radiation therapy, and surgery which lack this selective nature on the cellular scale. Additionally, low temperature plasma jets are at a temperature suitable for biological material, making them appropriate to use on human tissue.

1.1 Hydroxyl Radicals and DNA Damage

Low temperature plasmas produce an abundance of reactive species, including reactive oxygen species (ROS). One important ROS that is generated is the hydroxyl radical, which is the neutral form of hydroxide. Hydroxyl radicals are highly reactive and oxidizing (with a redox potential of 2.8 V), damaging cancerous cells and leading to cell death. Hydroxyl radicals have specifically been correlated with DNA damage [3][4] and studies have shown that DNA damage increases with irradiation time [5].

1.2 The Need for Indirect Quantification

Given the short lifetime of the free hydroxyl radical ($\sim 10^{-9}$ s), this species is especially difficult to quantify. Therefore, an indirect method of quantification is needed. We chose to utilize the method outlined by Ducrozet et al. [6]. The coumarin present in our samples reacts with the hydroxyl radicals produced by the plasma jet and forms 7-hydroxycoumarin. Therefore, quantifying the amount of 7-hydroxycoumarin produced provides the amount of hydroxyl radicals produced. 7-hydroxycoumarin has a high fluorescence yield, therefore fluorescence spectroscopy is an effective and sensitive measurement technique [6]. The measured fluorescence intensity value of our samples can be converted to a value of 7-hydroxycoumarin concentration.

The study conducted by Ducrozet et al. performed an analysis of the extremes of the plasma jet's parameters (8 kV at 1 kHz and 10 kV at 4 kHz) [6]. These results provided the range of the amount of hydroxyl radicals that can be produced by a low temperature plasma jet. In order to understand how the plasma parameters of voltage and frequency can affect hydroxyl radical production, we need to conduct measurements at values in between these extremes. The optimal plasma parameters to use in a clinical setting are still disputed and knowing the amount of radicals produced at various parameters will help in determining the optimal parameters and further the development of plasma-based cancer treatments.

In this study, we will vary the voltage and frequency of a low temperature atmospheric pressure plasma jet and quantify the amount of hydroxyl radicals produced based on the resulting 7-hydroxycoumarin concentration. We will then discuss the trends that arise from varying these parameters.

2 Background

The mechanisms behind the selective nature of plasma that allow the plasma-produced radicals to kill cancer cells while healthy cells remain intact has to do with the biological differences between these cells. Cancerous cells metabolize lipids differently than healthy cells, which leads to negative

impacts on the structure of the cancerous cell membrane. The cancer cells' membranes allow higher rates of diffusion of plasma-produced radicals into the cellular interior [1]. The presence of reactive oxygen and nitrogen species produced by the low temperature plasmas in the cancerous cell leads to damage of the mitochondria, destruction of the antioxidant system, initiation of cell cycle arrest, DNA damage (including double strand and single strand breaks), and apoptosis [1][5][7]. Apoptotic cell death is preferred to necrotic cell death, as the apoptotic bodies are phagocytosed, preventing inflammation.

3 Methods

3.1 Plasma Irradiation

Samples of ultra-pure water, 1.5 mM coumarin, and 10 mM phosphate buffer (500µL total) were prepared to be plasma-irradiated. Phosphate buffer was included in the samples to ensure we maintained a constant pH [6]. We maintain a constant pH because plasma irradiation causes a decrease in pH, which can affect our measurements by increasing the fluorescence intensity [6]. The irradiation was performed by a helium-fed (99.999% purity) atmospheric pressure low temperature plasma jet ignited by a dielectric barrier and fed at a steady 2 standard liters per minute (slm). A more complete description of the plasma jet set-up is given in Ducrozet et al. [6]. We irradiated samples at voltages of 8 kV, 9 kV, and 10 kV and frequencies of 1 kHz, 2 kHz, 3 kHz, and 4 kHz, with every combination of parameters being tested. For every combination of voltage and frequency, we irradiated samples from 0 s to 90 s.

3.2 Fluorescence Spectroscopy

Before performing fluorimetry analysis, calibration samples were prepared of ultra-pure water, coumarin, and 7-hydroxycoumarin with different 7-hydroxycoumarin concentrations to quantify the amount of 7-hydroxycoumarin produced in the irradiated samples. The irradiated and calibration samples were analyzed by an Infinite 200 Pro microplate reader fluorescence spectrometer

(Tecan Group Ltd, Switzerland) with an excitation beam of 326 nm and fluorescence emission was measured in a wavelength range of 380-600 nm. We were then able to convert the fluorescence intensity values to 7-hydroxycoumarin concentration using the values obtained from the calibration samples.

4 Results

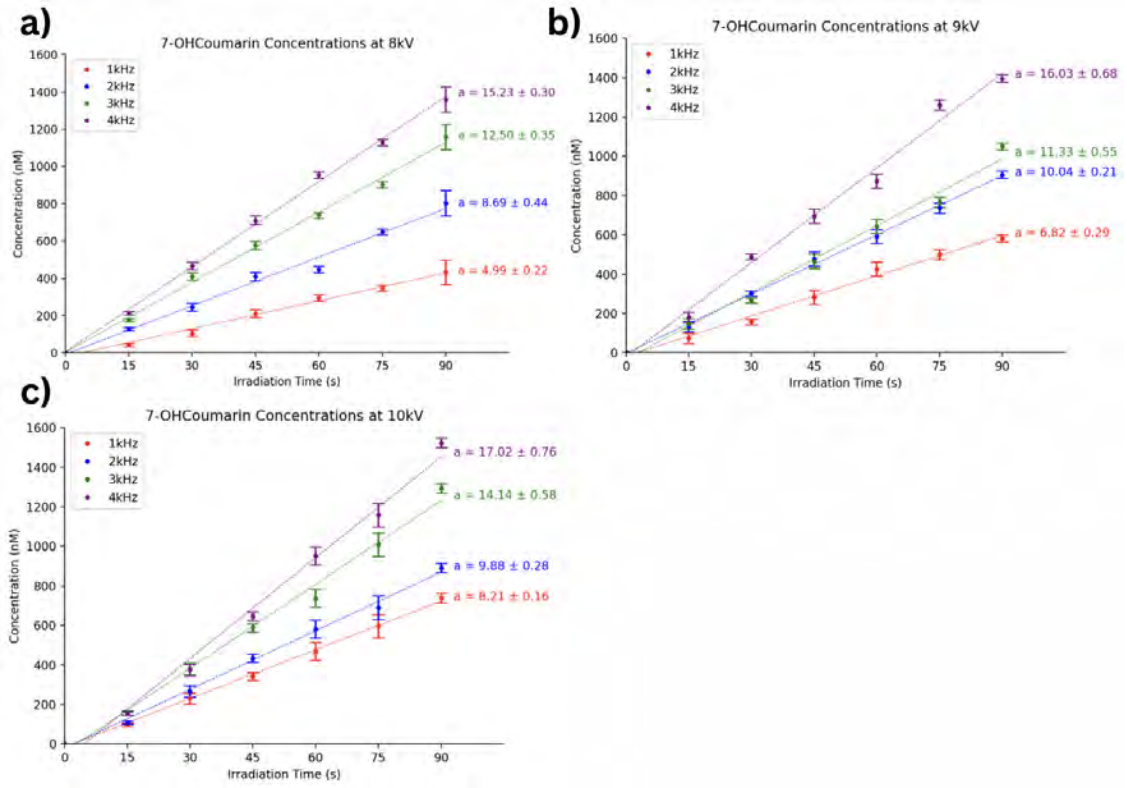

Figure 1: 7-hydroxycoumarin concentration as a function of irradiation time at constant voltages where (a) is at a voltage of 8 kV, (b) is at a voltage of 9 kV, and (c) is at a voltage of 10 kV.

Fig. 1a shows that at a voltage of 8 kV, the concentration of 7-hydroxycoumarin increases as the plasma frequency increases. The slope of the line of best fit for 8 kV and 1 kHz aligns with the results found in Ducrozet et al. [6]. We notice that at 8 kV, an increase in frequency from 1 kHz to 4 kHz about triples the slope of 7-hydroxycoumarin concentration over irradiation time. In Fig 1b, we observe a similar trend as in Fig 1a, with the concentration of 7-hydroxycoumarin increasing with an increase in plasma frequency at a voltage of 9 kV. Each of the line of best fit slopes in Fig.

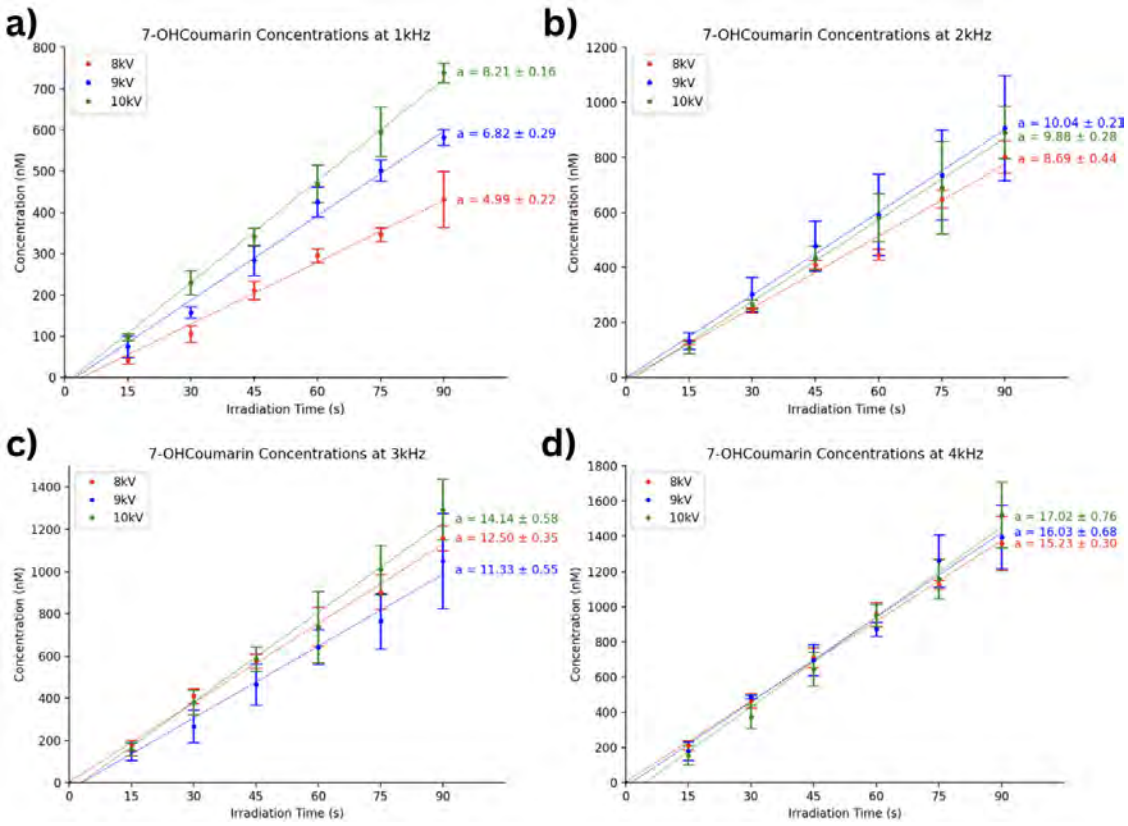

Figure 2: 7-hydroxycoumarin concentration as a function of irradiation time at constant frequencies where (a) is at a frequency of 1 kHz, (b) is at a frequency of 2 kHz, (c) is at a frequency of 3 kHz, and (d) is at a frequency of 4 kHz.

1b increased from the slopes in Fig. 1a at their respective frequencies except for at 3 kHz, which had a slight decrease. We also note that the slope of 7-hydroxycoumarin concentration over irradiation time more than doubles from 1 kHz to 4 kHz at 9 kV. As in Fig. 1a and Fig. 1b, we observe in Fig. 1c that the concentration of 7-hydroxycoumarin increases with increasing plasma frequency at 10 kV. All of the slopes in Fig. 1c increase from their values in Fig. 1b at their respective frequencies except for at 2 kHz. The slope of 7-hydroxycoumarin concentration over irradiation time about doubles from 1 kHz to 4 kHz.

Based on Fig. 2a and Fig. 2d, we observe that at plasma frequencies of 1 kHz and 4 kHz the slope of 7-hydroxycoumarin concentration over irradiation time increases with an increase in plasma voltage. This trend is not necessarily observed in Fig. 2b and Fig 2c at 2 kHz and 3 kHz. It is also important to note that in Figs. 2b, 2c, and 2d (frequencies of 2 kHz, 3 kHz, and 4 kHz)

there is significant overlapping of error bars between values at the different voltages.

It has been established by previous studies that high humidity conditions increase the amount of radicals produced in an atmospheric plasma jet [8][9]. During the 9 kV measurements, there was a higher level of humidity than there was during the other measurements. Most of the experiments were done at humidities $< 61\%$, but all of the 9 kV trials were done with humidities $> 61\%$. We believe that this has contributed to some of the error. More trials could be done in less humid conditions to decrease the error.

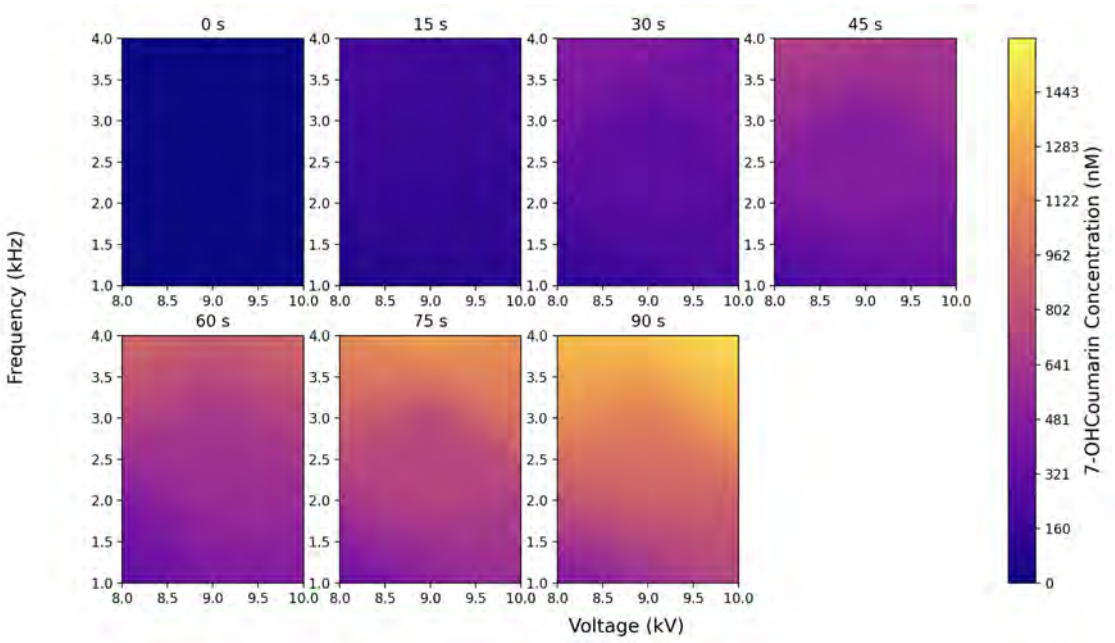

Figure 3: 7-hydroxycoumarin concentration heat map where each subfigure represents a different irradiation time with frequency varying on the y-axis and voltage varying on the x-axis.

Fig. 3 allows us to better visualize the trends as both voltage and frequency change. From this, we can conclude that generally increases in voltage, frequency, and irradiation time will increase the concentration of hydroxyl radicals produced by the plasma jet. It appears that changes in frequency have a stronger and more consistent effect on the concentration of hydroxyl radicals than changes in voltage do.

5 Conclusion

In this study, we examined the effect that plasma parameters have on the production of hydroxyl radicals in a low temperature atmospheric pressure plasma jet. We found that increasing the frequency of the plasma to 4 kHz can increase the rate of hydroxyl radical production by anywhere from double to triple the rate at 1 kHz. We believe that increasing the voltage increases hydroxyl radical production as well, but more trials need to be conducted to establish clearer trends. Observing these trends allows us to better understand radical production in plasma jets when translating this technology to medical treatments.

6 Acknowledgements

I would like to thank Dr. Sylwia Ptasinska for providing me with this opportunity to work and learn from the Ptasinska lab. I would also like to thank graduate student Cecilia Garcia Villavicencio for her mentorship and help. Thank you to Dr. Umesh Grag and Ms. Kristen Amsler for organizing the 2024 Notre Dame REU program. Finally, thank you to the NSF for the funding for this project.

References

[1] E. Alizadeh and S. Ptasinska, Biophysica **1**, 48 (2021).

[2] K. P. Arjunan, V. K. Sharma, and S. Ptasinska, International Journal of Molecular Sciences **16**, 2971 (2015).

[3] D. O'Connell, L. J. Cox, W. B. Hyland, S. J. McMahon, S. Reuter, W. G. Graham, T. Gans, and F. J. Currell, Applied Physics Letters **98**, 043701 (2011).

[4] S. Ptasinska, B. Bahnev, A. Stypczyńska, M. Bowden, N. Mason, and N. S. J. Braithwaite, Physical Chemistry Chemical Physics **12**, 7779 (2010).

[5] E. R. Adhikari and S. Ptasinska, The European Physical Journal **70**, 180 (2016).

[6] F. Ducrozet, A. Sebastian, C. J. Garcia Villavicencio, S. Ptasinska, and C. Sicard-Roselli, Royal Society of Chemistry **26**, 8651 (2024).

[7] M. P. Lesser, Annual Reviews **68**, 253 (2006).

[8] D. Han, Current Applied Physics **18**, 1375 (2018).

[9] E. R. Adhikari, V. Samara, and S. Ptasinska, Journal of Physics D: Applied Physics **51**, 185202 (2018).

Corotation Model for the Circumgalactic Medium of the Andromeda Galaxy

LUCY COLLINS

2024 NSF/REU Program
Department of Physics and Astronomy
University of Notre Dame

ADVISOR(S): Professor J. Christopher Howk

Abstract

This project seeks a better understanding of the kinematic properties of M31's circumgalactic medium (CGM) by determining the extent of the gaseous halo's corotation with the galaxy disk. Through the kinematic properties of a CGM, we gain insight into the formation of the galaxy and its halo, as well as its ongoing evolution, including processes such as accretion, outflows, and tidal streams. We developed a model that assumes corotation to predict the line-of-sight velocity at various sightlines of quasi-stellar objects (QSOs), depending on QSO position relative to the galaxy. This model will be used for comparison with observational data from QSOs surrounding M31, to measure the prevalence of corotation, and allow a greater understanding of the formation history and ongoing evolution of M31.

1 Introduction

In the process of studying the formation and evolution of galaxies, and more broadly the cosmology of the universe, a common observational method of astrophysics has been to utilize the light spectra produced by quasi-stellar objects (QSOs). The light from QSOs that pass through the area around a galaxy and the absorber particles along the sightline, grants a valuable opportunity to study the circumgalactic medium (CGM) of many galaxies [1].

The CGM of a galaxy is a gaseous halo that extends in all directions beyond the stellar disk, generally reaching as far as the virial radius of the galaxy, which contains the matter gravitationally bound to it (often around 200 kpc) [1]. The spectroscopy of background light sources offers a glimpse of the elements and molecules present in the halo, as well as the velocity of these absorbers (projected along the line of sight).

Project AMIGA (Absorption Maps In the Gas of Andromeda) uses QSO spectroscopy to study the CGM of a single galaxy, M31 (the Andromeda Galaxy) [2]. Project AMIGA has examined dozens of QSO sightlines through the CGM of M31, characterizing this gas halo in great detail.

The kinematics of the CGM are a crucial aspect of understanding M31 and other galaxies. Simulations have suggested that inflows bring halo gas into the galaxy, feeding star growth, and outflows push gas out of the disk and into the CGM [1]. Additionally, gas moves from the intergalactic medium (IGM), which sparsely populates the space between galaxies. This inflowing gas

is of particular interest, as it may provide disks with angular momentum as it infalls—causing rotation and possibly causing a galaxy's CGM to corotate with its disk [3]. Thus, the kinematics of the CGM are crucial to understanding the formation and evolution of galaxies, as the disk, CGM, and IGM interact with one another throughout a galaxy's lifetime.

One approach to this issue has been to model how the CGM might move if it was assumed to corotate with its host galaxy, taking into account the distance from the disk's center [4] [3]. When using the spectra of QSOs, only velocities along the sightline can be detected, so the actual velocity of absorbers may be larger than what we detect depending on the direction of motion. Therefore, the goal of this project was to create a model that assumes halo gas in the CGM is corotating with the disk, that takes into account the position of the QSOs and the manner of the galaxy rotation to predict the velocities that could be measured.

By comparing the model line-of-sight velocities with the measured velocities, we can determine the extent of corotation present in the CGM of M31. Additionally, due to the large scope of Project AMIGA's QSO sightline observations, we may also be able to examine how the prevalence of corotation is affected by a variety of factors, including the azimuth angle in the plane of the galaxy, and distance from the center. The extent of corotation will grant insight into the kinematics of a CGM and its host galaxy and the formation and evolution of galaxies over time.

2 Background

This research follows many other efforts to examine the kinematics of the CGM of various galaxies with similar methods. In particular, the model produced is largely based on the model created by Steidel et al. (2002) [4], later reproduced by French & Wakker (2020) [3], which assumes halo corotation with the galaxy disk, using an extended thick disk model and adjustable parameters for z dependence (z being the height above the disk).

Determining the extent of corotation by comparing modeled velocities with measured velocities will grant significant insight into the kinematics of the CGM and its host galaxy. In particular, this could indicate the extent of different accretion models: "hot-mode" and "cold-mode" accretion from

the IGM. Hot-mode accretion describes gas that approaches the galaxy CGM, and "shock-heats at the virial radius," which then causes the inner regions of the halo to fall down to the disk as the gas cools [3]. In contrast, in cold-mode accretion, cool gas from IGM filaments "merge smoothly with the disk," which allows for the infall velocity to contribute to the galaxy's rotational velocity by bringing significant angular momentum [3] [5]. Observing corotation in the CGM would indicate a history of recent cold-mode accretion, as more recently accreted gas rotates in an extended disk, far into the CGM [5].

Thus, the extent of corotation present in the CGM can provide insight into the processes dominating its gas, like the particular accretion process fueling star formation in galaxies. By comparing models with measured velocities, we can look for matching kinematics. For example, Diamond-Stanic et al. (2016) used similar models to look for a variety of kinematic possibilities, including the corotation of an extended disk, an outflowing wind, and high-velocity clouds (HVCs), among other phenomena [5].

This project's focus on modeling rotation in the halo gas of M31 is just one aspect of Project AMIGA, which is surveying the CGM with numerous QSO sightlines [2]. Rather than looking at one or few sightlines for many galaxies, the choice to study M31's CGM in-depth grants a thorough understanding of one CGM's composition and kinematics—which will offer crucial insight into the processes of a galaxy very similar to the Milky Way. Thus this project will contribute to the understanding of our home galaxy and its evolutionary history.

3 Methods

To best model the kinematics of halo gas, we established coordinate systems to describe the geometry of the disk and surrounding halo both in the perspective of viewing it two-dimensionally against the plane of the sky, and considering the three-dimensional orientation of the disk in space. The 2D system was largely based on a previous system used by Project AMIGA, while the 3D system was inspired by the models in Steidel et al. (2002), French & Wakker (2020), and Diamond-Stanic et al. (2016) [4] [3] [5].

The 2D system views M31 against the plane of the sky, with the origin set at the galaxy center and a simple XY Cartesian system. The disk of M31 is at a position angle α of 45° east of north (from the Y-axis, with the additional consideration that the coordinates run counterclockwise here: N, E, S, W). Either X and Y, or the impact parameter ρ and α, can be used to identify points.

The 3D system sets the origin at the galaxy center, with the x-axis following the major axis (as viewed from Earth) and the y-axis following the minor axis (along the plane of the disk). The z-axis is perpendicular to the galaxy disk and reflects height above and below the galaxy. Another crucial measurement is the inclination angle θ_i of the galaxy, which describes the angle between the plane of the sky and the galaxy disk (with 90° meaning the galaxy is viewed edge-on). For M31, the inclination angle $\theta_i = 77.5°$.

After establishing the coordinate systems and how to convert between them, we created a model that uses the galaxy's orientation to determine how the rotation velocity of the CGM would appear projected along the line of sight. By inputting the X and Y coordinates of a sightline, as well as a distance along the line of sight (with D_{los} being zero where it intersects the galaxy plane), we calculate the x, y, and z coordinates, then use these to calculate the velocity along the line of sight v_{los}. We followed Steidel et al. (2002), in modeling it as an extended disk, with variable z dependence, causing a decrease in velocity with height. This velocity scale height h_v reduces the $v_{los}$for greater heights as shown in equation 1. The following equation is a function of the circular velocity v_c, the inclination angle θ_i, x, y, and y_0 (the y coordinate where the sightline intersects the galaxy plane, based on equation 6 in Steidel et al. (2002) [4].

$$v_{los} = \frac{-v_c}{\sqrt{1 + (y/x)^2}} e^{-(y-y_0)/\tan\theta_i h_v} \tag{1}$$

The circular velocity v_c is particularly important for an accurate model. We used a flat rotation curve for initial programming and tests, with a circular velocity that remained constant regardless of location or radius. However, to be more accurate to the actual motion and matter distribution of galaxies and their CGMs, we utilized the Navarro–Frenk–White (NFW) profile for the distribution

and movement of dark matter halos to calculate a variable rotation curve, as done in French & Wakker (2020) [6] [3]. This model takes into account the galaxy mass, virial radius R_{200}, virial velocity v_{200}, and x to calculate v_c at various radii, as shown in equation 2. In this equation, $x = R/R_{200}$ and the concentration c (which had a value of 7.94 for M31) [3]. This equation allows us to create a rotation curve of v_c that is more accurate to the varying enclosed masses and radii at different locations.

$$v_c(R) = v_{200}\left[\frac{\ln(1+cx)) - cx/(1+cx)}{x[\ln(1+c) - c/(1+c)]}\right]^2 \tag{2}$$

Ultimately, we completed a versatile model that is adaptable for various scale heights, circular velocity models, and galaxies of various orientations.

4 Results

To test the model, we chose a point based on the impact parameter and position angle, choosing a spot 50 kpc from the galaxy center, along the line of the disk ($\rho = 50$ kpc, $\alpha = 270°$), and we calculated v_{los}. We initially utilized a flat rotation curve of $v_c = 220\ \mathrm{km\,s^{-1}}$. Additionally, we examined the impact of a varying ρ. As shown in Figure 1, which plots the relationship between $v_{los}$and D_{los}, the curve becomes steeper for lower impact parameters, showing that the velocity decreases more rapidly for sightlines closer to the galaxy center.

Another crucial parameter was the velocity scale, h_v, which controls the extent of z dependence, with smaller values of h_v causing a more rapid drop in velocity with height. As shown in Figure 2, for lower h_v, the v_{los}increases more slowly as D_{los}approaches 0, as expected.

Next, we used a more accurate model of v_c, instead of the flat rotation curve used in the last two graphs. This model calculates v_c as a function of radius, based on the NFW profile. Figure 3 is almost identical to Figure 1, and plots the v_{los}vs. $D_{los}$for each of the same impact parameters, but demonstrates how the graph is altered when the rotation curve is no longer flat.

Finally, we applied this model to the sightlines being studied in Project AMIGA. For each sightline, we calculated the $v_{los}$from D_{los}= -300 kpc to 300 kpc, and then determined the minimum and

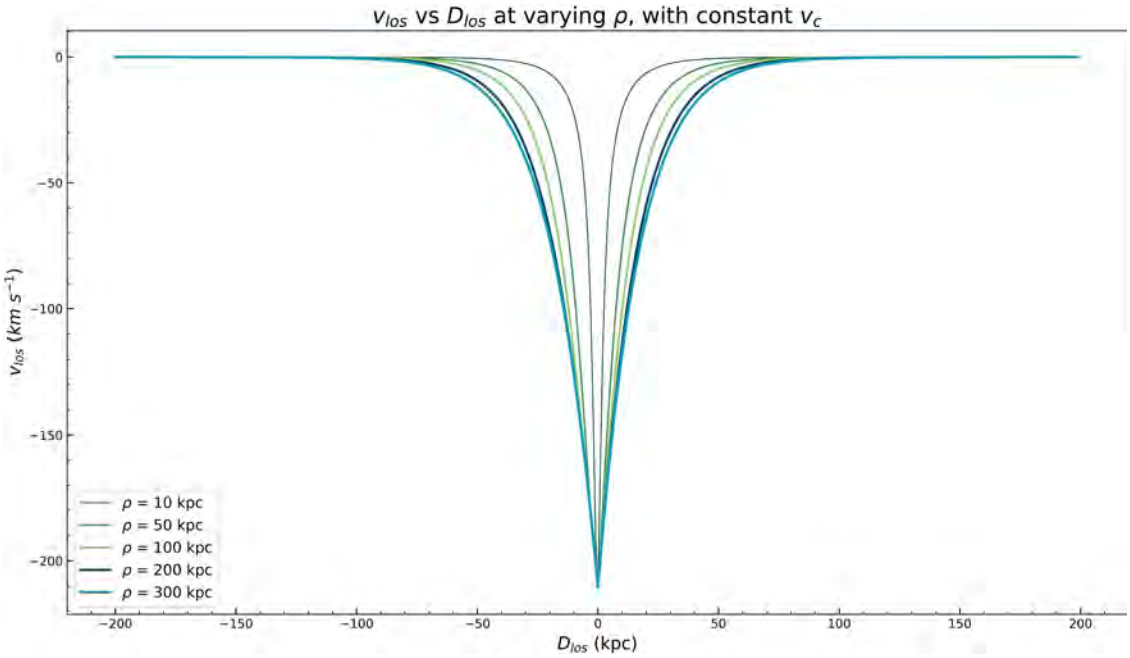

Figure 1: This plot shows v_{los}vs. D_{los}, at a sightline located at a $\alpha = 270°$, for varying impact parameters ($\rho = 10, 20, 50, 100, 200, 500$ kpc). The velocity scale height h_v used was 20 kpc. The v_c is a constant 220 km s^{-1}for this plot. Note that $D_{los}$is 0 at the center of the x-axis and $v_{los}$is 0 at the top of the y-axis.

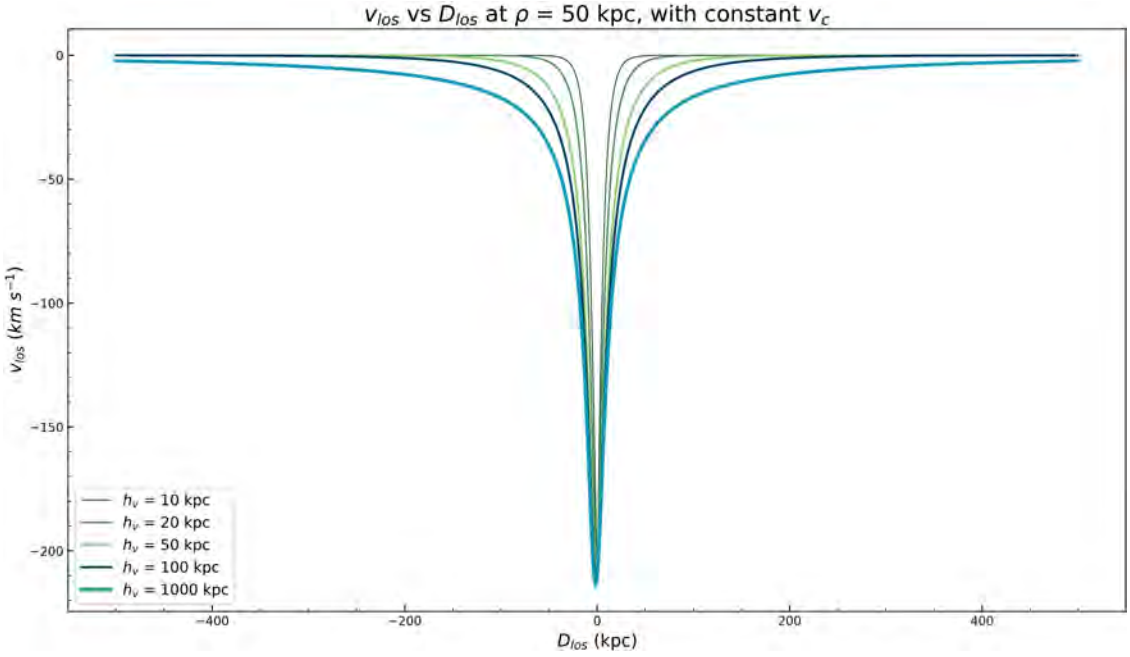

Figure 2: This plot shows v_{los}vs. D_{los}, at a sightline located at a sightline located at $\rho = 50$ kpc, α= 270°, for varying velocity scale (or $h_v = 10, 50, 100, 200, 500, 1000$ kpc). The v_c is a constant 220 km s^{-1}for this plot. Note that $D_{los}$is 0 at the center of the x-axis and $v_{los}$is 0 at the top of the y-axis.

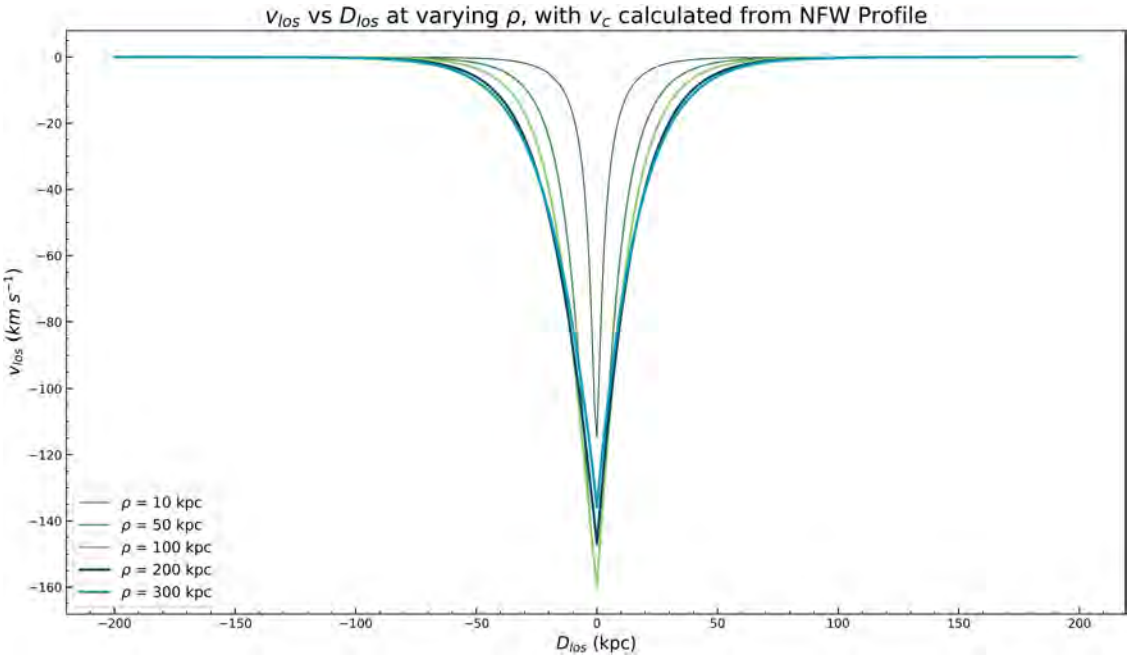

Figure 3: This plot shows v_{los}vs. D_{los}, at a sightline located at a $\alpha = 270°$, for varying impact parameters (ρ = 10, 20, 50, 100, 200, 500 kpc). The velocity scale height h_v used was 20 kpc. The v_c is not constant, but instead calculated as a function of radius for this plot. Note that $D_{los}$is 0 at the center of the x-axis and $v_{los}$is 0 at the top of the y-axis.

maximum velocity for each of them (after adding an estimated systemic velocity of -300 km s^{-1}to account for the overall movement of M31 towards the local standard of rest). This data, as well as the coordinates and ρ of each QSO, can be found in Table 1. These calculations were completed with $h_v = 20$ kpc and v_c calculated with the NFW profile.

Table 1: This table lists ten sightlines used to study the CGM of M31 in Project AMIGA. It gives the X and Y coordinates of the sightline, as well as the impact parameter ρ. For each of these sightlines, the $v_{los}$was calculated along D_{los}= -300 to 300 kpc, and the table shows the minimum and maximum values for each sightline.

Sightline	X **(kpc)**	Y **(kpc)**	ρ **(kpc)**	**Min** v_{los} (km s^{-1})	**Max** v_{los} (km s^{-1})
IVZw29	-1.2	-12.4	12.5	-300	-430
QSO0043+4234	2.8	17.1	17.3	-159	-300
RXJ0046.9+4220	10.2	14.2	17.5	-159	-300
RXJ0046.9+4220	10.2	14.2	17.5	-159	-300
RXJ0048.3+3941	14.1	-20.7	25.0	-158	-300
M31Halo_105_025	24.1	-6.5	25.0	-161	-300
M31Halo_000_025	-0.0	25.0	25.0	-151	-300

Sightline	X **(kpc)**	Y **(kpc)**	ρ **(kpc)**	**Min** v_{los} $(\mathrm{km\,s^{-1}})$	**Max** v_{los} $(\mathrm{km\,s^{-1}})$
M31Halo_075_025	24.1	6.5	25.0	-157	-300
M31Halo_285_025	-24.1	6.5	25.0	-300	-439
SDSSJ003125.36+403222.0	-28.2	-9.1	29.6	-300	-449

5 Conclusion

The model created in this project will be a valuable tool in studying the kinematics of the CGM, in M31 (with Project AMIGA) and other galaxies. In the future, the model will be applied alongside observational data, to compare the measured velocities from each sightline with the model's predictions—which will grant valuable insights into the kinematics of the CGM. The extent of rotation present will show the processes that dominate these kinematics and give information about the broader interactions between the galaxy disk, CGM, and IGM. Additionally, we will learn more about our own galaxy, the Milky Way, through understanding the formation history of M31 and its ongoing evolution.

References

[1] J. Tumlinson, M. S. Peeples, and J. K. Werk, **55**, 389 (2017), arXiv:1709.09180 [astro-ph.GA] .

[2] N. Lehner, S. C. Berek, J. C. Howk, B. P. Wakker, J. Tumlinson, E. B. Jenkins, J. X. Prochaska, R. Augustin, S. Ji, C.-A. Faucher-Giguère, Z. Hafen, M. S. Peeples, K. A. Barger, M. A. Berg, R. Bordoloi, T. M. Brown, A. J. Fox, K. M. Gilbert, P. Guhathakurta, J. S. Kalirai, F. J. Lockman, J. M. O'Meara, D. J. Pisano, J. Ribaudo, and J. K. Werk, **900**, 9 (2020), arXiv:2002.07818 [astro-ph.GA] .

[3] D. M. French and B. P. Wakker, **897**, 151 (2020), arXiv:2006.09323 [astro-ph.GA] .

[4] C. C. Steidel, J. A. Kollmeier, A. E. Shapley, C. W. Churchill, M. Dickinson, and M. Pettini, **570**, 526 (2002), arXiv:astro-ph/0201353 [astro-ph] .

[5] A. M. Diamond-Stanic, A. L. Coil, J. Moustakas, C. A. Tremonti, P. H. Sell, A. J. Mendez, R. C. Hickox, and G. H. Rudnick, **824**, 24 (2016), arXiv:1507.01945 [astro-ph.GA] .

[6] J. F. Navarro, C. S. Frenk, and S. D. M. White, **490**, 493 (1997), arXiv:astro-ph/9611107 [astro-ph] .

Modeling Chemical Parameters for Ultracool Dwarf Benchmarks in Binary Systems

LUCIA FISHER

2024 NSF/REU Program
Department of Physics and Astronomy
University of Notre Dame

ADVISOR(S): Roman Gerasimov, Evan Kirby

Abstract

Ultracool dwarfs (UCDs) are cool, dim stars that can be as old as the Galaxy and have atmospheres with complex molecular chemistry, making them valuable targets for studies in Galactic Archaeology, and modern telescopes have made large-scale observations of these faint objects possible. Due to the difficulty in modeling molecular spectra, the approach taken in this research was to locate UCDs in binary systems with sun-like primaries and analyze the spectra of these primaries. Assuming binaries formed from the same material, the chemical parameters from the primaries can be extrapolated to the secondary UCDs, which can then be used as benchmarks for UCD analysis outside of binaries. The python package chemfit was adapted for the primary spectra obtained from APF observations, with resulting parameters that indicate these binaries lie along the main sequence and within the thin disk of the Galaxy, as expected, and a high-resolution fit of star HIP 80232 gives parameters that agree with data from APOGEE. Future work to support this benchmark method would be an analysis of a larger sample of stars - particularly to find the old, metal-poor ones in the halo - as well as direct observations of the secondaries with which to compare the model parameters.

1 Introduction

Galactic archaeologists are constantly searching for and studying the oldest celestial objects to give them a better sense of what the composition and conditions of the early universe were like. Ultracool dwarfs are of particular interest because they can be as old as the universe, they are present everywhere, and their highly molecular atmospheres mean that their molecular abundances (and therefore spectra) will change dramatically with small changes in atomic abundances. However, since they are dim and their atmospheres host atoms and molecules with many millions of absorption lines, they are difficult to observe and complicated to model. A way to circumvent this issue is to find UCDs in binary systems and model the brighter primary stars. Since binary systems formed from the same material, the secondary star (the UCD) can be assumed to have the same chemical abundances as the primary star. These stars, whose composition would then be known, could subsequently be used as standards or benchmarks in modeling the composition of other UCDs. The python package chemfit, originally designed for Subaru Prime Focus Spectrograph (PFS) spectra, will be adapted for the higher resolution spectra of the bright primaries, obtained from recent Automated Planet Finder (APF) observations.

2 Background

2.1 Ultracool Dwarf Benchmarks

Ultracool dwarfs (UCDs) are low-mass stars and brown dwarfs with masses less than a tenth of the sun's and temperatures of 3000 K or less, and they are ideal subjects for galactic archaeology. Not only are some of them as old as the Galaxy – unlike high-mass stars which have short lifespans – but they are also nearly ubiquitous. Their cool temperatures mean less dissociation of molecules in their already molecule-rich atmospheres, which means they have good absorption features in their spectra. This, in conjunction with their ages, makes them perfect indicators of the chemical conditions of the early universe. They dim steadily over time, and their chemical composition is relatively unchanging, because they almost completely lack H-fusion in their cores, making them ideal for measuring how much the chemical composition of the surrounding stars and the Galaxy as a whole have changed over time [1].

These ultracool dwarfs are at the cooler end of the spectral types (M, L, T, and Y) [2]. Since they are very faint, they are difficult to observe, and since they have a lot of molecular absorption, they are complicated to model. One way around this problem is to locate ultracool dwarfs in binary systems with a brighter, sun-like star, typically of spectral types F, G, or K. Since binary systems formed from the same material, if the brighter primary star can be modelled, the secondary UCD can be assumed to have the same chemical parameters as the primary. These UCDs can be used as benchmarks for other UCDs that are not in binary systems by comparing their now known compositions with existing models to evaulate the models' accuracy, as well as by adjusting the parameters of the models to better correspond to the data. Once Recently the Automated Planet Finder (APF) has taken spectra of several of these binary systems, allowing us to model the primaries.

2.2 chemfit

To do this, we are adapting a python package called chemfit (Gerasimov, Kirby 2024), which was originally developed for data from the Subaru Prime Focus Spectrograph (PFS). The PFS uses

multiple "arms" or channels to cover a wide range of wavelengths, whereas APF uses echelle spectroscopy. Echelle spectra use wide-ruled diffraction gratings to cover different wavelength ranges called orders, and the ranges for adjacent orders can overlap. Each order follows a blaze function, which means that the edges of each order are less sensitive to light than the middle of the order, and the spectra are curved rather than following a straight continuum. Additionally, the APF spectra are of much higher resolution than the PFS spectra. All three of these features of echelle spectroscopy – the order overlap, the blaze function, and the higher resolution – must be accounted for in adapting chemfit.

chemfit is designed to find effective temperature (Teff), the surface gravity of the star (log(g)), the abundance of "metals" (i.e., all elements except H and He) in the star as compared to the sun ([Fe/H]), the abundance of alpha elements in the star, i.e. O, Ne, Mg, Si, S, Ar, Ca, Ti, relative to the sun ([a/Fe]), the Doppler shift of the star's spectrum (radial velocity, or redshift). chemfit finds these parameters using a grid of models based on known physics in stars (Grid7 [3] and GridIE [4] - currently these grids do not include stars with a supersolar metallicity ([Fe/H] > 0) or a log(g) greater than 5). chemfit compares the models to the observed spectrum and interpolates between them to find the one where the difference between the two is the smallest – the best fit model. Once it has the best fit model, it gives the parameters of the model, and we assume that those are the parameters of the star. When these parameters are obtained for a downsampled (lower-resolution) spectrum, they can be used as starting points around which higher-resolution models can be computed. These models give better estimates for stellar parameters as they are making full use of all the information in the observed spectra instead of blurring the features together by downsampling for a simpler fit.

3 Methods

3.1 Obtaining Stellar Spectra

Binary systems with sun-like primaries and UCD secondaries were selected for modeling from the Gaia eDR3 survey [5]. Stars with similar velocities and positions in the sky were located by El-Badry *et al.* [6] and added to APF's observation queue. The Automated Planet Finder at Lick Observatory was designed for exoplanets but has the right wavelength range and high resolution for measuring the chemical abundances of the primaries in these binary systems. The reduction of the spectra was carried out by our colleagues at Caltech and made available on the JUMP website [7]. Since chemfit models 1D spectra, the fluxes were pulled order by order from the files and used along with their corresponding wavelengths provided by APF [8] for their spectra.

3.2 Echelle Spectra and Redshift Corrections

Originally, chemfit fit all orders with one continuum fit - however, in echelle spectra each order follows a blaze function, which means that the edges of each order are less sensitive to light than the middle of the order, and the spectra are curved rather than following a straight continuum (see Figure 1. chemfit was adapted to account for this by fitting each order with its own continuum fit. It was also adapted for the overlap regions of the APF spectra orders by removing the "priority" feature which only used the data from whichever section was given priority in the overlap region when it was used for PFS "arms". In addition, many of the APF stars have multiple spectra, sometimes taken on different nights (Figure 1). For any given night, the earth is moving in a different direction toward or away from the star, so to combine these exposures, the redshift of each exposure must be calculated and applied to the wavelengths to perform heliocentric correction, i.e. convert them to their rest-frame (stationary) values.

3.3 Telluric Masks

The model fits and observed spectra for each order were graphed for a quick preliminary visual check that the models looked reasonable. In areas where there were consistent bad fits across multiple stars, masks were defined, which consist of a wavelength range for the fitter to exclude. All the ranges excluded were due to telluric features. These lines are quite strong and result from absorption by oxygen and other molecules in Earth's atmosphere. The groups of telluric lines were easily found by using a star of spectral type A as a template, which is largely featureless except for H-alpha, so any other features are not from the actual star but due to something else such as (in this case) atmospheric absorption (Figure 1). There were some other unwanted features in the spectra such as emission peaks from cosmic rays, but the majority are removed by identifying pixels more than 3 standard deviations away from the rest of the spectrum removing those pixels.

3.4 Excluding Orders

Only orders 20-56 of the 80 orders in APF spectra were used in modeling these stars. Orders 0-19 (defining order 1 to be 0 due to Python for loop conventions) and orders 72-79 were excluded because the chemfit model does not currently cover those wavelength ranges. The radial velocity became inconsistent for orders higher than order 57 - this is indicative of a bad fit because the radial velocity of the star should be constant across all orders, since the orders are from the same star which is moving at the same speed away from the earth. Radial velocity is also not tied to other parameters in the way that other parameters (such as temperature and metallicity) could be. Therefore the increase in scatter for these radial velocity values is a good indication that these fits should be excluded.

3.5 High-Resolution Fits

The maximum resolution of APF spectra is $R = 120,000$, which a given wavelength value is divided by to give the smallest resolvable feature at that wavelength. Since the exact resolution of the instrument is uncertain, the model was first blurred using a Gaussian FWHM of 0.5 sigma

HIP 80232	teff	logg	zscale	alpha
APOGEE	5335	4.66	-0.21	0.012
chemfit	5305	4.69	-0.27	0.114

Table 1: APOGEE parameters compared with chemfit parameters. There is reasonable agreement between the two.

to make a simpler, low-resolution fit. Once those parameters were calculated, they were used as starting points around which high-resolution models were calculated.

4 Results

A graph of alpha abundance vs metallicity (Figure 3) indicates the origin of stars - the halo, thick disk (high [α/Fe]), and thin disk (low [α/Fe], where the sun is). Given that the vast majority of stars lie in the thin disk, it is consistent that the sun-like binaries analyzed using chemfit lie mostly in the thin disk region of parameter space in this plot. The graph of surface gravity vs temperature (Figure 2) is similar to a color-magnitude diagram and indicates the evolution of the stars. As expected, these binaries lie along the main sequence. The two outliers on the far right are early M-type stars. Not shown in the plots are the three A-type stars in the sample - chemfit is not designed for hot stars so their parameters are unreliable.

Parameters for one star in the sample analyzed (HIP 80232) were available on APOGEE (Table 1). These were compared with chemfit parameters as a check that the values obtained from the model were reasonable.

5 Conclusion

The binaries analyzed appeared as expected - in the thin disk of the galaxy and along the main sequence of stellar evolution. The parameters from APOGEE for star HIP 80232 agree with the parameters obtained from chemfit. These are good signs that the benchmark system of modeling simpler sun-like stars and extrapolating their chemical abundances to their secondary UCDs may be a reasonable approach. However, this is far from proven and there is much work to be done

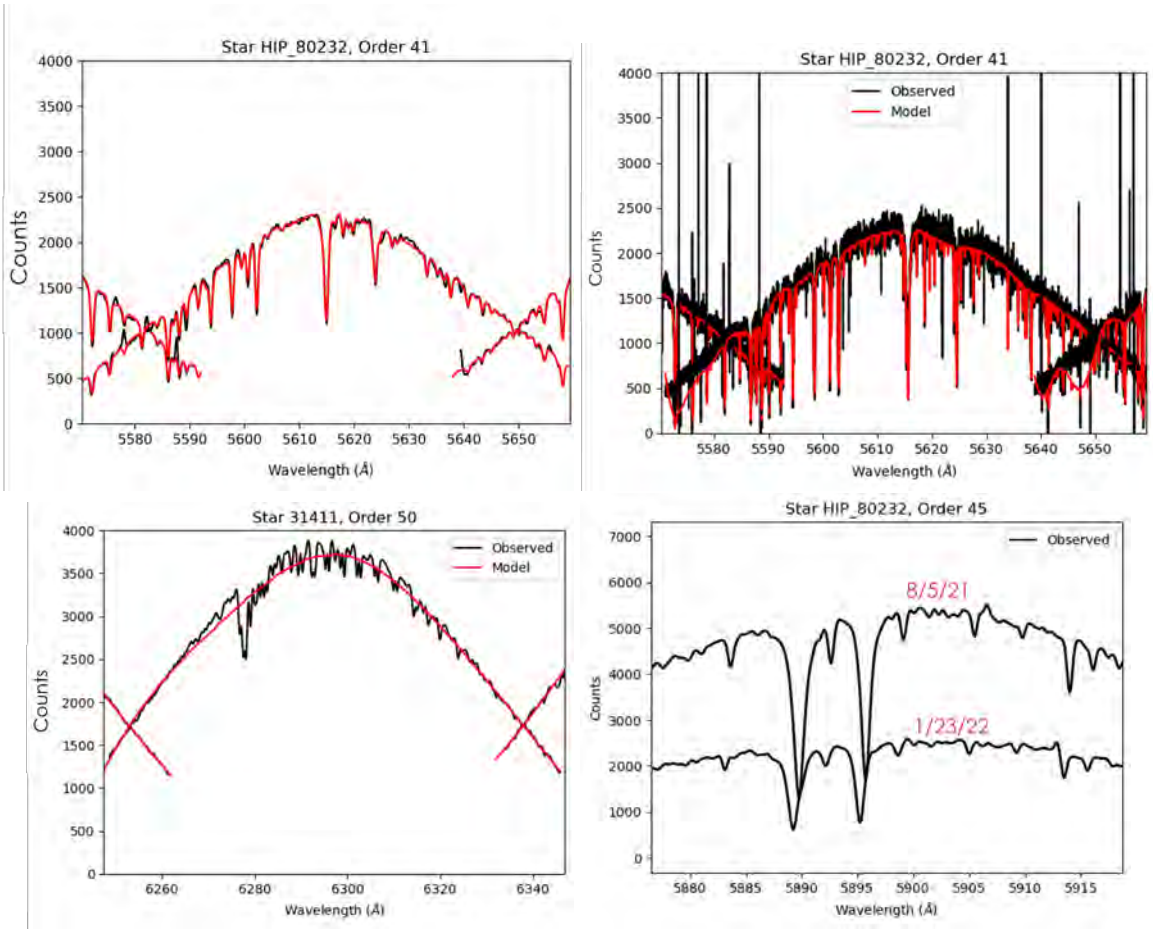

Figure 1: Low-resolution (left) and high-resolution (right) fits for star HIP 80232. Bottom left: A section of telluric features in a hot star used for masking. Bottom right: Two exposures from two separate nights with different redshifts.

in this area. There is currently another sample of APF spectra that has not yet been reduced by JUMP to be analyzed. It would be helpful to have much older, more metal-poor stars from the halo of the galaxy to analyze, as these stars are the most useful in studying the origins of the Galaxy. These stars comprise only 0.5% of the Galaxy [11], so a larger sample would be helpful. They could also be selected using velocities, since stars in the halo generally move away from us much faster than disk stars [12]. It would also be very useful to have actual observations of the UCD secondaries to compare with the model parameters inferred from the primaries - this requires a large telescope ideally in the infrared (e.g. Keck NIRES), since UCDs emit mostly in IR. Some

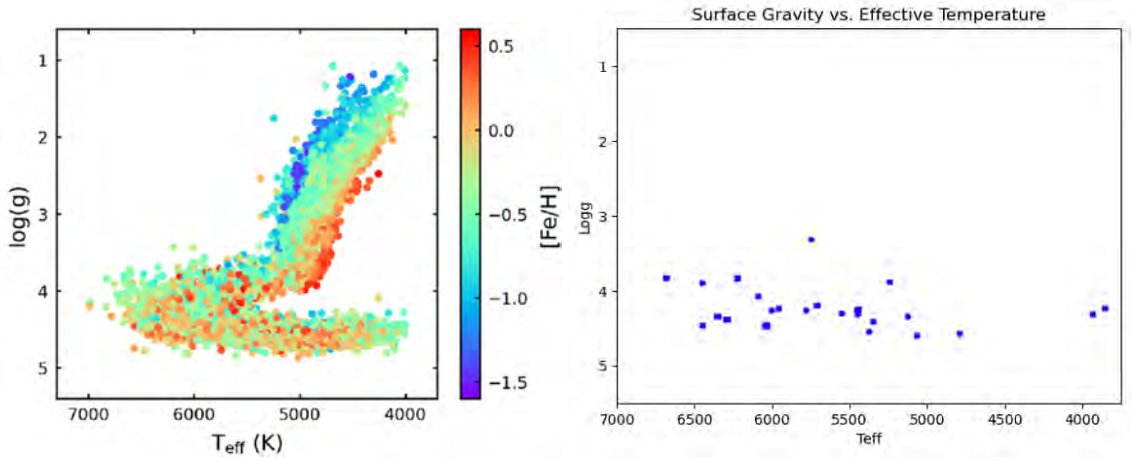

Figure 2: Left: A Kiel diagram adopted from [9]. Right: The corresponding region of surface gravity vs temperature for the stars modeled by chemfit. As expected, they lie along the main sequence of stellar evolution.

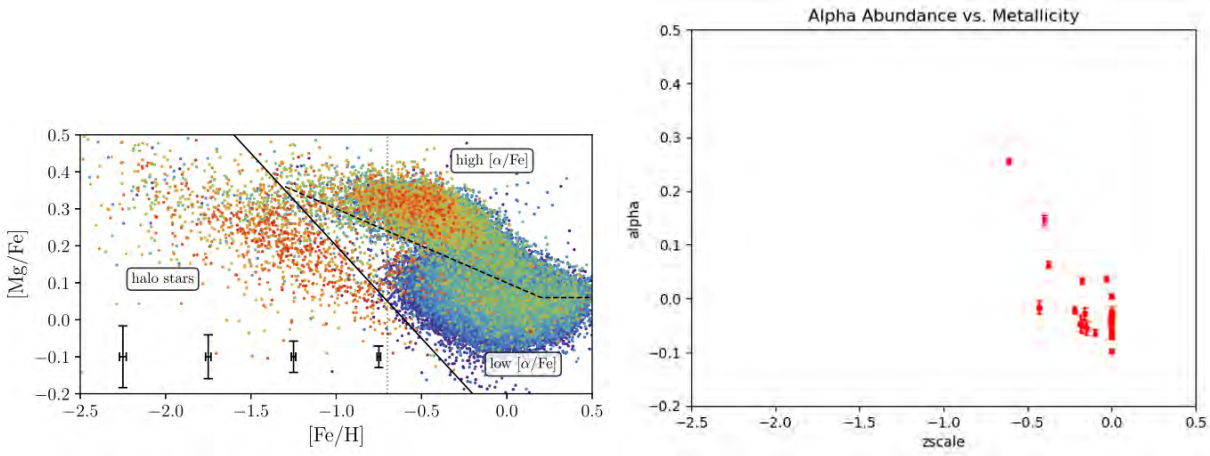

Figure 3: Left: The [α/Fe]–[Fe/H] plane for FGK primaries analyzed with chemfit. Adopted from Mackereth *et al.* [10]. Right: Alpha abundance vs metallicity for the stars analyzed by chemfit, in the region corresponding to the thin disk (low [α/Fe]) in the Mackereth plot. The grids do not currently contain models for stars with [Fe/H] > 0.

upcoming surveys of large numbers of UCDs are Rubin, [1], Roman [2], and JWST. It is important to develop analysis methods such as chemfit given that mass observations of UCDs are relatively new because telescopes have just recently been advanced enough to conduct these mass surveys of UCDs.

[1] https://rubinobservatory.org/news/rubin-detect-brown-dwarfs/

[2] https://www.stsci.edu/contents/events/roman/2021/april/galactic-archaeology-with-brown-dwarfs-with-the-nancy-grace-roman-space-telescope/

References

[1] A. J. Burgasser, in *The Ages of Stars*, Vol. 258, edited by E. E. Mamajek, D. R. Soderblom, and R. F. G. Wyse (2009) pp. 317–326, arXiv:0811.2508 [astro-ph] .

[2] J. D. Kirkpatrick, **43**, 195 (2005).

[3] E. N. Kirby, **123**, 531 (2011), arXiv:1103.1385 [astro-ph.SR] .

[4] I. Escala, E. N. Kirby, K. M. Gilbert, E. C. Cunningham, and J. Wojno, **878**, 42 (2019), arXiv:1811.09279 [astro-ph.GA] .

[5] K. El-Badry, H. Rix, and T. M. Heintz, **506**, 2269 (2021), arXiv:2101.05282 [astro-ph.SR] .

[6] K. El-Badry, H.-W. Rix, and T. M. Heintz, **506**, 2269 (2021), arXiv:2101.05282 [astro-ph.SR] .

[7] B. J. Fulton, L. M. Weiss, E. Sinukoff, H. Isaacson, A. W. Howard, G. W. Marcy, G. W. Henry, B. P. Holden, and R. I. Kibrick, **805**, 175 (2015), arXiv:1504.06629 [astro-ph.EP] .

[8] B. J. Fulton, L. M. Weiss, E. Sinukoff, H. Isaacson, A. W. Howard, G. W. Marcy, G. W. Henry, B. P. Holden, and R. I. Kibrick, **805**, 175 (2015), arXiv:1504.06629 [astro-ph.EP] .

[9] Ambrosch, M., Guiglion, G., Mikolaitis, Š., Chiappini, C., Tautvaišienė, G., Nepal, S., Gilmore, G., Randich, S., Bensby, T., Bayo, A., Bergemann, M., Morbidelli, L., Pancino, E., Sacco, G. G., Smiljanic, R., Zaggia, S., Jofré, P., and Jiménez-Esteban, F. M., AA **672**, A46 (2023).

[10] J. T. Mackereth, R. P. Schiavon, J. Pfeffer, C. R. Hayes, J. Bovy, B. Anguiano, C. Allende Prieto, S. Hasselquist, J. Holtzman, J. A. Johnson, S. R. Majewski, R. O'Connell, M. Shetrone, P. B. Tissera, and J. G. Fernández-Trincado, **482**, 3426 (2019), arXiv:1808.00968 [astro-ph.GA] .

[11] M. Jurić, Ž. Ivezić, A. Brooks, R. H. Lupton, D. Schlegel, D. Finkbeiner, N. Padmanabhan, N. Bond, B. Sesar, C. M. Rockosi, G. R. Knapp, J. E. Gunn, T. Sumi, D. P. Schneider, J. C. Barentine, H. J. Brewington, J. Brinkmann, M. Fukugita, M. Harvanek, S. J. Kleinman, J. Krzesinski, D. Long, J. Neilsen, Eric H., A. Nitta, S. A. Snedden, and D. G. York, **673**, 864 (2008), arXiv:astro-ph/0510520 [astro-ph] .

[12] T. Bensby, S. Feltzing, and I. Lundström, **410**, 527 (2003).

Simulated Beginnings for the Exploration of the Properties of Neutrinos with EMPHATIC

SARAH FOESS

2024 NSF/REU Program
Department of Physics and Astronomy
University of Notre Dame

ADVISOR(S): Prof. Laura Fields

Abstract

Research in neutrinos has become a recent focus in most particle physics, and for good reason. Neutrinos offer us much insight into cosmological happenings as they are emitted as a byproduct of radiation, produced alongside gamma ray bursts, neutron stars, etc. A particular behavior of neutrinos, which has not been fully explored, is the occurrence of flavor oscillation. As neutrinos travel, they are theorized to oscillate between three distinct flavors: electron, tau, and muon neutrinos. EMPHATIC is an experiment at the Fermi National Accelerator Laboratory which utilizes the NuMI Beam to create controlled beams of pions that decay into neutrinos. While Phase I utilized a thin controlled beam, Phase II uses a horn to scatter the beam particles after passing through the long target. Simulation of the secondary phase is necessary to ensure our future measurements have value and meaning, and to work out any issues with our equipment well in advance. As a proof of concept for the DUNE experiment between Fermilab and the Sanford Underground Research Facility, it is important to account for every error and issue long beforehand, and so we can gain a deeper understanding of how and why these oscillations occur. We are also equally expanding our knowledge on the standard model, and contributing to a better understanding of a most elusive particle.

1 Introduction

Neutrinos are one type of subatomic particle that are emitted by high-energy processes that occur around black holes, neutron stars, etc. as a result of radiation. Although they are incredibly abundant, they are nearly massless and electrically neutral, leading to limited interactions. By studying neutrinos with particularly high-energy, we develop a better understanding of the formation of galaxies and other high-energy radioactive events. However, perhaps the most intriguing focus is the theorized neutrino flavor oscillations.

Flavor, or type, oscillation, is when neutrinos change between three distinct flavors while on their path. These three are tau, electron, and muon. We can observe this change by seeing their partner particle appear once the neutrino finally interacts. This partner particle indicates which flavor the neutrino was before collision. While a seemingly easy theory to prove, neutrinos lack regular interaction, making them one of the most elusive particles [1].

EMPHATIC, (Experiment to Measure the Production of Hadrons at a Testbeam In Chicagoland), is an experiment housed within the Fermi National Accelerator Laboratory, or Fermilab. It will

make measurements of hadrons, subatomic particles made of quarks, gluons, and antiquarks, by using NuMI, (Neutrinos at the Main Injector), an instrument at Fermilab. NuMI is critical in this experiment as it can replicate a neutrino beam that decays into neutrinos, muons, and other particles [2].

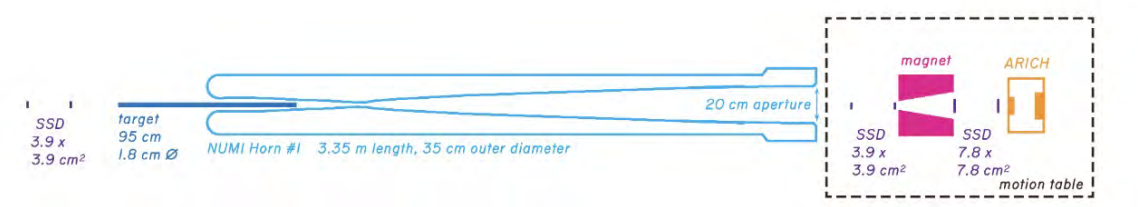

Figure 1: Schematic of the EMPHATIC small-acceptance spectrometer, or Phase II, to measure charged-particle momenta downstream of the NuMI target and horn, drawn to scale.

Phase II, or Long Target Phase, shown in Figure 1, of EMPHATIC utilizes NuMI alongside a horn to replicate a spray, or scatter, of particles. While the actual measurement will not be taking place until a later time, simulation of this phase allows us to observe and characterize potential interactions between particles, giving insight into what our measurement might show us [3][4].

EMPHATIC is also exciting because it is a proof-of-concept for the DUNE (Deep Underground Neutrino Experiment) between Sanford Underground Research Facility (SURF) and Fermilab. Fermilab will accelerate protons at their facility and send them 1300 kilometers through the earth to the underground particle detector built at the 4850 level (or 4850 feet below the surface), of SURF. One of the main priorities of this experiment is the investigation of the neutrinos' role in our Universe and their oscillations. By simulating this experiment on a much smaller scale with EMPHATIC, we can create expectations of what to see and ensure this is even possible [5].

2 Methods

Firstly, we created a new feature branch, `phase2simulation`, so any modifications we made to the code would not affect the `main` branch. This way, we are able to test and break code without ruining code that already works. While our new branch is a copy of the original, modifications are

made to two files: BeamGen.fcl and BeamGen-module.cc.

Previously written Phase I code, plotptpz.C, plotTvxTvy.C, and hadd-result-final-50.root, forms the basis of TTree references, which we will call g4numi. BeamGen-module.cc uses information from g4numi to fill out variables in its code. These are event number or numi-event-num, particle identification number or numi-tptype, particle x, y, and z position, and momentum. Particle masses are hard-coded and energy is solved for.

BeamGen-module.cc was originally a template. Initially, this skeleton was ran with hard-coded values for particle x, y, z, and its momentum just to correct any syntax errors and ensuring it compiles properly. After success, g4numi variables are filled in for proper variable reference.

We can confirm finished code compiles with a command buildtool --generator=ninja, which builds the code to be ready to used with ROOT, completing with SUCCESS. Using an Event Processing Framework called art, we can create all of our plots.

Unfortunately, at the final art command needed to produce our plots, we had a segmentation fault. This is when the code tries to access restricted memory, which is not true in this case: nothing should be restricted from our code. While this is an unfortunate set back, work is being done to fix this fault.

3 Results

Although construction of the new plots was not possible at this time, we do gain insight from running the original code.

In Figure 2, we can see the particle distribution of the thin beam characteristic of Phase I. With successful implementation of the Phase II code, we would expect a scatter or spray within this x-y space plot.

In Figure 3, the code identifies all particles from the beam as protons, which then fills in numi-ttype with 2212, the particle identification number. This is expected when the code is not running through phase2simulation branch and subsequently BeamGen-module.cc.

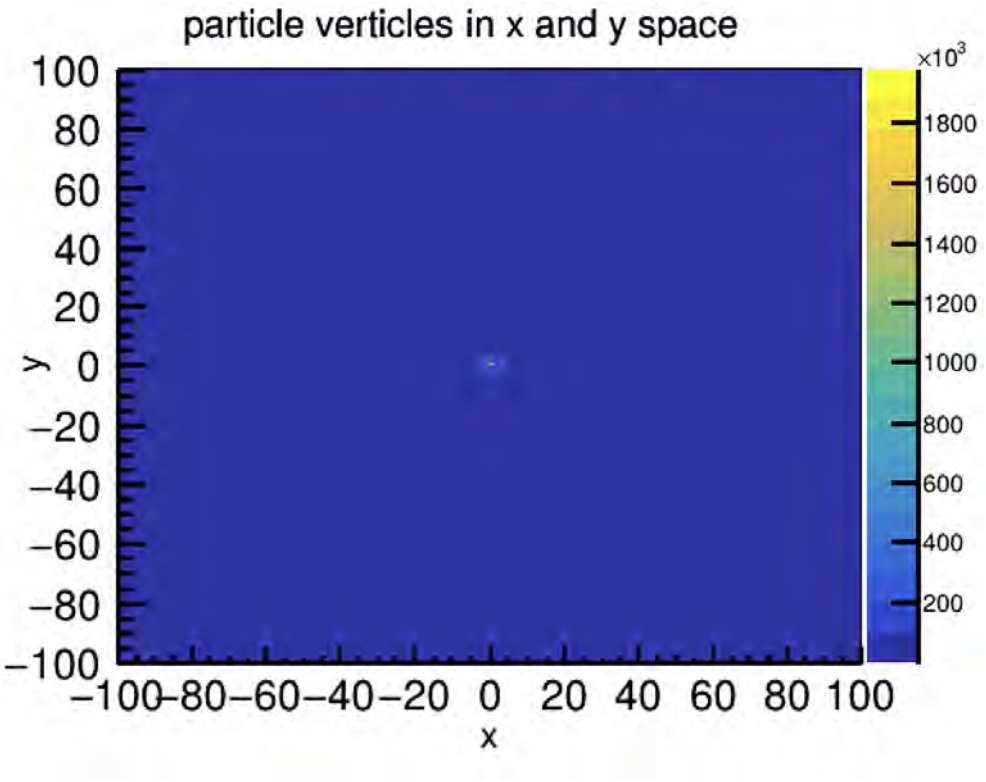

Figure 2: This is a visualization of pencil-thin beam of particles from Phase I, we are looking for scatter or spray of particles!

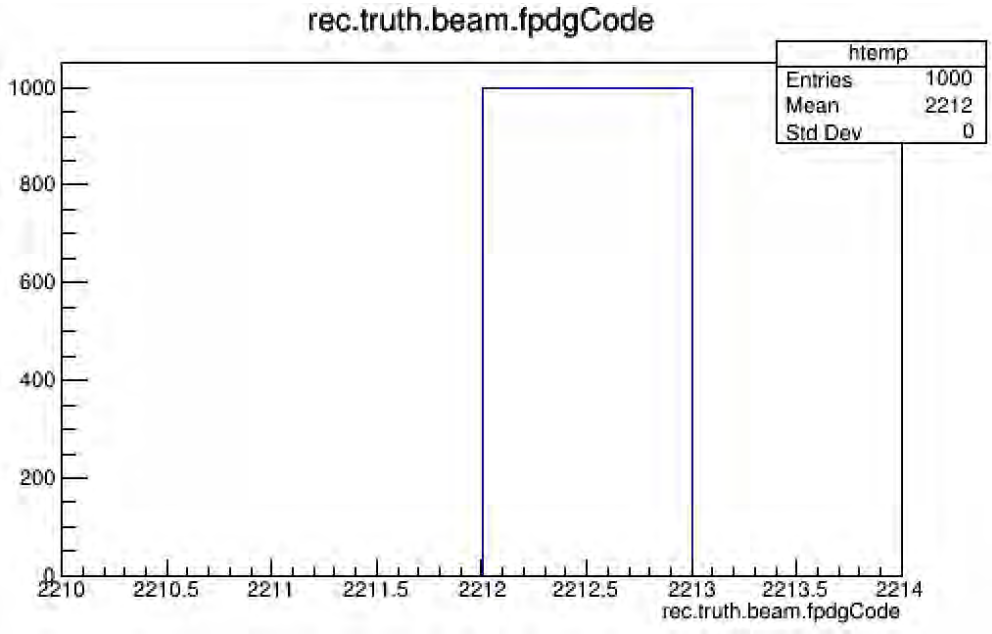

Figure 3: Protons are identified as 2212 - this shows all hits are protons, as expected in Phase I when new code is not implemented.

4 Conclusion

While unable to produce the anticipated result in time, the code written is a great start to continue troubleshooting with internal errors. The bulk of the work has been done, with minimal improvements that could be made to the existing code.

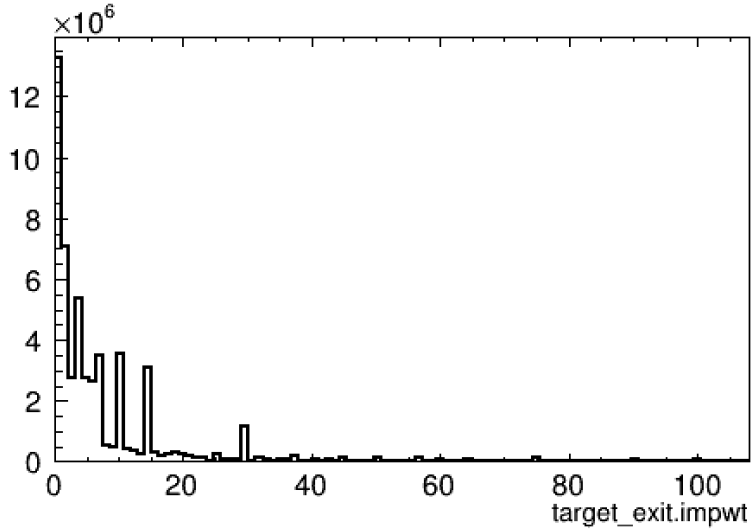

Figure 4: Weighted values of `impwt` necessary to propagate through art for proper distribution.

Firstly, there exists a weighted value `impwt`. In order to create a correct simulation, these values, shown in Figure 4, must be propagated through `art` and applied to any distribution plotted.

Secondly, much of the code is written with some level of redundancy. When solving for energy of particle, it must be identified by its mass. While the code parses for `numi-ttype`, it hard codes seven possible particle types and their masses, matching with the identification. While this is efficient now, it does not cover all possible cases. Therefore, by accessing the TTree through `PDatabasePDG.cxx`, which has a class `TParticlePDG`, which includes `fMass`, a reference can be made to allow for all known particle types.

References

[1] Fermi Research Alliance, All Things Neutrino (2024).

[2] K. Yonehara, S. Ganguly, and D. Athula Wickremasinghe, Fermilab Pub (2023).

[3] The EMPHATIC Collaboration, Fermilab Pub (2019).

[4] M. Pavin and et al., Fermilab Pub (2021).

[5] Fermi Research Alliance, Deep Underground Neutrino Experiment (2020).

The Nolen-Schiffer Anomaly with IMSRG(2) Calculations

BENICIO GUTIERREZ

2024 NSF/REU Program
Department of Physics and Astronomy
University of Notre Dame

ADVISOR(S): Prof. Ragnar Stroberg

1 Abstract

The Nolen-Schiffer anomaly, a discrepancy between theoretical and experimental binding energy differences of mirror nuclei, is investigated with IMSRG(2) calculations. With IMSRG(2), binding energies for mirror nuclei from A = 7 to A = 49 are calculated using various interaction models. These models are tested by calculating their charge radii. Compared to previous reports, the anomaly is resolved for most light nuclei, with remaining discrepancies at A = 13, 15, 37, and 39. A 3f2 correction improves the discrepancy but does not fully resolve it. Adding a Gaussian charge symmetry-breaking potential also fails to improve results. These findings highlight the accuracy of IMSRG(2) compared to previous many-body methods.

2 Introduction

The difference between theoretical and experimental binding energy differences for mirror nuclei (the Nolen-Schiffer anomaly) is a longstanding problem in nuclear physics [1] [2] [3] [4]. The problem is investigated by calculating the binding energies of various mirror nuclei with IMSRG(2) calculations. IMSRG(2) is of interest because more traditional calculations are less accurate with two-body systems, and play around with parameters of the nuclear force based on experimental data, which affects the binding energy differences. In comparison, IMSRG(2) starts with the Hartree-Fock mean-field calculation and adjusts the interactions so the HF energy is accurate. Then, the ab initio method solves for the energies as accurately as possible, using no ad hoc modifications.

The Coulomb force and strong force contribute to the binding energy of a nucleus, which is the energy required to separate the nucleus into individual nucleons. Experimentally, this is equal to the difference between the mass of a nucleus and the sum of masses of the individual nucleons. With the strong force having approximate isospin symmetry (the strong force treats both neutrons and protons similarly), the main contribution to the difference of binding energies between two nuclei is from the Coulomb force.

Although determining binding energy differences seems simple, especially because the Coulomb

force is well-understood, calculations consistently disagree with experiment. In this paper, the Coulomb displacement energy is defined as the difference between the binding energy of the proton-rich nucleus and the neutron-rich nucleus, $\Delta E \equiv E_{proton-rich} - E_{neutron-rich}$. The Nolen-Schiffer anomaly is the discrepancy between the theoretical and experimental energy differences between mirror nuclei, which have the same total number of nucleons, with the number of protons and neutrons switched. In previous studies, the calculated Coulomb displacement energies are consistently 4-10% smaller than experimental values [3] [4]. These studies suggested possible charge-symmetry-breaking of the strong force.

3 IMSRG

This section, detailing IMSRG, is based on Hergert et al. [5].

The Hamiltonian for a nucleus can be written using Fock space representation:

$$\hat{H} = E + \sum_{i,j} f_{ij}\{a_i^\dagger a_j\} + \frac{1}{4}\sum_{i,j,m,n} \Gamma_{ijnm}\{a_i^\dagger a_j^\dagger a_m a_n\} + \frac{1}{36}\sum_{i,j,k,l,m,n} W_{ijklmn}\{a_i^\dagger a_j^\dagger a_k^\dagger a_l a_m a_n\} + \dots$$

E is the energy of a reference state. f, Γ, and W are the one, two, and three body parts of the Hamiltonian. $a^\dagger$ and a are creation and annihilation operators. The curly brackets represent that these operators are normal-ordered with respect to the reference state. For a particular calculation, the Hamiltonian is created based on a model for the strong force. This paper uses calculations from IMSRG(2), which means that the one and two-body terms are included in the Hamiltonian. To incorporate important parts of the three-body force, the expectation value of the three-body term is added to the existing terms.

The difficulty of understanding the nucleus comes from the presence of multiple particles with many interactions; the goal is to solve the Schrodinger equation for many nonindependent particles. The Coulomb force exists between two different protons, while the strong force consists of many-body interactions. To simplify the problem, IMSRG block-diagonalizes the Hamiltonian. The Hamiltonian contains details regarding the interactions between particles, including those that cause

nucleons to undergo energy transitions. The nuclear shell is separated into three sections: the core (inner), the valence (outer), and the excluded region (which is ignored). The Hamiltonian is also partitioned into several parts: H_{PP} (upper left region of the matrix), H_{PQ} (upper right), H_{QP} (lower left), and H_{QQ} (lower right). Terms in H_{PQ} and H_{QP} represent interactions that cause nucleon transitions between the three nucleus sections. With IMSRG, these off-diagonal terms approach zero, which simplifies diagonalization.

IMSRG takes advantage of the symmetry of the Hamiltonian under unitary transformations; under a unitary transformation, the Hamiltonian has the same energy eigenvalues. A unitary transformation of the Hamiltonian is as follows:

$$H(s) = U(s)H(0)U^{\dagger}(s)$$

Here, the transformation is parameterized with parameter s. The unitary matrix U is given the condition $\frac{d}{ds}U = \eta(s)U(s)$. The generator η (known as the White generator) is determined with the equation $\langle a|\eta|b\rangle = \frac{\langle a|H^{od}|b\rangle}{\langle a|H^{d}|a\rangle - \langle b|H^{d}|b\rangle}$.

In terms of s, the derivative of H is:

$$\frac{d}{ds}H = (\frac{d}{ds}U)H(0)U^{\dagger} + UH(0)(\frac{d}{ds}U^{\dagger}) = \eta(s)H(s) - H(s)\eta(s) = [\eta(s), H(s)]$$

For the equation, as $s \to \infty$, H_{PQ} and $H_{QP} \to 0$.

The unitary transformation U is parameterized based on the Magnus formalism of IMSRG:

$$U(s) = e^{\Omega(s)} \qquad , \qquad \frac{d}{ds}\Omega(s) = \sum_{k=0}^{\inf} \frac{B_k}{k!}[\Omega(s), \eta(s)]^{(k)}$$

B_k is the kth Bernoulli number. $[\Omega(s), \eta(s)]^{(k)}$ is the k-fold nested commutator.

Calculations using IMSRG involve two parts. VS-IMSRG maps the nuclear physics to the valence space and performs the unitary transformations. KSHELL takes the valence space configurations and diagonalizes the simplified matrix.

3.1 Binding Energy Differences

Chiral Effective Field Theory (EFT) is a method for describing nucleon interactions by exploiting the chiral symmetry of Quantum Chromodynamics (QCD) at low energies. It builds a hierarchy of nuclear forces from simple to complex, allowing for systematic improvements in accuracy while connecting fundamental QCD principles with practical nuclear models.

In this section, three models for the original Hamiltonian $H(0)$ are compared. These models utilize Chiral Effective Field Theory to construct the Hamiltonian. The models that are compared here are: EM 1.8/2.0 [6], N2LOsat [7], and N2LODeltaGO [8]. All three of these models can be used to calculate various properties of nuclei (energies, radii, etc.), with varying success.

Figure 1 shows the IMSRG(2) calculations for the difference in binding energy for mirror nuclei in comparison with experiment. The experimental values are obtained from The AME 2020 atomic mass evaluation [9]. Calculations are performed with models EM 1.8/2.0, N2LOsat, and N2LODeltaGO, with $e_{max} = 12$ (e_{max} is the maximum single-particle energy level included in the model space). For EM 1.8/2.0, A = 7, 9, and 17 to 31 are in relatively good agreement with experiment. In comparison, N2LOsat and N2LODeltaGO are in good agreement with experiment at A = 41 to 49. The spread in values between the three models indicates uncertainty in ΔE due to uncertainty in parameters for the strong force. From A = 33 to 49, the values from EM 1.8/2.0 have a positive shift relative to N2LOsat and N2LODeltaGO. For all three models, the regions of large discrepancy are A = 13, 15, 37, and 39.

There are several possible sources for the remaining discrepancies: a problem with the interaction models, which also affects the nuclear structure (section 4.1); the approximations made by IMSRG(2) (section 4.2); underlying charge-symmetry-breaking of the strong force (section 4.3).

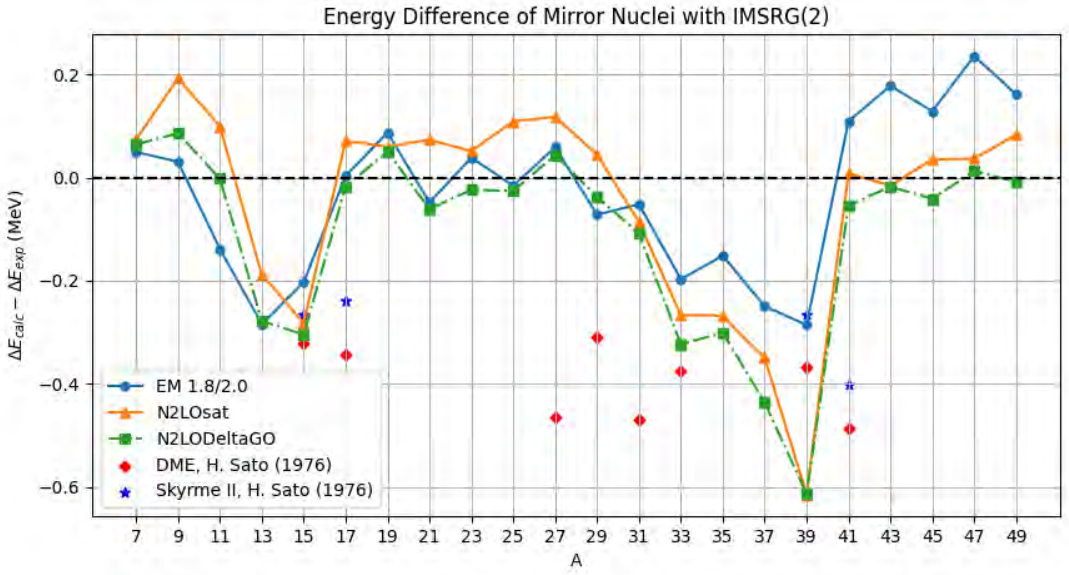

Figure 1: Plot of the difference of binding energy of mirror nuclei for odd A, A = 7 to 49, in relation to experimental data ΔE_{exp}. The unconnected points are from Sato (1976) [4].

4 Analysis

4.1 Charge Radius with IMSRG(2)

One of the previous challenges of the Nolen-Schiffer anomaly is that the discrepancy exists despite using models with accurate wavefunctions. This section uses the models used previously to calculate the charge radius of the nuclei of interest, to test the accuracy of these models in terms of nuclear structure. The charge radius is defined as the root-mean-square distance of the proton charge distribution from the figure of the nucleus. IMSRG(2) is used to calculate the point-proton radii, r_{pp}, which physically represents the spatial distribution of protons within a nucleus. To calculate the charge radius, the following equation is used, from Ekstrom et al. [7]: $\langle r_{ch}^2 \rangle = \langle r_{pp}^2 \rangle + \langle R_p^2 \rangle + \frac{N}{Z}\langle R_n^2 \rangle + \frac{3\hbar^2}{4m_p^2c^2}$. $R_p = 0.8775$ fm, $R_n^2 = -0.1149$ fm^2. The relativistic correction term is $\frac{3\hbar^2}{4m_p^2c^2} = 0.033$ fm^2.

Figure 2 shows the charge radius as obtained from EM 1.8/2.0, N2LOsat, and N2LODeltago ($e_{max} = 12$). Experimental values are according to Angeli (2013) [10]. There is a large discrepancy between the three models and experimental values for 7Li, 7Be, 9Be, 19F, 19Ne, 21Ne, and 21Na.

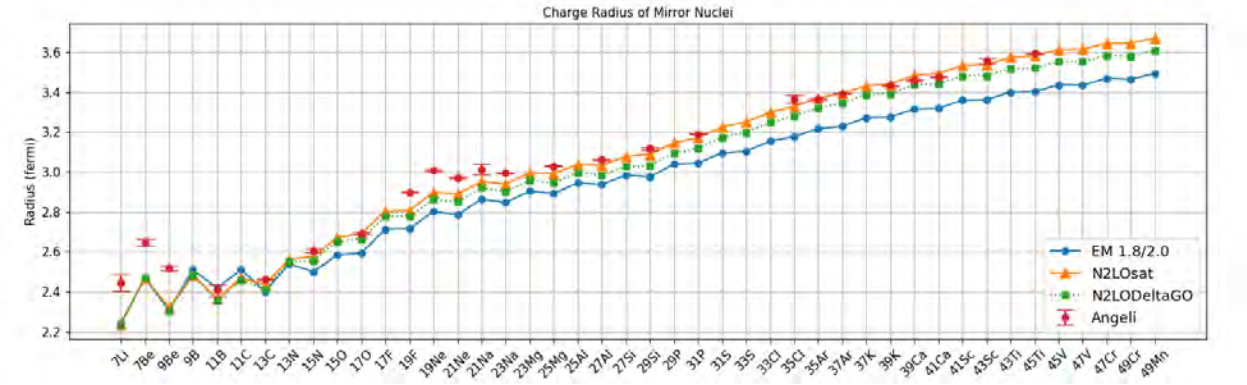

Figure 2: Charge radius according to EM 1.8/2.0, N2LOsat, and N2LODeltaGO ($e_{max} = 12$). The unconnected data points are according to Angeli (2013) [10].

For $A \geq 25$, N2LOsat has the greatest agreement with experimental values. At larger A, the radii according to EM 1.8/2.0 are significantly less than those of N2LOsat and N2LODeltago.

EM 1.8/2.0's smaller values of charge radii are correlated with the larger values of ΔE for mirror nuclei with A = 41 to 49. Meanwhile, the larger values of charge radii with N2LOsat and N2LODeltago remove the Nolen-Schiffer anomaly for these nuclei, as seen in Figure 1.

4.2 3f2 Correction, FCI

In previous IMSRG(2) calculations, the Hamiltonian operator only contains the one-body and two-body terms (section 3). Because the three-body term has six indices, it is computationally expensive. The 3f2 correction attempts to include intermediate three-body interactions by combining them with the terms from IMSRG(2).

Figure 3 is a plot of the difference in binding energies according to EM 1.8/2.0 in comparison with the applied 3f2 correction. From A = 17 to A = 29, EM 1.8/2.0 exhibits an oscillatory nature. The 3f2 correction removes this behavior. In regions of a large negative discrepancy, A = 13, 15, 37, and 39, the discrepancy is improved. For A = 41 to 49, the discrepancies are similar.

To test the approximations of IMSRG(2), IMSRG(2) can be compared with the results of FCI (Full Configuration Interaction), which diagonalizes the Hamiltonian exactly. Figure 4 shows A = 7 FCI calculations with $\hbar\omega$ truncation, which limits the included configurations to those with

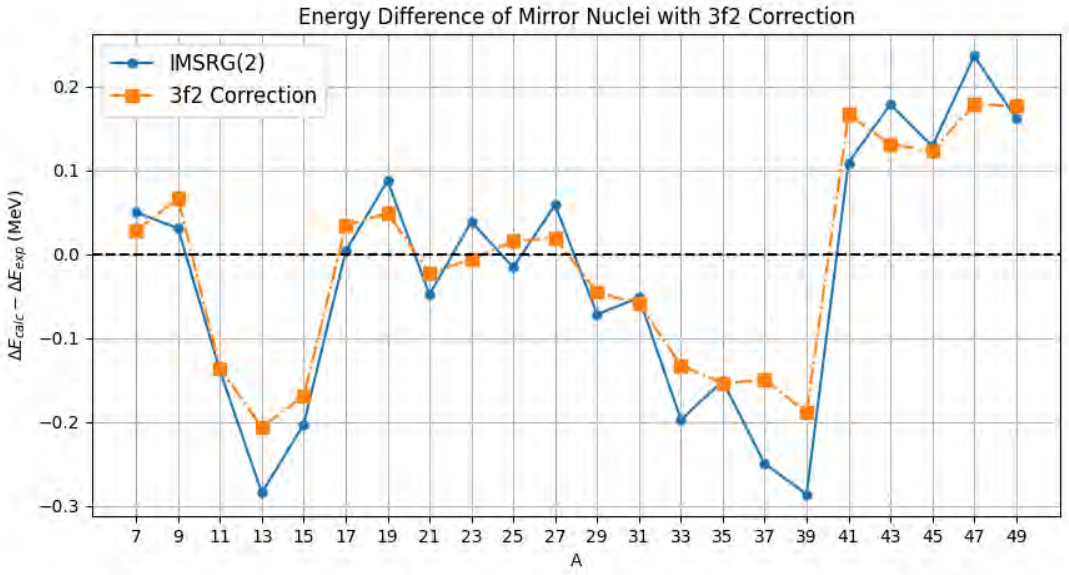

Figure 3: Plot of binding energy difference for mirror nuclei with EM 1.8/2.0 and the 3f2 correction ($e_{max} = 12$).

total harmonic oscillator energies below a specified cutoff. The FCI calculations are compared to IMSRG(2) and 3f2 calculations, at $e_{max} = 3$. As the cutoff for $\hbar\omega$ truncation increases, the FCI calculations approach a value close to IMSRG(2). This indicates that the approximations of IMSRG(2) produce results that are close to an exact solution.

4.3 Corrective Gaussian Potential

Historically, one method of resolving the Nolen-Schiffer anomaly is by adding a charge symmetry-breaking (CSB) potential, V_{CSB}. To observe how this solution affects results, a Gaussian potential $V_{CSB} = C * T_z * V_{Gaus}$ is added to EM 1.8/2.0 calculations. T_z is the two-particle isospin projection: $T_z = +1$ for proton-proton interactions, $T_z = -1$ for neutron-neutron interactions, and $T_z = 0$ for proton-neutron interactions. Amplitude coefficient C is chosen to be $C = 0.2$ MeV, $T_z = +1$, and the Gaussian width is 1.0 fm.

In Figure 5, the original EM 1.8/2.0 calculations are compared to EM 1.8/2.0 with V_{CSB}. There is a global positive shift with the potential. Although coefficient C can be modified to improve the theoretical values for A = 13, 15, 37, and 39, the global shift will increase the anomaly for all other

mirror nuclei. Therefore, adding a charge symmetry-breaking potential is not a viable method of resolving the Nolen-Schiffer anomaly.

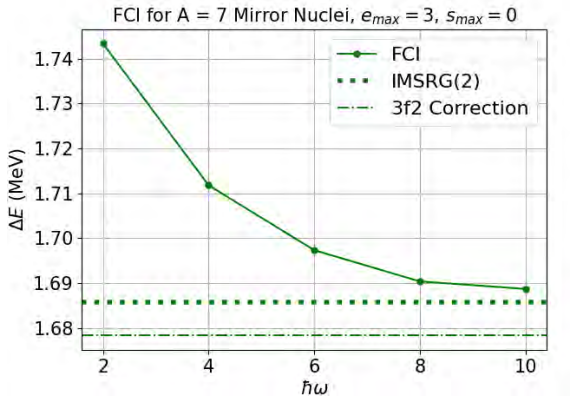

Figure 4: A = 7, $e_{max} = 3$ calculations with FCI, IMSRG(2), and 3f2.

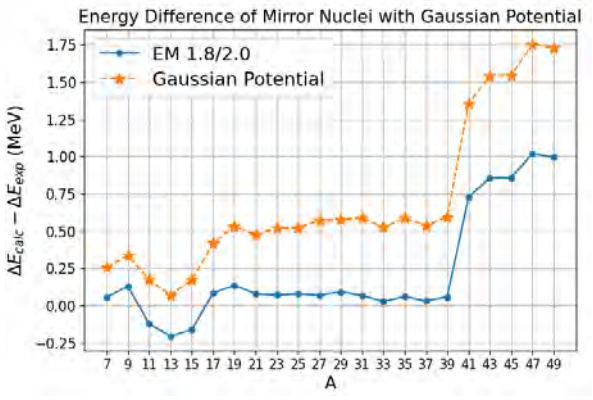

Figure 5: Energy differences of mirror nuclei with EM 1.8/2.0 and an additional Gaussian charge symmetry-breaking potential, $e_{max} = 4$.

5 Discussion and Conclusion

The three interaction models are in approximate agreement with each other on the binding energy differences of the mirror nuclei. The IMSRG(2) calculations reveal how sensitive the Coulomb energy difference is to the strong interaction; any variation between the models is primarily due to the lack of precision of the strong force between each model. For A = 33 to 49, there is a positive shift in the energy differences from EM 1.8/2.0, in comparison to N2LOsat and N2LODeltaGO. This is caused by the way choice of parameters between the models. N2LOsat and N2LODeltaGO yield more accurate results for larger nuclear radii, which correlates with the shift in the energy difference compared to EM 1.8/2.0. With N2LOsat and N2LODeltaGO, the Nolen-Schiffer anomaly is resolved for A = 41 to 49.

For mirror nuclei with odd A ranging from 7 to 49, the Nolen-Schiffer anomaly is resolved in most regions; however, the anomaly persists at A = 13, 15, 37, and 39. The resolution of the Nolen-Schiffer anomaly for many mirror nuclei demonstrates the accuracy of IMSRG(2) in comparison with previous many-body methods of nuclei energy calculation. To check if the remaining anomaly was caused by approximations made by IMSRG(2), the energy difference calculations

are performed again, applying a 3f2 correction. For the problematic regions, the correction improves the anomaly, but is not enough to resolve it. For A = 7, the exact FCI result is compared to IMSRG(2) to verify the quality of approximations made by IMSRG(2).

By applying a charge breaking-symmetry potential, the calculated results are positively shifted. For Coulomb displacement energies that agree with experiment, this would only create a new discrepancy. Therefore, adding a charge symmetry-breaking potential is not a solution to the Nolen-Schiffer anomaly. This also means that contrary to previous studies, there is no evidence for additional charge symmetry-breaking in the strong force.

The anomaly is likely the result of an error with the IMSRG many-body calculation method, which needs to be investigated further. In the future, the anomaly should be investigated using other IMSRG corrections and modern many-body methods.

References

[1] K. Okamoto, Phys. Lett. 11, 150 (1964).

[2] J, A. Nolen and J. P. Schiffer Annu. Rev. Nuc. Sci. 19, 471 (1969).

[3] Shalom Shlomo, Rep. Prog. Phys. 41, 957 (1978).

[4] H. Sato, Nuclear Physics A 269, 378 (1976).

[5] H. Hergert, S. K. Bogner, et al., Physics Reports 621, 165 (2015).

[6] K. Hebeler, S. K. Bogner, et al., Phys. Rev. C 83, 031301(R) (2011).

[7] A. Ekstrom, et al., Phys. Rev. C 91, 051301(R) (2015).

[8] W.G. Jiang, et al., Phys. Rev. C 102, 054301 (2020).

[9] Meng Wang et al., Chinese Phys. C 45, 030003 (2021).

[10] I. Angeli, K.P. Marinova (2013), Atomic Data and Nuclear Data Tables 99, 69 (2013).

Searching for Exoplanets Near Low Metallicity Stars

THOMAS HARE

2024 NSF/REU Program
Department of Physics and Astronomy
University of Notre Dame

ADVISOR(S): Prof. Lauren Weiss

Abstract

Since the early universe was poor in metal, the first stars in the Milky Way Galaxy formed in environments with low metallicity. Exoplanet hunting often neglects the regime of low metallicity hosts, and so, the formation of planets during the early universe is not well understood. This project seeks to build a data pipeline that analyzes photometric TESS data of metal-poor candidate stars to search for transiting exoplanets. From a list of 50 known exoplanets, the pipeline was able to recover over 70% of transits. In future analyses, the pipeline can be used to scan catalogs of low metallicity stars to search for new exoplanets. This can be used to place limits on the metallicity of stars that are capable of hosting planets, as well as to categorize the types of exoplanets found near metal-poor stars.

1 Introduction

Exoplanets are objects of great interest in the field of galactic archaeology. They can provide information about stellar history and the formation of star systems in the Milky way Galaxy. One key interest is finding and characterizing the types of exoplanets orbiting low metallicity stars. Metallicity is the proportion of metals, which are elements heavier than helium, to hydrogen. Since low metallicity stars are often some of the oldest stars in the galaxy, studying exoplanets in these systems will provide insight into planet formation in the early universe. Due to the rarity of metal-poor stars, there have been very few of these exoplanets discovered. However, recent photometric surveys have expanded our catalog of low metallicity stars, providing a unique opportunity to look for new planets. This project sees develops a data pipeline that can detect transiting exoplanets by using photometry from the Transiting Exoplanet Survey Satellite (TESS). This pipeline will provide the means to find and characterize exoplanets near these metal-poor stars, which will further our understanding of planet formation.

2 Background

Surveys of transiting exoplanets have revealed a strong planet-metallicity correlation. The occurrence of large gas giants increases with metallicity, while small planets demonstrate little to no significant correlation [2]. In such surveys, very few stars lie on the extreme low metallicity end of

the spectrum. This is in many ways a consequence of the rarity of low metallicity stars, as well as the difficulty in accurately measuring their metallicities [2]. Many low metallicity stars are also far away and therefore are faint, with magnitudes between 14-16, which make them poor candidates for exoplanet surveys [2].

Since the start of the Gaia mission, over three million low metallicity stars have been identified with precise measurements of their parallaxes and their ages using photometric data from four surveys, the SkyMapper Southern Survey (SMSS II) [3], the Javalambre-Photometric Local Universe Survey (J-PLUS)[5], the Southern-Photometric Local Universe Survey (S-PLUS) [5] and the Stellar Abundances and Galactic Evolution Survey (SAGES) [4]. The TESS mission has observed many of these stars, and so, more complete analyses of the planet-metallicity correlation can be conducted for metal-poor stars. In the early universe, the first generations of stars formed in low metallicity environments. Sampling stars in the low metallicity regime means sampling from some of the oldest stars in the galaxy. Understanding how low metallicities affect planet occurrence will bolster our understanding of planet formation in the early universe.

We can classify exoplanets into distinct groups: gas giants, like Jupiter and Saturn, and smaller planets, which contain gaseous sub-Neptunes and rocky planets [2]. Is there a minimum metallicity beyond which the formation of certain types of planets is impossible? Will the occurrence of gas giants be lower than the occurrence of small planets? It is thought that metals contribute to the accretion of gaseous envelopes that is necessary for the formation of large gas giants [2]. The reduced abundance of metallic particles in low metallicity star systems may decrease the rate of solid coagulation, and so, it is thought most planets orbiting low metallicity stars are rocky planets or sub-Neptunes [6].

3 Methods

3.1 Methods for Detection

There are a variety of methods that have been used to find exoplanets; however, the most common methods are the radial velocity (RV) method and transit photometry. The RV method detects the Doppler shift in the starlight as the star moves due to the influence of gravity of the exoplanet [7]. Transit photometry detects dips in the brightness of the star as the exoplanet passes directly between the star and the observer [7]. Since the RV method relies on spectroscopic data for detection, the metal abundance of the star affects the quality of the measurement. Photometry allows for the observation of thousands of stars at a time, whereas high resolution spectroscopy can only make observations of single stars. Publicly available TESS data provides photometry of millions of stars. The absorption characteristics of starlight are weaker with low metallicities, and so they are not the optimal method to detect exoplanets near metal-poor stars [3]. Instead, this project relies on photometric data to detect transiting exoplanets.

Transiting exoplanets produce a characteristic signal. Assuming there is minimal variability in the light curve, as the exoplanet begins passing in front of the star, there is a sharp decrease in the flux over time before the flux bottoms out as the exoplanet moves fully in front of the star [7]. Then, once the exoplanet begins exiting the transit, the flux sharply increases until returning to normal [7]. This process can be roughly modeled by a boxcar fit. A boxcar fit to a transit signal has three parameters: the duration of the transit, the depth of the transit, and the orbital period of the planet. These parameters can be converted to the orbital distance and physical radius of the planet.

3.2 Obtaining a Transit Signal

In order to obtain a transit signal, the data pipeline needs to be able to access photometric data from TESS, remove any signals from background sources, and eliminate any noise that might obscure the transit. This project utilizes the Python package LightKurve to perform these analyes. First, the pipeline searches for and downloads a target pixel file from TESS photometry via the Mikulski

Archive for Space Telescopes (MAST). Then, the pipeline creates a mask that selects for the flux near the star, as well as a mask for background flux. Data from the target pixel file is then converted into a light curve, which measures photon flux and time in Barycentric Julian Date (BJD) days.

There are many sources of noise that can affect a light curve. This can include large peaks caused by cosmic ray particles or micrometeorite impacts[1]. As TESS samples the sky, there are epochs where TESS is reoriented, which can create thermal transients which can shift the values of the flux and introduce gaps in the data [1]. If a star is located in close proximity to other stars such that the pixels on TESS cannot effectively separate them, then this can introduce confusion. There are also phenomena, such as stellar variability which can create periodic signals that might be mistaken for transiting exoplanets.

The data pipeline uses pixel level decorrelation to remove sources of noise. This method uses polynomial splines that take the form of

$$m_i = \sum_l a_l \frac{f_{il}}{\sum_k f_{ik}} + \sum_l \sum_m b_{lm} \frac{f_{il} f_{im}}{\left(\sum_k f_{ik}\right)^2} + ... \tag{1}$$

to create a noise model, where f_{il} is the flux of the l'th pixel, a_l is a first-order coefficient and b_{lm} is the second-order coefficient of the l'th and m'th pixel pair. A chi-square test is performed on the data, and the chi-square is minimized, producing a fit to the noise. The data is then flattened and normalized to a mean flux of 1.0. These processes can be seen in Figure 1.

Once noise has been removed from the data, a box least squares (BLS) periodogram is run on the light curve, as seen in Figure 2. The periods with the best fit have the greatest power. If there is a strong transit signal, the pipeline selects the period with the largest power as the orbital period of the planet candidate. The pipeline folds the light curve according to this period revealing the characteristic transit signal, which can be seen in Figure 3.

3.3 Creating a Filter

The second function of the data pipeline is to filter out signals that do not contain transiting exoplanets. The pipeline accomplishes this by constraining the boxcar parameters and by performing

chi-square tests on the data and boxcar model. If the data does not contain multiple transits, the orbital period of the planet cannot be known, and so the planet cannot be confirmed. Therefore, any suspected exoplanet that contains only one signal will not be counted by the pipeline. Additionally, there are some physical phenomena that can resemble transiting exoplanets. For example, eclipsing binary stars can produce transits. They create deep eclipses much greater than what planets can produce because stars are larger than planets. By limiting the transit depth to less than 10%, we can remove the most obvious binaries.

After noise correction, observations of most stars will yield flat normalized light curves with no signals. The pipeline distinguishes transits from flat light curves by applying two reduced chi-square tests on the data, one using the boxcar model, given by,

$$\chi^2_{\text{boxcar}} = \frac{1}{N} \sum_i \frac{\left(f_i - m_i\right)^2}{\sigma_{f_i}} \tag{2}$$

and the other using a constant function around 1.0:

$$\chi^2_{\text{line}} = \frac{1}{N} \sum_i \frac{\left(f_i - 1.0\right)^2}{\sigma_{f_i}} \tag{3}$$

where N is the number of flux points, f is the value of one flux point, m is the value of the boxcar, and σ_f is the error on the flux.

Taking the difference between these gives a new parameter:

$$\Delta\chi^2_{\text{Filter}} = \chi^2_{\text{line}} - \chi^2_{\text{boxcar}}. \tag{4}$$

Light curves with no signal will have a very small $\Delta\chi^2_{\text{Filter}}$, whereas prominent signals will have a larger $\Delta\chi^2_{\text{Filter}}$. Occasionally, stellar variation or other sources of noise will not be completely removed by noise correction, especially if there are few flux points. This may in turn fool the chi-square tests. A transiting exoplanet only produces one dip in a folded light curve. However, noise can create multiple dips or other artifacts on a folded light curve. By applying a chi-square test

on the regions of the light curve outside of the boxcar model, poor data will produce very large chi-squares while cleaner data will yield values closer to 1.0.

4 Results

As a demonstration of the pipeline, we perform it on TESS object of interest (TOI)-1194, which is a main sequence star with a Jupiter-sized planet.

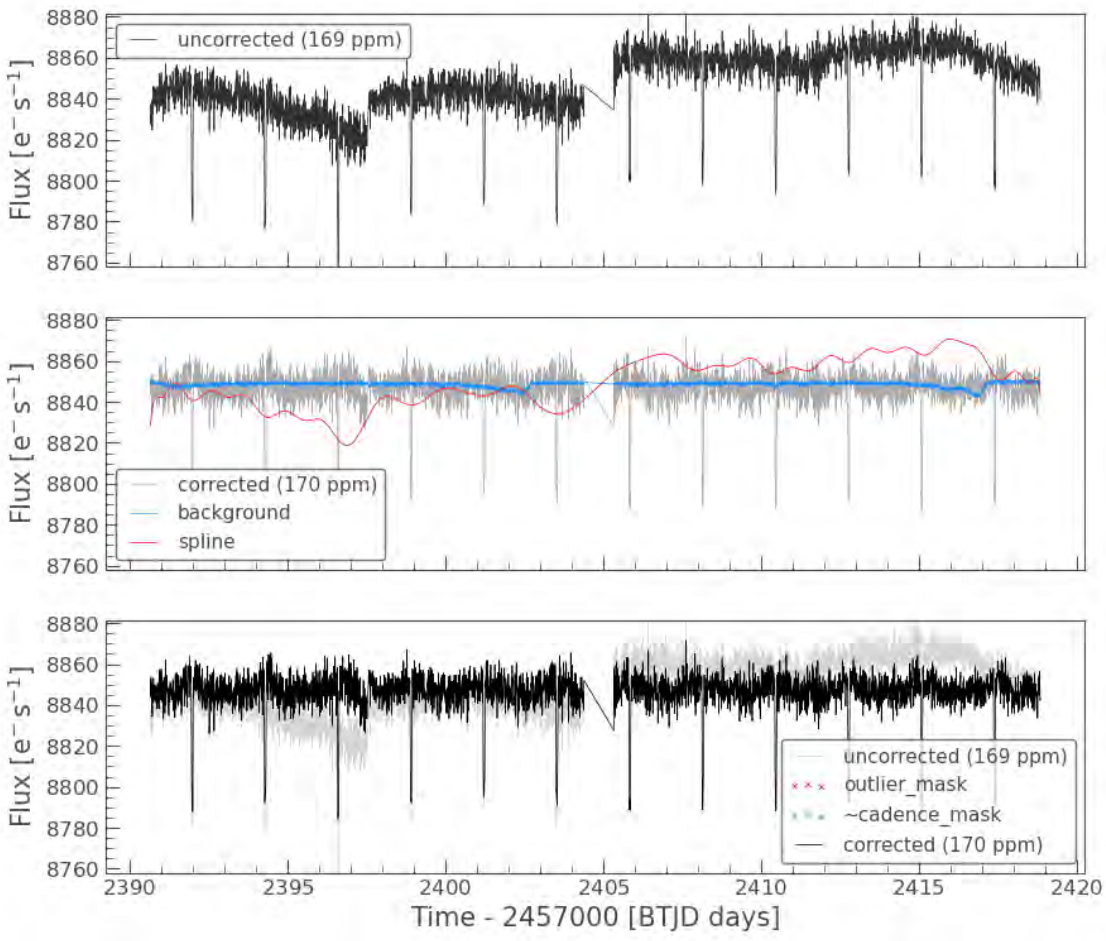

Figure 1: Plot of the light curves for TOI-1194 showing the removal of noise using Pixel Level Decorrelation. The top plot shows the original uncorrected light curve. Between gaps in the data, the flux shifts due to thermal transients as TESS's orientation changes. The middle plot shows the polynomial fit to the noise and background flux. The bottom plot shows the corrected light curve overlayed on top of the original.

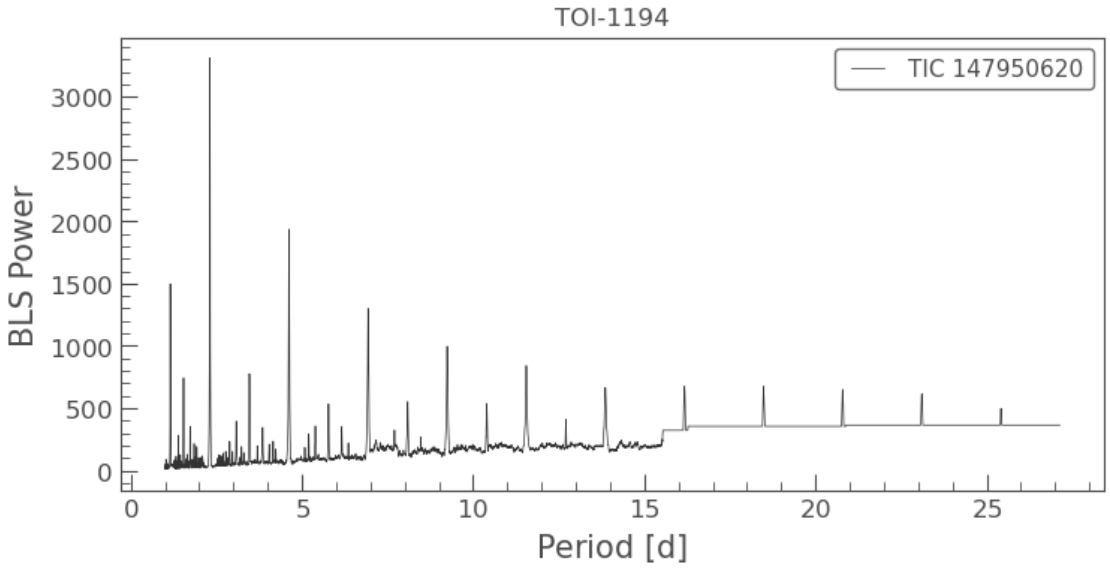

Figure 2: Plot of the periodgram in terms of days. At around 2.3 days, there is a strong peak associated with the orbital period of the planet. As the periods approach the observation baseline, the periodgram flattens out. Additional peaks are harmonics of the true period.

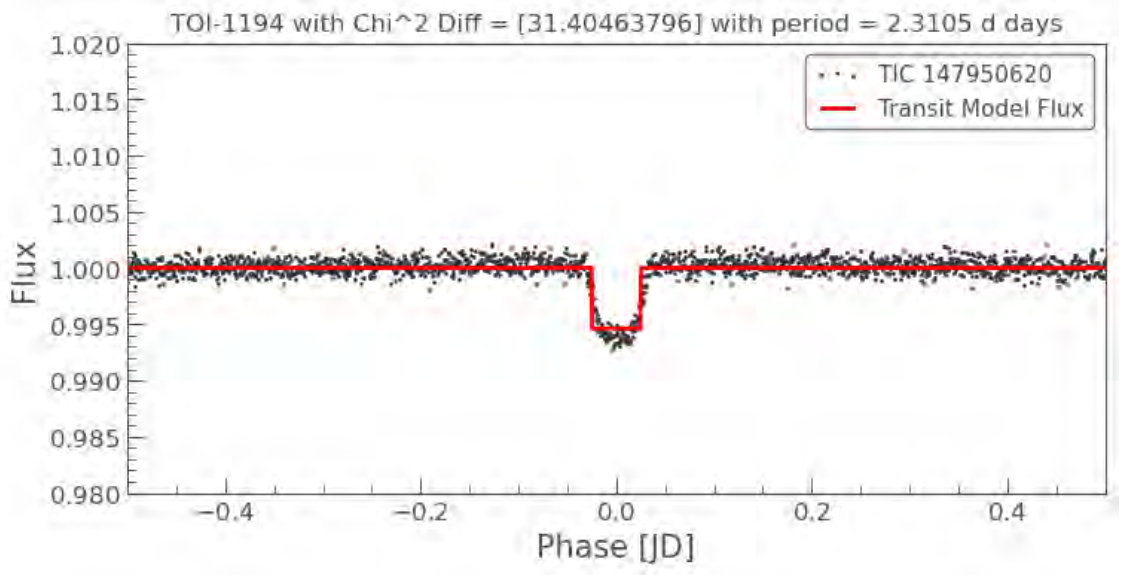

Figure 3: Plot of phase folded light curve. The transit model is based on a boxcar fit. The $\Delta\chi^2_{\text{Filter}}$ is given as Chi^2 Diff. This is a very large value, which suggests that this is not well modeled by a constant function. The orbital period for this planet was calculated to be close to 2.3 days.

Parameterizing these values will require running the data pipeline on known transiting exoplanets. We can change the parameters until we optimize the number of recovered transits. For a list of 50 TESS objects of interest, the pipeline was able to recover a maximum of 36 transiting exoplanets with a $\Delta\chi^2_{\text{Filter}} = 0.8$. Out of the exoplanets not recovered, most either had very noisy light curves or transits that occurred only once. One exoplanet that was not recovered, TOI-1607, had a very shallow depth, resulting in a small $\Delta\chi^2_{\text{Filter}}$.

Because the photometric method relies on the dimming in the flux of the star during the transit, larger planets that are capable of producing deeper transits are more likely to be detected. The photometric method also requires multiple transits in order to confirm an exoplanet, and so detecting shorter period planets close to their hosts is more probable. This leads to a bias towards hotter and larger planets, which must be corrected when determining the occurrence of exoplanets near metal-poor stars.

5 Conclusion

The data pipeline is successful at detecting transiting exoplanets from TESS photometric data. From a sample of 50 known transiting exoplanets, the pipeline is able to recover over 70% of the transits. This suggests that if there are any transiting exoplanets in a light curve, there is a reasonably high probability that it will be detected. In future work, running the pipeline on a larger sample of known exoplanets along with a sample of stars with no transiting planets may help refine the parameterization and optimize the filter. Once the filter parameters are selected, the pipeline will be ready to search for exoplanets orbiting low metallicity stars. A catalog of a few thousand to a few million stars could reveal enough exoplanets to exhibit planet-metallicity correlations which may extend our understanding of planetary systems in the young Milky Way Galaxy.

6 Acknowledgements

I would like to thank my research adviser, Professor Lauren Weiss and the Astroweiss research group for guidance on the project. This research was supported by the 2024 Notre Dame REU program and the NSF. This research made use of Lightkurve, a Python package for Kepler and TESS data analysis (Lightkurve Collaboration, 2018).This research has made use of the NASA Exoplanet Archive, which is operated by the California Institute of Technology, under contract with the National Aeronautics and Space Administration under the Exoplanet Exploration Program. All of the data presented in this paper were obtained from MAST at the Space Telescope Science Institute.

References

[1] Cardoso, J. V. D. M., Hedges, C., Gully-Santiago, M., Saunders, N., Cody, A. M., Barclay, T., ... & Lightkurve Collaboration. (2018). Lightkurve: Kepler and TESS time series analysis in Python. *Astrophysics Source Code Library*, ascl-1812.

[2] Fischer, D. A., & Valenti, J. (2005). The planet-metallicity correlation.*The Astrophysical Journal*,*622(2)*.

[3] Huang, Y., Beers, T. C., Wolf, C., Lee, Y. S., Onken, C. A., Yuan, H., ... & Fan, Z. (2022). Beyond spectroscopy. I. Metallicities, distances, and age estimates for over 20 million stars from SMSS DR2 and Gaia EDR3.*The Astrophysical Journal*,*925(2)*, 164.

[4] Huang, Y., Beers, T. C., Yuan, H., Tan, K. F., Wang, W., Zheng, J., ... & Zhao, G. (2023). Beyond Spectroscopy. II. Stellar Parameters for over 20 Million Stars in the Northern Sky from SAGES DR1 and Gaia DR3. The Astrophysical Journal, 957(2), 65.

[5] Huang, Yang, Timothy C. Beers, Kai Xiao, Haibo Yuan, Young Sun Lee, Hongrui Gu, Jihye Hong et al. "J-PLUS: Beyond Spectroscopy III. Stellar Parameters and Elemental-abundance Ratios for Five Million Stars from DR3." arXiv preprint arXiv:2408.02171 (2024).

[6] Petigura, E. A., Marcy, G. W., Winn, J. N., Weiss, L. M., Fulton, B. J., Howard, A. W., ... & Johnson, J. A. (2018). The California-Kepler survey. IV. Metal-rich stars host a greater diversity of planets. *The Astronomical Journal*, *155(2)*, 89.

[7] Winn, J. N. (2010). Transits and occultations. *arXiv preprint arXiv:1001.2010*.

Bridging the Gap: Unveiling Superconductivity and Exciton Dynamics in WTe_2

ANYA E. JOHNSON

2024 NSF/REU Program
Department of Physics and Astronomy
University of Notre Dame

ADVISOR(S): Prof. Yi-Ting Hsu

Abstract

The quest for identifying and harnessing materials with exotic quantum properties has become a frontier in modern condensed matter physics. Topological superconductors are of particular interest among such materials due to their potential applications in quantum computing and unconventional superconductivity. This research focuses on creating and analyzing a comprehensive model for the topological superconductor Tungsten Ditelluride (WTe_2). By leveraging computational methods and quantum mechanical modeling, we dissect the electronic properties and the topological nature contributing to the superconductivity observed in WTe_2. Using first-principles calculations, we examine the electronic band structure and Fermi surfaces that manifest in WTe_2 under various conditions. Furthermore, we explore the impact of impurities on the system's critical temperature (T_c). This report delves into the distinctive superconductivity and topological phases exhibited by WTe_2, what was learned to create a model, and what mysteries remain.

1 Introduction

The transition metal dichalcogenides (TMD) family is unique because they exhibit the necessary qualities for superconductivity and quantum computing applications. The focus material, WTe_2, is a member of this family and holds promising topological superconducting characteristics. This material is particularly noteworthy due to its robust electron correlation effects and presence of strong spin-orbit coupling, which are critical for the realization of exotic quantum states. Furthermore, WTe_2 is associated with the quantum spin Hall effect, where an insulating bulk coexists with superconducting edge states that are protected by time-reversal symmetry. These edge states allow for dissipationless spin transport, making WTe_2 a compelling candidate for quantum computing technology and novel electronic devices. This unique combination of properties in WTe_2 opens new possibilities for significant advancements in these fields.

2 Background

2.1 Preliminary Experiment

The discovery of WTe_2 as a topological insulator and its manifestation of the quantum spin Hall effect marked the beginning of an era of understanding more materials of its forms. This breakthrough emerged from various experiments to uncover materials with unique electronic properties and topological states. One experiment provided compelling evidence that WTe_2 could host topologically protected surface states. These states are robust against local perturbations and disorder, a hallmark of topological insulators. The experiment utilized angle-resolved photoemission spectroscopy (ARPES), a technique used for probing the electronic structure of materials with high precision [1]. ARPES measurement revealed distinctive surface states within the band structure of WTe_2, indicative of an unusual spin texture where electron spins were locked perpendicular to their momentum – a signature of the quantum spin Hall effect.

Furthermore, subsequent experiments confirmed that WTe_2 exhibited a non-trivial band topology, strengthening its classification as a topological insulator. These findings opened doors for exploring quantum phenomena and potential applications in quantum computing. Since then, more experiments have shown that WTe_2 can become superconducting given the right conditions [2]. As seen in Figure 1, the right conditions are when the temperature is around 1K, and when more electrons are added to the system by way of electrostatic gating. This discovery has led to a race to understand the phase transition from a topological insulator to a superconductor.

New discoveries often led to a cloud of confusion and this was no different. For example, do the helical edge modes persist when superconductivity is restored? What is the nature of the coupling between superconductivity and edge conduction, or do the edge states also develop a superconducting gap? Most importantly, what is the gap function and what is the superconducting nature of WTe_2? Our goal was to understand the gap symmetries and figure out what kind of superconductivity is exhibited in this system by studying the effect of disorders when added to the material. This would help overall in finding our wanted superconducting model (see methods).

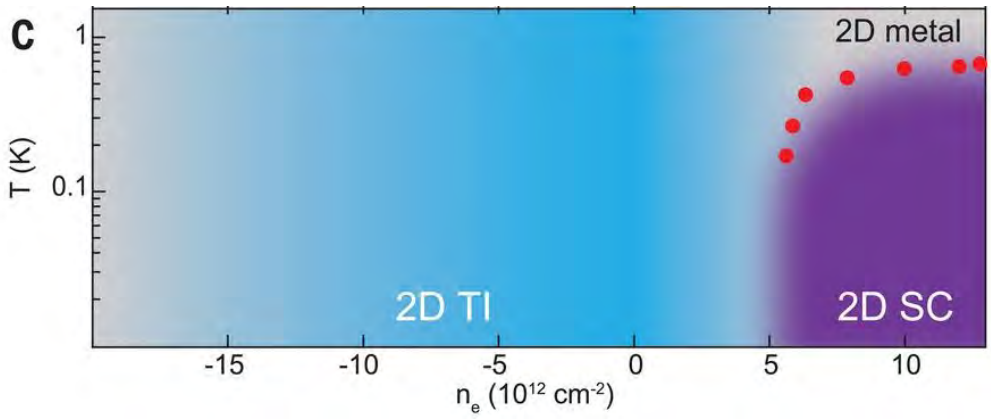

Figure 1: Phase diagram of WTe_2 system transitioning from topological insulator to superconductor by way of electrostatic gating [2].

2.2 Preliminary Theory

The first part of the project consisted of gaining an understanding for experiments concerning WTe_2 then connecting it to the theory. Theorectical predictions are what led to the experimental investigations that have validated many of the characteristics of WTe_2. These theories have not only predicted the experimental findings stated previously, such as WTe_2 being a topological insulator and the material's band structure, but have also reinforced these ideas. To create a model for the superconductive state in WTe_2, we need to understand the topological nature of the material and how doping affects the system.

One crucial aspect of understanding WTe_2's topological nature involves examining the band gap function. In topological insulators, a band inversion occurs due to strong spin-orbit coupling, forming a band gap at the Fermi level [3]. The theory has predicted that this band inversion happens at specific points in the Brillouin zone. The band structure for this can be calculated by diagonalizing the full normal state Hamiltonian for WTe_2 (Eq.1) and plotting the eigenvalues [4] (see methods).

$$H_0(k) = \hat{s}_0 \otimes (\hat{h}_0 - \mu) + V_{soc}\hat{s}_z\hat{\sigma}_z\hat{l}_y \tag{1}$$

Researchers can map out the gap function by analyzing the symmetry properties and the elec-

tronic structure and uncover regions where topologically protected surface states arise. However, there is no known gap function, H_Δ, as this system's superconductivity type is unknown. For the project, understanding the doping, or impurity, effect is significant in helping discover the gap function. Doping can modify the carrier's concentration and induce phase transitions between electronic states. Theory and experiment shows varying doping levels could tune the band gap and influence superconductivity. This would also include a direct effect to the T_c. In this case, the T_c can be enhanced and the superconducting phase can happen at higher temperatures or it can be lowered. By studying this impact, we have explored the robustness of WTe_2 and are some steps closer to identifying the symmetry and convention of the superconductivity.

3 Methods

My project involved learning about WTe_2, condensed matter theory methods, and applying what I learned. After learning the importance of band structures and why they are unique to their systems, I recreated the band structure in momentum space in Mathematica using the full normal state Hamiltonian from Eq.1 and the listed parameters from the Hsu paper [4]. This recreation can be seen in Figure 2. The band structure is a visual representation of the allowed quantum states of the electrons and shows that this material is an insulator as there is a gap, indicating there is no state continuum. To go over this gap, the electrons would have to jump quantum states. Further indicating some form of insulation.

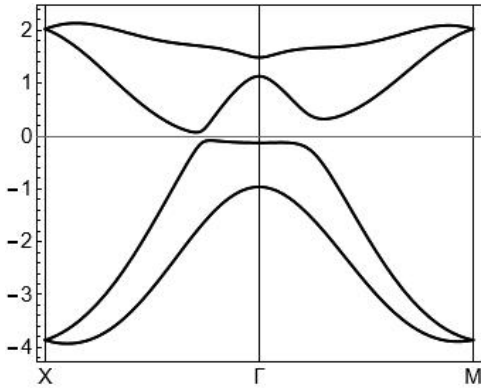

Figure 2: Band structure for WTe_2.

Later on, I learned about Fermi surfaces and their representation of the energies on a particular band. The Fermi Surface, a contour plot from Mathematica, was created while focusing on one of the bands and the different energies on that band lie along the contours. Furthermore, I analyzed different gap symmetries to understand the meaning of gap functions and how they change from s-wave to other waves, such as p-wave or d-wave. My most significant impact on the project was the comprehensive study of WTe_2 and the effects of disorders on the system.

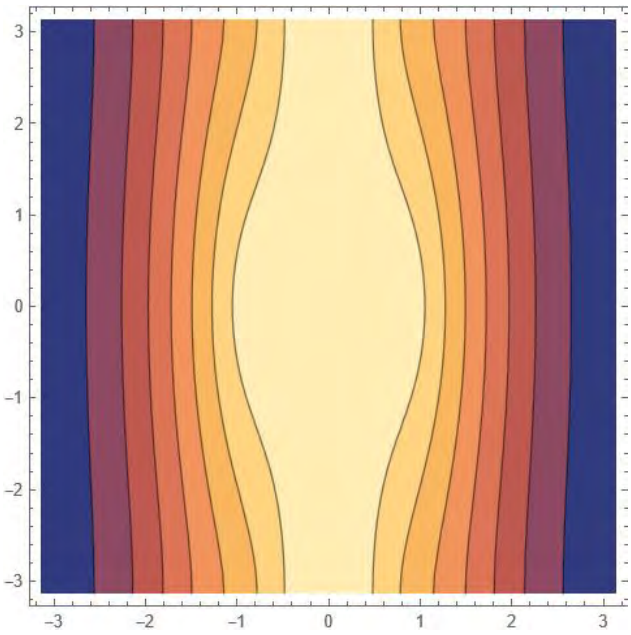

Figure 3: Fermi Surface for WTe_2 of the band eigenvalue 1.48891 from Figure 2.

Taking our preliminary theoretical models and knowledge of the WTe_2 system, we can improve the full normal state model, H_0 to include the exciton order parameters, H'_{Δ}, which is shown in Eq.2. We would then have to create a gap function, H_{Δ} and add this to our superconducting model, H_{sc}, (Eq.3). Once there is a complete model then we apply the mean field approximation to obtain a Bogoliubov-de Gennes Hamiltonian.

$$H'_0 = H_0 + H'_{\Delta} \tag{2}$$

$$H_{sc} = H'_0 + H_{\Delta} \tag{3}$$

4 Conclusion

Since I did not make a model for the superconducting behavior in the system, further work on this project would warrant the H_{sc} model and a mean field approximation of the resulting Hamiltonian. The disorder parameters would have to be added to the model following the approximation, then we could calculate the T_c for the phase transition. Afterwards, we would calculate the the T_c dependence against the disorder strengths. Finally, we would pass our results to willing experimentalists to test these predictions.

My project concludes that we are on the road to making this model and making the necessary calculations to pass it along. The mystery remains around the superconducting gap function and the type of superconducting system WTe_2 exhibits. Once we get experiments to confirm or disprove our model and calculations, then we can analyze the results and find a gap function that includes the symmetry of the system that is breaking to reach the superconducting phase. In addition, finding the gap function will determine if the superconductor is conventional (s-wave) or unconventional (p-wave or d-wave). Thus, most of the mystery would be cleared, and the condensed matter community would have gained valuable insight that can help apply this material to quantum computing and understand more materials like it.

References

[1] S. Tang, C. Zhang, D. Wong, Z. Pedramrazi, H.-Z. Tsai, C. Jia, B. Moritz, M. Claassen, H. Ryu, S. Kahn, *et al.*, Nature Physics **13**, 683 (2017).

[2] E. Sajadi, T. Palomaki, Z. Fei, W. Zhao, P. Bement, C. Olsen, S. Luescher, X. Xu, J. A. Folk, and D. H. Cobden, Science **362**, 922 (2018).

[3] S. Ok, L. Muechler, D. Di Sante, G. Sangiovanni, R. Thomale, and T. Neupert, arXiv preprint arXiv:1811.00551 (2018).

[4] Y.-T. Hsu, W. S. Cole, R.-X. Zhang, and J. D. Sau, Physical Review Letters **125**, 097001 (2020).

[5] X. Qian, J. Liu, L. Fu, and J. Li, Science **346**, 1344 (2014).

[6] Z. Fei, T. Palomaki, S. Wu, W. Zhao, X. Cai, B. Sun, P. Nguyen, J. Finney, X. Xu, and D. H. Cobden, Nature Physics **13**, 677 (2017).

[1] [2] [5] [6] [3] [4]

Constructing a Telescope Simulator Enclosure and Testing the Integral Field Spectrograph of the Gemini Planet Imager

GWYNETH LANNON

2024 NSF/REU Program
Department of Physics and Astronomy
University of Notre Dame

ADVISOR(S): Prof. Jeffrey Chilcote

Abstract

The Gemini Planet Imager (GPI), an instrument used in the direct detection of exoplanets, is currently being upgraded. In order to ensure the success of the upgrade, the instrument and its components need to be tested and characterized. This summer, I worked to build an enclosure for the telescope simulator used to run these tests on GPI and participated in the testing by mapping the dead zones around the limit switches used to control the motion of the prism slide in GPI's integral field spectrograph (IFS) and analyzing the deterioration of the detector in the IFS. In this paper, I present the design and construction of the enclosure for the telescope simulator, as well as results from the testing of the IFS and detector analysis. The enclosure for the telescope simulator was successfully constructed and installed. While the edges of the limit switch dead zones were found to be fixed in some places and variable in others, every dead zone had at least one fixed edge, so using the limit switches to guide the movement of the slide is viable and repeatable. Finally, the percentage of bad pixels on the old detector was found to be significantly higher than is projected in a replacement detector. This information can be used in the future to predict how much a new detector will improve GPI's performance.

1 Introduction

Currently, we know very little about the process by which planets and solar systems form. Our solar system, for example, formed with small, rocky planets close to our sun, and the much larger gas giants further away. Every other solar system astronomers have discovered, however, has large planets close to their stars. How both kinds of solar systems are formed, and why ours formed differently from all the others we've found are questions we have yet to answer. The study of extrasolar planets, or exoplanets–planets orbiting a star other than our sun–is a way to change that.

One method of studying exoplanets is direct detection. In this method, a telescope is used to directly image a star which an exoplanet might be orbiting. Ordinarily, because a star is so much brighter than the planets which might orbit it, starlight would make it impossible to see exoplanets in the images. In order to solve this, a coronagraph is used to remove starlight from the images, allowing any exoplanets to be seen. The greatest advantage of using direct detection to study exoplanets, rather than using the radial velocity or transit methods, is that because the exoplanets are being directly observed, direct imaging provides some very specific and detailed information about them. Unlike other methods of studying exoplanets, direct imaging can tell astronomers about the

composition of an exoplanet's atmosphere, for example, and also provide information about how an exoplanet formed.

Among the instruments designed for use in direct detection is the Gemini Planet Imager, or GPI. Featuring an adaptive optics (AO) system, coronagraph masks, calibration interferometer, integral field spectrograph (IFS), opto-mechanical superstructure, and data reduction pipeline, GPI is capable of taking light collected by a telescope and correcting for distortion caused by Earth's atmosphere as well as removing starlight, allowing for the detection of exoplanets [1]. GPI is optimized for detecting young (newly formed), Jupiter-like exoplanets, which are still warm enough to show brightly in the infrared [1]. Soon, it will see an increase in its capabilities: GPI is currently at the University of Notre Dame undergoing testing in Professor Jeffrey Chilcote's lab as part of the process of upgrading it to GPI 2.0. This upgrade will include a new pyramid wavefront sensor, new coronagraph masks, a new instrument calibration unit with a new-generation self-coherent camera, and upgraded spectral resolution prisms [2]. These upgrades will allow GPI to meet new science goals, including a large-scale survey with an emphasis on cold-start planets, searches for higher-mass planets around older nearby stars, and studies of very young stars [2].

In order to verify that GPI 2.0 will be able to meet all of these science goals, the instrument needs to be tested as part of the upgrade process. Since GPI cannot be connected to the Gemini telescope while it is in the lab receiving upgrades, a telescope simulator is used to feed GPI a replica of the telescope's output. This telescope simulator consists of a fiber source for a laser beam, two pairs of off-axis parabolic mirrors, and a final focusing lens. The pupil mask and phase aberration plate allow the simulator to replicate the Gemini telescope beam and disturbances generated by Earth's atmosphere, while the mirrors and focusing lens redirect and focus the simulator's beam. By not only replicating the Gemini telescope beam but also atmospheric disturbances, the telescope simulator allows the upgraded GPI to be tested as thoroughly as possible in the lab before it is returned to the observatory. An opaque enclosure is used to block off-axis light (extra light coming from sources in the room, such as ceiling lights) from blending with the simulator beam, which would confuse GPI. Previously, a cardboard box fulfilled this purpose. Many of the optics in both

GPI and the telescope simulator itself are extremely sensitive to particles, and need to be housed in a clean room. Cardboard gives off an unfortunately high number of particles, so this box needed to be replaced. I designed and helped to construct a new plastic enclosure for GPI's telescope simulator.

Among the many upgrades to GPI the telescope simulator will be used to test are a new set of spectral resolution prisms in GPI's integral field spectrograph, or IFS. Before input from a telescope reaches the IFS, other systems in GPI correct for disturbances caused by Earth's atmosphere and remove starlight. The IFS then takes the resulting beam of light and, by passing it through various filters and prisms on its way to an infrared detector, samples both its spatial and spectral information [1]. This allows exoplanets to be distinguished from meaningless speckles in the image [1]. The new prisms the IFS is receiving as part of the upgrade will enable the instrument to achieve new observing resolutions, including both a low-spectral-resolution mode and a higher resolution mode [2]. A slide is used to shift these prisms in and out of the beam of light. To do so, it must move precisely under vacuum and in a cryogenic environment. Furthermore, once the upgrades are finished, the slide will be nearly impossible to access and must operate reliably for the next decade. I tested this slide to determine the repeatability of its motion, finding the dead zones surrounding limit switches used to set the position of the slide.

Besides the new prisms, another component of the IFS being upgraded is its HAWAII-2RG (H2RG) detector. A detector is made up of pixels. When incoming photons (such as those in the beam being sampled by the IFS) strike these pixels, electrons are released and collected in wells, allowing the detector to store information about the light which struck it [3]. Detector pixels can sometimes release electrons spontaneously, however. This is called dark current, and pixels with a dark current high enough to skew the data are bad pixels. The number of bad pixels in GPI's IFS has grown dramatically since the upgrade began, so it must be replaced. I analyzed detector images taken with no light source, called darks, which allow bad pixels to be detected, in order to determine the extent of the H2RG's deterioration.

2 Methods

2.1 Designing and Building the Enclosure for the Telescope Simulator

The first iteration of my design for the telescope simulator's new enclosure was a simple box with no bottom and a hinged lid, intended to sit on the table on which the telescope simulator was mounted. The hinged lid allowed for easy access to the simulator inside. The sides of the box would have been sheets of plastic screwed together at the corners. After a round of feedback, the design was modified as shown in Figure 1 to include a neck extending from the main body of the enclosure to GPI's aperture so the simulator beam would be completely enclosed. The dimensions of the table, telescope simulator, old enclosure, and GPI aperture were measured with a tape measure to determine what the dimensions of the new enclosure should be. After another round of feedback on the new design, a frame of aluminum rods was added, both to reinforce the plastic sheets and for them to screw onto, as the plastic being used was too thin to securely be screwed together on its own. The enclosure was constructed based on this final design.

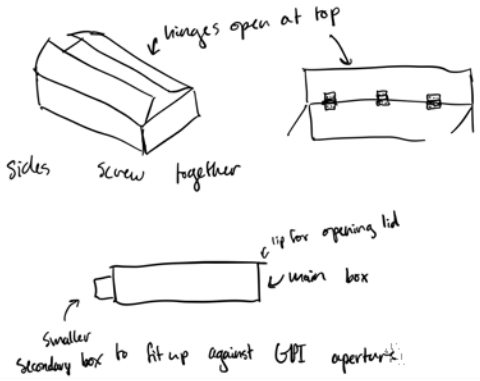

Figure 1: Sketch of my design for the telescope simulator enclosure. Sketch illustrates the design's neck and hinged lid.

The materials used to construct the enclosure were sheets of Delrin machinable plastic, aluminum rods and slats, and assorted screws and hinges. The plastic sheets and aluminum were cut to the proper size, and holes for screws were drilled and tapped. The enclosure was then assembled and transported to the clean room housing GPI for installation.

2.2 Testing Limit Switches for Dead Zones

As shown in Figure 2, the IFS prism stage consists of three prisms on a slide driven back and forth by a stepper motor such that different prisms can be positioned in the beam at different times, allowing both spectral and polarization observations to be made [1]. The stepper motor driving this motion is controlled by a Galil DMC-2183 controller. Since the IFS does not have encoders, positional switches must be used to precisely and repeatably position the prisms in the beam. A switch is depressed when the prism slide moves onto it, and is released when the slide moves off of it. These switches, however, turn on when the slide is in a slightly different position than when they turn off, leading to "dead zones," or areas where the switch can be off or on depending on which direction the prism slide is moving. Outside of a dead zone, the switch is either always on or always off. See Figure 4 for an example of a dead zone.

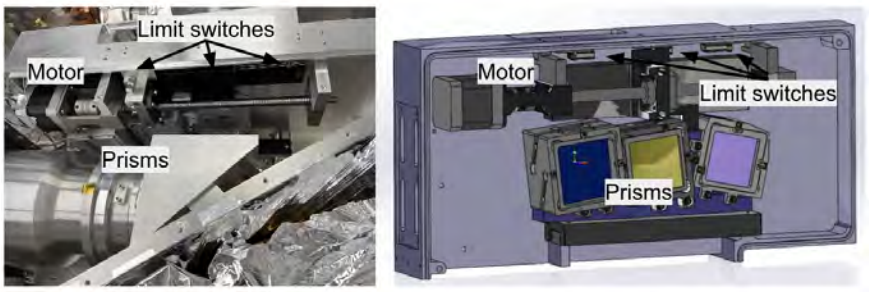

Figure 2: Photograph (left) and 3-D model of the IFS prism stage (right), with the positions of the prisms (on slide), limit switches, and motor labeled.

In order to ensure that the limit switches can reliably be used to determine the location of the prism slide, the locations of these dead zones need to be known. To find where a particular switch turned on, the slide was positioned in a location where the switch being tested was always off, and then inched towards towards the switch until it turned on. To find where the switch turned off, the slide was positioned in a location where the switch was always on and inched away from the switch until it turned off. In both cases, increments of 50 or 100 motor steps were used, giving a smaller range where the on or off point could be. The increments were then decreased to 25 or 15 steps and the process repeated to get a more accurate measurement. Once the point where the switch turned on or off had been located, the slide was returned to the starting point and sent directly to the on

or off point to test the repeatability of the measurement. This process was repeated at least three times.

2.3 Analysis of Detector Deterioration

Two different thresholds were used to determine the number of bad pixels present in the IFS detector at different times: 1 electron per second, the standard in use when the old detector was manufactured, and 0.1 electrons per second, the standard currently in use (and which the replacement detector would be held to). In order to determine the number of bad pixels on the detector at a given time, a set of twenty darks, all taken on the same day, were averaged together. The thresholds for bad pixels, in units of e-/s, were both multiplied by 59.6 seconds/frame, and the values in the darks, in units of data numbers (DN) per frame, were multiplied by 3.04 e-/DN to convert both thresholds and data to a common unit of e-/frame. The percentage of bad pixels in the averaged dataset was then calculated using both the old and new threshold.

3 Results

3.1 The Finished Enclosure

The first iteration of the new enclosure contained a design flaw: the neck extending to GPI's aperture did not line up properly. To fix this, new panels were cut for the front of the main body and the neck was shifted over to align with GPI's aperture. After this correction, the enclosure was successfully installed (see Figure 3).

3.2 Dead Zone Maps

Testing showed that all four of the dead zones had one repeatable side and one variable side. For all of the dead zones except the one on the right side of the center switch (see Figure 4), the repeatable side of the zone was where the switch turned off, and the side where the switch turned on was variable. In the remaining dead zone, this was reversed. The stable, repeatable end of each dead

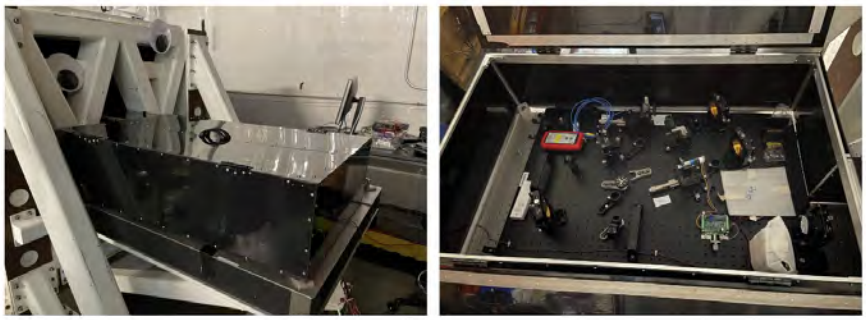

Figure 3: The finished enclosure installed on GPI (left) and the enclosure open with the telescope simulator inside (right).

zone, whether the switch comes on or off there, can become a known point in the path of the prism slide, allowing it to reliably return to that place.

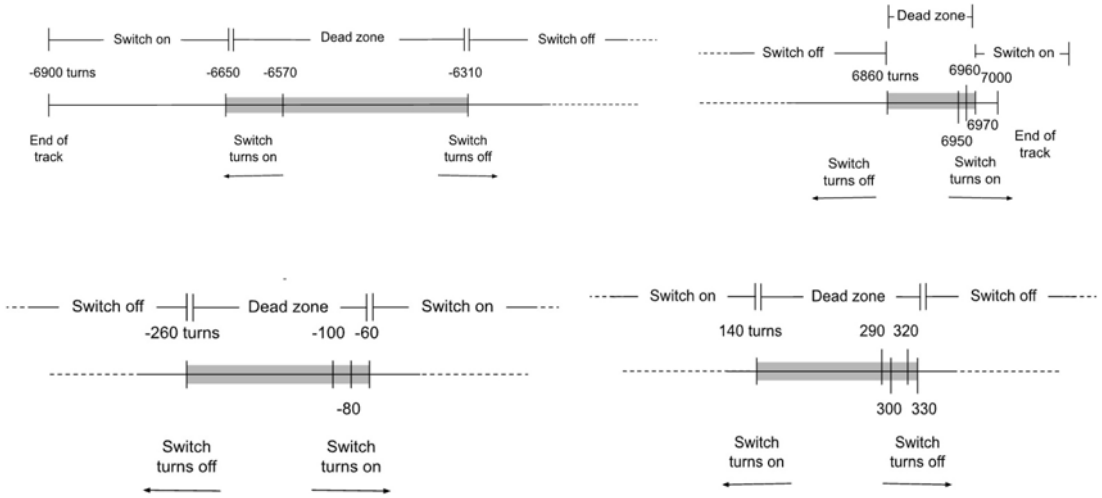

Figure 4: Map of dead zones on the two limit switches at either end of the prism stage (top) and either side of the center limit switch (bottom). Each location where the switch turned on or off is marked.Location along the prism slide is measured in motor turns (backwards or forwards) from the slide's equilibrium position shown in the right half of Figure 2.

3.3 Extent of Detector Deterioration

Even in 2014, when GPI's current detector was nearly new and over 99 percent of its pixels were considered good by the old standard, a bare 20 percent met the new standard. Already this proves that a new detector, manufactured to comply with the newer, stricter standard will improve GPI.

Furthermore, while the deterioration from 2014 to 2019 was slight–a drop of only 0.8 percent–between 2019 and 2022 the proportion of good pixels fell to 68.5 percent. That sudden drop is likely due to a design flaw in the detector similar to the one which plagued the James Webb Space Telescope's detectors [2]. Detector designs have since been corrected, so a new detector would not have this flaw.

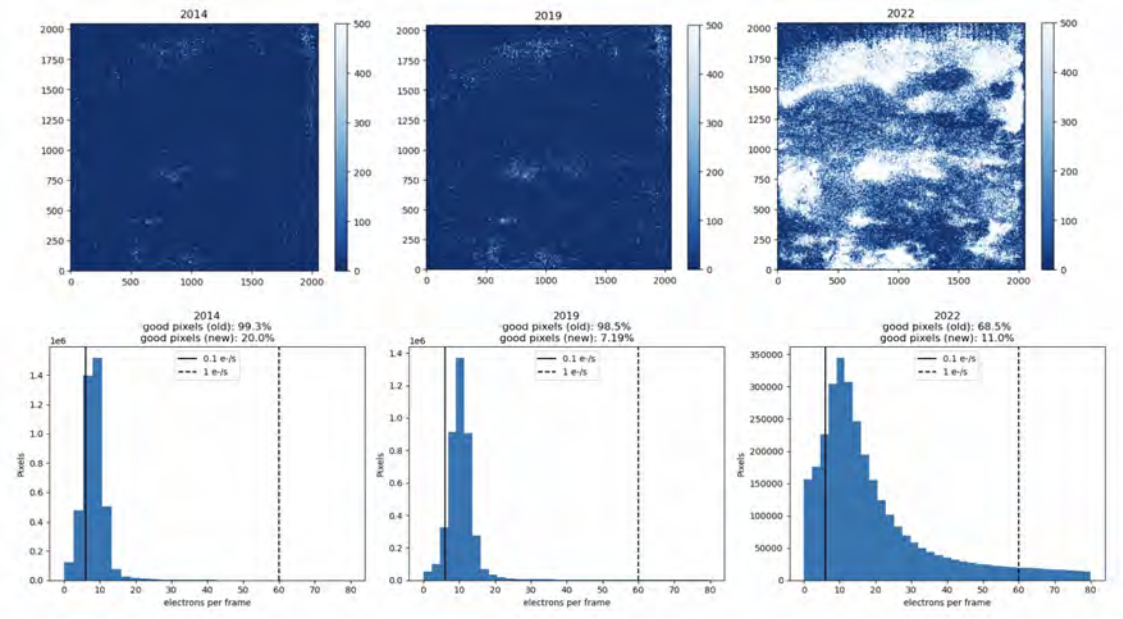

Figure 5: Histograms of pixel distribution in the detector and accompanying darks from 2014, 2019, and 2022. In the histograms, the dashed line represents the old standard used to determine bad pixels, and the solid line represents the new standard. In the darks, white spots represent bad pixels.

4 Conclusion

Currently, the new enclosure for GPI's telescope simulator has been installed. Testing of the limit switches on the IFS prism stage has shown that one side of every dead zone is stable, proving that the limit switches are viable and repeatable location markers. Additionally, analysis of GPI's current IFS detector has shown that its percentage of bad pixels, when measured by using the newer, stricter standard, is much higher than it would be in a new detector, even before the dramatic increase in bad pixels over the past couple of years.

The upgrade of GPI is still in progress, however. Some of the testing and characterization yet to come will build off the work presented in this report: the construction of a new enclosure for the telescope simulator will allow that simulator to be used to conduct future tests. The confirmation that the limit switches are viable as location markers for the IFS prism slide enables further testing of the prism slide mechanism, including at the cryogenic temperatures at which the IFS operates. Testing the switches before testing the slide cold is essential because during those tests, the slide must be sealed inside a box under vacuum. If something goes wrong, the only indication of what the problem might be will come from the positional switches. Finally, knowledge of the IFS detector's past and current performance makes it possible to compare the old detector to the projected performance of the new detector once it arrives and can be tested, which will provide an estimate of how much a new detector will improve GPI's capabilities. This future work on the upgrade of GPI will in turn lead it to become a better, more powerful instrument, capable of discovering more exoplanets and unearthing new information about planet formation.

References

[1] J. Chilcote, *Direct Observation of Extrasolar Planets and the Development of the Gemini Planet Imager Integral Field Spectrograph*, Ph.D. thesis, UCLA (2014).

[2] J. Chilcote, Q. Konopacky, R. Hamper, B. Macintosh, C. Marois, D. Savransky, R. Soummer, J.-P. Veran, G. Agapito, A. Aleman, M. Bonaglia, M.-A. Boucher, J. Burke, V. Chambouleyron, R. J. De Rosa, C. Do Ó, J. Dunn, M. Engstrom, S. Esposito, G. Filion, J. Joeleff Fitzsimmons, O. Galvan, D. Kerley, J.-T. Landry, O. Lardiere, D. Levinstein, M. A. Limbach, J. Maire, A. Matzner, T. Mocnik, B. Nickson, E. L. Nielsen, J. Nguyen, M. Nguyen, S. Perera, D. Peng, M. D. Perrin, E. Por, L. Pueyo, C. Quiroz, F. Rantakyrö, B. Sands, A. Seifahrt, G. Singh, and W. Eduardo, Proceedings of SPIE **13096** (2024).

[3] S. B. Howell, *Handbook of CCD Astronomy* (Cambridge University Press, 2006).

Restoration and Optimization of a Coincidence Plunger for Recoil Distance Doppler-Shift Measurements at Notre Dame's Nuclear Science Lab

ANTONIO MARTINEZ

2024 NSF/REU Program
Department of Physics and Astronomy
University of Notre Dame

ADVISOR(S): Prof. Ani Aprahamian, Dr. Wanpeng Tan

Abstract

"Plungers" are devices used for measuring the lifetimes of excited nuclear states using the Recoil Distance Doppler-shift (RDDS) method. The measurement involves the gamma rays depopulating excited states of a given nucleus. This report explains the basics of a plunger device received from the University of Cologne via Yale University and Argonne National Laboratory. It is presently in the Nuclear Science Laboratory (NSL) of the University of Notre Dame. This report details the present condition of the device, the repairs addressed, and the remaining issues that need to be resolved. Once resolved, the plunger device will be available for a wide range of lifetime measurement experiments in the NSL.

1 Introduction

A functional plunger device can be invaluable in nuclear physics for determining the lifetimes of excited nuclei. The crucial parts for experiments reside in the target chamber, where a target foil is set at a specific distance from a stopper foil using the micrometer precision of an inchworm motor. It is the precision of this motor that allows the extraction of lifetimes as a function of distance. A particle beam is typically used to excite or create nuclei via reactions. The gamma rays de-excite the nucleus and are Doppler-shifted if emitted in flight. The ratio of shifted to unshifted gamma rays and the known distance between the target and stopper foils can then be used to measure the lifetimes of the excited states. The lifetimes are then useful for determining transition probabilities and hence the matrix elements connecting states, providing insight into the nuclear structure [1] of the states.

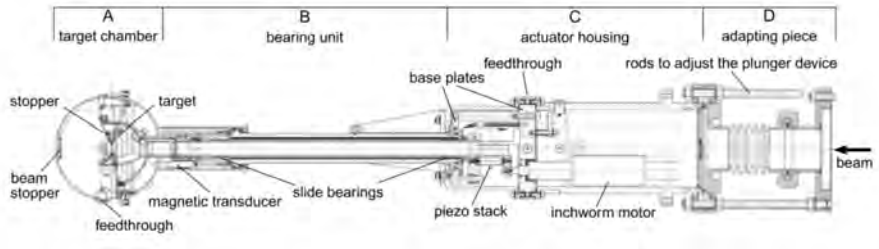

Figure 1: Overview of Plunger

This report is divided into five parts: an overview of the plunger, a breakdown of the sections worked on, documentation of repairs, a summary of remaining needs, and a conclusion on the

plunger's outlook at the NSL.

2 Overview of the Plunger

The plunger's piezoelectric inchworm motor drives a shaft that is located inside of the bearing unit with these two parts linked through a PS-motor-shaft assembly. The piezo stack (PS) is at the center of this assembly, with a metal block anchored to each end of the PS through a series of springs and pins. One of these metal blocks is clamped to the actuator housing (AH) end of the shaft and the other block is secured to the inchworm motor with a screw. During the course of an experiment, the distance between the target and stopper foils may start to fluctuate due to a number of factors, but this is accounted for through a capacitance feedback system between the two foils. When the distance changes, so does the capacitor voltage, and this change in voltage causes the PS to contract or relax, maintaining the distance between the foils. The initial distance setting, capacitance measurements, and distance corrections can all be automated through Labview software.

2.1 Basics of RDDS method

The energy of the Doppler-shifted gamma rays, γ, can be calculated using the equation:

$$E_{sh} = E_0 \frac{\sqrt{1-\beta^2}}{1-\beta\cos(\theta)} \tag{1}$$

Where E_0 is the energy of unshifted γ, $\beta = \frac{v}{c}$ and θ is the angle between the beam line and the detector. The decay curve, $R(t)$, can be defined by two equations

$$R(t) = \frac{I_0}{I_0 + I_{sh}} \tag{2}$$

$$R(t) = N(0)e^{\frac{-t}{\tau}} \tag{3}$$

Where I_0 and I_{sh} are the intensities of the unshifted and shifted energy peaks respectively, $N(0)$ is the initial population level and τ is the lifetime. This simplification of how lifetimes can be

calculated is only applicable in the scenario of transitions of a single level, and at speeds that are $\lesssim 4\%$ of the speed of light before relativistic effects come into play. Since our project was never able to run the experiment, this should suffice for the purposes of this paper, but more in-depth breakdowns of the calculations, and other possible effects can be found in references [1], [2].

3 Sectional Breakdown

3.1 Labview

Labview is a visual programming language widely used for the automation and control of instrumentation. This software is beneficial for creating programs to automate processes involving measurement instruments. The Labview software written for this device was created at the University of Cologne and included various virtual instruments (VIs) for measurements of different plunger components. At this point, we were only trying to utilize the simpler 2-foil system of the Cologne plunger and because of this we only have a need for 8 of the included Vis.

1. Motor.vi: Operates the inchworm motor through the Labview software allowing repositioning of the target foil while the plunger is under vacuum.

2. Micrometer.vi: Displays the micrometer position of the foil holder in Labview

3. Piezo-voltage.vi: Used to change the voltage amplitude applied to the PS to induce changes in position through the PS.

4. MCA.vi: Reads the voltage from the capacitor of the foils.

5. Eichpunkte.vi: Calculates measurement points of distance and saves them into the calibration file.

6. Discal_single_test.vi: Runs through the measurement points of eichpunkte and measures the voltage at each point, completing the distance vs voltage calibration file

7. Splinecurve.vi: Solely used to inspect the curve of the calibration file.

8. Regelung_single.vi: The capacitance feedback control system used during the experiment to maintain the distance between the foils.

From the start of the project, none of these vi's opened correctly as there were a number of broken file paths, causing vi's to be nonoperational and show errors when we tried to run them.

3.2 Actuator Housing

The AH contains the inchworm motor and the PS. In order to drive the motor, an external Burleigh motor controller was necessary. A controller was purchased second hand that was the same model Cologne had used. The PS also required us to purchase a piezo amplifier in order to provide the correct voltage. On the external shell of the plunger's AH are LIMO ports for connecting a micrometer to measure the location of the target foil and a port to connect the piezo amplifier to the PS, as well as a number of unused port holes.

Motor: The motor would make sound but did not produce any movement. The motor controller was also unstable and would not turn on at times.

Piezo Stack: The LIMO cable was disconnected from the PS. Due to this and Labview not being operational, we were unable to test the PS at the beginning of the summer.

3.3 Target Chamber

The target chamber (TC) contains the magnetic transducer, which acts as the probe for the micrometer. The TC also contains the target and stopper foil holders. On the external side of the TC are a number of LIMO ports, though we were only interested in the ports for the target and stopper foils to measure voltage. The target foil cone is housed in a unit that is fastened to TC end of the shaft with three screws and springs placed between the housing and the shaft, allowing precise adjustments to keep the two foils parallel for optimal capacitor performance. The stopper foil cone is fastened

with screws into 3 metal caps that are glued to the top of 3 plastic blocks on a metal ring. These plastic blocks provide the insulation between the stopper foil and the plunger body.

Magnetic Transducer: The probe had a wire that had become unattached.

Foil Holders: The wires that connect the LIMO ports of the target and stopper were disconnected.

4 Repairs and Emerging Complications

4.1 Labview

We discovered that many errors preventing VIs from opening were due to missing sub-VIs in the main programs. With assistance from a Labview expert from the University of Cologne, we received updated versions of the Labview software, now at version v3_2. This resolved several issues, but some programs are still not fully operational.

Motor.vi: Labview cannot produce movement. We traced the pins and verified the wiring of the DAQ and motor controller. Using Labview's parent company's app, NI MAX, we found that the motor can be controlled via the computer, indicating that the issue lies within Labview.

Micrometer.vi: This program should display the position of the target foil continuously but only displays "0" unless the "M/O" button on the micrometer is pressed. When pressed this VI displays the position momentarily. Purchasing a new bidirectional, duplex optical cable did not resolve this issue, rather with this new cable, the position would not display even with the button press.

Piezo-voltage.vi: This program now runs with no errors.

Mca.vi: This program is fully functional with the new Labview version.

Eichpunkte.vi: No errors are displayed, but have not been able to test it due to the motor control issue.

Distcal_single_test.vi: No errors are displayed, but we can't test it fully due to motor and the micrometer issues with Labview. Also of note, the expert told us that this VI is only to test and that there is another VI, Distcal_single_normal.vi that can be used, though it has the same issues at the moment.

Note: A workaround is possible thorough manual motor control and MCA.vi, which enabled us to create a manual calibration file. This file was generated by recording micrometer positions and their corresponding voltages.

Regelung_single.vi: Not yet tested due to time constraints and previous VIs not being fully operational. Future experiments depend on this VI running correctly to maintain foil distance.

4.2 Actuator Housing

Motor: The ND electrical expert fixed the faulty connections inside the controller, but this did not fix the motor. With the help of an expert on the mechanical aspects of the plunger, we disassembled the motor, and attempted to lubricate the inner mechanisms. We still could not produce anything other than sound. The University of Cologne loaned us a replacement motor that had been tested in their facilities. After connecting this motor to the controller, the motor exhibited the same issue. We inspected the controller more thoroughly and found a blown fuse in the high-voltage circuit board. Replacing the fuse resolved the motor issue.[1] The replacement motor connects through two 6-pin connectors, unlike the original motor's three 4-pin connectors. Wiring this motor to the DAQ/controller with the plunger fully intact will need to either be through unused port holes on the AH or rewiring the new motor to the old motor's housing to use the existing 3 4-pin ports.

Piezo Stack: We resoldered the LIMO cable and reassembled the PS-motor-shaft assembly. Testing revealed inconsistent movement when adjusting voltage through Labview and when adjusting the controls on the piezo amplifier. Reason for this inconsistency is unknown, and testing of Regelung_single.vi is needed to determine if the PS performs as needed or should be replaced.

4.3 Target Chamber

Micrometer: After fixing a broken wire, the micrometer correctly measured the target foil position. As stated, information is still not constantly transferred to Labview. This Labview issue must be

[1] Since the new motor exhibited the same behavior as the original, it's possible the old motor is functional. If reassembled, the original motor could potentially be a viable option or back up.

resolved so micrometer measurements can be used in VIs that require position.

Foils/Capacitance: Wires for stopper and target foil holders were resoldered and labeled. While working on the foil holders, we found over-tightening screws that fasten stopper cone to metal caps can cause them to detach from white plastic blocks. We used epoxy to resecure them, but these caps can easily detach again with too much force. Early tests of measuring a voltage across foils was inconsistent due to the precision needed. Foil quality, including flatness and residue-free surfaces, and foils being extremely parallel are crucial for consistent voltage measurements. We found best technique for foil quality is to epoxy the foil to the outer side of ring and to push the cone of the target or stopper up against the foil.

5 Summary of Remaining Needs

Essential Pre-Experiment Needs:

- **Motor Wiring:** Rewire the motor through the plunger's external casing to connect it to the controller/DAQ while the plunger is sealed.
- **Regelung_single.vi Test:** Verify the feedback system maintains the correct foil distance and assess the PS's performance to determine if replacement is needed.
- **Vacuum Test:** Check the plunger under vacuum for leaks to ensure proper operation during experiments.

Additional Needs:

- Resolve Labview issues with the motor to improve efficiency and avoid the need to make manual adjustments in the target room. This will also enable automation of the calibration process with eichpunkte.vi and improve accuracy.
- Ensure Labview consistently receives/displays the micrometer's measurements.

Note: This summer's timeframe was insufficient to address all plunger aspects. Further issues with the physical apparatus or Labview VIs may arise and may need to be resolved before full operation or experiments.

6 Conclusion

This summer, we made significant progress in restoring the plunger to an operational state, addressing and correcting various issues along the way. Although the project requires more time than a single summer can provide, our progress and detailed documentation of remaining issues will greatly contribute to adding a valuable new instrument to the NSL. This tool will enhance experimental possibilities in a lab that is well-equipped to utilize the plunger to its full potential.

7 Acknowledgements

I would like to express my deepest gratitude to my colleagues, Miles Mamigonian and Pedro Souza, for their invaluable contributions to this experiment. Additionally, thanks to Casper Lakenbrink (Argonne National Laboratory, University of Cologne) for his assistance with Labview programming, Dr. Claus Müller-Gatermann (Argonne National Laboratory) for his troubleshooting expertise with the inchworm motor, and Dr. Edward Stetch (Notre Dame University) for his explanations of the Labview software.

8 References

[1] Beckers, M. (2023). Development of a new compact three-foil plunger device and lifetime measurements using the recoil distance Doppler-shift method. Inaugural-Dissertation zur Erlangung des Doktorgrades der Mathematisch-Naturwissenschaftlichen Fakultät der Universität zu Köln

[2] Dewald, A., Möller, O., & Petkov, P. (2012). Developing the Recoil Distance Doppler-Shift technique towards a versatile tool for lifetime measurements of excited nuclear states. Progress in Particle and Nuclear Physics, 67, 786-839. Elsevier.

Ab Initio Calculations for Nuclear Pairing in Oxygen Isotopes

KAYLA O'DONNELL

2024 NSF/REU Program
Department of Physics and Astronomy
University of Notre Dame

ADVISOR(S): Prof. Mark Caprio

Abstract

Ab initio methods allow predictions to be made about the overall properties of nuclei directly from internuclear interactions. In this work, we employ the no-core configuration interaction (NCCI) approach to explore nuclear shell structure and pairing in oxygen isotopes. To understand how this structure contributes to the *ab initio* wavefunctions, we use the Lanczos decomposition method to obtain the decomposition of low-lying states with respect to the number and quasispin operators for each orbital in the valence neutron shell. The resulting decompositions allow us to see the extent to which the *ab initio* results follow the patterns expected from a simple shell-model interpretation.

1 Introduction

Understanding nuclear structure facilitates the interpretation of experimental observables such as transition energies and scattering cross-sections. One approach to nuclear structure theory is the *nuclear shell model*, which assumes a particular central-potential form for the overall nuclear Hamiltonian. Another, more fundamental approach, known as *ab initio*, builds the nuclear Hamiltonian directly out of interaction terms between groups of two to three nucleons. To explore nuclear structure using either of these approaches, we can diagonalize our Hamiltonian to find the energy eigenstates of our nuclei, which become our nuclear wavefunctions. We can then explore structural properties of these wavefunctions. One possible contribution to nuclear shell structure is known as *nuclear pairing*, where two like nucleons in the same angular momentum orbital couple to zero angular momentum to form a quasi-bosonic pair. In this work, we use *ab initio* methods to investigate shell structure and pairing structure in even-mass oxygen isotopes.

2 Background

2.1 Multi-Fermion States

Consider the space of all configurations of a variable number of identical particles, known as *Fock space*. We work in the fermionic case, in which all elements of the Fock space are normalized antisymmetrized products of single-particle wavefunctions. Elements of the fermionic Fock space

can be labeled based on which single-particle states are occupied, with the vacuum state receiving the label $|0\rangle$. These states can be modified by the particle creation operator $a_i^\dagger$ or the particle annihilation operator a_i. For instance,

$$a_1^\dagger|0\rangle = |1\rangle,\ a_2^\dagger a_1^\dagger|0\rangle = a_2^\dagger|1\rangle = |2,1\rangle,\ a_1^\dagger|1\rangle = 0,\ a_2|2,1\rangle = |1\rangle,\ a_1|1\rangle = |0\rangle,\ a_2|1\rangle = 0. \quad (1)$$

The anticommutation relations of the particle creation and annihilation operators are as follows:

$$\{a_i^\dagger, a_j^\dagger\} = \{a_i, a_j\} = 0,\ \{a_i, a_j^\dagger\} = \delta_{ij}, \quad (2)$$

where $\{A, B\} = AB + BA$.

2.2 Nuclear Shell Model

We can model the nucleus as a A-fermion state consisting of Z protons and N neutrons under the influence of a central potential. For simplicity and calculational ease, this central potential is frequently taken to be the harmonic oscillator potential. Our single-particle states can therefore be labeled using harmonic-oscillator quantum numbers n, l, and m_l, and their energy shells are labeled by $N = 2n + l$. We use the convention that $n = 0$ for the lowest radial wave function at each l.

In addition to the harmonic oscillator quantum numbers, our single-particle states also carry the quantum numbers that are always associated with nucleons: m_s and t_z. For our calculations, we work in the basis where l and s are coupled to definite angular momentum j, so we instead label our states by n, l, j, m, and t_z. Since our Hamiltonian is rotationally invariant, the energy of our single-particle states is independent of m. We therefore organize our harmonic-oscillator states into degenerate-energy orbitals labeled by n, l, j, and t_z. Traditionally, these orbitals are labeled $n\ell_j$, where ℓ is a letter that represents the l quantum number (s for $l = 0$, p for $l = 1$, d for $l = 2$, and following the alphabet starting at f for larger l). For instance, the $0d_{5/2}$ orbital has $n = 0$, $l = 2$, $j = 5/2$. Each of these orbitals has degeneracy $2j + 1$.

In the non-interacting shell model, our overall nuclear state is therefore simply the normalized

antisymmetrized product of A single-particle states. Due to the spin-orbit-corrected harmonic-oscillator shell structure, there are large ground-state-energy gaps when the number of nucleons of a particular type reaches 2, 8, 20, 28, 50, 82, 126, and 184. These are known as *magic numbers*. In this work, we investigate semi-magic nuclei, where the number of protons, but not the number of neutrons, is a magic number. This allows us to focus on the structure of the partially-filled "valence" neutron shell. In the interacting shell model, the Hamiltonian includes not only the central potential term, but also residual interactions between valence nucleons. The remaining nucleons form a core that is treated as inert.

2.3 *Ab Initio* Methods

In contrast to traditional shell-model approaches, *ab initio* methods explore nuclear structure directly by diagonalizing a Hamiltonian with model two-body and/or three-body interactions in the many-body space. Since we are interested in the intrinsic structure of the nucleus, we use the Hamiltonian $H = T_{\text{rel}} + V$, where T_{rel} is the relative kinetic energy between nucleons and V contains all the interaction terms.

In a no-core configuration interaction (NCCI) approach, one works in a basis of normalized antisymmetrized products of A single-particle states. In the no-core shell model (NCSM) [1], these single-particle states are taken to be the spin-orbit-coupled harmonic-oscillator states. The excitation of a basis state can be characterized by the *number of excitation quanta* N_{ex}. This can be found by summing the number N of oscillator quanta across all single-particle states, and subtracting the lowest Pauli-exclusion-principle-allowed sum of the number N of oscillator quanta. The no-core-shell-model basis is in principle infinite, but we can truncate it by considering only basis states such that $N_{\text{ex}} \leq N_{\text{max}}$ for some N_{max}.

2.4 Nuclear Pairing

In this work, we investigate pairs of neutrons in the same orbital that are coupled to zero angular momentum. We define the *quasispin* operators for a shell-model orbital $k = (nljt_z)$ as follows:

$$S_{k+} = \frac{1}{2}\sum_m a^\dagger_{km} a^\dagger_{k\bar{m}} = \frac{1}{2}\hat{j}_k \left(a^\dagger_k \times a^\dagger_k\right)_{00} \tag{3}$$

$$S_{k-} = \frac{1}{2}\sum_m a_{k\bar{m}} a_{km} = -\frac{1}{2}\hat{j}_k \left(\tilde{a}_k \times \tilde{a}_k\right)_{00} \tag{4}$$

$$S_{k0} = \frac{1}{4}\sum_m \left(a^\dagger_{km} a_{km} - a_{km} a^\dagger_{km}\right) = -\frac{1}{4}\hat{j}_k \left[\left(a^\dagger_k \times \tilde{a}_k\right)_{00} + \left(\tilde{a}_k \times a^\dagger_k\right)_{00}\right], \tag{5}$$

where $\hat{j}_k = \sqrt{2j_k+1}$, $a^\dagger_{k\bar{m}} = (-1)^{j_k-m} a^\dagger_{k,-m}$, and $\tilde{a}_k = (-1)^{j-m} a_{-k}$ [2].

Note that the quasispin operators obey the SU(2) commutation relations

$$[S_{k0}, S_{k+}] = S_{k+},\ [S_{k0}, S_{k-}] = -S_{k-},\ [S_{k+}, S_{k-}] = 2S_{k0}. \tag{6}$$

Therefore, the operator

$$\mathbf{S}^2_k = S^2_{k0} + \frac{1}{2}\left(S_{k+}S_{k-} + S_{k-}S_{k+}\right) = S_{k0}\left(S_{k0} - 1\right) + S_{k+}S_{k-} \tag{7}$$

has eigenvalues $S_k(S_k+1)$, where S_k is an integer or half-integer; and the operator S_{k0} has eigenvalues M_k, where $M_k \in \{-S_k, -S_k+1, \ldots, S_k-1, S_k\}$ [2].

To extract physical meaning from the quasispin quantum numbers S_k and M_k, we can look at the *occupation quantum number* N_k and the *seniority quantum number* v_k. The occupation-seniority quantum numbers are related to S_k and M_k as follows:

$$S_k = \frac{1}{2}\left(\Omega_k - v_k\right), M_k = \frac{1}{2}\left(N_k - \Omega_k\right), \tag{8}$$

where $\Omega_k = \frac{1}{2}(2j_k+1)$ is the pair degeneracy of the orbital k. The occupation quantum number N_k represents the total number of nucleons in the orbital k and can take on any integer value between

0 and $2\Omega_k$ (inclusive), while the seniority quantum number v_k represents the number of unpaired nucleons in the orbital k and can take on any integer value between 0 and $\min(N_k, 2\Omega_k - N_k)$ (inclusive) that has the same parity as N_k. From the above relations, the eigenvalues of $S_{k+}S_{k-}$ are given by [2]:

$$\langle S_{k+}S_{k-}\rangle = -\frac{1}{4}\left[N_k\left(N_k - 2\Omega_k - 2\right) - v_k\left(v_k - 2\Omega_k - 2\right)\right]. \quad (9)$$

We can therefore study the shell and pairing structure of a state by decomposing its wavefunction into simultaneous eigenstates of N_k and $S_{k+}S_{k-}$ and solving for the seniority quantum number v_k.

3 Methods

Our aim is to explore the shell structure and pairing structure in ^{18}O, ^{20}O, ^{22}O, and ^{24}O. We employ an NCSM approach. Since oxygen isotopes are semi-magic nuclei, their energy eigenstates can be approximately described as fully-occupied $N = 0$ and $N = 1$ proton and neutron shells and a partially-filled $N = 2$ neutron shell. We are therefore interested in the spectrum of occupation and seniority quantum numbers associated with the $N = 2$ spin-orbit-coupled harmonic-oscillator neutron orbitals: $1s_{1/2}$, $0d_{3/2}$, and $0d_{5/2}$.

We begin by diagonalizing the *ab initio* nuclear Hamiltonian. We then decompose the resulting wavefunctions into eigenstates of the operator

$$a_1 N_{1s1/2} + a_2(S_+S_-)_{1s1/2} + a_3 N_{0d3/2} + a_4(S_+S_-)_{0d3/2} + a_5 N_{0d5/2} + a_6(S_+S_-)_{0d5/2} + a_7 N_{\mathrm{ex}}, \quad (10)$$

where N_{ex} is the operator for the number of excitation quanta and the coefficients a_i are chosen to minimize eigenvalue degeneracy [3]. To accomplish this, we use a technique called Lanczos decomposition [4]. Each eigenvalue of this operator corresponds to a unique set of occupation-seniority quantum numbers for the $N = 2$ neutron shell and excitation quantum number N_{ex}. We restrict our analysis to $N_{\mathrm{ex}} = 0$ to capture activity in the $N = 2$ neutron shell.

Both the wavefunction generation and the decomposition are performed using the MFDn v15 code [5]. For the Hamiltonian, we use the Daejeon16 two-body interaction [6]. We use a harmonic-

oscillator basis with oscillator length $\hbar\omega = 15$ MeV, truncated at $N_{\max} = 4$. We then decompose the wavefunction of each state of ^{18}O, ^{20}O, ^{22}O, and ^{24}O below 20 MeV that has a large (> 50%) total $N_{\text{ex}} = 0$ contribution into eigenstates of the above operator. We report the $N_{\text{ex}} = 0$ component of these decompositions.

4 Results and Discussions

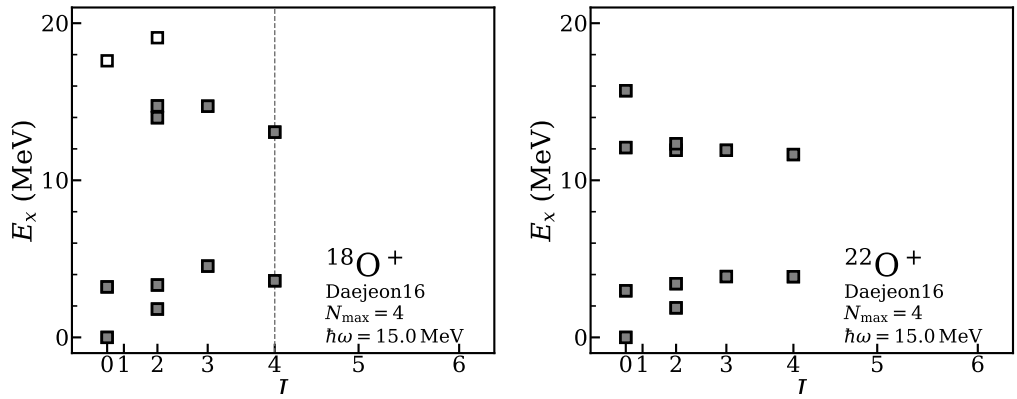

Figure 1: An energy diagram of the calculated energy eigenstates for ^{18}O and ^{22}O. States in gray have a large (> 50%) total $N_{\text{ex}} = 0$ contribution and were included in our analysis.

Each isotope under consideration showed two distinct groups of states below 20 MeV with similar energies, with the exception of ^{24}O, which had three distinct groups below 20 MeV. The energies of states in ^{18}O and ^{22}O are plotted in Figure 1. All of the states in the lowest energy group were dominated by occupation-seniority states with an empty $0d_{3/2}$ orbital, while all of the states in the second energy group were dominated by occupation-seniority states with one nucleon in the $0d_{3/2}$ orbital. As an example, Figure 2 shows the probability contribution from the $N_{\text{ex}} = 0$ component of each $(N_{1/2}, v_{1/2}, N_{3/2}, v_{3/2}, N_{5/2}, v_{5/2})$ occupation-seniority state for selected 2^+ states of ^{18}O. In ^{24}O, all states in the third energy group had two nucleons in the $0d_{3/2}$ orbital. These findings suggest that the energy required to occupy the $0d_{3/2}$ orbital is much greater than the energy required to occupy either the $0d_{5/2}$ orbital or the $1s_{1/2}$ orbital, and that the energy difference between the $0d_{5/2}$ orbital and the $1s_{1/2}$ orbital is negligible in comparison (see Figure 3). We can

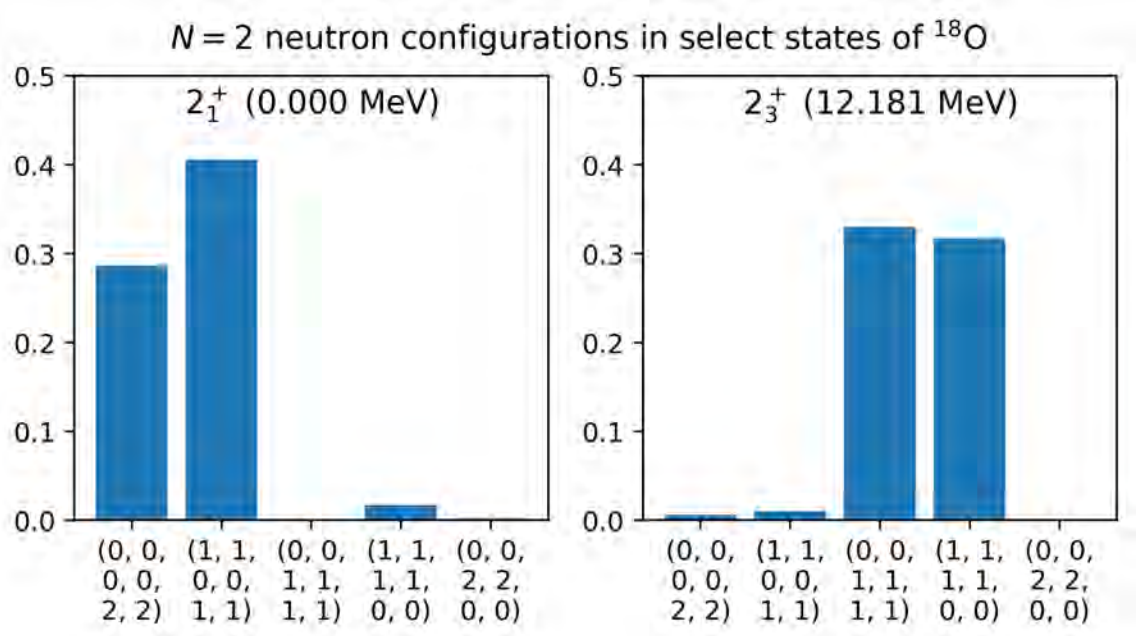

Figure 2: The $N_{\text{ex}} = 0$ component of the occupation-seniority eigenvalue decomposition for the first and third 2^+ states of ^{18}O with a large ($> 50\%$) $N_{\text{ex}} = 0$ component. We use the Daejeon16 interaction with a basis oscillator length $\hbar\omega = 15$ MeV and a basis truncation $N_{\text{max}} = 4$. State energies provided are relative to the lowest-energy 2^+ state. The x-axis labels represent the quantum numbers $(N_{1/2}, v_{1/2}, N_{3/2}, v_{3/2}, N_{5/2}, v_{5/2})$, and the y-axis represents the probability of that occupation-seniority state. We note that both low-lying states are dominated by empty $0d_{3/2}$ orbitals, while both higher-energy states are dominated by partially-filled $0d_{3/2}$ orbitals.

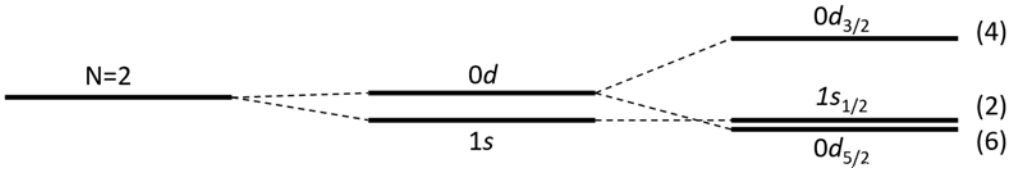

Figure 3: A schematic diagram of the structure of the $N = 2$ neutron shell in oxygen isotopes. The numbers in parentheses represent the maximum occupations for each orbital.

therefore group the $0d_{5/2}$ and the $1s_{1/2}$ orbitals together as a "subshell" of the $N = 2$ neutron shell and consider the $0d_{3/2}$ orbital a separate higher-energy "subshell". This means that for states of ^{20}O with unoccupied $0d_{3/2}$ orbitals, exactly half of the $0d_{5/2} - 1s_{1/2}$ neutron "subshell" is occupied.

We also observe that $0d_{5/2} - 1s_{1/2}$ neutron particles and pairs of particles in ^{18}O roughly correspond to $0d_{5/2} - 1s_{1/2}$ neutron holes and pairs of holes in ^{22}O, and vice versa, in low-lying states with unoccupied $0d_{3/2}$ orbitals. Figure 4 provides an example of this. The $(1, 1, 0, 0, 1, 1)$ bar in the

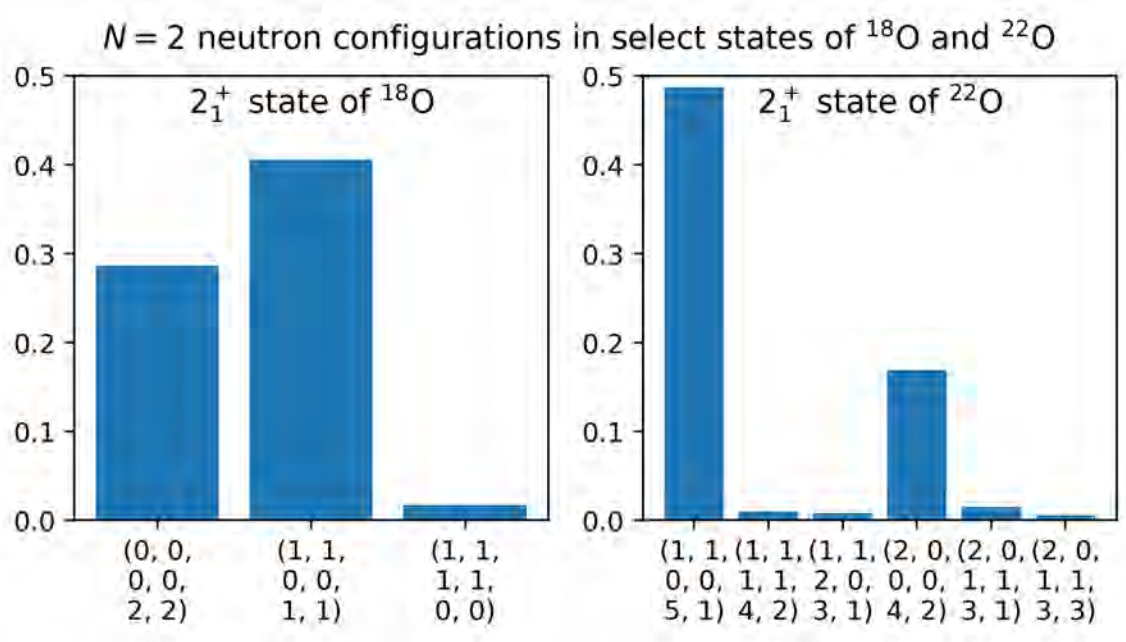

Figure 4: The $N_{\text{ex}} = 0$ component of the occupation-seniority eigenvalue decomposition for the first 0^+ and 2^+ states of ^{18}O and ^{22}O with the same run parameters and axis labels as in Figure 2. All occupation-seniority states with probability greater than 0.005 are shown. This figure illustrates the correspondence between particles in ^{18}O and holes in ^{22}O (see text).

^{18}O state corresponds to the $(1, 1, 0, 0, 5, 1)$ bar in the ^{22}O state, since one particle in $1s_{1/2}$ and one in $0d_{5/2}$ corresponds to one hole in $1s_{1/2}$ and five in $0d_{5/2}$. Also, each unpaired particle corresponds to an unpaired hole. The $(0, 0, 0, 0, 2, 2)$ bar in ^{18}O and the $(2, 0, 0, 0, 4, 2)$ bar in ^{22}O are related in a similar way. These relations were observed for all states in ^{18}O and ^{22}O with unoccupied $0d_{3/2}$ orbitals. The correspondence between the low-lying states in ^{18}O and ^{22}O is also reflected in the fact that their energies relative to their respective ground states are similar (see Figure 1).

5 Conclusions

Our analysis of the occupation-seniority structure of majority-$N_{\text{ex}} = 0$ states in even-mass oxygen isotopes did not yield much clear information about the effect of pairing on the energies of the states, likely due to the energy proximity of the $1s_{1/2}$ and $0d_{5/2}$ orbitals. However, our analysis showed several clear indications of shell structure. We have therefore observed the emergence of shell structure from purely *ab initio* calculations. In future work, we will decompose shell-model

wavefunctions obtained with phenomenological interactions between valence neutrons in the same way. This will allow us to compare in more detail the occupation-seniority structure predicted by *ab initio* calculations and that predicted by the shell model, with intent to explore the extent to which the shell model is consistent with purely *ab initio* calculations.

Acknowledgements

The author would like to acknowledge her advisor, Prof. Mark Caprio, for his consistent guidance and support throughout the project, and Dr. Patrick Fasano for his significant contributions to the code used in the project. The author would also like to acknowledge Prof. Umesh Garg and Kristen Amsler for running the Notre Dame REU program and making possible her involvement in this project. Supported by US NSF under Award No. PHY-2050527 and US DOE under Award No. DE-FG02-95ER-40934. Computational resources provided by NERSC (US DOE Contract No. DE-AC02-05CH11231).

References

[1] B. R. Barrett, P. Navrátil, and J. P. Vary, Prog. Part. Nucl. Phys. **69**, 131 (2013).

[2] M. A. Caprio, J. H. Skrabacz, and F. Iachello, J. Phys. A **44**, 075303 (2011).

[3] M. A. Caprio, A. E. McCoy, P. J. Fasano, and T. Dytrych, Bulg. J. Phys. **49**, 57 (2022).

[4] R. R. Whitehead, in *Theory and Applications of Moment Methods in Many-Fermion Systems*, edited by B. J. Dalton, S. M. Grimes, J. P. Vary, and S. A. Williams (Plenum, New York, 1980) p. 235.

[5] P. Maris, M. Sosonkina, J. P. Vary, E. Ng, and C. Yang, Procedia Comput. Sci. **1**, 97 (2010).

[6] A. M. Shirokov, I. J. Shin, Y. Kim, M. Sosonkina, P. Maris, and J. P. Vary, Phys. Lett. B **761**, 87 (2016).

Mapping Resonance Levels in ^{11}B

NICHOLAS RADEN

2024 NSF/REU Program
Department of Physics and Astronomy
University of Notre Dame

ADVISOR(S): Prof. Ani Aprahamian

Abstract

A narrow near-threshold proton resonance in ^{11}B was proposed near E_x=11.44 MeV to explain the branching ratio discrepancy of ^{11}Be→^{10}Be. The proton resonance was thought to enhance the β-delayed proton emission in ^{11}Be and leads to a larger than expected decay branch to ^{10}Be. To further this research, experiments were conducted in order to find the many resonances of ^{11}B. These experiments were located at ISNAP at the University of Notre Dame and used a ^{7}Li target with an alpha projectile for a stable beam. This resulted in resonances for the elastic scattering, inelastic scattering, the excited state for ^{7}Li, and the upper limit of a potential proton emission resonance. This gives a much clearer idea of the structure of ^{11}B and helps with identifying the decay of ^{11}Be. There is still work being done with the program AZURE2 with finding and fitting various resonances.

1 Introduction

A nucleus can undergo many forms of decay with some decays being more likely, depending on the nucleus involved. Two such decays are beta minus decay and proton emission. Many neutron rich nuclei undergo beta minus decay where a neutron becomes a proton along with some other factors. Some very proton rich nuclei undergo proton emission where a proton is jettisoned from the nucleus. The combination of these two decays is known as β-delayed proton emission and is theorized to be the cause of a problem with ^{11}Be.

A sample of ^{11}Be was observed and the amount of products recorded. It was found that there was more ^{10}Be than what theory had predicted so a few ideas were generated [1]. One such was that ^{11}Be underwent β delayed proton emission, first decaying to ^{11}B and then decaying to ^{10}Be. The reason why this could make up for the discrepancy in the decay of ^{11}Be would be the existence of a resonance level in ^{11}B. A resonance is a case where a certain energy level has a heightened chance of a reaction occurring. A classical example of this would be pushing someone in a swing. With proper timing, they go even higher. With a proper energy, the reaction probabilities increase.

Should there be a near-threshold resonance in ^{11}B for proton emission, the extra ^{10}Be would be accounted for. This is also backed by past experiments which found the branching ratio of the ^{11}Be(βp)^{10}Be decay. To better understand if there is a resonance, more energy levels of ^{11}B would be examined. However, there is a chance that this decay does not explain the difference in mass

and it could be a more exotic decay which causes this.

2 Background

Resonance is a topic found in all fields of physics. Whether it be a swing in classical motion or resonance in a cavity for a laser, it is everywhere. In nuclear physics, it is more closely related to the probabilities of reactions, also known as cross sections. Generally, cross sections decrease as energies increase since more energy needs to be stopped and transferred for the reaction to occur. The same reason why beta radiation can travel farther than alpha radiation. On average, beta particles are more energetic than alpha particles. Only when all of their energy is spent can the particles react.

Resonance somewhat violates this idea. Due to the structure of certain nuclei, they have a sharp increase in reaction cross section at certain energy levels. There are different resonances for different reactions for every nuclide. Due to the complexity of nuclides and the many bodies that are present, it is extremely difficult to create a model for all interactions so most resonances and energy levels are found experimentally.

The reactions used in this study is ^{7}Li(α,α)^{7}Li,^{7}Li(α,α')^{7}Li and ^{7}Li(α,p)^{10}Be. Specifically, a bunched beam of α particles, ^{4}He, were fired onto an enriched ^{7}Li target in order to produce ^{11}B* so we can check for different resonance levels. Though the excitation energies from 10.27 MeV to 11.848 MeV, a thinner target was used in a proposed energy range for the proton resonance. The supposed resonance energy level is located around 11.44$\pm$0.04 MeV [2]. And so the beam energy will be tuned to scan these range of energies which also includes known energy levels and known resonances to help verify. To find the energy the beam should be fired at, we just use energy and mass conservation using the energy and mass equivalent

$$E_{4He} + E_{CM} + E_{7Li} = E_{11B} + E^{*}_{11B}$$

$$E_{CM} = E_{11B} + E^{*}_{11B} - E_{4He} - E_{7Li}$$

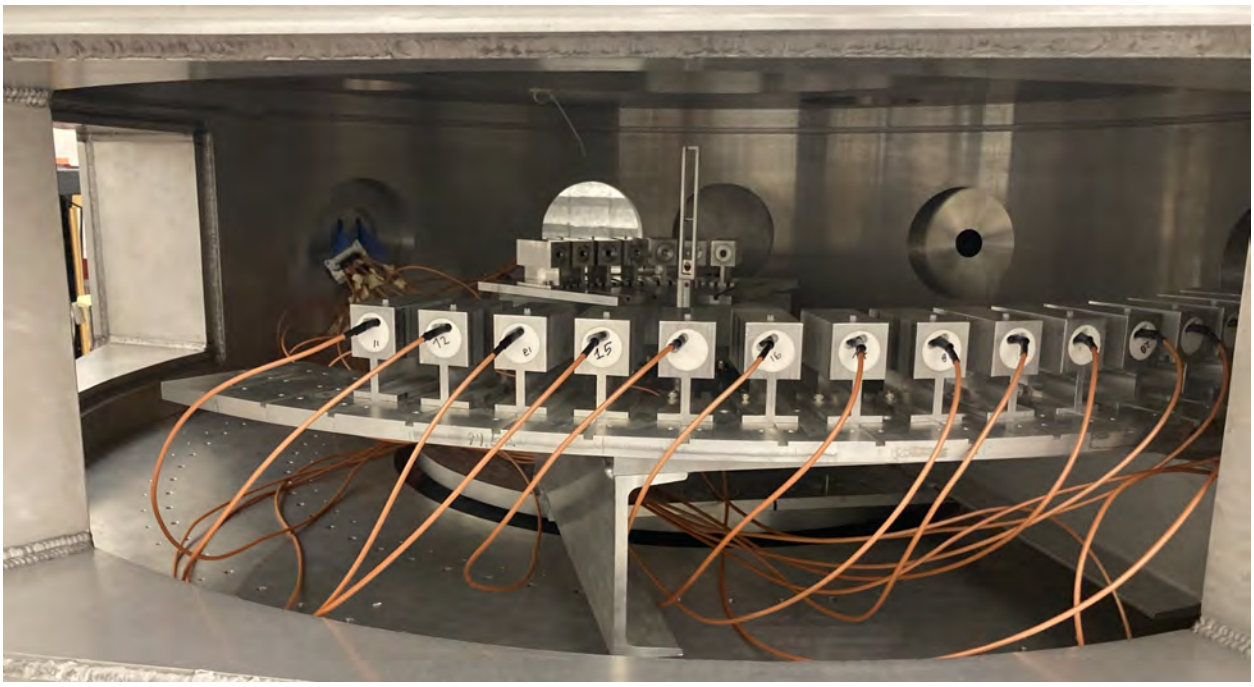

Figure 1: Inside of R2D2 at ISNAP with all 22 silicon detectors and the target ladder in place

$$T_{4He} = E_{CM}\frac{E_{7Li} + E_{4He}}{E_{7Li}}$$

where E represents the rest mass of the isotope, E_{cm} is the center of mass energy, T is the kinetic energy and E* is the excitation energy of ^{11}B*. In this case, T_{4He} would be the beam energy as that is the kinetic energy of the α particles being accelerated.

3 Experimental Setup

To examine the proton emission of ^{11}B*, a bunched beam of α particles is accelerated onto a thin foil of ^{12}C which has enriched ^{7}Li on top of it. For the α source, the HIS (Helium Ion Source) was used to produce the α particles. Bending and focusing corrections are made along the way as the particles travel to the accelerator. They then arrive at the FN Tandem accelerator wherein the energy was varied to test the different excitation levels of ^{11}B. The particles are then accelerated to the target and while travelling, the beam is bunched. Because the beam is bunched, we are capable of time of flight calculations which prior experiments were not capable of.

To make the targets, first a carbon foil with a thickness of 20 μg/cm^2 was placed on a collimator to act as a backing. Then, natural lithium was evaporated and then deposited onto the carbon backing. A few different target thickness were made, one being 10 μg/cm^2 and the other 6 μg/cm^2. The 6 μg/cm^2 was used for the proposed energy range. Because enriched lithium-7 and not natural lithium was used, there was next to no lithium-6 contamination. The targets also did not enter an evacuated chamber immediately which would normally lead to the oxidation of lithium since lithium oxidizes fast. However, the target was made of the enriched lithium-7 in combination with natural fluorine, so fluorine-19. This meant the lithium would not oxidize and the fluorine data would give us a baseline to adjust for Rutherford scattering. There was also exposure to moisture in the atmosphere but that was minimized by placing the lithium in a desiccator but there are still possible contaminants.

The scattering itself takes place in a setup known as R2D2. R2D2 is essentially a large vacuum chamber with two concentric tables, one upper and one lower. Both tables can be rotated independent of each other and due to the size of the chamber, it is well suited for measuring time of flight. The lithium targets were placed on the target ladder after the detectors had been setup and calibrated. For the detectors, 22 silicon detectors were used as seen in the figure. 15 were placed in the forward angle from 20 degrees to 90 degrees and 7 were placed in the back angle from 90 degrees to 150 degrees. In order to calibrate, a mixed alpha source of americium-241 and gadolinium-148 was placed in the chamber and multiple runs were performed to get the correct calibration for the DAQ program. For the DAQ a Meystec digital acquisition system was used with an mdpp-16 digitizer.

4 Data and Analysis

In January 2024, over 100 experimental runs were conducted regarding alpha elastic and inelastic scattering. The beam energies varied from 5 MeV to 2.525 MeV with steps of 0.025 MeV between each run. The exception to this step size were runs 87 through 93 which consisted of 0.005 MeV steps as the beam energies in those runs corresponded to the proposed near-threshold resonance. Due to how thin this resonance might be, a thinner target was used with smaller steps to better

characterize the energy range. The actual excitation energy of ^{11}B ranged from 10.288 MeV to 11.848 MeV. The energy range of the fluorine is less important as the main use was to normalize the rest of the data by for Rutherford scattering. For that, the data from the lowest beam energy for the fluorine was used.

The program AZURE2 has been used and is still in use in finding the different resonances located in this energy range for ^{11}B. There are a few different analysis files that have been created to test out different resonances without the loss of prior data due to overwriting it with a new fit for the data. One such example of this fit would be in Figure 1 which was the data from the 30 degree angle. This happens to be one of the better fits and maps the resonances quite well. Some of this does has to do with the existence of Rutherford scattering. At lower angles, Rutherford scattering will dominate the cross section and the inelastic scattering will not be as visible.

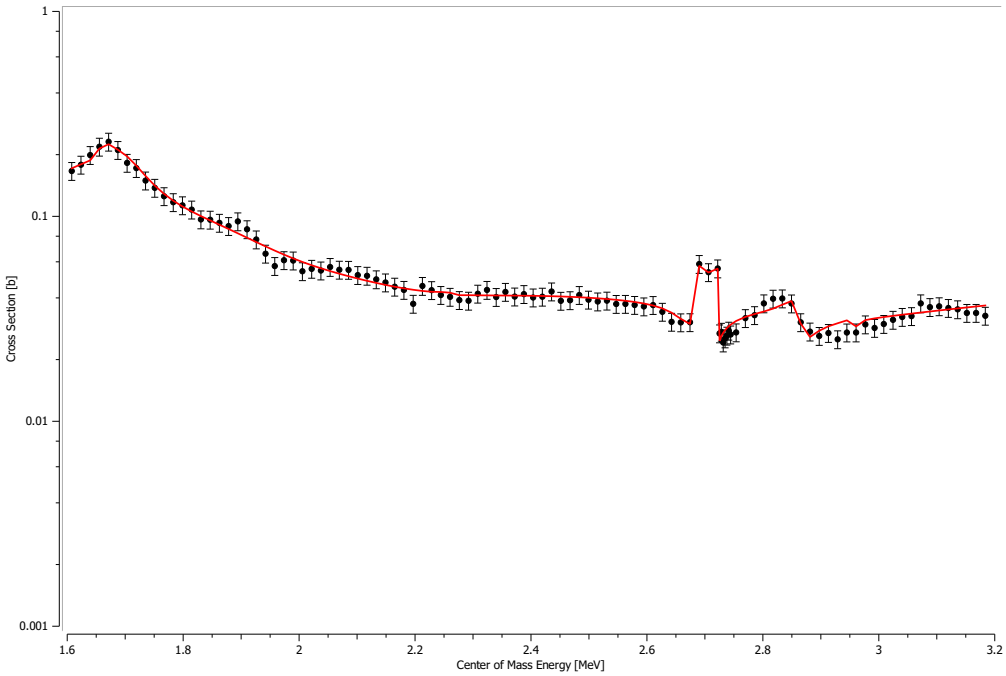

Figure 2: Full beam energy range of ^{7}Li reaction with α at 30 degrees

Adding on more segments, more angels and different reactions, adds in more restrictions and forces a better fit. This is especially helped when adding in a ^{7}Li(α,α')^{7}Li* reaction as that is guaranteed to be an inelastic scattering. Both Figure 2 and Figure 3 come from a different file which had a greater focus on using the inelastic data. This file is still in the process of fitting

different resonances and so the fits will not look nearly as good as Figure 1 did. As seen in Figure 2, there are more pronounced individual peaks since Rutherford scattering is less likely at greater angles. That has to do with the $\sin^{-4}\frac{\theta}{2}$ term in the cross section calculation. As seen in Figure 3, the peaks are even more pronounced and are the dominating factor in the cross section. More fitting needs to be done but the resonance fittings are only getting better.

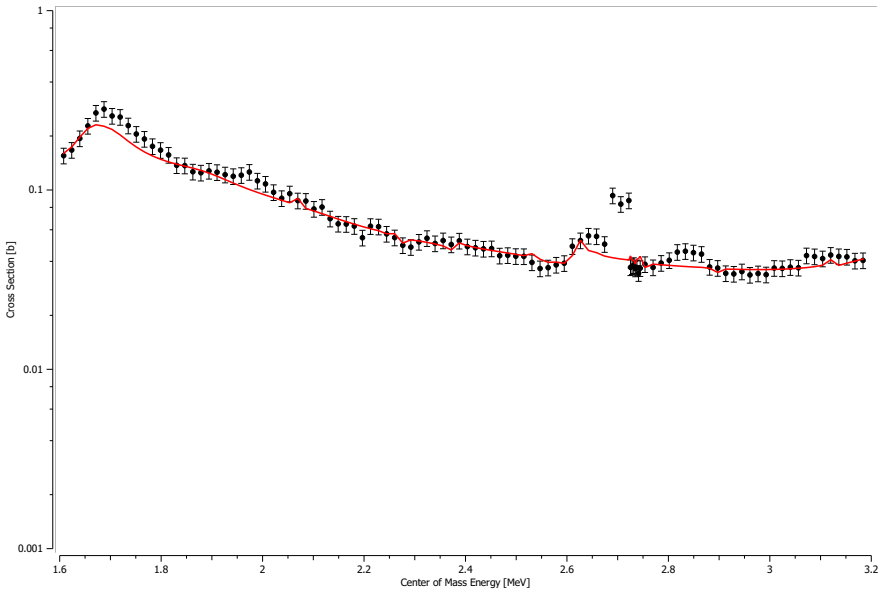

Figure 3: Full beam energy range of ^{7}Li* reaction with α at 55 degrees

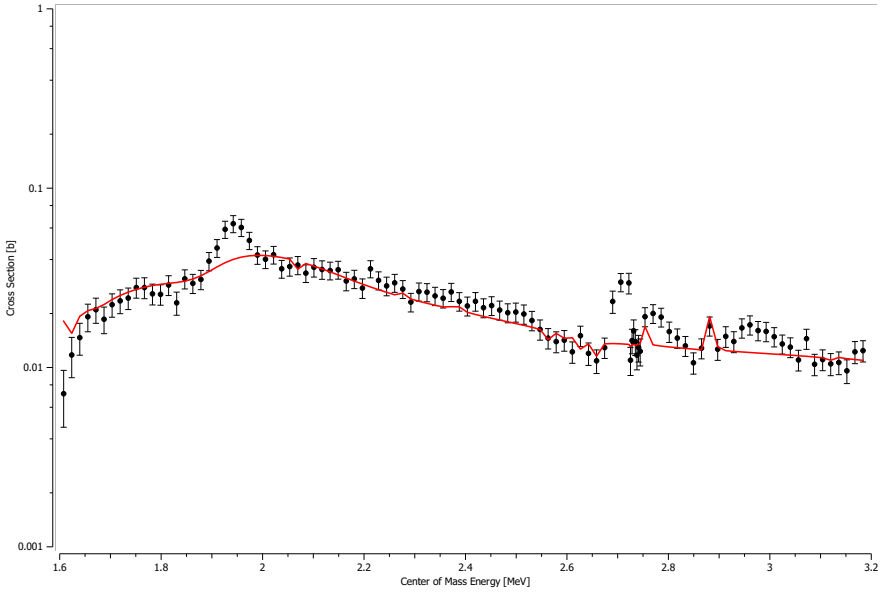

Figure 4: Full beam energy range of ^{7}Li reaction with α at 35 degrees

There is still work being done in AZURE2 to get proper fits but that is most of what has come from the runs in January 2024. The second half of the experiments had a focus on the ^{7}Li(α,p)^{10}Be reaction. All of the possible protons from the data were counted from the Particle Identification curves. Figure 4 is an example of the PIDs where the box is marking the region where protons should be. Due to the very low counts, multiple runs at the same energy were compiled together with all of their counts. Even then, this only yielded 5-6 angles with data for each energy.

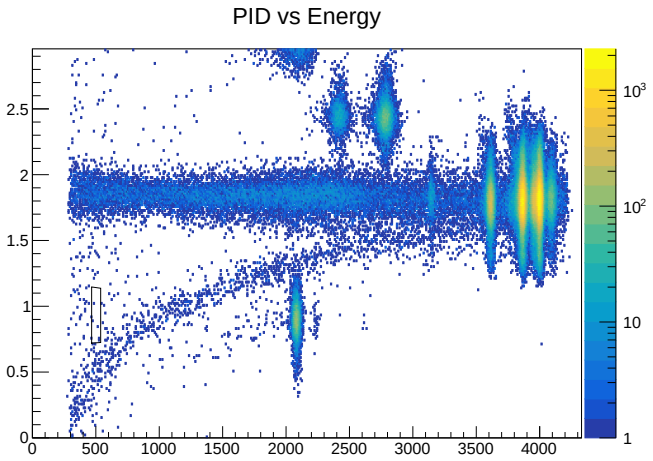

Figure 5: Particle Identification curve at 4.32 MeV at 25 degree angle

The next step taken with this data was to perform Bayesian Analysis. Bayesian analysis is a relatively new technique for analysis that has been adopted by the nuclear physics community recently. The idea behind Bayesian analysis is that instead of using a hypothesis to figure out where the data should be, the data is used to figure out what the hypothesis should be. The foundations of this is built on Bayes' Theorem [3] and it can be used for upper limit calculations. Using a program created in Mathematica, the upper limit cross sections for the three beam energies used was found. These upper limits are found in figures 6, 7, and 8 which are figures created in Excel.

5 Conclusion

Though this research may not instantly bear fruit, it is a stepping stone towards a bigger goal. Finding out the structure of nuclides is always an important task and mapping the resonances serves

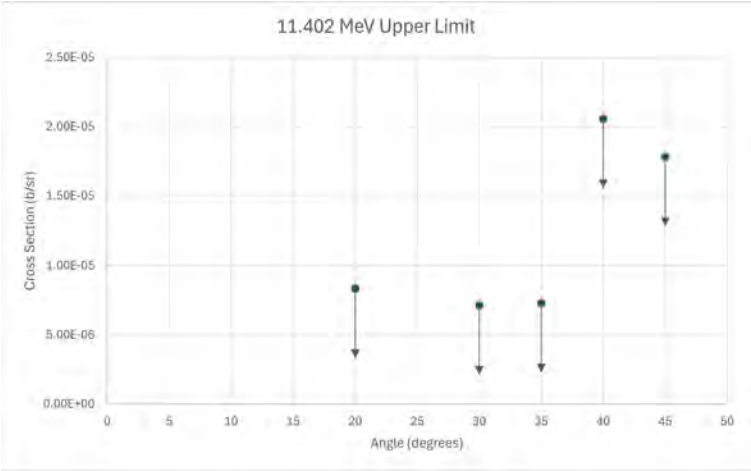

Figure 6: Beam energy of 4.3 MeV which corresponds to 11.402 Mev for excitation energy

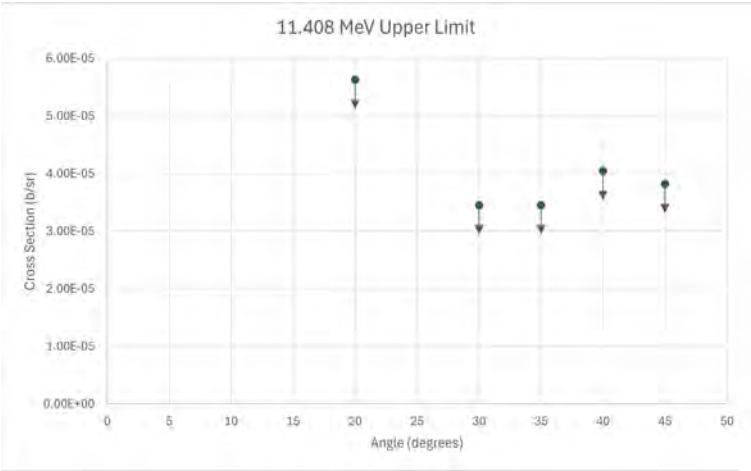

Figure 7: Beam energy of 4.31 MeV which corresponds to 11.408 Mev for excitation energy

a purpose. Namely, to help determine whether a near-threshold proton emission resonance actually exists. Finding all of the alpha resonances serves this purpose as well due to possible overlapping resonances.

6 Acknowledgements

I would like to thank Dr. Shelly Lesher for giving me the chance to participate in this REU and Dr. Umesh Garg for running and organizing it. I also want to express my thanks to Dr. Wanpeng Tan as this project was his idea and I helped with it. Were it not for him, I may not have had a project

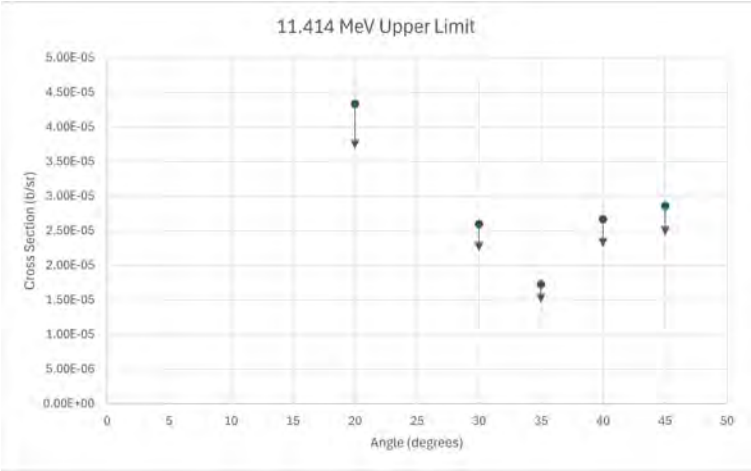

Figure 8: Beam energy of 4.32 MeV which corresponds to 11.414 Mev for excitation energy

this summer. Another deserving of thanks would be Kevin Lee, the understanding graduate student that proved to be a lot of help. This experience has given much to think about and will hopefully be a good influence on the choices I will end up making in the near future.

References

[1] Y. Ayyad, B. Olaizola, W. Mittig, G. Potel, V. Zelevinsky, M. Horoi, S. Beceiro-Novo, M. Alcorta, C. Andreoiu, T. Ahn, M. Anholm, L. Atar, A. Babu, D. Bazin, N. Bernier, S. S. Bhattacharjee, M. Bowry, R. Caballero-Folch, M. Cortesi, C. Dalitz, E. Dunling, A. B. Garnsworthy, M. Holl, B. Kootte, K. G. Leach, J. S. Randhawa, Y. Saito, C. Santamaria, P. Šiurytė, C. E. Svensson, R. Umashankar, N. Watwood, and D. Yates, Phys. Rev. Lett. **123**, 082501 (2019).

[2] E. Lopez-Saavedra, S. Almaraz-Calderon, B. W. Asher, L. T. Baby, N. Gerken, K. Hanselman, K. W. Kemper, A. N. Kuchera, A. B. Morelock, J. F. Perello, E. S. Temanson, A. Volya, and I. Wiedenhöver, Phys. Rev. Lett. **129**, 012502 (2022).

[3] H. S. D. D. A. V. Andrew Gelman, John Carlin and D. Rubin, *Bayesian Data Analysis* (Department of Statistics - Columbia University, 2013).

Crystal Growth and Physical Properties of $ErFe_6Ge_6$

EMILY RAPP

2024 NSF/REU Program
Department of Physics and Astronomy
University of Notre Dame

ADVISOR(S): Prof. Nirmal Ghimire

Abstract

In the search for new quantum materials with potential to be utilized in advanced spintronics application, the hexagonal R166 family of compounds has been of particular interest. The unique crystal structure with lattice spacing of these kagome compounds have been known to yield exotic magnetic properties. Here, single crystals of the R166 compound $ErFe_6Ge_6$ were synthesized utilizing the flux-growth method. These samples were then characterized using powder X-ray diffraction and energy-dispersive spectroscopy. Using a 9-T Quantum Design PPMS, properties such as magnetic susceptibility, magnetization, and resistivity were measured. Our findings revealed interesting structural, magnetic and transport measurements that warrants further study of $ErFe_6Ge_6$.

1 Introduction

Research on quantum materials that exhibit exotic topological magnetic and electric properties has been increasing in popularity in the past few years. YMn_6Sn_6, space group *P6/mmm*, has shown particularly interesting magnetic behavior. As depicted in Fig. 1a, the 6 Mn atoms form a hexagonal kagome net of corner sharing triangles. The layered nature of this compound also gives rise to interesting magnetic behaviors. The interactions within one layer of Mn atoms, indicated by J_p in Fig. 1a, are ordered ferromagnetically. The interactions between the first and second layer of Mn atoms, denoted J_1, are ferromagnetically coupled while the interaction between the second and third Mn layer, denoted J_2, is antiferromagnetic. The next nearest neighbor interaction (i.e., interaction between Mn layers 1 and 3, indicated by J_3 in Fig. 1a) is ferromagnetic. The different interactions between magnetic layers give rise to parametric frustrations and lead to the various magnetic phases seen in Fig. 1b.

Looking for more new R166 compounds, as a part of this REU project, we realized that some of the R166 compounds are reported in orthorhombic crystal structure. An example is $ErFe_6Ge_6$ which is reported to have an orthorhombic structure in space group *Immm* [1]. A sketch of this crystal structure is shown in Fig. 2(a). We found that this structure has some similarities and some differences with the structure of the hexagonal R166 compounds. The similarities are that: 1) This structure has kagome nets of Fe atoms stacked along a crystallographic direction [b-axis in this case,

see Figs. 2(a,b)], and (2) The kagome layers along this direction are separated by atomic blocks of two unequal lengths. For example, the distance between layer 1 and layer 2 represented by d_1 is 4.13253 Å and that between layers 2 and 3 represented by d_2 is 3.97047 Å [1]. The main difference, on the other hand, are: 1) The crystal structure is orthorhombic, 2) The kagome net is made up of unequal bonds labelled as b_1, b_2, b_3 in Fig. 2(c). Because of these similarities and differences, it would be of interest how the physical, and magnetic properties change in this compound as compared to the hexagonal R166 compounds. For this reason, we decided to synthesize $ErFe_6Ge_6$ in single crystalline form and study its physical properties, mainly magnetic and transport properties.

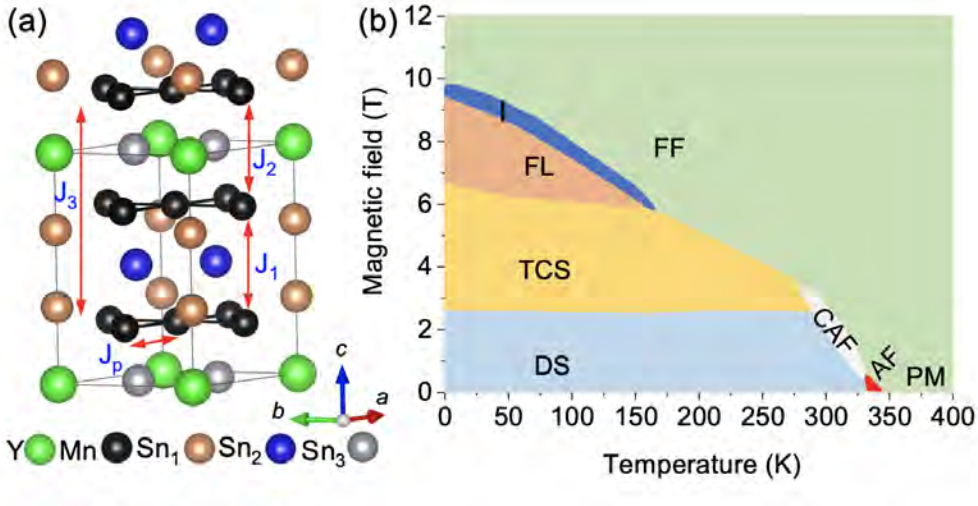

Figure 1: The Crystal Structure of (see left figure) and the in-plane magnetic phase diagram (see right) of YMn_6Sn_6. In sub-figure b., DS, TCS, FL, FF, CAF, AF, and PM are distorted spiral, transverse conical spiral, fan like, forced ferromagnetism, canted anti-ferromagnetism, anti-ferromagnetism and paramagnetism, respectively. This figure was adopted from [2].

2 Methods

2.1 Flux Growth Method

Single crystals of our target compound were produced using the molten-metal flux growth method using Sn as the flux. Each element was measured out in a ratio of 1.5:6:18:100 for Er, Fe, Ge, and Sn, respectively. The elements were placed into a small alumina crucible and sealed in a fused

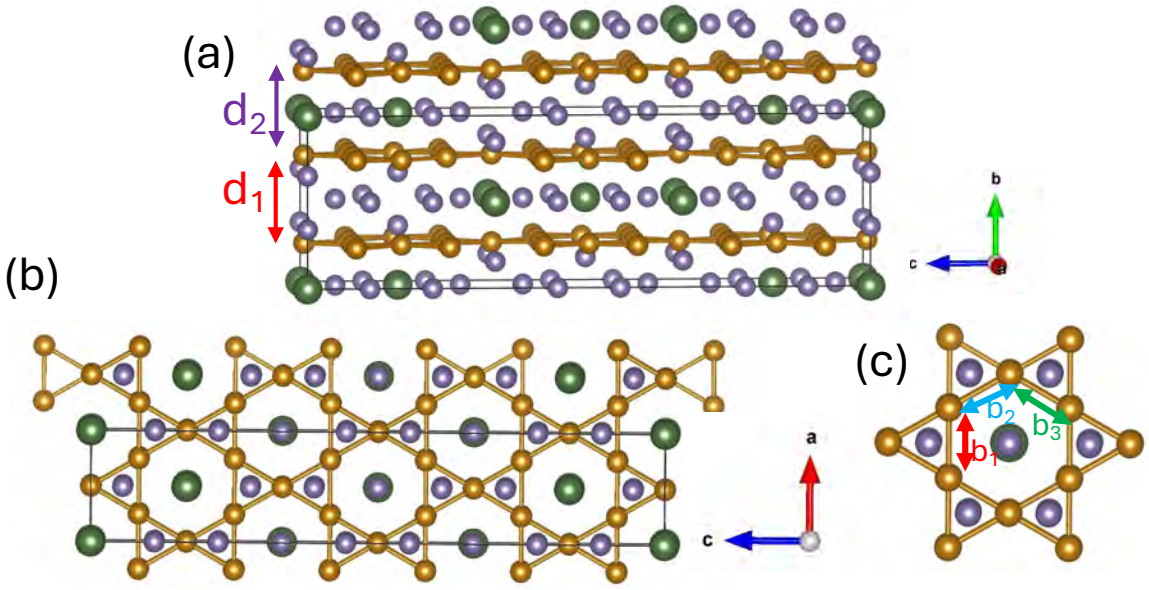

Figure 2: a) A sketch of crystal structure of $ErFe_6Ge_6$ in the orthorhombic space group Immm. In this figure, Er is represented by large green atoms, Fe by perfectly layered gold atoms and Ge by light purple atoms. d_1 and d_2 represent the distance between the first and the second Fe layers, and the second and the third Fe layers, respectively. b) A b-axis view of the structure in panel (a). c) One kagome net showing that the the kagome net is made up of three unequal bonds b_1, b_2, and b_3. These figures were created using *Vesta* visualization software.

silica ampule.

The ampules were then placed in a furnace and heated to 1150°C over 10 hours. The ampules were held at 1150°C for 24 hours and allowed to homogenize then slowly cooled to 625°C over 100 hours. While the Sn flux was still molten, the ampules were removed from the furnace, quickly inverted and centrifuged, separating the flux from the crystals. Once the crystals were removed from the ampule, any remaining flux was scraped or polished away.

2.2 Thermal, Transport, and Magnetic Measurements

Electrical transport and magnetic properties were measured using a 9-T Quantum Design Physical Property Measurement System. For electrical transport measurements, samples were polished into rectangular shapes and and 25 μm platinum wire contacts were affixed to the sample using Epotek H20E silver epoxy for contacts. Magnetic properties were measured using a Quantum Design VSM SQUID in FC (field cooled) mode, between 1.8K and 400 K and with an applied magnetic field of

0.1 T. Samples were mounted in quartz holder or a brass holder for B along a-axis or B perpendicular to a-axis. Field-dependent magnetization was measured from -9 to 9 T at 1.8 K, 10 K, 20 K, 30 K and 50 K.

3 Results

3.1 Crystal Structure

The crystal structure or space group of $ErFe_6Ge_6$ has been the subject of much debate in the past few decades. In 1994, Wang, et al. [3] reported that the compound ordered with a hexagonal structure in the *P6/mmm* or 191 space group. In 1992, Venturini, et al. wrote that this compound crystallized in the *Immm* space group with an orthorhombic structure [4].

First, to confirm the structure of the crystals, powder x-ray diffraction was preformed using a Rigaku Miniflex Diffractometer. The diffraction patterns were refined using the Rietveld method and *FullProf* software, the resulting diffraction pattern is included in Fig. 3 and is consistent with $ErFe_6Ge_6$. To rule out other crystal structures, this pattern was compared to *P6/mmm* and *Cmcm* crystals. The orthorhombic *Immm* was determined to be the best fit.

The composition was further confirmed using energy dispersive x-ray spectroscopy (EDS). A ratio of Er:Fe:Ge of 1:5.8:6.6 was found which confirmed (within the uncertainty limit of the measurement) that the crystals had the composition of our target compound.

4 Magnetic and Transport Properties

4.1 Magnetic Susceptibility

The graph of magnetic susceptibility vs temperature is included in Fig. 4. The susceptibility parallel to the b-axis (along the length of the needle shaped crystal) shown in the red curve sharply increases below about 50 K. But it does not show any clear sign of magnetic transition. On the other hand, the susceptibility measured with the magnetic field perpendicular to the *b*-axis (black curve) shows

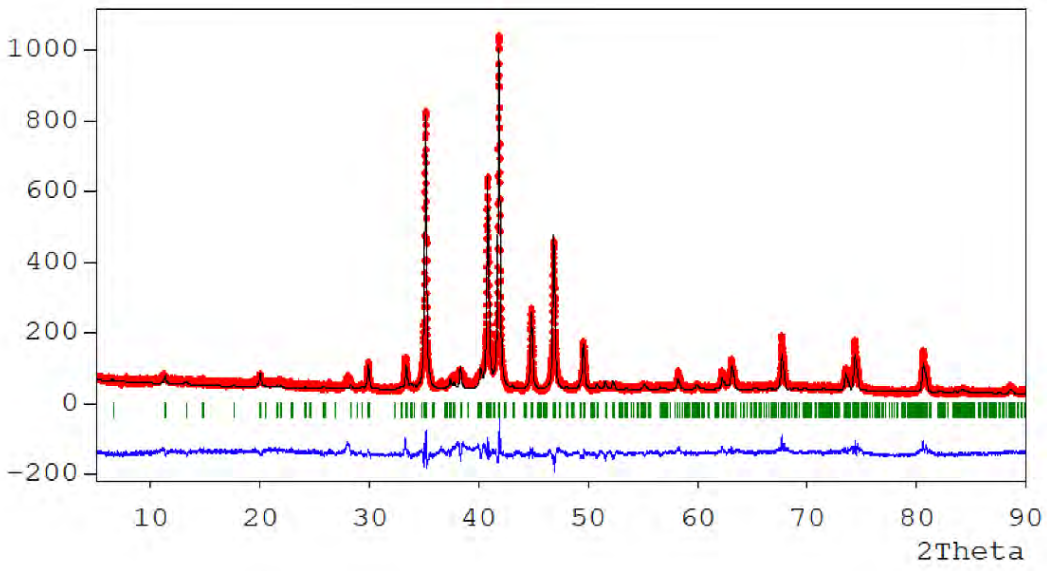

Figure 3: Rietveld refinement of x-ray powder diffraction pattern of $ErFe_6Ge_6$ measured on ground single crystals grown using the flux method. The refinement shows that this pattern matches the orthorhombic space group *Immm*.

a hump-like feature centered around 50 K, then shows a sharp increase below about 10 K, without any other remarkable feature. The hump-like feature is likely due to crystal field effect (to be determined). In this direction also, there is not clear sign of magnetic transition. However, it has been reported[1]) that Fe atoms order antiferromagnetically well above 400 K, which we did not measure as the maximum temperature we could measure in the PPMS was 400 K.

4.2 Magnetization

Fig. 5 shows a graph of magnetization vs magnetic field measured from -9 to 9 T for the field applied perpendicular to the *b*-axis. Here, we can see a clear ferromagnetic behavior between 1.8 K and 20 K. The magnetization saturates quickly at 1.8 K and this saturation is attained at higher magnetic fields with the increase in temperature. Fig. 6 shows magnetization vs magnetic field data for the magnetic field applied parallel to the *b*-axis. In this orientation, the magnetization plots are linear at lower fields and show some upturn at higher fields possibly due to spin flop. These two sets of data indicate that the magnetic moments are along the *b*-axis, which is perpendicular to the kagome plane, despite the fact that a clear magnetic transition is not visible in the susceptibility

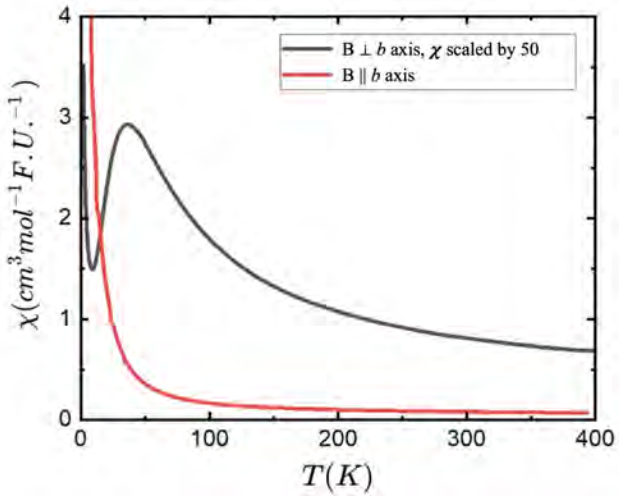

Figure 4: A graph of magnetic susceptibility (χ) vs temperature parallel (red curve) and perpendicular (black curve) to the *b*-axis. These measurements were conducted using field-cooled(FC) protocol with the magnetic field of 0.1 T.

data.

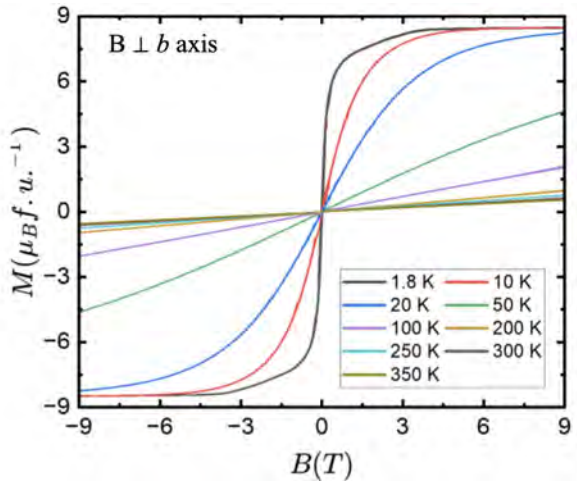

Figure 5: A graph of magnetization vs magnetic field measured at nine different temperatures indicated with field parallel to the *b*-axis.

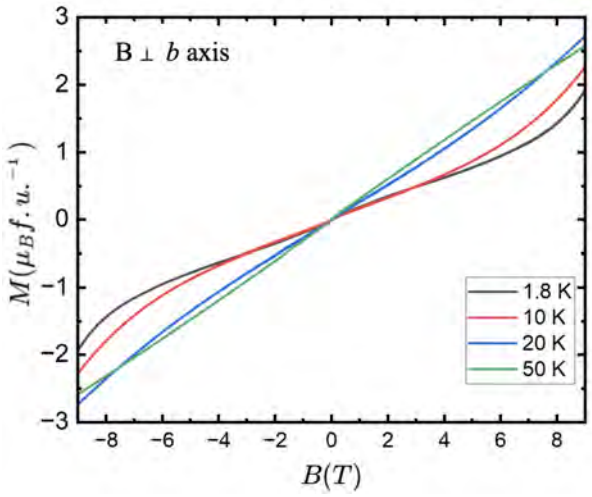

Figure 6: A graph of magnetization vs magnetic field measured at nine different temperatures with field perpendicular to the *b*-axis.

4.3 Resistivity

Graph of resistivity vs temperature for electric current (I) parallel to the *b*-axis is shown in 7. The fact that the resistivity decreases with decreasing temperature shows the metallic behavior of the

compound. A small wiggle is observed at around 265 K. The temperature derivative of resistivity presented in Fig. 8 shows this more clearly. At this time, origin of this feature is unknown and is a subject of further study. The Residual Resistance Ratio (RRR) calculated from data shown in Fig. 7 is found to be 12.13, this ratio is a measure of the quality of a conductive material. RRR is be calculated as $\rho(300K)/\rho(1.8K)$.

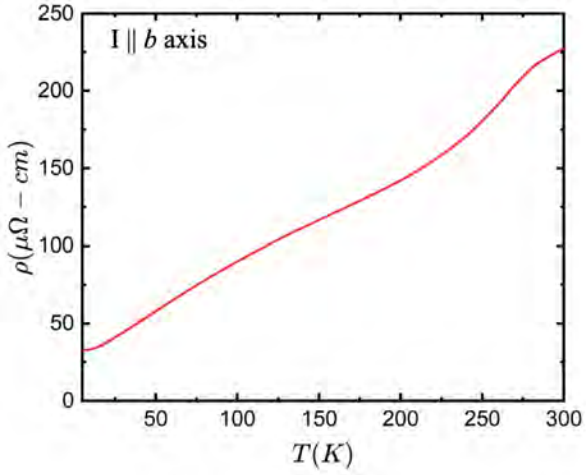

Figure 7: A graph of ρ or resistivity in $\mu\Omega - cm$ vs temperature in Kelvin.

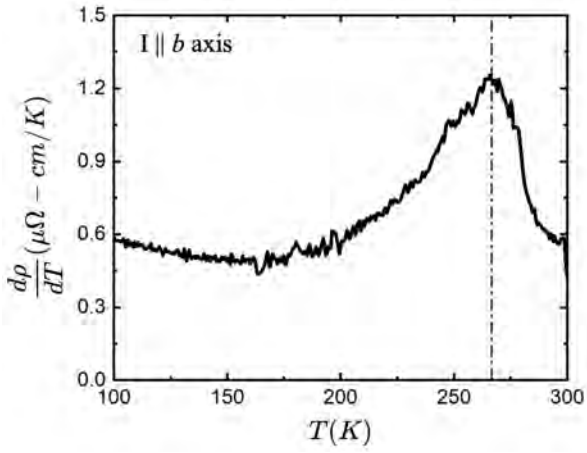

Figure 8: A graph of the change in resistivity with respect to temperature.

4.4 Magnetoresistance

Fig. 9 includes a graph of magnetoresistance (MR) vs magnetic field for 5 different temperatures. Magnetoresistance is calculated by $(\rho_B - \rho_0)/\rho_0 \times 100\%$, where ρ_B is the longitudinal resistivity at certain magnetic field and ρ_0 is the longitudinal resistivity at zero field. MR shows positive linear behaviour at lower temperatures, while it exhibits quadratic behaviour at temperatures above 20 K. The linear behavior in the lower temperature MR lines suggests an interesting property that could mean topological features in the electronic structure [5]. Further measurements are needed to pinpoint the cause of this linear behavior.

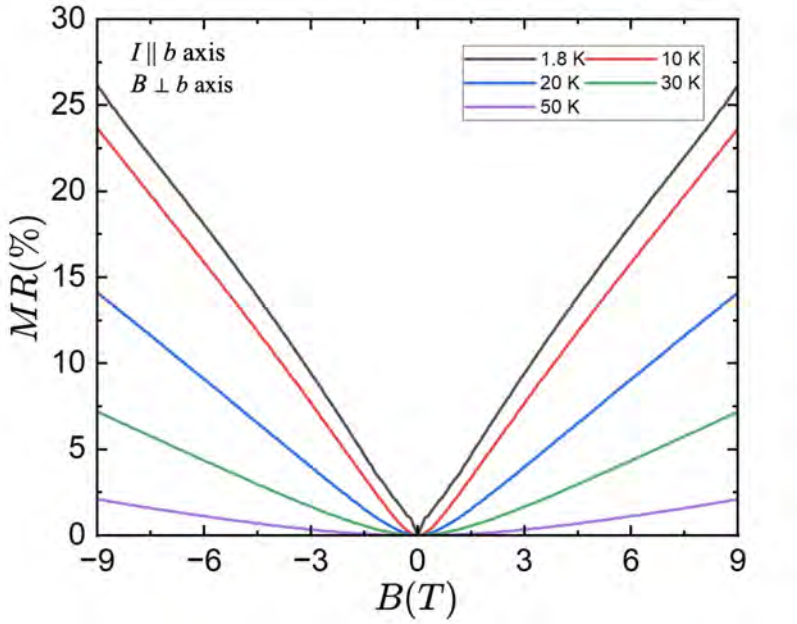

Figure 9: A graph of magnetoresistance vs magnetic field for five temperatures indicated.

5 Conclusion

As $ErFe_6Ge_6$ is a member of the R166 family of kagome compounds, it is expected to exhibit interesting magnetic and electronic behaviors, due to their layered structures. To investigate these behaviors, we grew single crystals of $ErFe_6Ge_6$ using the molten-metal flux growth method. The interactions between the layers of Fe and Er in this compound result in both ferromagnetic and antiferromagnetic behavior in different orientations. Our measurements confirmed that this compound exhibits linear MR which indicates possible interesting electronic band structures and is a good candidate for further investigation.

6 Acknowledgements

This work was funded by the NSF and made possible by the much-needed assistance of my lab members: Hari Bhandari, Mohammed El Gazzah, Resham Regmi, Abhijeet Nayak and Sekh Jamaluddin. I would like to extend my gratitude to my PI, Dr. Nirmal Ghimire for guiding me in this endeavor, to Kristen Amsler and Dr. Umesh Garg for ensuring that this program was such a great

experience.

References

[1] G. Venturini, R. Welter, and B. Malaman, Journal of alloys and compounds **185**, 99 (1992).

[2] H. Bhandari, R. L. Dally, P. E. Siegfried, R. B. Regmi, K. C. Rule, S. Chi, J. W. Lynn, I. I. Mazin, and N. J. Ghimire, (2023).

[3] Y. Wang, D. Wiards, D. Ryan, and J. Cadogan, IEEE Transactions on Magnetics **30**, 4951 (1994).

[4] G. Venturini, R. Welter, and B. Malaman, Journal of Alloys and Compounds **185**, 99 (1992).

[5] P. E. Siegfried, H. Bhandari, J. Qi, R. Ghimire, J. Joshi, Z. T. Messegee, W. Beeson, K. Liu, M. P. Ghimire, Y. Dang, H. Zhang, A. Davydov, X. Tan, P. M. Vora, I. I. Mazin, and N. J. Ghimire, (2022).

Determining the Composition of Limestone Used in the Archaic Temple of Isthmia

EDGAR ROBLES

2024 NSF/REU Program
Department of Physics and Astronomy
University of Notre Dame

ADVISOR(S): Prof. Khachatur Manukyan

Abstract

This paper is part of a larger project in understanding the historical and archaeological context behind the Temple of Isthmia in Corinth, the earliest known Greek temple. The aim of this paper is to determine the molecular and elemental makeup of the construction materials used in the temple. Samples from the site have been extracted and analyzed using non-destructive techniques in XRF, XRD, and SEM-EDS. Corinth is home to a large amount of oolitic limestone, which would have been widely available to the ancient Corinthians. This material is prominent in the analysis of the limestone brick. High amounts of quartz and iron have also been identified, as well as varying amounts of other trace elements. Characterizing the minerals associated with each prominent trace element provides a point of reference for future projects in conservation and restoration. This is critical for preserving the integrity of this cultural heritage site.

1 Introduction

Hundreds of years before The Hellenistic Age, the ancient Corinthians designed a monumental temple along the Isthmian coast: The Temple of Isthmia, dedicated to Poseidon. This temple was constructed in the first half of the 7th century BCE, and serves as one of the earliest known examples of Greek temples as we know them today. Sometime between 460 and 450 BCE, it is believed that a fire had destroyed part of the temple, cracking the temple rock. A temple in the Classical style was then built on top of the site of the Temple of Isthmia, which was also destroyed in a fire shortly after. [1]

In the region, there is an abundance of oolitic limestone, known for its softness and ease of stone-working. Bricks made from this stone were used as the primary building material. Though limestone is easily accessible throughout Isthmia, a particular quarry of origin has not been identified for the Isthmian temple. [2] Properly understanding the composition of the limestone brick is imperative for the preservation of cultural heritage, and is critical in both the conservation and restoration of the site.

Samples from the temple have been extracted from 15 different bricks. A few of these samples come from the stucco surface used on the interior [3]. Non destructive techniques are applied to identify the trace elements in the limestone. Due to the cultural significance of these samples, non-

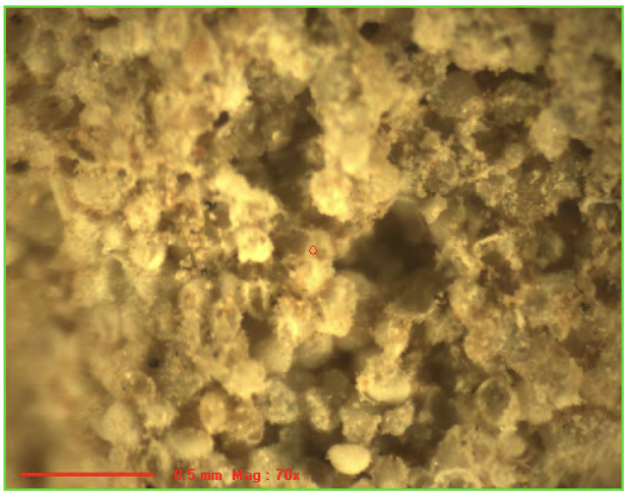

Figure 1: Oolitic limestone

destructive techniques are essential. X-ray fluorescence, Powder X-ray diffraction, and SEM-EDS are applied to understand the chemical and mineralogical composition of the stones.

Having identified the material of the temple rock, a local quarry or limestone source may be correlated to the temple. This preserves the integrity of the temple in a potential restoration attempt.

2 Background

Though the temple is widely understood to be built of oolitic limestone [1], this only provides a broad understanding of the elemental and mineralogical composition of the material at hand. Generally, limestone consists of some calcium carbonate ($CaCO_3$) mineral, whether it be calcite, dolomite, or aragonite, as its primary component. Quartz (SiO_2) is often a major component in limestone, as well as magnesium, both typically up to 10 wt.%. Metals, like iron, titanium, and copper may appear in trace amounts (over 1 wt.%). [4] *Oolitic* refers to the appearance and creation of the limestone. It is a sedimentary rock formed by many small egg-shaped rocks, called *ooids*. These ooids are formed in marine environments as calcite precipitates and accumulates around a small particle, usually of some biological material. [5]

3 Research Methods

The samples were extracted from the site for analysis by professor Alessandro Pierattini, from the University of Notre Dame, School of Architecture.

3.1 X-Ray Diffraction

X-ray diffraction (XRD) and X-ray fluorescence (XRF) use similar methods to determine the composition of a material. Powder x-ray diffraction uses an X-ray source and detector rotating in tandem about a powder. The atomic planes of a crystalline material diffract the x-rays. The angle at which the source x-rays reach the detector is dependent on the spacing and structure of the atomic planes, giving each mineral a particular XRD pattern.

X-Ray diffraction analysis was performed using small amounts of powder from each sample, providing a mineralogical classification of each selected sample.

3.2 X-Ray Fluorescence

X-ray fluorescence also uses an X-ray source and detector, though specific elements are identified based on the characteristic X-rays released. These characteristic X-rays are produced through the charging and subsequent freeing of an inner shell electron via X-ray. The energy of these X-rays is dependent on the composition of the atom, and on the shell of the inner shell electron. Electron shell transitions produce characteristic x-rays, and are common with heavier elements. Because the energy of a characteristic X-ray is dependent on the atom, magnesium and other lighter elements are difficult to identify by XRF.

Small fragments of the stones were chipped off and analyzed using a tabletop XRF device, under vacuum. Small amounts of powder from each sample were deposited onto aluminum stubs fitted with adhesive carbon paper. This allowed for an in depth analysis of individual particles.

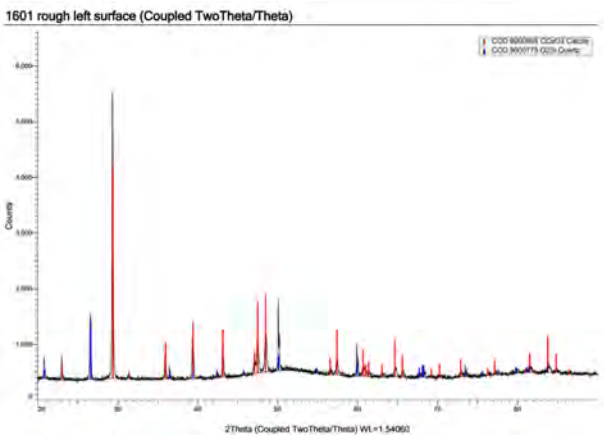

Figure 2: A typical XRD spectrum

3.3 Scanning Electron Microscope/Energy Dispersive X-Ray Spectroscopy

SEM-EDS has been used on 8 of the 24 samples. SEM imaging provides a detailed look at the texture of oolitic limestone. The potential to accurately identify magnesium is higher using SEM-EDS than it is with XRF, as magnesium sits right at the limits of XRF's capabilities.

4 Results

4.1 XRD Results

Samples used in XRD most commonly feature calcite ($CaCO_3$) and quartz (SiO_2). Trace amounts of gypsum, dolomite, and aragonite are observed, but uncommon. Mg-rich calcite often, but not always, fits better than pure $CaCO_3$ calcite, though their peaks are very similar. Although labeled "Mg-rich", the Mg:Ca ratio associated with this label is 0.03 to 0.97, so only trace amounts of magnesium are expected in these samples.

4.2 XRF Results

X-ray fluorescence revealed the presence of at least 4 distinct groups each particle could be roughly sorted into: Calcium-rich, silicon-rich, iron-rich, and trace metals. Ca, Si, and Fe are often seen together in a sample, but the ratios between them differ greatly depending on their miner-

alogical structure. The elemental composition of calcium-rich particles is consistent with calcium carbonate and its potential trace elements. The samples are mostly homogeneous, largely consisting of calcite. Aluminum, potassium, and other metals appear in trace amounts throughout these samples. Samples identified to have large amounts of variation have been mapped at a low resolution. The sample shown in Figure 3 (above) illustrates the variation between particles and the relation-

Figure 3: XRF Map of a diverse rock cluster

ship between these elements. In the sample above, calcium seems to show up in each particle to some extent. Silicon and iron are found together. Aluminum is found almost exclusively in the iron particle.

4.2.1 Calcium-Rich

By far the most abundant of the particle distinctions, calcium-rich particles have little variation. Besides silicon and iron, magnesium, phosphorous and sulfur are common trace elements in these particles. Often, calcium appears in these particles at >90 wt. %. Typically, they appear to be yellowish in color,

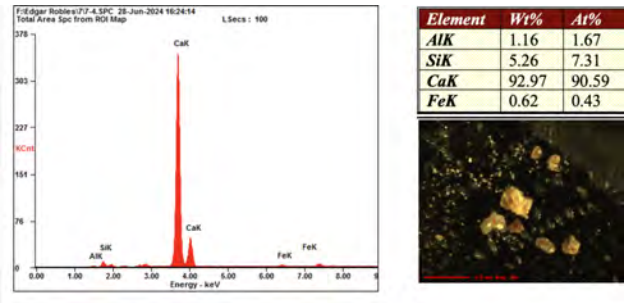

Element	Wt%	At%
AlK	1.16	1.67
SiK	5.26	7.31
CaK	92.97	90.59
FeK	0.62	0.43

Figure 4: Example of Ca-rich particle

Variation between Ca-rich particles comes from differing concentrations of trace metals.

4.2.2 Silicon-Rich

Silicon-rich particles are the second most common particles in the rock samples. These particles are most likely to be small pieces of quartz, as the silicon is relatively pure. Silicon rich particles often appear alongside smaller quantities of Ca and Fe. The color on Si-rich particles varies. They are often gray, but can have brown or red hues.

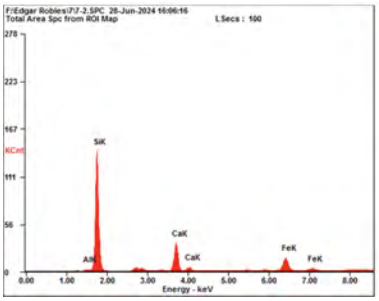

Element	Wt%	At%
AlK	1.74	1.91
SiK	80.58	85.36
K K	0.97	0.74
CaK	14.71	10.92
FeK	2.00	1.07

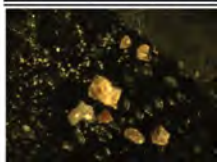

Figure 5: Example of a Si-rich particle

4.2.3 Iron-Rich

Though these iron-rich particles also contain high amounts of Si, they have been named "iron-rich" for the purposes of this paper. A particular mineral has not yet been identified for these particles, though their glassy texture and brown coloration is consistent with certain quartz varieties, containing high amounts of iron. The ratio of Si:Fe seems to be consistent across various samples, though the presence of pure quartz often disrupts this. Besides a few particular trace metals, this classification is the least abundant particle in the sample set.

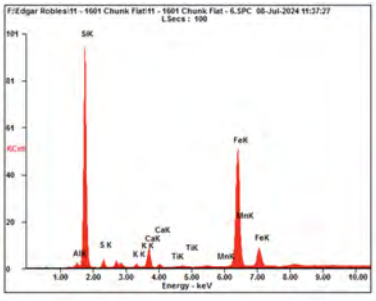

Element	Wt%	At%
AlK	2.89	3.46
SiK	67.01	77.04
S K	2.30	2.32
K K	0.91	0.75
CaK	3.90	3.14
FeK	22.99	13.29

Figure 6: Example of Fe-rich particle

4.2.4 Trace Metals

Various particles are particularly diverse in their composition. Most commonly, samples from the stucco plaster of the temple's interior contain higher counts of trace metals than a typical sample from one of the limestone bricks.

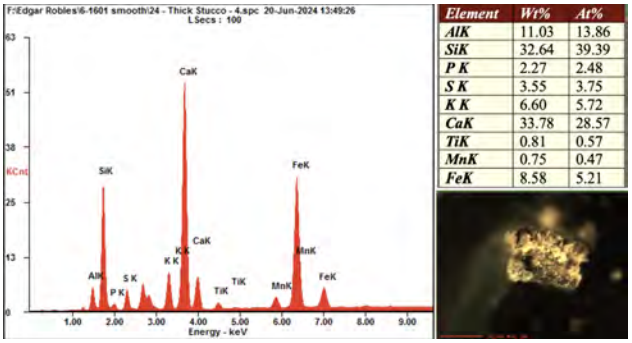

Element	Wt%	At%
AlK	11.03	13.86
SiK	32.64	39.39
P K	2.27	2.48
S K	3.55	3.75
K K	6.60	5.72
CaK	33.78	28.57
TiK	0.81	0.57
MnK	0.75	0.47
FeK	8.58	5.21

Figure 7: Stucco sample, diverse composition

Individual particles of unusual trace metals have been identified as well. A singular particle of Chromium-rich rock was identified, embedded in a large sample of oolitic limestone from the temple.

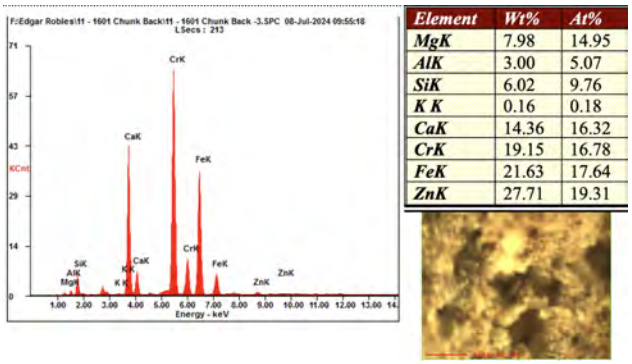

Element	Wt%	At%
MgK	7.98	14.95
AlK	3.00	5.07
SiK	6.02	9.76
K K	0.16	0.18
CaK	14.36	16.32
CrK	19.15	16.78
FeK	21.63	17.64
ZnK	27.71	19.31

Figure 8: Chromium-rich particle

Further testing is required to validate other suspected trace elements, such as yttrium or palladium.

Spectrum: 7- 1601 rough-left- surface.spx

El	AN	Series	unn. C [wt.%]	norm. C [wt.%]	Atom. C [at.%]	Error (1 Sigma) [wt.%]
O	8	K-series	48.12	51.36	71.78	5.90
Mg	12	K-series	0.42	0.45	0.41	0.05
Al	13	K-series	1.56	1.67	1.38	0.10
Si	14	K-series	1.84	1.97	1.57	0.11
Ca	20	K-series	41.74	44.55	24.86	1.24
		Total:	93.68	100.00	100.00	

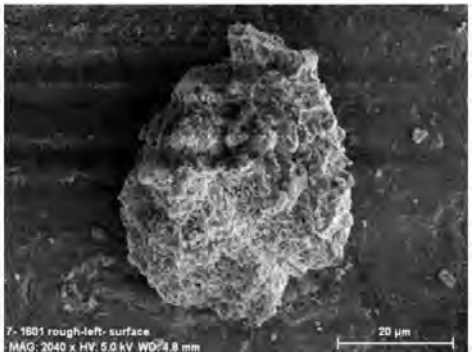

Figure 9: SEM-EDS

4.3 SEM-EDS Results

The data points for SEM-EDS are limited. Largely, the results are consistent with results of XRF data from Ca-rich particles. SEM-EDS picks up oxygen, while XRF does not, leading to smaller percentage values for quartz (SiO2) and calcite (CaCO3), as well as a handful of other trace minerals. An advantage to using SEM-EDS is its potential to identify magnesium with higher accuracy. Despite being from the same sample as Fig. 4., magnesium was only properly identified in SEM-EDS, as it appears in small trace amounts (Fig. 9.) Samples with up to 2.71 wt. % of Mg has been identified in SEM-EDS, consistent with XRD results.

5 Discussion

The analysis of these samples is ongoing. Raman spectroscopy, SEM-EDS, and a higher resolution instrumentation for XRF are all being considered for further analysis. Each sample has only been run once on XRD, mostly consisting of the Ca-rich regions of the rock. An iron-rich mineral has not been identified in XRD. The variation between the composition of individual particles is a concern for further XRD testing, as particles tested under XRF can not be examined under XRD without destroying the integrity of the prepared sample.

A few XRD samples have comparatively unusual peaks. A large peak appearing right beside Mg-rich calcite has not been identified. Furthermore, although Mg-rich calcite is often a better fit than pure calcite, it is still imperfect. Considering prior studies on the variation of XRD of limestone

exposed to high heat, it is possible that a fire had altered the structure of the stone, though much more analysis is needed to draw a conclusion. [6]

To determine the provenance of the stone, Samples from various quarries around Isthmia would need to be analyzed under the same methods. By doing so, similarities between quarry environments may be compared to the temple rock. This sort of study is indispensable in a restoration effort. [7]

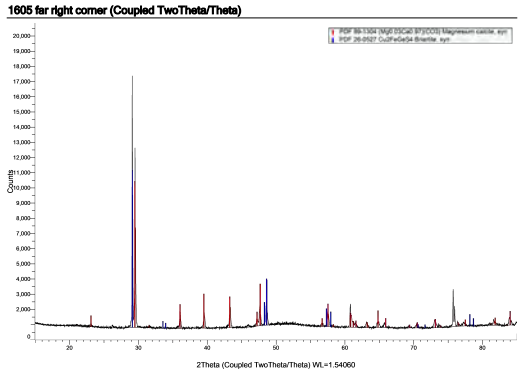

Figure 10: XRD spectrum with unidentified peak, possibly briartite

6 Conclusion

The Temple of Isthmia in Corinthia seems to be made of a largely homogeneous limestone. Consisting primarily of calcite and quartz, with traces of iron and other metals, the rock is likely local. Whether or not an ancient fire had cracked the rocks in the 7th century BCE remains undetermined. Further investigation is needed to verify various trace metals in the samples. Upon identifying a quarry of provenance, the characteristics of fresh limestone may be compared to the bricks of the ancient temple. This sort of study is necessary to develop a full, archaeological and historical understanding of the construction of the ancient temple.

References

[1] F. Hemans, The American School of Classical Studies at Athens (2015).

[2] A. Pierattini, *The Origins of Greek Temple Architecture* (Cambridge University Press, 2022).

[3] A. Pierattini, The Annual of the British School at Athens **114**, 167–206 (2019).

[4] D. Michalska and M. Szczepaniak, *Geosciences in Archaeometry. Methods and Case Studies* (Bogucki Wydawnictwo Naukowe, 2014).

[5] M. R. Diaz and G. P. Eberli, Earth-Science Reviews **190**, 536 (2019).

[6] K. S. Karunadasa, C. Manoratne, H. Pitawala, and R. Rajapakse, Journal of Physics and Chemistry of Solids **134**, 21 (2019).

[7] L. Bianco, Romanian Journal of Physics **62** (2017).

Commissioning and Simulation of the St. Benedict Extraction Beamline and Paul Trap

DANIEL SCHROEDER

2024 NSF/REU Program
Department of Physics and Astronomy
University of Notre Dame

ADVISOR(S): Prof. Maxime Brodeur

Abstract

The University of Notre Dame's Superallowed Transition Beta-Neutrino Decay Ion Coincidence Trap (St. Benedict) is being constructed with the aim of measuring the beta-neutrino angular correlation parameter for superallowed mixed beta-decay transitions between mirror nuclei. This allows testing of the theoretical corrections in the determination of the V_{ud} element of the Cabibbo-Kobayashi-Maskawa matrix. Determination of this value enables testing of the unitarity of the matrix, which can then act as a test for the completeness (or incompleteness) of the Standard Model. There are four main components to the St. Benedict system: a gas catcher to thermalize the radioactive ion beam, followed by a differentially pumped extraction system, a radio-frequency quadrupole cooler-buncher to further cool the beam and prepare it for entry into the final element – the Paul trap used to observe the beta decay. This report details the commissioning and simulation of the extraction beamline (which carries the ions from the cooler-buncher to the Paul trap) as well as the Paul trap.

1 Introduction

The Standard Model is, so far, the most successful model for describing the interactions between fundamental particles. However, the Standard Model is known to be imperfect and is expected to be incomplete because it is unable to explain observed phenomena such as neutrino masses and oscillation or our understanding of gravitational interactions. It also does not motivate the presence dark matter and dark energy. This disagreement with observation has led many to search for physics Beyond the Standard Model (BSM) [1].

The Large Hadron Collider (LHC) has not only been useful in validating the Standard Model with the discovery of the Higgs boson, but also in searching through a wider zone of experimental physics for anything BSM. However, this search has provided no signs of new physics in the range of energies available to current colliders. This guides research in the other complementary direction to search for BSM physics in the low-energy regime via the weak interaction [2].

The weak interaction allows quarks to mix across all three generations. This mixing is governed

by the Cabibbo-Kobayashi-Maskawa (CKM) matrix,

$$\begin{bmatrix} d' \\ s' \\ b' \end{bmatrix} = \begin{bmatrix} V_{ud} & V_{us} & V_{ub} \\ V_{cd} & V_{cs} & V_{cb} \\ V_{td} & V_{ts} & V_{tb} \end{bmatrix} \begin{bmatrix} d \\ s \\ b \end{bmatrix} \tag{1}$$

via its various matrix elements V_{ij}. This matrix translates from the space formed by a quark's mass eigenstates (unprimed) to the space formed by its weak eigenstates (primed).

Completeness of the Standard Model necessitates unitarity of this matrix, hence any observed deviation from unitarity can be indicative of BSM physics. To test unitarity, one can check if the norm of any given row or column is equal to one. Currently, the most precise test comes from the top row. The smaller elements of that row, V_{us} and V_{ub}, are determined from kaon decays and semileptonic B hadron decays, respectively. The matrix element V_{ud} can be determined from four different types of superallowed β-decay transitions. These are the decay of the pion, neutron, mixed transitions between mirror nuclei, and pure Fermi transition between 0^+ states. The most precise value of V_{ud} currently comes from the latter type of decay. Nevertheless, the unitarity of the CKM matrix currently fall short by about 3σ, which generates interest in improving the precision on V_{ud} from other types of decays including superallowed mixed beta decay. At the moment, the uncertainty in V_{ud} for superallowed mixed beta decay is rather large, as it has only been measured for a few transitions [3]. St. Benedict (the Superallowed Transition Beta-Neutrino Decay Ion Coincidence Trap) at the University of Notre Dame focuses on determining the V_{ud} element for many more transitions in order to reduce its uncertainty. This will be enabled by a measurement of the beta-neutrino angular correlation parameter ($a_{\beta\nu}$), as explained in more detail in Sec. 2.

St. Benedict, shown in Fig. 1, receives a radioactive ion beam (RIB) from Notre Dame's TwinSol facility, stops, extracts, bunches, and transports it into a Paul trap where the decay is measured. The work presented in this report focuses on the latter half of St. Benedict meant to prepare the beam for measurement in the Paul trap. Every component up to and including the cooler-buncher has been commissioned separately as well and also used with on-line beams from

TwinSol. The work detailed presents simulations of the beam transport to the next components: the extraction beamline (see Sec. 3) and its capture into the Paul trap (see Sec. 4).

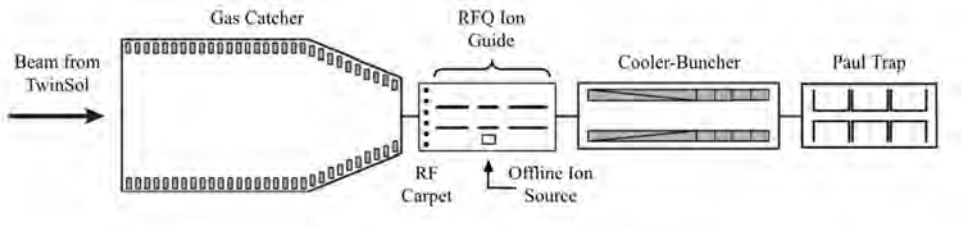

Figure 1: St. Benedict consists of four major components: a gas catcher to thermalize a radioactive ion beam; an extraction system comprised of a radio-frequency (RF) carpet and a radio-frequency quadrupole (RFQ) ion guide to extract the cooled ions; an RFQ cooler-buncher to further cool the beam and prepare it for entry into the final element, the Paul trap, used to observe the beta decay with sensors detecting coincident daughter particles and positrons. The extraction beamline connects the cooler-buncher to the Paul trap.

2 Background

The extraction of V_{ud} from the decays of atomic nuclei, which are complex multi-nucleon systems, relies on the determination of various comparative half-life ($f_V t$) values. Additionally, for superallowed mixed transitions, a determination of the Fermi to Gamow-Teller mixing ratio (ρ) is required. The relationship between V_{ud} and $f_V t$- values is given by:

$$f_V t \left(1 + \delta_R\right)\left(1 + \delta_{NS} - \delta_C\right) = \frac{K}{2G_F^2 V_{ud}^2 \left(1 + \Delta_R\right)\left(1 + \frac{f_A}{f_V}\rho\right)}. \tag{2}$$

This expression includes known constants (K and G_F) and theoretical corrections (δ_i and δ_R). Aside from ρ, experimental quantities include atomic masses entering in the calculation of the statistical rate functions for the vector (f_V) and axial vector (f_A) parts of the interaction, as well as half-lives ($t_{1/2}$) and branching ratios used to calculate the partial half-life (t) [3]. ρ can be determined via the

measurement of the beta-neutrino angular correlation parameter $a_{\beta\nu}$ via the following equation

$$a_{\beta\nu} = \frac{1 - \frac{\rho^2}{3}}{1 + \rho^2}. \tag{3}$$

At St. Benedict, $a_{\beta\nu}$ will be obtained by fitting the time-of-flight distribution of recoiling daughter nuclei emitted after the β-decay.

3 The Extraction Beamline

Figure 2: The elements of the extraction beamline are as follows: 1 – Cooler-Buncher Extraction Optics, 2 – Rey Time of Flight (ToF) Tube, 3 – Einzel Lens 1, 4 – Steerer 1, 5 – Einzel Lens 2, 6 – Pre-BNG Drift Tube, 7 – Bradbury-Nielsen Gate (BNG), 8 – Post-BNG ToF Tube, 9 – Einzel Lens 3, 10 – Paul Trap Side ToF Tube, 11 – Paul Trap Aperture. This image is an example of what the ion optical simulations looked like, where the black lines are the paths taken by ions.

The cooler-buncher extraction beamline, as shown in Fig. 2 consists of a series of drift tubes, steerers, and Einzel lenses to focus the beam into the Paul trap. Prior to this work, it housed a silicon detector immediately before the Bradbury Nielson Gate. Recently, however, a better location and detector design was found. As a result, it was replaced with a drift tube. This tube was designed in SolidWorks and constructed to be screwed onto a flange. The addition of the new tube required new ion-optical simulations to ensure the ions would still be transported efficiently. The steerers and drift tubes make up the interior of the beamline and are held at a constant potential difference of -1000 V, and the focusing of the beam is done by the three einzel lenses. Thus, tuning the beamline from a simulation standpoint consisted of optimizing the potentials for these three lenses.

3.1 Simulations

The ion optical simulations were performed using the SIMION 8.1 software. A collection of 500 ions of mass 39 amu and charge +1 e, resulting from a simulated bunch leaving the cooler-

buncher, were flown through the extraction beamline at various Einzel lens voltages. The beam profile at the entrance of the Paul trap was plotted and the lenses were tuned by prioritizing a small beam profile and a large number of ions reaching the end of the beamline. This tuning scanned a range from 0 V to -5000 V for each Einzel lens individually, creating plots like depicted in Fig. 3. Ultimately, Einzel lens 1 was set to -1930 V, Einzel lens 2 to -1610 V, and Einzel lens 3 to -1500 V. This tune resulted in the beam profile seen in the top-middle of Fig. 3. However, this tune is not ideal, as the goal was to constrain the beam to a radius of 1 mm. As seen in Fig. 3, it was difficult to achieve this without causing more outlying ions. It was concluded that additional tuning of the cooler-buncher would be needed to further constrain the beam entering the extraction beamline because the beam spread too far in the z direction. Subsequently, tuning moved onto the Paul trap to better understand how it will trap the bunches of beam generated by the cooler-buncher.

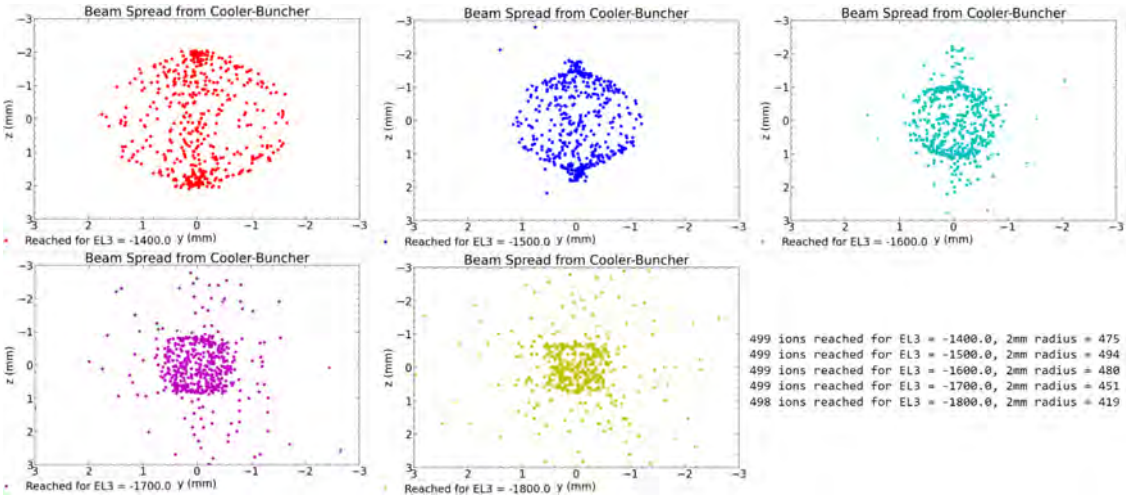

Figure 3: Each Graph is a direct image of the beam crossing the plane into the Paul trap. Travelling down the extraction beamline is the x axis, so this cross section is the y-z plane with units millimeters. Additionally, it was found how many ions reach this plane as well as how many that reached the plane fall into a circle of 2mm radius. This particular plot is a scan of Einzel lens 3 (EL3).

4 The Paul Trap

The Paul trap at the end of St. Benedict consists of a set of segmented radio-frequency quadrupoles that confine ions radially with out-of-phase radio-frequencies while a constant po-

tential applied on these segments generates an axial potential well, fully confining the ions. The quadrupoles are surrounded on two sides with microchannel plate (MCP) detectors used to detect the daughter particle resulting from the beta decay of the trapped ion bunches. The other two sides house double-sided silicon strip detectors with photomultiplier tubes used to detect the resultant positrons from the decay [4]. Together, these allow for measurement of coincident arrivals of daughter particles and positrons from the same decay. Then $a_{\beta\nu}$ is determined by fitting the distribution of differences in times of arrival for these two particles, as described in [5].

4.1 Simulations

The mechanics of trapping in the Paul trap were also simulated in SIMION. The RF quadrupoles are segmented into three sections, each carrying its own static potential. The center section is held at -60 V while the other two are held at 10 V, creating a small potential well in the center section. Ultimately, the potential well confines ions in the x direction, and the radio-frequency applied to the rods in the quadrupole section confines the ions radially. At some point, this well must be "opened" to allow a bunch of ions to enter and then promptly "closed." This was achieved in SIMION by keeping the first RFQ section at a potential difference similar to that of the center. Then, as soon as the ions reached the center of the trap, the program would flip the voltage back to 10 V, trapping the ions in the middle section. This is dependent on the energy of the ions, since the trap depth is kept small. Earlier, the ions were found to enter the Paul trap with a rough average kinetic energy of 720 eV, enough to easily escape a trap with a depth of 70 V. Thus, the first step in simulating the Paul trap was tuning it to "slow down" the ions such that they have the lowest possible energy in the center of the trap. This was accomplished by adjusting the potential on the tube at the entrance to the trap, to provide a "pull" on the ions causing them to lose energy. It was assumed the entirety of the 720 eV kinetic energy was from the z-component of travel, so the resulting kinetic energy in the z direction was plotted for every available potential at the entrance of the trap–shown in Fig. 4.

Figure 4 suggests the potential should be of the highest possible magnitude while still allowing ion bunches to enter the trap. It is desirable to successfully trap the greatest number of bunches over

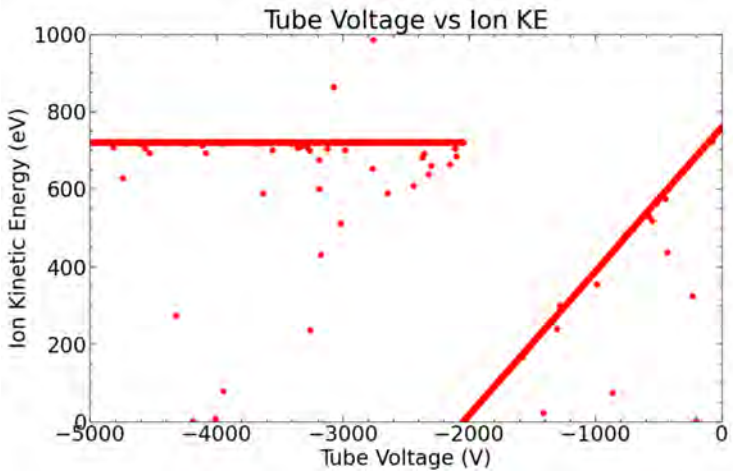

Figure 4: The potential difference of the tube is plotted against the resulting z-component of kinetic energy of the ions at the center of the trap. The straight segment located around 720 eV results from the potential being negative enough for ions to hit the inside of the tube, ending the simulation.

a large sample, but it is also important that the ions have a low energy, so they are well behaved and can cool to nearly stationary. To gather this information, 1000 ion bunches were simulated for potentials ranging from -1930 V to -2060 V. A trapping was considered successful when an ion survived longer than 50 μs. The energy was recorded as soon as the simulation ended (either after 50 μs or when the ion collided with the trap wall). This resulted in the data presented in Fig. 5.

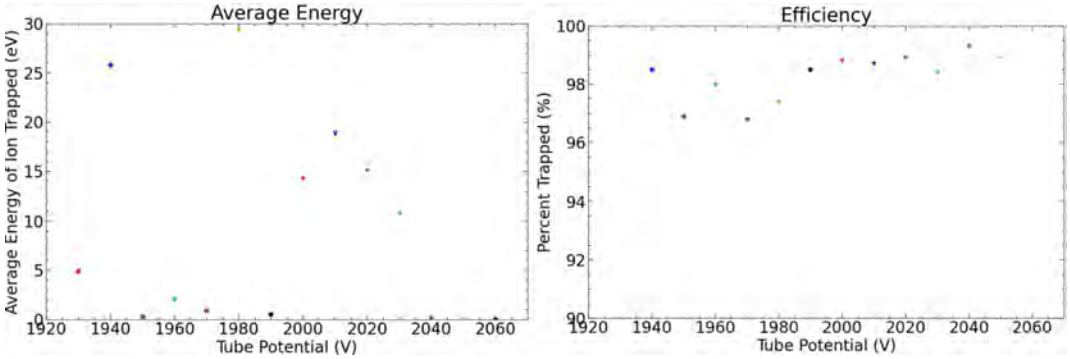

Figure 5: Pre-Paul trap drift tube's potential against final kinetic energy of the ion (left) and the percent of 1000 trials which were successfully trapped (right). A range of -2040 V to -2050 V is ideal, as most of the ions are trapped while having low kinetic energy.

However, ions are meant to cool down and become nearly stationary over time due to collisions with helium atoms causing the ions to lose energy and ultimately settle in the potential well. This was not observed in these SIMION simulations, as the kinetic energy of the ions did not decrease

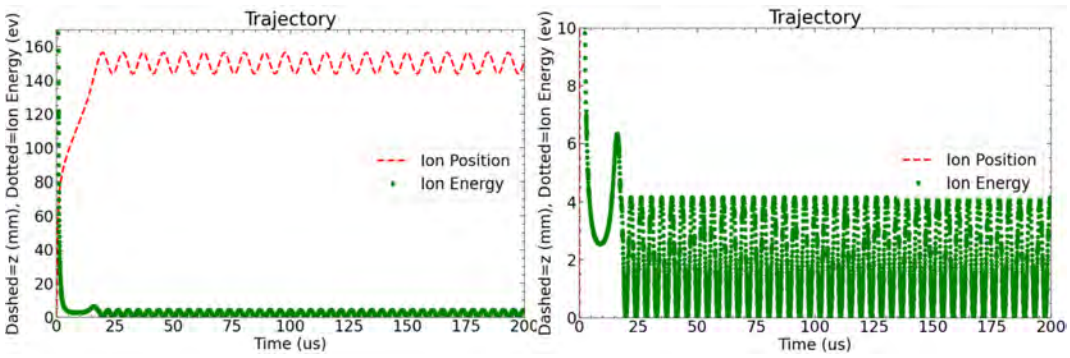

Figure 6: The graph on the right depicts a zoomed in section of the bounds containing the ion kinetic energy portion of the graph on the left. The ion's kinetic energy oscillates around a fixed value rather than decaying to zero, indicating the ion is not cooling in the trap as a result of gas particle collisions during a time period of 200 μs. These simulations were done for a pressure of 1×10^{-5} Torr.

over the simulated time scale as shown in Fig. 6. This is indicative that at a pressure of $1{\times}10^{-5}$ Torr, the ions need more than 200 μs to cool via collision with helium. We also observed that sometimes ions would collide with the walls of the central RFQ portion. Simulating the complete cooling of each ions in a bunch would require holding them 10s of milliseconds each, which would be computationally long. This meant it was not possible to model the entire lifetime of a trapped ion, so a successful trapping was considered to be an ion trapped for a few microseconds. Complete simulations of the cooling of the ion will require the use of a code that allows for parallel computing (unlike SIMION) to minimize the duration of the simulations down to manageable time scales.

5 Conclusion

The St. Benedict system, under construction at the University of Notre Dame's Nuclear Science Laboratory aims at testing the Standard Model by measuring $a_{\beta\nu}$ in superallowed mixed β-decay transitions. The most upstream components of the system, namely the gas catcher, its extraction system, and the cooler-buncher all have beam commissioned and received RIB from TwinSol. The work presented focused on the remaining components of the system: the cooler-buncher extraction beamline and the Paul trap. Both have been assembled, but have yet to be connected to the rest of the system. As part of this work, a new drift tube was added to the extraction beam

line and simulations were conducted for both the extraction beamline and the Paul trap. The simulations served as proof of effective transport of bunched ions from the cooler-buncher to the trap, and provided a starting point for future tuning with an ion source. Additionally, they are useful in identifying areas that could be better tuned and point out particularly sensitive components of the system. From here, further tuning of the cooler-buncher will improve transmission through the extraction beamline. Additionally, further simulation of the Paul trap to implement time-based static potential switching will better reflect the actual operation of the trap

6 Acknowledgements

I am grateful for the opportunity to have worked in Notre Dame's Nuclear Science Lab, and I owe thanks to Professor Brodeur for the opportunity to contribute to his lab. Additionally, I must thank Dr. O'Malley and the graduate students of the lab: Sam Porter, Rey Zite, Fabio Rivero, Olivia Bruce, and Alicen Houff, for their help. Finally, I would like to thank Dr. Garg and Kristen Amsler for making the summer program possible, as well as the NSF for funding under grant number PHY-2050527 (REU program) and PHY-2310059 (Nuclear Science Laboratory).

References

[1] T. Lagouri, Symmetry **14**, 10.3390/sym14071299 (2022).

[2] J. Beacham, C. Burrage, *et al.*, Journal of Physics G: Nuclear and Particle Physics **47**, 010501 (2019).

[3] W. Porter, D. Bardayan, *et al.*, Atoms **11**, 10.3390/atoms11100129 (2023).

[4] M. Brodeur, T. Ahn, *et al.*, Nuclear Instruments and Methods in Physics Research Section B: Beam Interactions with Materials and Atoms **541**, 79 (2023).

[5] G. Ban, D. Durand, *et al.*, Annalen der Physik **525**, 576 (2013), https://onlinelibrary.wiley.com/doi/pdf/10.1002/andp.201300043 .

A Simulator of The Enge Split Pole Spectrograph, and Extracting Relative Differential Cross Sections by Exploiting Target Contaminants

ALAND SINJARI

2024 NSF/REU Program
Department of Physics and Astronomy
University of Notre Dame

ADVISOR(S): Scott Carmichael and Prof. Daniel Bardayan

Abstract

Nuclear reaction differential cross section data is critical for constructing computational models of nucleosynthetic astronomical phenomena. At the University of Notre Dame, an Enge Split Pole Spectrograph (SPS) has recently been commissioned, partially to gather the aforementioned data. In this work we discuss the construction of a simulator of the Enge SPS. We then detail the development of a systematic methodology to convert the raw data from the Enge SPS into differential cross sections utilizing target contaminants for normalization. We demonstrate how starting from the literature's experimental data on ^{12}C(^{3}He, α)^{11}C, where the residual is in the ground state, we are able to reproduce within a factor of 3 the literature's differential cross sections for ^{12}C(^{3}He, α)^{11}C, where the residual is in the first excited state. Furthermore, we report the differential cross section for ^{58}Ni(^{3}He, α)^{57}Ni, which has had little experimental data hitherto. Multiple avenues are suggested to improve our method.

1 Introduction

It is understood that nucleosynthesis in dramatic astronomical conditions, such as in stars and supernovae, is responsible for the creation of nearly all of the elements. Currently, theorists attempt to understand these events by creating computational models which rely on various nuclear reaction data, such as nuclear reaction rates. There is a present demand for more measurements in order to determines these reaction rates and bolster these models.

At the University of Notre Dame, an Enge Split Pole Spectrograph (SPS) [1] has been installed to determine various forms of nuclear data from astrophysically relevant nuclei and reactions. At the time of writing, the first sets of experimental data from the Enge SPS have been obtained, including 21 MeV ^{3}He beam on a ^{58}Ni target runs that we will discuss in this report. To aid in the analysis of this data, a simulator has been constructed that outputs the particle bending radii we expect to find in our Focal Plane Detector (FPD) given a certain nuclear reaction and various experimental parameters. This simulator is further applied to develop a methodology to obtain differential cross section measurements by utilizing target contaminants for normalization.

2 Background

2.1 The Enge Split Pole Spectrograph

A charged particle with constant velocity in a uniform magnetic field will experience the Lorentz force, resulting in a circular motion with the radius

$$\rho = \frac{p}{QB} \tag{1}$$

where ρ is bending radius, p is momentum, Q is charge, and B is magnetic field strength [2].

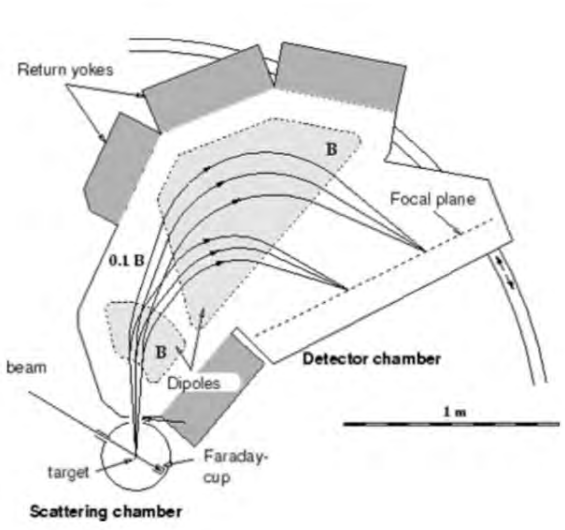

Figure 1: A diagram of the Enge SPS [1]. Note how particles with the same momenta but different angles of incidence still get focused to the same position on the FPD.

The Enge SPS exploits this fact to spatially separate charged particles. Once charged particles enter the apparatus, they move through two separate pole pieces which shape the magnetic fields to ensure that the particles will be focused onto the same plane which contains our FPD [1]. In other words, particles of the same momenta will end up in the same position on the FPD despite their angles of incidence. Once a nuclear reaction has occurred, the ejectile nucleus travels through the Enge SPS and enters the FPD. From the position on the FPD (that is, ρ), we can find the momentum of the ejectile and gain information about the nuclear reaction which produced it.

2.2 Nuclear Reactions and Relativistic Reaction Kinematics

Consider the following nuclear reaction:

$$i + T \rightarrow R + e \tag{2}$$

where i is the incident nuclei, T is the target, R is the residual nuclei, and e is the ejectile nuclei. This reaction is abbreviated to $T(i, e)R$. For any reaction there are multiple possible residual excitation levels. Due to conservation of energy, we see lower ejectile kinetic energies for higher excited residual states. Furthermore, the probability of the residual being excited into a specific state influences the differential cross section corresponding to that excited state.

If the residual is in the ground state, the kinetic energy of the ejectile nucleus is

$$\sqrt{T_e} = \frac{\sqrt{m_i m_e T_i}\cos\theta \pm \sqrt{m_i m_e T_i(\cos\theta)^2 + (m_R + m_e)(m_R Q_0 + (m_R - m_i)T_i)}}{m_R + m_e} \tag{3}$$

where T represents kinetic energy, m represents mass, $Q_0 = (m_I + m_T - m_R - m_E)c^2$ is the Q-value of the reaction where all the particles are in their ground states, and θ is the scattering angle in the lab frame [3]. If the residual nucleus is left in an excited state, we must replace Q_0 in Eq. 3 with Q_{ex}, which is defined as

$$Q_{ex} = Q_0 - E_{ex} \tag{4}$$

where E_{ex} is the excitation energy of the residual nucleus [3].

3 Methods

3.1 Bending Radius to Ejectile Kinetic Energy

If we set c = 1, and note that $T_e = E - m$, where $E = \sqrt{p^2 + m^2}$ is the total relativistic energy, we can utilize Eq. 1 to yield

$$T_e = \sqrt{(\rho BQ)^2 + m^2} - m \tag{5}$$

We use this equation both in our experimental analysis to find out the energies of the ejectiles using the FPD as well as in our simulator to convert ejectile kinetic energy from our relativistic reaction kinematics to bending radius, which is what the simulator outputs.

3.2 The Design of The Enge Split Pole Spectrograph Simulator

The Enge SPS simulator requires a database of the excitation energies of various nuclei, experimental parameters (beam energy, spectrograph angle, etc.), as well as data about the nuclei involved in the reaction (mass, Z, A) as inputs. We use relativistic reaction kinematics to find the kinetic energy of the ejectile of a given reaction for the first X excited states, where X is set by the user. We then use Eq. 5 to convert the kinetic energy of the ejectile to the bending radius, which is outputted to a GUI. The intended usage of this program is to compare the outputted bending radii to the bending radii from our experimental data, in order to assist in identifying the reactions responsible for the peaks in the data.

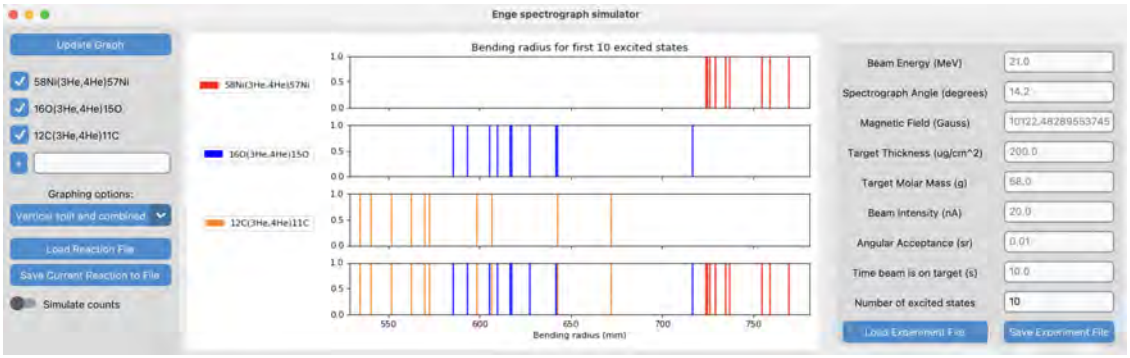

Figure 2: The Enge SPS simulator's GUI. Various parameters can be modified dynamically, in case an experimentalist is using this program during beam time to check results as they come in.

3.3 Finding Differential Cross Sections using Target Contaminants

Our Enge SPS simulator helped reveal a large presence of contaminants on our ^{58}Ni target. In this subsection, we detail a systemic method to gain differential cross section measurements using these contaminants. First, we identify a reaction whose differential cross section is well understood (in our case, ^{12}C(^{3}He, α)^{11}C's ground state), and one whose differential cross section we wish to

determine (^{58}Ni(^{3}He, α)^{57}Ni's ground state and ^{12}C(^{3}He, α)^{11}C's first excited state). Using the FPD data, we perform a Gaussian fit on all of the relevant peaks. The parameters from our fit (peak height, standard deviation) are used to solve for the number of counts, which is directly proportional to the area of the Gaussian.

Second, we ideally find experimental data that describes the differential cross section of our known reaction at the angles and beam energy we used. In our case, data from the literature [4] did not have enough a wide enough angle range or the corresponding beam energy for our experiment, so we interpolated data from 20 MeV and 22 MeV to our beam energy of 21 MeV, and extrapolated to get the angle range we required.

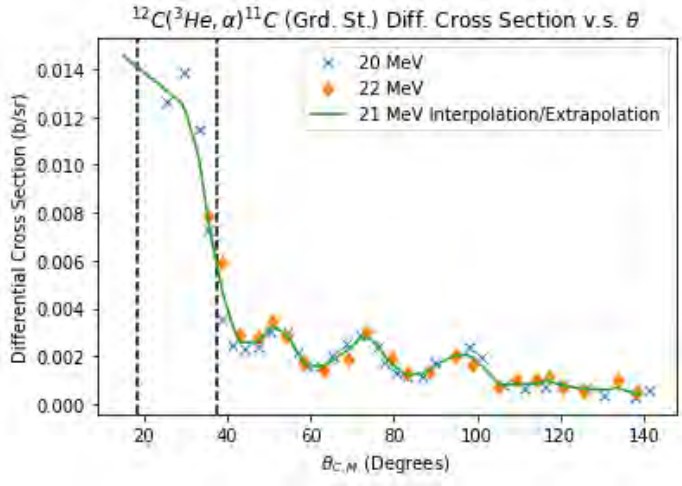

Figure 3: Plot containing the literature's data [4] from 20 MeV and 22 MeV runs, as well as the 21 MeV function that we use in our analysis. The dashed lines represent the angle range in which we took data from the Enge SPS.

To convert from our known differential cross section data to other residual excitation energies of the same reaction, we must start from the equation

$$\frac{d\sigma}{d\Omega} = \frac{1}{\Omega I_a N}\frac{C}{t} \tag{6}$$

where $\frac{d\sigma}{d\Omega}$ is the differential cross section, C is the counts, t is time, I_a is the incident particles per unit time, Ω is the solid angle opening of the Enge SPS, and N is target nuclei per unit area [3]. If we take a different excited level, solve for the experimental constants (Ω, I_a, N, t) and set

them equal to one another, we yield our desired equation, where the subscript k denotes our known reaction, and the subscript u denote our unknown reaction:

$$\frac{d\sigma}{d\Omega_u} = \frac{C_u}{C_k}\frac{d\sigma}{d\Omega_k} \tag{7}$$

The analysis becomes more complicated if we wish to use our known reaction to probe reactions containing a different target nucleus, since we cannot assume that N is the same. We can assume that I_a is the same, and using Eq. 6, we get

$$\frac{1}{\Omega N_k}\frac{C_k}{t}(\frac{d\sigma}{d\Omega_k})^{-1} = \frac{1}{\Omega N_u}\frac{C_u}{t}(\frac{d\sigma}{d\Omega_u})^{-1} \tag{8}$$

$$\rightarrow \frac{d\sigma}{d\Omega_u} = \frac{C_u}{C_k}\frac{d\sigma}{d\Omega_k}\frac{N_k}{N_u} \tag{9}$$

Now, we only need to find $\frac{N_k}{N_u}$ in order to be able to obtain $\frac{d\sigma}{d\Omega_u}$. Since $\frac{N_k}{N_u}$ is constant across different types of nuclear reactions if the physical target is not changed, we decided to investigate elastic scattering on our known (^{12}C(^{3}He, ^{3}He)^{12}C) and our unknown (^{58}Ni(^{3}He, ^{3}He)^{58}Ni) reactions. If we let the subscript ϵ denote the elastic scattering reaction, we measure $\frac{Nk}{Nu}$ by solving

$$\frac{N_k}{N_u} = \frac{d\sigma}{d\Omega_{u,\epsilon}}\frac{C_{k,\epsilon}}{C_{u,\epsilon}}(\frac{d\sigma}{d\Omega_{k,\epsilon}})^{-1} \tag{10}$$

The counts ratio is measured using our experimental data. In order to model the ratio of the differential cross sections, we use the Rutherford scattering equation:

$$\frac{d\sigma}{d\Omega_\epsilon} = (\frac{zZe^2}{4\pi\epsilon_0})^2(\frac{1}{4T_i})^2\frac{1}{\sin(\frac{\theta}{2})^4} \tag{11}$$

where z, Z represents the incident and target nuclei atomic number respectively, ϵ_0 is vacuum permittivity, T_i is the incident nuclei's kinetic energy, and θ is the scattering angle. The Rutherford scattering equation is a good approximation in our regime, as we are at relatively low kinetic energies and forward angles, meaning that the Coulomb interaction dominates over any nuclear inter-

actions [3]. For our target, we found a $\frac{N_k}{N_u}$ (or more specifically, $\frac{N_{^{12}C}}{N_{^{58}Ni}}$) value of 2.36714975845.

4 Results

4.1 The Accuracy of the Enge Split Pole Spectrograph Simulator

The Enge SPS simulator is accurate, and it revealed the presence of multiple different nuclei on our ^{58}Ni target. It confirmed the presence of ^{12}C from our target's carbon backing, as well as the presence of ^{16}O contamination, which is most likely from residual water molecules. We note that the presence of carbon is so high that there are peaks corresponding to the presence of carbon's second most abundant isotope, ^{13}C. Below we compare some previously identified states to bending radii (ρ) from our simulation, and we find similar results. The run displayed below was taken with the Enge SPS at 14.3 degrees in the lab frame.

(Target, Excitation Level)	ρ, exp. (mm)	ρ, sim. (mm)	Difference (mm)
(^{58}Ni, 0)	768.010751 $\pm$ 2.1996e-05	767.724608	0.286143
(^{58}Ni, 1)	757.960973 $\pm$ 5.7157e-05	757.690226	0.270747
(^{16}O, 0)	715.203274 $\pm$ 2.6817e-04	715.188607	0.014667
(^{12}C, 0)	670.473221 $\pm$ 8.0477e-05	670.504908	$-$0.031687

4.2 Differential Cross Section Measurements

We applied our method from Sec 3.3, using the ground state of ^{12}C(^{3}He, α)^{11}C as our known cross section. We checked our accuracy by comparing our calculation of the first excited state of the aforementioned reaction versus the literature's experimental data on said reaction. We find that our results deviate from the literature by up to a factor of three, as seen in Fig. 4.

It is difficult to validate our measurement of the ^{58}Ni(^{3}He, α)^{57}Ni differential cross section due to the lack of good experimental evidence available. The only experimental data available is a single measurement at 25 MeV and 5 degrees (C.M. frame), which reports a differential cross section of 0.00154 $\frac{b}{sr}$ [5]. Our results are incomparable due to the difference in experimental parameters.

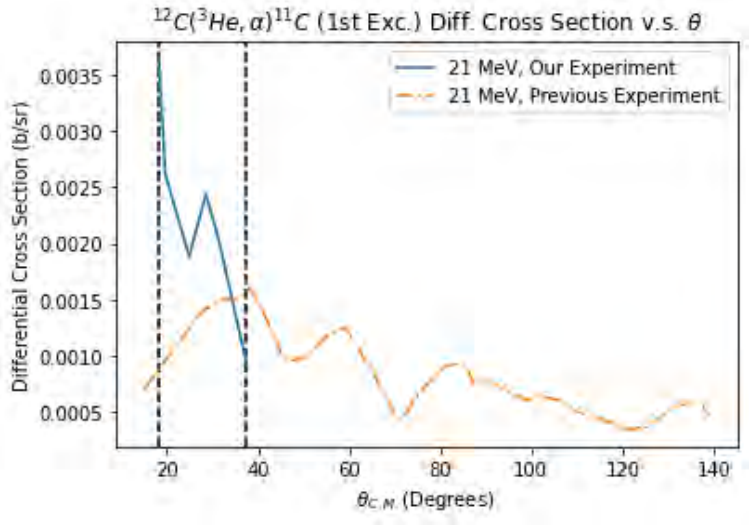

Figure 4: Our experimental data versus the previous experiment reported in the literature [4] on the ^{12}C(^{3}He, α)^{11}C reaction, with the residual in the first excited state. The previous experiment function was found by using the same method as used in Fig. 3. The dashed lines represent the angle range in which we took data from the Enge SPS.

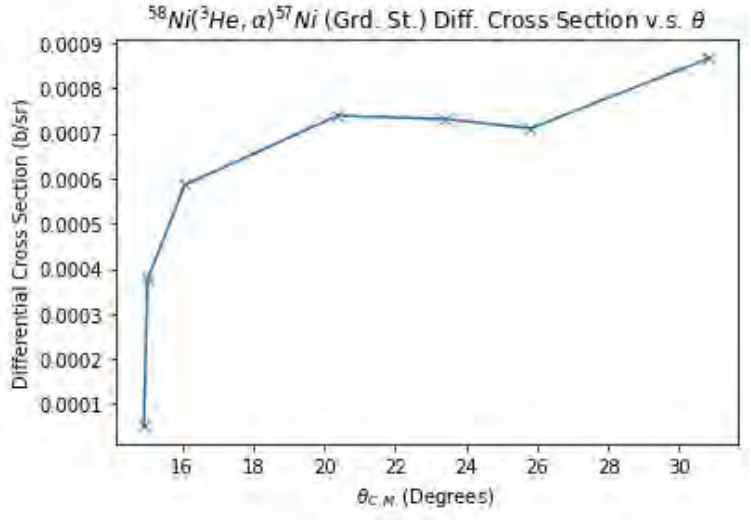

Figure 5: ^{58}Ni(^{3}He, α)^{57}Ni differential cross section with the residual being in the ground state. We believe that the decrease in cross section at forward angles is due to incorrect extrapolation on our normalization cross section (^{12}C(^{3}He, α)^{11}C).

5 Conclusion

Our differential cross section methodology is a good starting point, but more work is needed for it to become accurate. Fig. 3 shows our interpolated 21 MeV function is defined using sparse data within the required degree range. Thus it would be wise to test our methodology at greater angles.

Further improvements on our model focus on ensuring our interpolated 21 MeV function is more accurate. This can be achieved experimentally by measuring the ^{12}C(^{3}He, α)^{11}C reaction at forward angles and at a beam energy of 21 MeV. Alternatively, we can get shallow angle corrections from nuclear theory and use them to supplement our linear fit.

Another improvement on our calculation method would be to account for more center of mass effects. One should note that the solid angle changes in the center of mass frame, and is equivalent to the solid angle in the lab frame multiplied by a Jacobian. This Jacobian is dependent on the residual excitation level, kinetic energy, angle, etc. This means that the solid angle in Eq. 6 does not necessarily cancel out, and an adjusting factor multiplied to Eq. 7 and Eq. 9 would be required to make the rest of our methodology accurate.

It is unknown if our ^{58}Ni(^{3}He, α)^{57}Ni measurement is accurate. Our result can be checked by using a different differential cross section measurement technique and comparing. One candidate is to solve Eq. 6 by directly measuring I_a and N. Another option is using a different known reaction for normalization, then deriving data for the ^{58}Ni(^{3}He, α)^{57}Ni reaction, and seeing if our two normalizations agree. Given our data, a potential candidate for this is ^{16}O(^{3}He, α)^{15}O.

References

[1] J. Spencer and H. Enge, Nuclear Instruments and Methods **49**, 181 (1967).

[2] D. J. Griffiths, *Introduction to Electrodynamics* (Cambridge University Press, 2017).

[3] K. S. Krane, *Introductory Nuclear Physics* (Wiley, 1987).

[4] G. D. Adeev, A. M. Kazantseva, V. V. Kozyr, V. A. Matusevich, and I. P. Chernov, Soviet Journal of Nuclear Physics **26**, 361 (1977).

[5] J. P. Schiffer, C. R. Hoffman, B. P. Kay, J. A. Clark, C. M. Deibel, S. J. Freeman, M. Honma, A. M. Howard, A. J. Mitchell, T. Otsuka, P. D. Parker, D. K. Sharp, and J. S. Thomas, Physical Review C **87**, 034306 (2013).

Multiscale Scientific Analysis of Late 17th Century Cuzco Painting

MADELINE TRICARICO

2024 NSF/REU Program
Department of Physics and Astronomy
University of Notre Dame

ADVISOR(S): Prof. Khachatur Manukyan

Abstract

The paint used in Spanish American paintings from the Cuzco School are composed of a variety of pigments unique to the 17th century. The focus of this paper is the painting *Our Lady of Vizcaia* from the University of Notre Dame's Raclin-Murphy Museum of Art. Samples of four different pigments from *Our Lady of Vizcaia* were removed and analyzed: green, blue, and two red samples taken from different locations. Raman Spectroscopy, X-Ray Diffraction, and X-Ray Fluorescence were utilized to determine the chemical composition of these paint pigments. The results reveal that the green pigment contains orpiment, calcite, graphite, quartz, and litharge. The blue pigment contains Prussian blue, quartz, litharge, cerussite, and calcite. Both reds are composed of vermilion and quartz, and one additionally contains calcite. Knowing the chemical composition of these pigments will allow for art conservationists to better preserve the integrity of the painting going forward.

1 Introduction

The goal of this research project was to identify the chemical composition of pigments used in the painting *Our Lady of Vizcaia*, which is currently housed in Notre Dame's Raclin-Murphy Museum of Art. This painting originates from the Cuzco School. The "Cuzco School" refers to an artistic tradition that took place from the 16th-18th century in Cuzco, Peru and the surrounding region [1]. This analysis was done by utilizing Raman Spectroscopy, X-Ray Diffraction (XRD), and X-Ray Fluorescence (XRF). The results from this scientific analysis adds to a collective knowledge on Spanish-American paintings. This knowledge is used by art conservationists to preserve and restore historical paintings such as *Our Lady of Vizcaia*, which can be seen below in Figure 1.

The Cuzco School refers to the production of works of art from Cuzco, Peru, from roughly 1600-1760 AD [2]. In the 17th century, Europeans arrived in Peru and trained indigenous Spanish artists in the style now known as Spanish Mannerism. These paintings were used as an evangelization tool by Latin-American artists. Colonial Latin American paintings feature a mixture of European styles and native elements which were carried over from the Incan empire. Other native traditions from the Andean regions are also seen in paintings originating from the Cuzco School. The Cuzco School's style was additionally developed from Italian, Spanish, and Flemish models brought by English settlers. Spanish painters followed recipes to make their pigments. These recipes were in

Figure 1: *Our Lady of Vizcaia*

accordance with treatises that resulted from the European colonization of Latin America[1].

Commonly used pigments in green paint from the Cuzco School include copper resinate ($C_4H_6CuO_4 \cdot H_2O$), malachite ($Cu_2CO_3(OH)_2$), orpiment (As_2S_3), indigo ($C_{16}H_{10}N_2O_2$), and Prussian blue ($C_{18}Fe_7N_{18}$). Orpiment is a mineral that produces a yellow hue. Orpiment is often found with another blue pigment, either indigo or Prussian blue, in order to create a desired green pigment. Common red pigments found in Cuzco paintings include vermilion (HgS), hematite (Fe_2O_3), organic red lake ($AlK(SO_4)_2 \cdot 12H_2O$), and red lead (Pb_3O_4) [2]. White lead ($(PbCO_3)_2 \cdot (Pb(OH)_2)$) was commonly used as a white background for the artists to paint over.

In this scientific analysis, X-Ray Flourescence (XRF) is a method utilized in order to understand the pigment composition. XRF is a technique that utilizes high-energy radiation to excite the atom by shooting electrons out from the innermost atomic orbital. Outer-shell electrons relax to fill the inner-shell opening, and x-ray flourescence radiation is emitted. This emitted radiation is picked

up by the machine's detector, and a graph is produced. The emitted radiation is unique to each element, so it is easy to identify the elements in a sample based on the XRF peaks [3].

X-Ray Diffraction (XRD) is another technique utilized in this study. XRD utilizes x-ray beams by sending x-rays through a sample. Since the wavelength of x-rays is similar to the spacing of atoms, variety in the spacing of atoms in a molecule results in a different angle of diffraction. If a sample has a crystalline structure, then these x-rays bounce off the atoms in a sample and are reflected at a unique angle of diffraction. Constructive interference between these deflected waves results in a larger peak at the given angle of diffraction. The composition of the sample can then be determined by the angle of diffraction detected [4].

Raman Spectroscopy is a technique which reveals the chemical bonds in a sample. This works by focusing a high-intensity laser light source onto the sample. The incident light is then scattered by the molecules in the sample. Most of the scattered light is at the same wavelength as the light source and does not provide any useful information. This is called Rayleigh scattering. A small amount of light is scattered at different wavelengths, which depends on the composition of the sample. This scattered light is called Raman scattering. The detector picks up on this scattering and produces a Raman spectrum, which has peaks at various intensities and wavelengths depending on the molecular bond vibrations from the sample [5].

This study uncovers the composition of the pigments in *Our Lady of Vizcaia* in order to add to the collective knowledge of colonial Spanish-American paintings. This knowledge is essential in conservation and preservation efforts currently being made.

2 Methods

The nondestructive techniques utilized in this study were X-Ray Flourescence (XRF), X-Ray Diffraction (XRD), and Raman Spectroscopy. XRF was used to determine the elemental composition of the samples. XRD was used to determine the crystalline structures of the pigment components. Raman Spectroscopy was used to determine the compounds in the pigments. The resulting Raman peaks were cross-matched with online databases such as the Cultural Heritage Science Open Source

website.

When placing the samples on stubs, the green sample was initially placed on the carbon black tape so that the sample was centered on the stub. After completing XRF, metals such as aluminum were seen. It was hypothesized that these elements were coming from the stub the sample was placed on. When placing the blue and red pigments on the stubs, the carbon black tape was placed so that half of the tape had contact with the stub, and the other half was hanging off the side of the metal stub. The pigment sample was carefully placed on the tape hanging off the stub to try and eliminate any false readings coming from the metal stub.

3 Results

3.1 Green Pigment

The green pigment was evaluated using Raman, XRF, and XRD. XRF revealed the presence of Cu, Ca, Fe, Si, Pb, As, S, K, P, Al, and Mn. The detection of aluminum and manganese can most likely be attributed to the stub that the sample was resting on. The presence of arsenic and sulfur suggest an arsenic sulfide pigment, such as orpiment (As_2S_3) . Calcium can be attributed to the presence of calcite ($CaCO_3$) , and the lead can be attributed to a lead pigment such as lead white ($PbCO_3)_2 \cdot Pb(OH)_2$) or litharge (PbO) . The presence of silicon in XRF suggests the presence of quartz (SiO_2). The presence of copper, potassium, and phosphorus are unattributed at this time. These were not present in high quantities and could possibly be trace elements.

X-Ray Diffraction (XRD) revealed graphite, calcite, and quartz. Calcite and quartz could have possibly been used as a white pigment, or could be residual from the mineral that orpiment was obtained from. Graphite could have been from a chalk outline. Oftentimes, artists used graphite carbon to roughly outline the design before painting.

One peak in particular was difficult to identify on XRD. At 26.64°, a reflection peak was observed. This peak could either be attributed to the presence of graphite or quartz. A definitive conclusion was not reached. This graph is shown below in Figure 2.

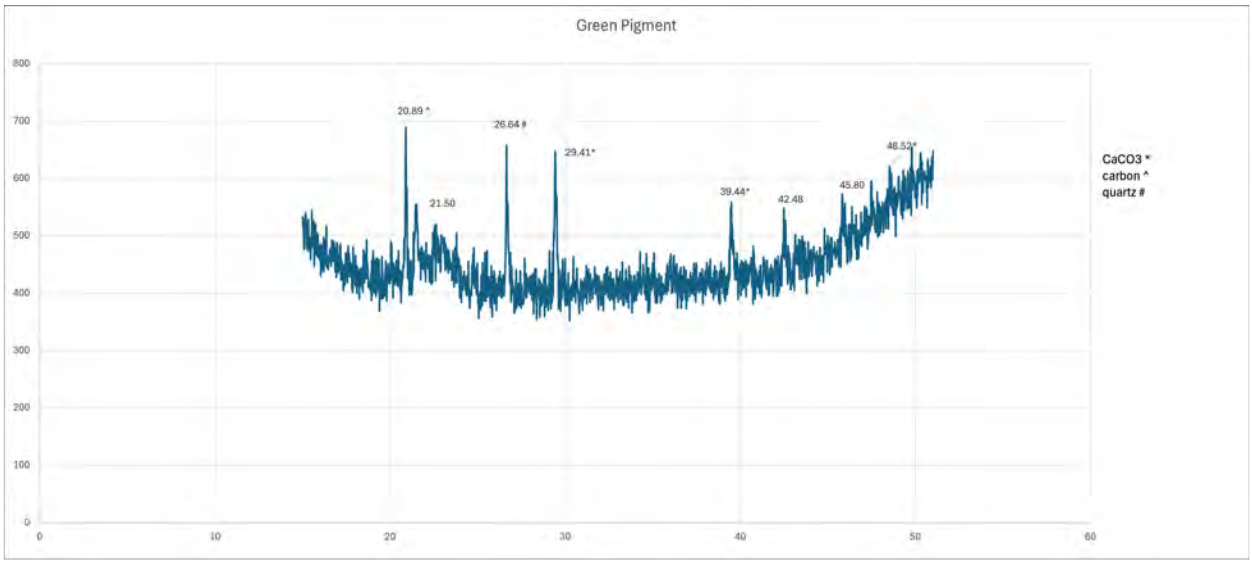

Figure 2: XRD Result for Green Pigment

Raman Spectroscopy revealed the presence of orpiment, litharge, carbon graphite, and calcite. Orpiment was most likely used as a yellow mixed with an unidentified blue pigment. Litharge is another possible yellow used in the mixture. Raman Spectroscopy peaks were difficult to find and identify, since the organic pigment produced high amounts of background fluorescence.

3.2 Blue Pigment

XRF revealed the elements Si, P, Pb, K, Ca, Mn, and Fe. The finding of silicon suggests the presence of quartz (SiO_2) in the pigment. The presence of lead suggests the presence of litharge or white lead. The finding of calcium suggests the presence of calcite. The presence of iron in XRF suggests that Prussian Blue may be the compound used for the blue. The values for phosphorous, manganese, and potassium were extremely small, which suggests these are trace amounts from the minerals used to create the pigments.

XRD on the blue pigment revealed cerussite ($PbCO_3$), quartz , and calcite ($CaCO_3$) . Cerussite can most likely be attributed to the decomposition of white lead ($(PbCO_3)_2 \cdot Pb(OH)_2$) [6].

Calcite and quartz could possibly have been used as a white pigment. Quartz could also be attributed to the methodology of attaining pigments. Many of these pigments are obtained from

natural minerals, such as the derivation of white lead from the mineral cerussite [6]. This methodology could result in the presence of quartz in the pigment. The exact reason for calcite and quartz is an ongoing investigation.

Raman Spectroscopy revealed Prussian Blue ($C_{18}Fe_7N_{18}$). The results from Raman Spectroscopy are still being analyzed.

3.3 Red Pigment 1

XRF revealed that this pigment contains Al, Si, P, Hg, S, K, Ca, Mn, Fe, and Pb. The detection of mercury and sulfur suggests the presence of vermilion (HgS). Silicon suggests the presence of quartz (SiO_2).

The XRF results demonstrated a significant iron percentage in the red pigment. The origin of this iron is still unknown, but it could possibly be ascribed to an iron oxide pigment. Hematite (Fe_2O_3) was an iron oxide commonly used in paint pigments from the 17th century [2]. This source also demonstrates that hematite was commonly used among Spanish-American painters. The XRF results demonstrating the presence of iron is shown in Figure 3.

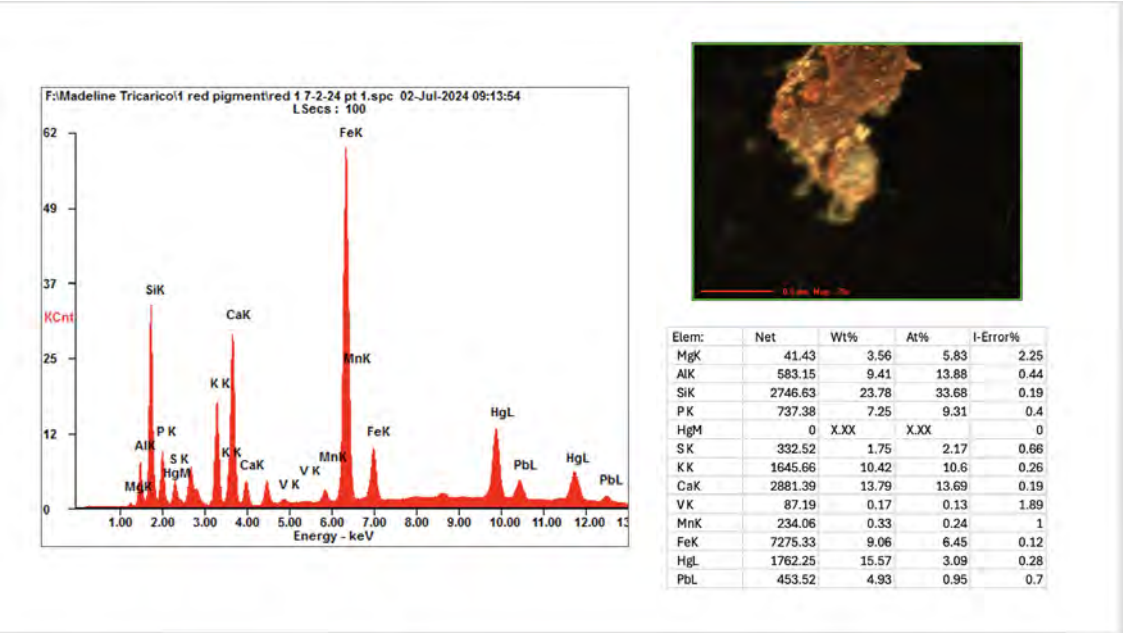

Elem:	Net	Wt%	At%	I-Error%
MgK	41.43	3.56	5.83	2.25
AlK	583.15	9.41	13.88	0.44
SiK	2746.63	23.78	33.68	0.19
PK	737.38	7.25	9.31	0.4
HgM	0	X.XX	X.XX	0
SK	332.52	1.75	2.17	0.66
KK	1645.66	10.42	10.6	0.26
CaK	2881.39	13.79	13.69	0.19
VK	87.19	0.17	0.13	1.89
MnK	234.06	0.33	0.24	1
FeK	7275.33	9.06	6.45	0.12
HgL	1762.25	15.57	3.09	0.28
PbL	453.52	4.93	0.95	0.7

Figure 3: XRF Results from Red Pigment 1

This graph demonstrates that iron is found in high quantities in this red pigment. Furthermore, this graph shows that silicon and calcium are both present in high concentrations, which possibly suggests that quartz and calcite were used in a white pigment instead of simply present in trace amounts.

The area scanned by XRF is shown in the upper right image. As can be seen, this area is a darker color than the rest of the sample, which primarily shows a presence of vermilion. This suggests a secondary pigment utilized to create the red in *Our Lady of Vizcaia.*

As is shown by the data, there is a high percentage of iron with a relatively low percent error. This supports the conclusion that XRF shows iron contained within the red pigment. As previously stated, silicon and calcium are both present in high amounts, while the amounts of mercury and sulfur are relatively low in this area when compared to the rest of the sample. The rest of the elements are present in low concentrations, suggesting trace amounts. The other elements shown in this table (V, Mg) have a high error percentage and are not definitively in the pigment.

XRD revealed the presence of vermilion and quartz in the first red pigment, taken from the left corner of the painting.

Raman Spectroscopy supported the vermilion finding from XRD. These graphs are still in the process of being analyzed.

3.4 Red Pigment 2

XRF revealed that this pigment contains Al, Si, P, Hg, S, K, Ca, Fe, Pb and Mg. The presence of silicon suggests the presence of quartz (SiO_2), and the presence of mercury and sulfur suggest that vermilion (HgS) was used for the red pigment. The finding of calcium suggests the presence of calcite ($CaCO_3$) in the pigment. The presence of lead suggests white lead ($PbCO_3)_2 \cdot Pb(OH)_2$) or litharge (PbO) in the pigment, which Raman spectroscopy may confirm. The presence of magnesium, aluminum, phosphorous, and potassium are most likely trace elements from how the minerals were obtained in order to create the pigments. The quantity of iron is much less in this pigment, yet still worth mentioning. A representative XRF graph can be seen below in Figure 4, along with

the image of the area scanned and a data table.

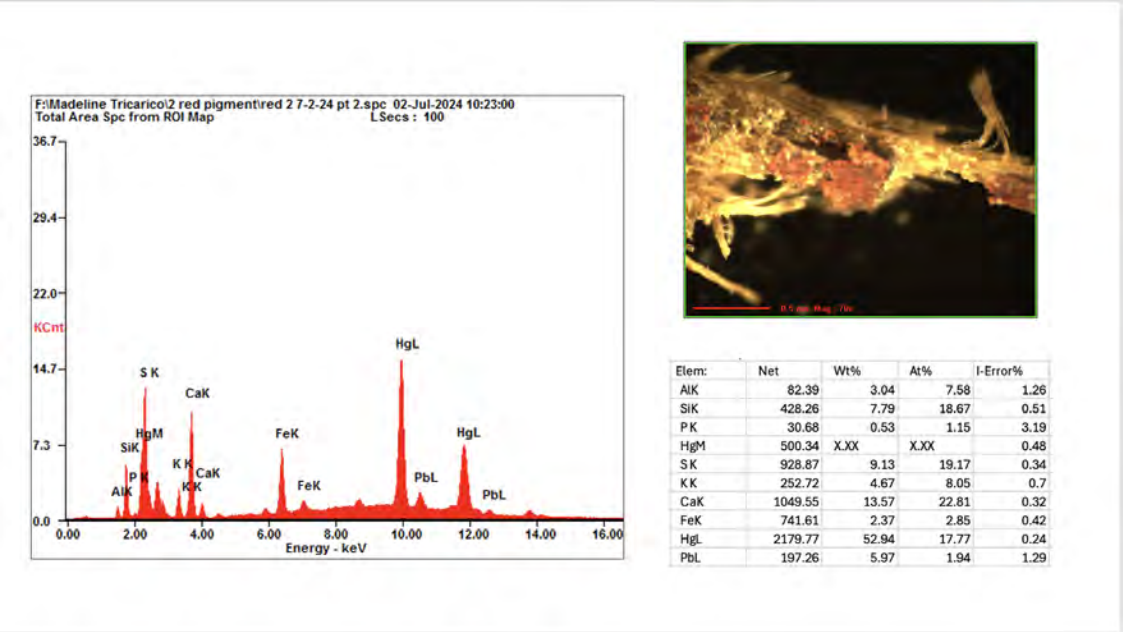

Elem:	Net	Wt%	At%	I-Error%
AlK	82.39	3.04	7.58	1.26
SiK	428.26	7.79	18.67	0.51
P K	30.68	0.53	1.15	3.19
HgM	500.34	X.XX	X.XX	0.48
S K	928.87	9.13	19.17	0.34
K K	252.72	4.67	8.05	0.7
CaK	1049.55	13.57	22.81	0.32
FeK	741.61	2.37	2.85	0.42
HgL	2179.77	52.94	17.77	0.24
PbL	197.26	5.97	1.94	1.29

Figure 4: XRF Results from Red Pigment 2

This graph shows a much higher concentration of mercury and sulfur when compared to the other elements present in this area. The concentration of iron is much lower in Figure 4 than in Figure 3. As can be seen in the image, this area is a red area with slight color imperfections. This suggests that there will be a higher concentration of vermilion, which is supported by the XRF data gathered.

As shown in the table, there are minimal amounts of iron within this pigment, especially when the atomic percentage in red pigment 2 are compared to the atomic percentage in red pigment 1. This again suggests the possibility of some sort of iron oxide pigment which is present in a lesser quantity in red pigment 2. The quantity of silicon and calcium are relatively high, which suggests the use of quartz and calcite as a pigment. Even so, it can clearly be seen that the concentrations of mercury and sulfur are higher in Table 2 than Table 1, which suggests that there is more vermilion present than other possible pigments.

XRD revealed vermilion, quartz , and calcite in the second red pigment, which was taken from the top right-hand side of the painting.

Raman Spectroscopy reaffirmed the presence of vermilion in this pigment. These results are still being analyzed.

4 Conclusion

This research is part of an ongoing study to uncover the chemical composition of the paint pigments used in *Our Lady of Vizcaia*. The methods used to uncover the chemical composition of the paint pigments were Raman Spectroscopy, XRD, and XRF.

The green pigment contains orpiment, litharge, quartz, graphite, and calcite. The blue pigment contains cerussite (possibly derived from decomposed lead white), litharge, quartz, Prussian blue, and calcite. The red pigment from the lower corner of the painting, referred to as Red 1, contains vermilion and quartz. The red pigment from the top right of the painting, referred to as Red 2, contains vermilion, quartz, and calcite.

Being able to identify the pigments used in *Our Lady of Vizcaia* aids art conservation efforts and helps restoration and preservation efforts being done in the Raclin-Murphy Museum of Art.

References

[1] Editors of Encyclopedia Britannica, Encyclopedia Britannica (2014).

[2] A. Seldez, J. E. Burucua, G. Siracusano, M. S. Maier, and G. E. Abad, Journal of the American Institute for Conservation **41**, 225 (2002).

[3] authors of Bruker.com, Bruker (2023).

[4] authors of chem.LibreTexts.org, Chemistry LibreTexts (2019).

[5] authors of Horiba.com, HORIBA Scientific .

[6] G. O'Hanlon, Natural Pigments (2013).

Calibration of HECTOR for Precision Cross-Section Measurements in Stellar Nucleosynthesis

COTY WALTERS

2024 NSF/REU Program
Department of Physics and Astronomy
University of Notre Dame

ADVISOR(S): Prof. Anna Simon-Robertson

Abstract

Accurate cross-section measurements are essential for improving stellar nucleosynthesis models and understanding the formation of nuclides. This paper discusses the calibration of the 4π γ-summing array HECTOR for these measurements. While the calibration is complete, it will be further improved for higher energies using the FN Tandem accelerator in September.

1 Introduction

Our understanding of the elemental abundances in and beyond our solar system depends on the complex models put forth by experts in the field of nuclear astrophysics. If the models of nuclei formation are incorrect or even slightly inaccurate, the assumptions about how certain isotopes are created could prove false. The 118 known elements expand into over five thousand distinct kinds of atoms, each with a unique number of protons and neutrons, known as nuclides. The origins of most of these nuclides remain uncertain. To understand the birthplace of so many special nuclei, physicists rely on cross-section measurements, which represent the probability of a nuclear reaction occurring. The most elusive group of nuclides, and the focus of the HECTOR project, are the p-nuclides, which are unique in that they are synthesized exclusively from seed isotopes that are heavier than the p-nuclide itself.

This group of stable nuclides, ranging from ^{74}Se to ^{196}Hg, are known as p-nuclides and have a higher proton-to-neutron ratio compared to other isotopes of the same element. The process accredited to the production of the p-nuclides is known as the p-process. The p-process occurs during stellar explosions with an associated rapid expansion and cooling of material [1]. The current accepted theory is that the p-process occurs in core-collapse supernovae when a shockwave passes through the oxygen-neon-rich layer of a massive star. Other sites that have been predicted to house the production of p-nuclides include supernovae of type Ia, Ib/Ic.

The production of p-nuclei is influenced by four main factors: temperature distribution, expansion time scales, the abundances of seed nuclei, and the hydrodynamic conditions of the explosion. P-nuclides are synthesized in stellar zones with specific peak temperatures. For nuclides with $A \leq 92$, the peak temperature is ≥ 3 GK. Those with $A \approx 92 - 144$ form at temperatures between

2.7 and 3.0 GK, while nuclides with $A \geq 144$ are produced at temperatures ≤ 2.5 GK. Generally, lighter nuclides are produced at higher temperatures.

Approximately 60% of the p-nuclides' abundances can be reproduced within a factor of three of their solar system values. However, there are significant discrepancies, particularly in the underproduction of certain light p-nuclides such as ^{92}Mo, ^{94}Mo, ^{96}Ru, and ^{98}Ru. Furthermore, the odd-A nuclides, including ^{113}Sn and ^{115}Sn, as well as the odd-odd species like ^{138}La, show significant deviations from expected abundances.

One of the goals of nuclear physicists is to enhance current nuclei formation models and provide experimentally validated cross-section measurements for the rare nuclides. Physicists aim to model different astrophysical environments to pinpoint the creation of these uncommon nuclei. At the University of Notre Dame, the 4π γ-summing array HECTOR, in conjunction with the FN Tandem accelerator, is used to measure and refine these cross-section data. HECTOR was last calibrated a few years ago when it used a different data acquisition system and since its recent update it has not been recalibrated. The rest of this paper covers the method used for the current calibration of HECTOR.

2 Background

The High Efficiency TOtal Absorption SpectrometeR (HECTOR) utilizes near 4π solid angle coverage to measure (p,γ) and (α,γ) reaction cross sections. Designed at the University of Notre Dame, HECTOR is composed of an array of sixteen 4"×8"×8" segments of NaI(Tl) crystals, each encased in 1mm thick aluminum. Manufactured by Saint-Gobain Crystals, each segment contains two 3" diameter 10-stage photomultiplier tubes (PMTs) that process the scintillation light from incoming radiation and send the output signal to the NSCL Digital Data Acquisition System (DDAS) [2]. HECTOR is cube-shaped and consists of sixteen segments, each with two photomultiplier tubes. These PMTs extend from both the top and bottom of the spectrometer. The top PMTs are labeled with a zero, while the bottom PMTs are labeled with a one. Each PMT is also assigned a second number from 0 to 7 to indicate its specific segment. Additionally, each PMT receives a final identi-

fier, either a 0 or a 1, to uniquely distinguish each PMT within a segment. Additionally, HECTOR is designed with a 60mm diameter bore hole through its central axis, allowing for target placement within the segmented array without compromising the 4π solid angle coverage. Figure 1 illustrates the labeling convention for HECTOR.

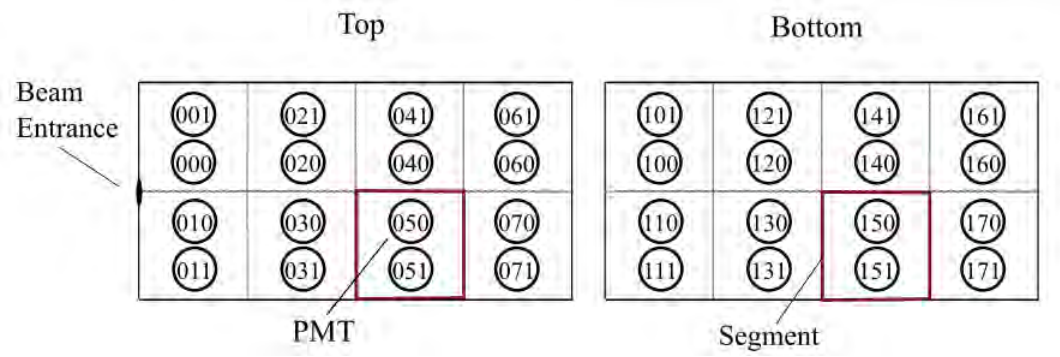

Figure 1: Diagram of HECTOR's PMT labeling convention. The top PMTs are labeled with a zero, the bottom PMTs with a one, and each PMT is assigned additional numbers to indicate its specific segment and unique identifier within the segment.

HECTOR utilizes the γ-summing technique for cross-section measurements. Following a particle capture, the resulting residual nucleus is excited with an energy $E_\Sigma = E_{\text{cm}} + Q$, where E_{cm} is the center-of-mass energy and Q is the reaction Q-value. The nucleus rapidly decays, emitting one or more γ-rays as it transitions to its ground state. Instead of analyzing each γ-ray individually, HECTOR simultaneously detects and accumulates the energies of all emitted γ-rays, resulting in a single peak known as the sum peak at E_Σ [3].

3 Methods

HECTOR's calibration process starts with a gain-matching procedure. This step ensures that each PMT produces consistent outputs for equivalent amounts of energy deposited in the crystal. Since this part of the calibration was completed before my arrival at Notre Dame, I will not delve into the specifics of this process.

Once all 32 PMTs have been individually gain matched, the energy of each pair of PMTs in a segment is added together. To ensure a high resolution of the spectrum, the data from individual

segments is calibrated before the measured signals are added together. This is completed using the known γ-ray energies from various calibrated sources. During the current calibration of HECTOR, we used a ^{60}Co source and the ^{208}Tl line in the room background, as well as the ^{19}F(p,$\alpha\gamma$)^{16}O reaction.

To begin the calibration process, an eight-hour background run is conducted and then scaled down to an appropriate length for subtraction from future runs. This extended trial helps establish baseline levels of background radiation, which is important for distinguishing between background noise and the actual signal from target radiation sources. Because background radiation can vary due to environmental factors like cosmic rays or nearby radioactive materials found in building materials, a long trial helps identify and account for these variations [4]. Figure 2 shows the spectrum of background radiation when HECTOR is used above ground on the Notre Dame campus.

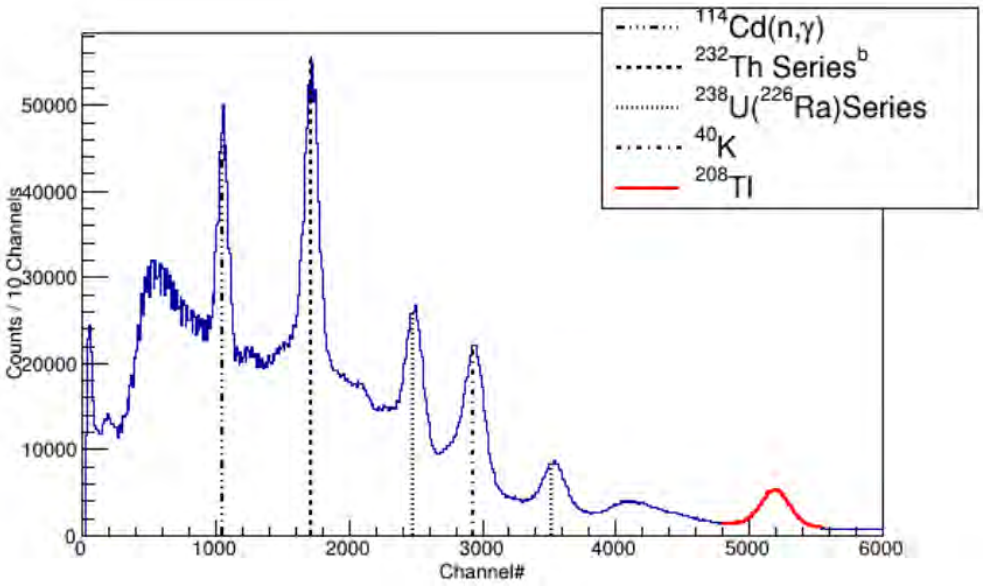

Figure 2: Background radiation levels from various sources detected in the absence of an active source. Includes a calibration fit for 208Tl.

After accounting for the background radiation, a ^{60}Co source is positioned at the center of HECTOR for a seven-minute run. HECTOR's 4π coverage allows a seven-minute run to collect sufficient data, ensuring low uncertainties and reliable statistics. The next step involves subtracting the scaled background counts and analyzing the ^{60}Co data. Using ROOT software, a widely used tool

for analyzing large data sets, we create a histogram of the data. We then fit the mean of the peaks for the known 1173-keV and 1332-keV γ-rays from the decay of ^{60}Co. The uncertainty of the mean channel number is determined by Root. For this fitting, a combination of a Gaussian and a linear function is used for each peak. By combining the Gaussian function with a linear function, one can effectively model both the sharp peaks of interest (the signal) and the underlying continuous background. Fitting the peaks with this method allows for the identification of the channel number that corresponds to the mean of the individual peaks. Figure 3 provides an example of the fitting procedure for segment 02.

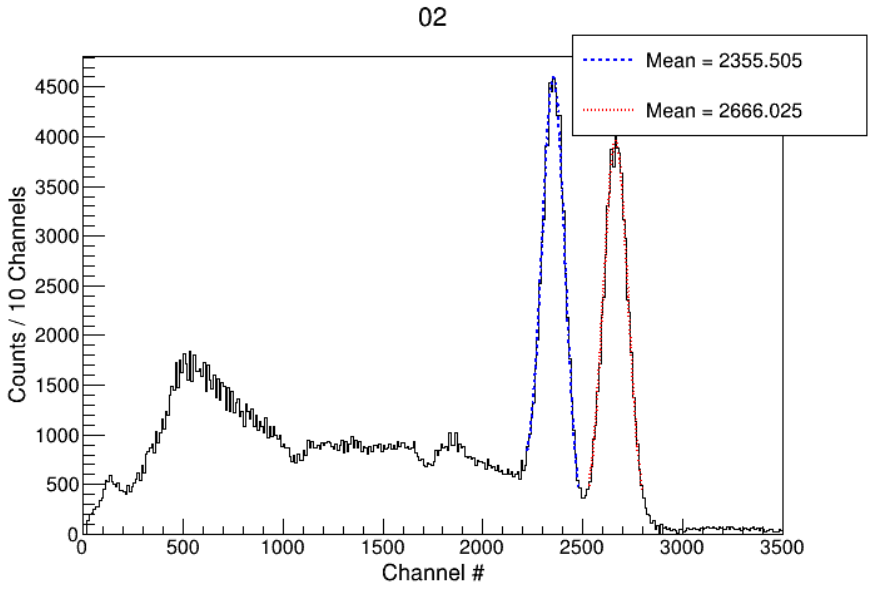

Figure 3: Peak fittings in segment 02 during the ^{60}Co calibration, where each bin represents 10 channel numbers. Fits 1 and 2 correspond to the emissions of the 1173-keV and 1332-keV γ-rays from the ^{60}Co source, respectively.

This procedure is repeated for all sixteen segments, with the peak means and their uncertainties recorded for use in later stages of the calibration process. Table 1 presents an example of the recorded peak means for all sixteen segments using the ^{60}Co source.

For calibration at a higher energy range, we utilize the natural ^{208}Tl peak observed in a prolonged background run. Figure 2 shows an example fit for thallium's signature 2614 keV γ-ray peak around channel # 5150. Recall that the individual PMTs for a segment are summed together for improved summing efficiency. Similarly, the mean for the peaks of each segment are recorded for use later in

Table 1: Parameters used for the energy calibration for all 16 segments.

Detector: HECTOR, Source: ^{60}Co		
Seg[ ][ ]	γ-1173 Peak	γ-1332 Peak
[0][0]	2346.68 ± 4.00	2659.71 ± 5.67
[0][1]	2350.31 ± 1.68	2591.40 ± 10.02
[0][2]	2355.13 ± 0.48	2666.00 ± 0.62
[0][3]	2352.09 ± 0.44	2660.39 ± 0.58
[0][4]	2357.11 ± 0.44	2667.24 ± 0.59
[0][5]	2351.02 ± 0.57	2665.31 ± 0.81
[0][6]	2346.89 ± 0.95	2656.15 ± 1.09
[0][7]	2341.49 ± 1.44	2648.26 ± 1.96
[1][0]	2345.30 ± 2.29	2650.57 ± 3.23
[1][1]	2350.92 ± 2.20	2662.26 ± 3.04
[1][2]	2348.75 ± 0.46	2658.75 ± 0.46
[1][3]	2349.08 ± 0.95	2602.74 ± 1.11
[1][4]	2358.15 ± 0.45	2670.20 ± 0.51
[1][5]	2353.06 ± 0.32	2663.38 ± 0.36
[1][6]	2343.30 ± 2.34	2658.54 ± 2.51
[1][7]	2347.91 ± 1.64	2665.34 ± 1.83

the calibration process.

Calibrating HECTOR for higher energy levels is important, and for this purpose, we utilize an unexpected contaminant. To perform a cross-section measurement, a natural tin target with a gold backing is placed inside HECTOR and positioned in the beam line of the FN Tandem accelerator. As protons are accelerated towards the target, some collide with the natural tin, while others hit the gold, inducing nuclear reactions. Interestingly, the ^{19}F used by the target material manufacturers to clean the samples leaves enough residue that we can use it as a reaction for calibration. When this fluorine contamination is struck by sufficiently energetic protons, it undergoes alpha decay, resulting in ^{16}O nuclei. These oxygen nuclei are produced in an excited state and emit a distinctive 6129-keV γ-ray upon de-excitation. This peak is then fitted using the same method as previously described, and the mean values are recorded. Further calibration at even higher energies requires additional beam time and hence will be the focus of runs conducted in September.

The final step in the calibration process is to plot the known γ-ray emissions from each source against the channel numbers corresponding to the peak means. This data is then fitted using a

second-order polynomial to correct for slight non-linearities observed for γ-ray energies above 10 MeV. for Figure 4 illustrates an example of an energy calibration curve for segment 02 with a second-order polynomial fit. This calibration is performed for all sixteen segments, not just one. Table 2 provides the parameters used for all sixteen segments.

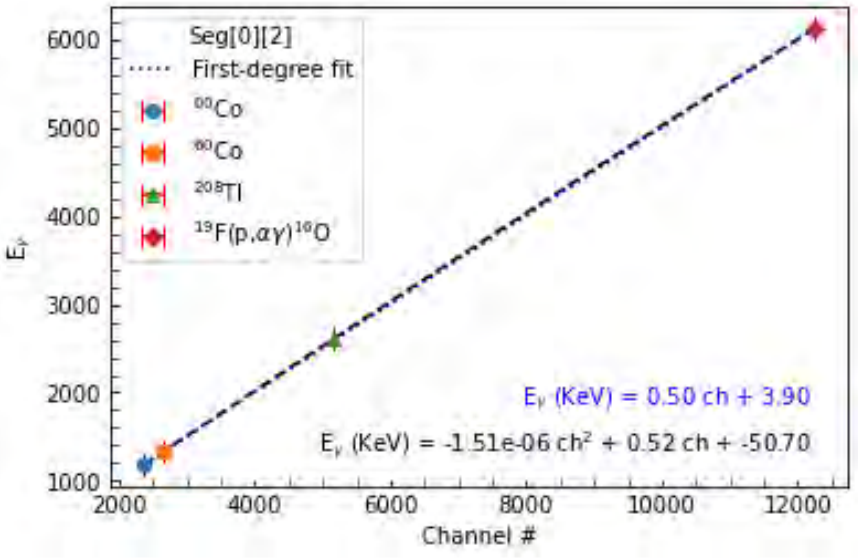

Figure 4: An energy calibration for segment 02 using a first and second-order polynomial.

4 Results

To confirm the accurate calibration of HECTOR, we examine data from a 20-minute run in which a natural tin ^{112}Sn target was positioned inside HECTOR and exposed to a 4 MeV beam from the FN Tandem accelerator. The natural tin target contains trace amounts of various tin isotopes, each of which can undergo proton capture to transform into different antimony isotopes, producing a distinctive sum peak. Figure 5 displays the sum peaks obtained from the natural tin target.

Using the equation $E_\Sigma = E_{\text{cm}} + Q$, we determine the theoretical sum peaks for various reactions. For the ^{19}F$(p, \alpha)^{16}$O reaction, gamma rays are expected to be emitted at two energies: 7116 and 6129 keV. Additionally, the theoretical sum peaks for other reactions are ^{118}Sn$(p, \gamma)^{119}$Sb at 9112 keV, ^{116}Sn$(p, \gamma)^{117}$Sb at 8403 keV, and ^{120}Sn$(p, \gamma)^{121}$Sb at 9790 keV. Comparing the experimental sum peaks, which have an uncertainty of either half the bin width or $\pm$ 5 keV, reveals a slight discrepancy

Table 2: Mean values for the individual peak fits obtained from the ^{60}Co data across all segments.

Fit parameters:	$E_\gamma = \mathbf{a}\cdot ch^2 + \mathbf{b}\cdot ch + \mathbf{c}$		
Seg[ ][ ]	Quadratic	Linear	Constant
[0][0]	-4.43×10^{-6}	0.55	-86.61
[0][1]	-9.88×10^{-7}	0.51	-09.01
[0][2]	-1.51×10^{-6}	0.52	-50.70
[0][3]	-1.49×10^{-6}	0.53	-58.58
[0][4]	-1.02×10^{-6}	0.52	-50.37
[0][5]	-2.71×10^{-6}	0.53	-70.39
[0][6]	-7.56×10^{-7}	0.52	-38.88
[0][7]	-1.38×10^{-6}	0.52	-46.10
[1][0]	-9.60×10^{-7}	0.52	-28.74
[1][1]	-1.51×10^{-6}	0.53	-56.08
[1][2]	-1.68×10^{-6}	0.53	-64.54
[1][3]	-5.19×10^{-7}	0.51	-03.73
[1][4]	-1.28×10^{-6}	0.52	-39.13
[1][5]	-1.58×10^{-6}	0.53	-56.87
[1][6]	-9.57×10^{-7}	0.52	-51.74
[1][7]	-1.82×10^{-6}	0.53	-73.90

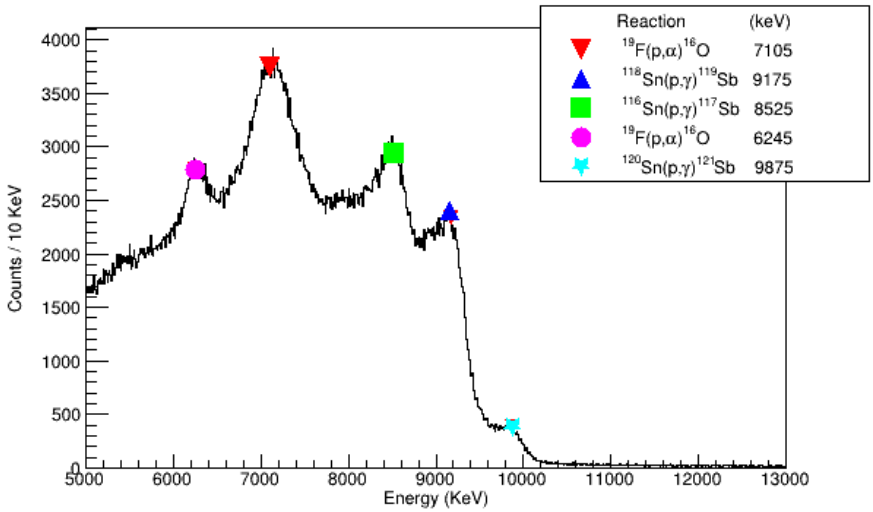

Figure 5: Sum peaks for different isotopes of tin and fluorine transitioning to their ground states.

with the theoretical values. This offset may be attributed to the fact that the location of the sum peaks were found using TSpectrum which extracts the bin with the most amount of data instead of fitting the peaks individually with a Gaussian. It should be noted, though, that a small offset in a

sum-peak position in the spectrum at such high energies does not impact the correct identification of the sum peak of interest. During the measurement an enriched target is usually used and and no beam induced background is present in the region, thus the sum peak can be easily idenitified.

5 Conclusion

In this paper, we discussed the calibration process for the 4π γ-summing array HECTOR and its role in improving cross-section measurements for stellar nucleosynthesis models. The calibration, performed using ^{60}Co, ^{208}Tl, and ^{19}F sources, effectively aligns the detector's response with known γ-ray energies, improving its precision for measuring sum peaks. Our results indicate that while the current calibration provides reliable data, there remains a slight discrepancy between experimental and theoretical sum peaks. This minor offset is likely due to the need for calibration at higher energies, which is the focus of upcoming runs using the FN Tandem accelerator in September. The anticipated additional γ-ray data from these runs will directly impact the accuracy of the sum peak measurements, enabling more precise cross-section determinations. Future work will focus on incorporating the new calibration data to resolve the observed discrepancies in the sum-peak position at high energies.

References

[1] C. Iliadis, *Nuclear physics of stars* (John Wiley & Sons, 2015).

[2] O. Olivas-Gomez, *Constraining the γ-Process Using HECTOR* (University of Notre Dame, 2022).

[3] O. Olivas-Gomez, A. Simon, D. Robertson, A. Dombos, F. Strieder, T. Kadlecek, M. Hanhardt, R. Kelmar, M. Couder, J. Görres, *et al.*, The European Physical Journal A **58**, 57 (2022).

[4] G. Gilmore, *Practical gamma-ray spectroscopy* (John Wiley & Sons, 2008).

Implementation of STM-VM Synchronizer Based on TCP communication

YIHANG WANG

2024 NSF/REU Program
Department of Physics and Astronomy
University of Notre Dame

ADVISOR(S): Prof. Xiaolong Liu

Abstract

This paper presents the implementation of a Scanning Tunneling Microscope-Vector Magnet (STM-VM) Synchronizer based on TCP communication, aimed at automating long-period joint experiments. The developed synchronizer, SVS, allows for coordination between the STM and VM systems, facilitating the detailed mapping of electronic states and superconducting properties of materials. The system was tested for stability under various conditions, demonstrating its efficacy in real experiments. Additionally, a set of spectral data acquired by SVS was visualized and found to be reasonable, validating the system's performance.

1 Introduction

Scanning Tunneling Microscopy (STM) is a powerful tool in the field of surface science, allowing researchers to visualize surfaces at the atomic level. Building upon the capabilities of STM, Scanning Tunneling Spectroscopy (STS) extends the functionality of this technique. By varying the bias voltage between the STM tip and the sample, the differential conductance dI/dV as a function of voltage V can be measured. This allows for the mapping of the local density of states (LDOS) of the material[1], providing detailed insights into its electronic structure.

Josephson Junction (JJ) is a fundamental element in the field of superconductivity, consisting of two superconductors separated by a thin insulating barrier. This configuration allows for the tunneling[2][3], where Cooper pairs can pass through the insulator, and the tunnelling current varies when different bias voltages are applied on the junction.

Quantum interference in JJ arises from the fluxoid quantization and the gauge-invariant superconducting phase difference ϕ across it. The interference of the superconducting wave functions in the junction leads to oscillations in the critical current I_J with applied magnetic flux Φ, resulting in the $I_J - \Phi$ Fraunhofer pattern[3][4][5].

One significant advantage of STS is its sufficient resolution both in location and bias voltage, making it possible to achieve imaging of various physical quantities[6]. To gain insight into quantum characteristics of superconducting materials, a JJ in STM can be constructed with a superconducting tip and sample, separated by an ultra-high vacuum insulating layer. By introducing a vector magnet (VM) into this system and enabling cooperative operation with the STM, we can achieve

detailed mappings of several values, including LDOS and cooper pair fluid flow in response to the field in a vortex within the sample[6]. Additionally, this setup allows visualization of the 2D $I_J - \Phi_{(x,y)}$ Fraunhofer pattern at different positions on the sample, which hasn't ever been achieved.

2 Methods

2.1 TCP Connection

The Transmission Control Protocol (TCP) is a basic standard that defines the rules of the internet that is widely-used for transmitting data over networks. It relies on a three-way handshake as shown in figure 1 to carry packets across the Internet, ensuring the successful delivery of messages.

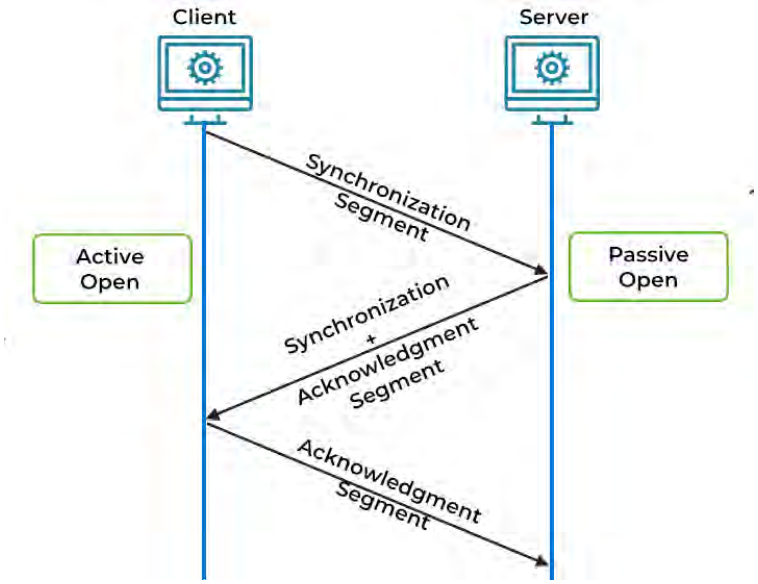

Figure 1: Functioning of transmission control protocol

STM-VM Synchronizer (SVS) acts as the client, sending commands to and receiving messages from the STM server and VM server. These two servers accept different message structures through TCP communication, with the STM server specifying the command length in advance and the VM server adding terminators at the end.

2.2 Program Structure

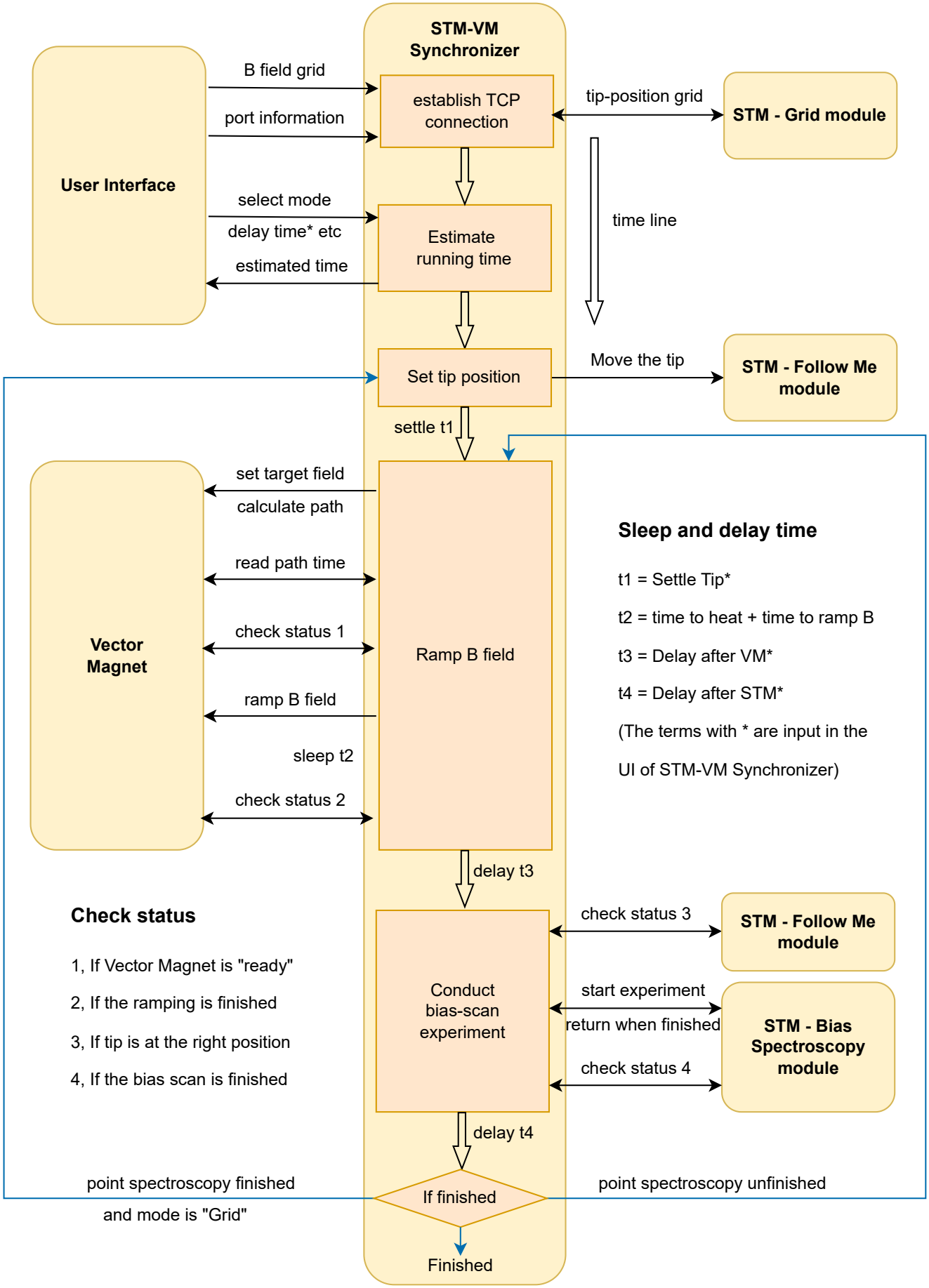
STM-VM Synchronizer
User Interface
B field grid
port information
select mode
delay time* etc
estimated time
establish TCP connection
tip-position grid
STM - Grid module
time line
Estimate running time
Set tip position
Move the tip
STM - Follow Me module
settle t1
Vector Magnet
set target field
calculate path
read path time
check status 1
ramp B field
sleep t2
check status 2
Ramp B field
Sleep and delay time
t1 = Settle Tip*
t2 = time to heat + time to ramp B
t3 = Delay after VM*
t4 = Delay after STM*
(The terms with * are input in the UI of STM-VM Synchronizer)
delay t3
Check status
1, If Vector Magnet is "ready"
2, If the ramping is finished
3, If tip is at the right position
4, If the bias scan is finished
check status 3
STM - Follow Me module
Conduct bias-scan experiment
start experiment
return when finished
check status 4
STM - Bias Spectroscopy module
delay t4
point spectroscopy finished
and mode is "Grid"
If finished
point spectroscopy unfinished
Finished

Figure 2: The simplified program diagram here illustrates how the STM-VM Synchronizer (SVS) operates. The yellow boxes represent relevant applications, including the SVS program, VM controller, and various modules of the STM controller (Nanonis software). The orange boxes and bold arrows within the SVS box display the global running sequence of SVS. One-way arrows indicate immediate one-way signals regardless of responses, while double-sided arrows indicate communications between different software that last for a period of time. SVS offers two scan modes: "Grid" mode and "Point" mode. In "Grid" mode, the tip position grid (edited in the Pattern-Grid module in STM) is used, while in "Point" mode, the experiment is conducted at the current tip position to obtain point spectroscopy (The aggregation of spectra measured under all specified magnetic fields at one point on sample). In addition, there are two coordinate modes offered for setting the ramping path of magnetic field: Cartesian mode and spherical mode, providing a choice for users to study different characteristics of the sample.

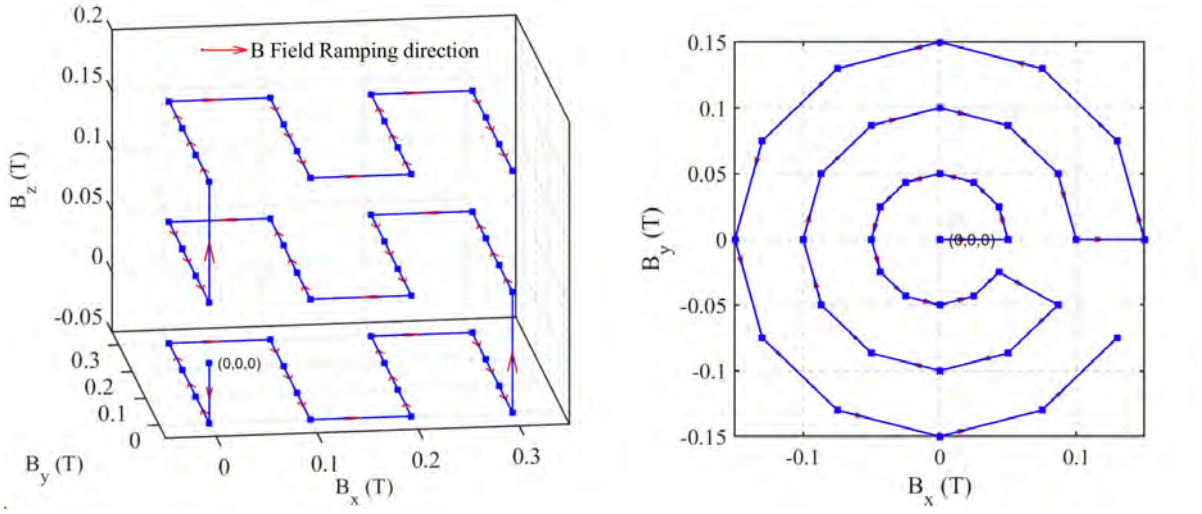

Figure 3: Field ramping paths in Cardesion coordinates and Spherical coordinates

SVS extracts the 3D magnetic field grid (the magnetic field values that will be adopted in the experiment) from its user interface and the 2D tip position grid (the points where the tip will be on the sample to measure bias spectra) from the Grid Module of STM. This determines the sequence of tip

movement and field ramping. To minimize tip drift during measurements at a single position, SVS enables STM to start measuring immediately when the field and sample are ready and optimizes field ramping to save time. SVS checks the statuses of VM and STM to ensure a tight command sequence without unexpected overlaps. Additionally, SVS instructs VM to ramp the field in an "S" pattern step-by-step, as shown in figure 3.

2.3 Pretest Before Experiment

The duration of the experiment can range from minutes to days, depending on the parameters entered. Therefore, a duration estimation module is necessary to ensure the experiment finishes before the liquid helium in STM runs out. In "Grid" mode, SVS provides approximate "Point Time" (the duration to finish a point spectroscopy) and "Total Time" (the time to complete the entire experiment). However, certain time costs, such as status checks and TCP communication delays, are not considered, making exact duration alignment difficult but sufficient for setting expectations.
The pretest module also verifies the experiment can be conducted correctly by checking:

1) Successful establishment of TCP connections and the opening of relevant modules.

2) Reasonableness and range compliance of the entered magnetic field grid.

3) Availability of the save path and absence of disturbing files.

4)] Estimation of approximate "Point Time" and "Total Time."

3 Results

Based on the above methods, a robust program with a clear UI (as shown in 4) has been implemented, featuring three input sections for relevant parameters:

- **Magnetic field Grid:** This section is for entering magnetic field ranges and ramping step lengths in three directions. Negative steps or out-of-range values cause errors in the pretest

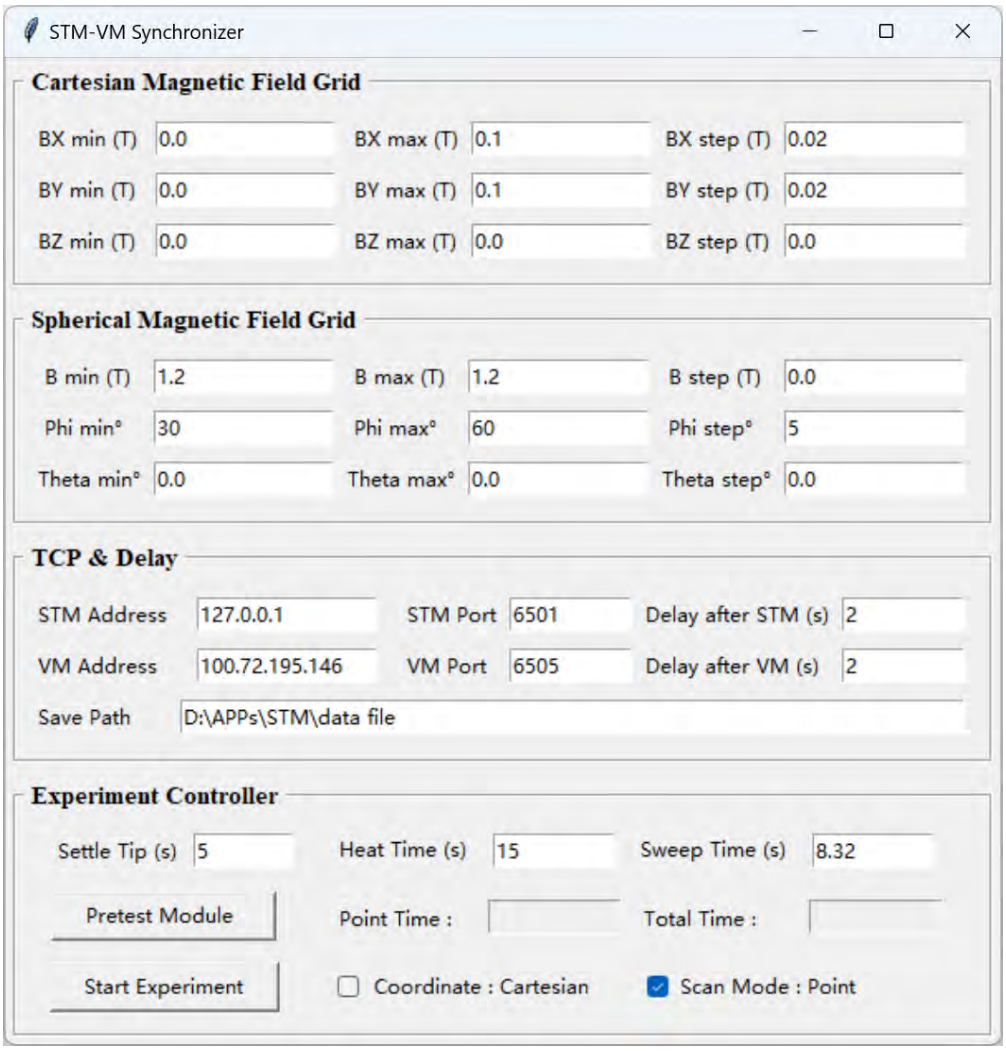

Figure 4: STM-VM Synchronizer user interface

module, preventing the experiment from starting. Also, warnings are issued if ranges and steps do not match so that the field is not able to cover the whole ranges.

- **TCP & Delay**: This section requires the IP addresses and communication ports of VM and STM. Two delay times specify the waiting period after setting the field (Delay after VM) and after measuring the spectrum (Delay after STM). Note that "Delay after VM" always exists, regardless of field changes between sub-experiments. All experiment data are saved in a new folder named after the experiment start time on the "save path", aligned with Nanonis settings.

- **Experiment Controller**: The "Settle Tip" parameter regulates tip settling time once moved. "Heat Time" and "Sweep Time" refer to the approximate durations to heat VM and complete a single spectrum measurement respectively, used only for duration estimation and declining the number of exchange messages to check status.

An " Ongoing activities " window is generated when the experiment starts, displaying ongoing activities. All information in this window and the specified parameters are saved in real-time in a notebook. As for robustness testing, SVS reacts properly to various situations, including unreasonable inputs, program crashes, and heavy CPU loads, demonstrating its stability in real experiments.

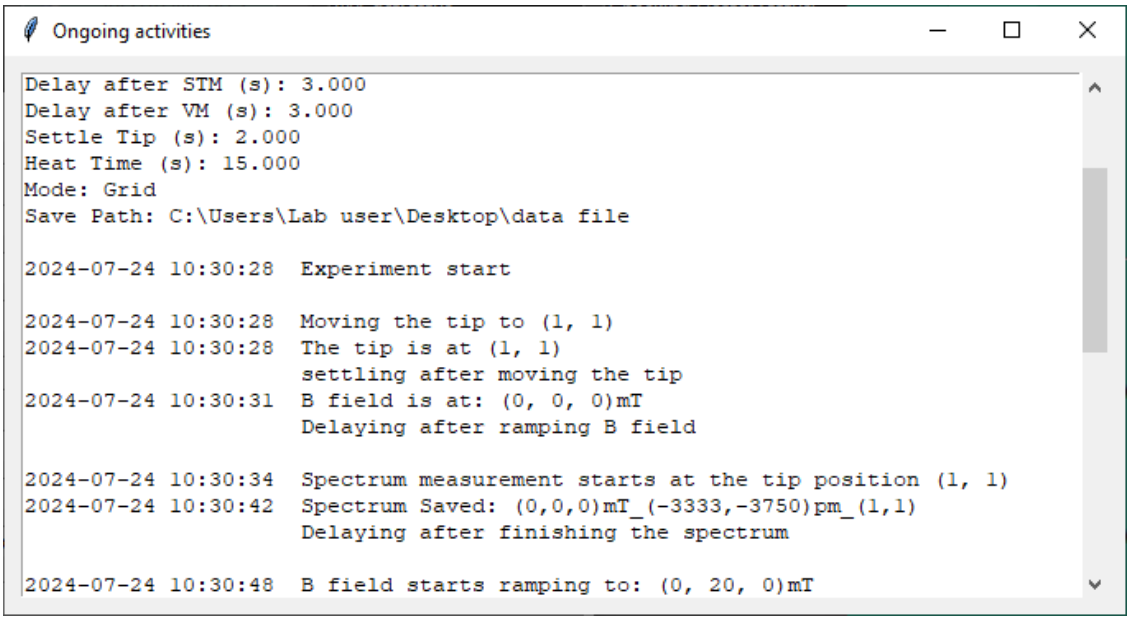

Figure 5: Ongoing activities window

We measured a series of bias spectra at a single sample point under various magnetic fields applied parallel to the tip. As shown in Figure 6a, the peak (with an x-coordinate representing the sum of the niobium tip energy gap Δ_t and the FeSe sample energy gap Δ_s at zero field) splits and the spacing between the split peaks increases as the field ramps up, qualitatively agreeing with the simulated results in reference [6]. By extracting the splitting gaps, we plotted the dependence of the Galilean energy boost δE_k on the magnetic field, as illustrated in Figure 6b. The increasing distance between the tip and the superconducting vortex core caused by the magnetic field likely

contributes to the observed change in δE_k. Although this inference requires further testing through vortex mapping, the current result is reasonable to prove the efficacy of SVS.

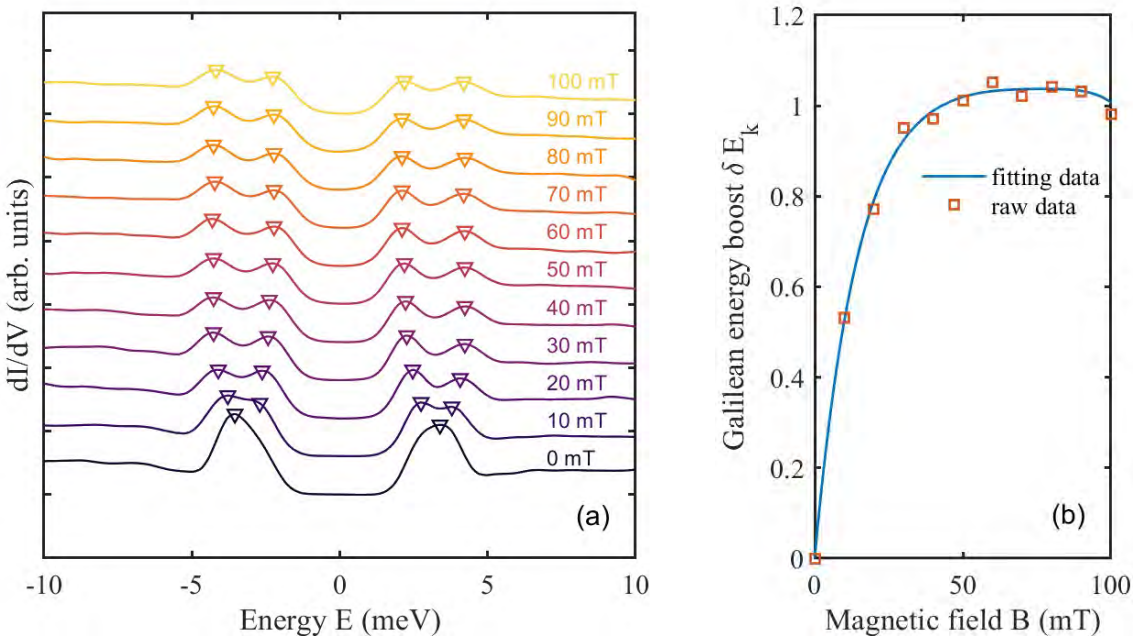

Figure 6: Gaussian filtered differential conuctance dI/dV vs. bias energy E under different field (a); The dependence of Galilean energy boost δE_k to field (b)

4 Conclusion

In this study, we successfully developed and tested an upper computer program, SVS, that enables cooperative operation of STM and VM systems through TCP communication. With SVS, long-period joint experiments can be conducted automatically to obtain high-dimensional data matrices, which is crucial for studying the 2D $I_J - \Phi_{x,y}$ Fraunhofer pattern of specific superconducting samples. Generally, it's also a useful tool to gain insight into the microscopic mechanism of materials.

Future advancements for SVS include adding a visualization tool to help users read and analyze data matrices. Moreover, by inserting additional modules like "spherical field setting" from VM and "Generic Sweeper" from STM, SVS can become a more general tool to conduct a wider range of experiments.

5 Acknowledgements

I would like to thank my advisor, Prof. Xiaolong Liu, for his patience and guidance. I am also grateful to graduate students Nileema Sharma, Matthew Toole, and James McKenzie in the lab for their encouragement and informative instructions.

Special thanks to Dr. Umesh Garg and Kristen Amsler for running the Notre Dame REU program, which provided us with an impressive summer program experience.

References

[1] M. Passoni, F. Donati, A. Li Bassi, C. S. Casari, and C. E. Bottani, Physical Review B—Condensed Matter and Materials Physics **79**, 045404 (2009).

[2] B. D. Josephson, Physics letters **1**, 251 (1962).

[3] R. De Luca *et al.*, Journal of Modern Physics **6**, 526 (2015).

[4] B. Börcsök, S. Komori, A. Buzdin, and J. Robinson, Scientific Reports **9**, 5616 (2019).

[5] C. Baumgartner, L. Fuchs, A. Costa, S. Reinhardt, S. Gronin, G. C. Gardner, T. Lindemann, M. J. Manfra, P. E. Faria Junior, D. Kochan, *et al.*, Nature nanotechnology **17**, 39 (2022).

[6] X. Liu, Y. X. Chong, R. Sharma, and J. S. Davis, Nature Materials **20**, 1480 (2021).

Band Structure Theory of MATBG and Fabrication of Two Dimensional Quantum Devices

ZIHAO WANG

2024 NSF/REU Program
Department of Physics and Astronomy
University of Notre Dame

ADVISOR(S): Prof.Stepanov

Abstract

Since the discovery of graphene, 2D materials have attracted substantial attention due to their unique physical and chemical features as well as their potential device applications. The magic angle twisted bilayer graphene(MATBG) outstands among all the promising stackings of 2D materials due to its high tunability and strongly correlated properties. In this report, the band structure theory of MATBG is reviewed based on Bistritzer and MacDonald's "Dirac Continuum Model". Then the artificial stacking technique also known as the transfer method is exhaustively introduced. In the end, the Resistivity-Voltage relation from the probe of the device made by me shows the unconventional superconductivity of MATBG.

1 Introduction

1.1 Two-dimensional(2D) materials

Among all the models created by condensed matter theory physicists, only a few really exist and can be fabricated so far. One of them is the well-known graphene, which is a layer of carbon atoms constructed in a way like a honeycomb. Since when Andre Geim and Konstantin Novoselov earned the Nobel Prize in Physics in 2010 for their contribution to work on graphene, 2D material has gradually grown into one of the most popular topics in condensed matter experimental physics. Geometrically, 2D materials are a class of materials that are quantum-confined in one dimension. Over the past several years, significant progress has been achieved in this area of 2D materials. At present, various 2D materials have been theoretically predicted and experimentally fabricated, including graphene, hexagonal boron nitride(hBN), and silicene. Moreover, many 2D materials with energy gaps ranging from semimetal to semiconductor, and to insulators are predicted and discovered, which makes 2D materials promising candidates for many potential application fields.

1.2 van der Waals heterostructure

An interface between two layers or regions of dissimilar semiconductors is called heterostructure1(a). High-performance functional devices are mainly based on heterostructures with controlled bandgap and doping profiles, while semiconductor heterostructures are the fundamental building

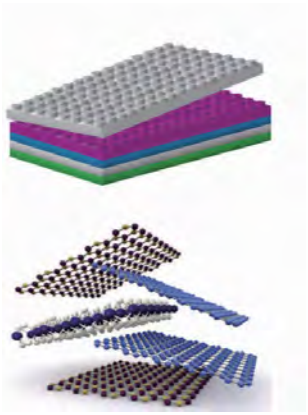

(a) 2D heterostructure

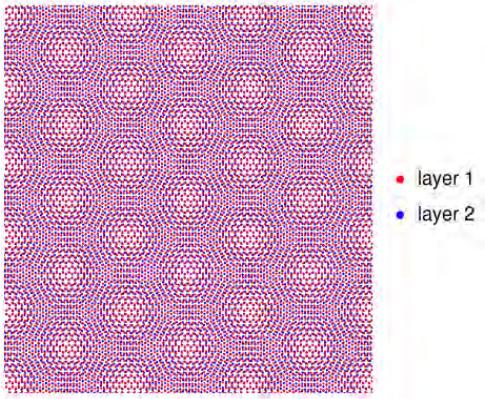

(b) Lattice of graphene

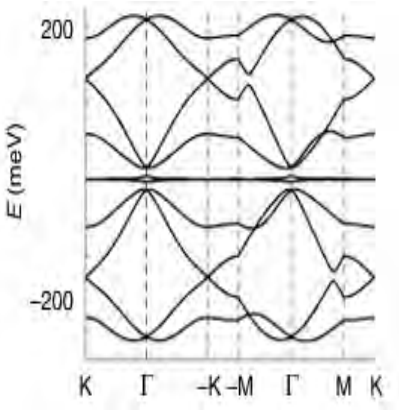

(c) Band structure of MATBG

blocks for modern high-performance electronic devices. But 2D materials with dangling-bond-free surfaces and relatively weak van der Waals(vdW) interactions have much better quality of heterostructure compared with conventional materials and fewer limits of fabrication since strong chemical bonding is replaced by vdW force at the interfaces.

1.3 Magic-angle twisted bilayer graphene

Many novel states and phase transitions can be induced in twisted Van der Waals heterostructures under the conditions of applied electric and magnetic fields, such as the strong correlation effect[1], unconventional superconductivity[2]. For the latter, when two layers of graphene are twisted by a specific angle of about 1.1°(the first 'magic' angle), its electronic band structure forms flat bands near zero Fermi energy and tunable zero-resistance states with a critical temperature of up to 1.7 kelvin are observed.

2 Theory

The dynamic properties of electrons are mostly governed by the band structure of the lattice. For single-layer graphene(SLG), the band structure deduced from the tight-binding model shows a linear dispersion relation near Dirac points. The hypothesis assumes that electrons are hopping between nearest neighbor atoms with a hopping parameter. However, the band structure of TBG

is way more complicated than SLG due to the moiré superlattice and interlayer hopping. Moiré patterns are large-scale interference patterns that can be produced when a partially opaque ruled pattern with transparent gaps is overlaid on another similar pattern1(b). According to Bistritzer and MacDonald's model for the Hamiltonian of tBLG's electrons, also known as the 'Dirac Continuum model'[3], the effective Hamiltonian of TBG system is divided into the interlayer component and the intralayer component. The intralayer component can be easily obtained based on the Hamiltonian of SLG, while the interlayer terms are only computationally possible and physically effective with few more approximations[3]. Applying the effective Hamiltonian to the Schrödinger equation and solving the eigenvalue of energy, we get the dispersion relation which shows a flat band at near-zero Fermi energy1(c).

3 Methods of Fabrication

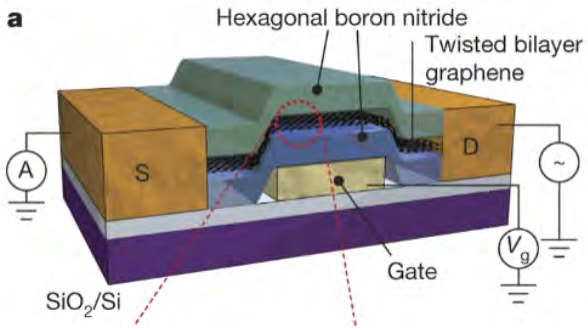

Figure 1: Schematic of a TBG device

Generally, heterostructures based on 2D layered materials consist of two geometric architectures: vertical heterostructures and lateral heterostructures. 2D vertical heterostructures, also called vdW heterostructures, are formed by vertically stacking one 2D material on another. The artificial stacking technique also called the transfer method, is the most commonly studied method for fabricating 2D heterostructures. This fabrication technique is based on the development of exfoliation and transfer techniques of 2D layered materials, which originated with the discovery of graphene. Graphene was first obtained by exfoliating and transferring 2D graphene layers from graphite using scotch tape, and this occurs due to the high separability between graphene layers as a result of the

weak interlayer vdW force.

During this summer program, the author was committed to making hBN/MATBG/hBN/gate stacks1, which would be cleaned and etched into a complete device. Firstly, monolayer graphene2(a) and hexagonal boron nitride (about 10–30 nm thick) 2(c)were exfoliated on Si chips, and high-quality flakes were picked using optical microscopy and atomic force microscopy. Then we used the AFM tip to separate a big flake of graphene into two pieces2(b), preparing for making MATBG(it's crucial to use two pieces from one graphene instead of using two different pieces since the constant of lattice might differ). Then we used a poly(bisphenol A carbonate)(PC)/polydimethylsiloxane

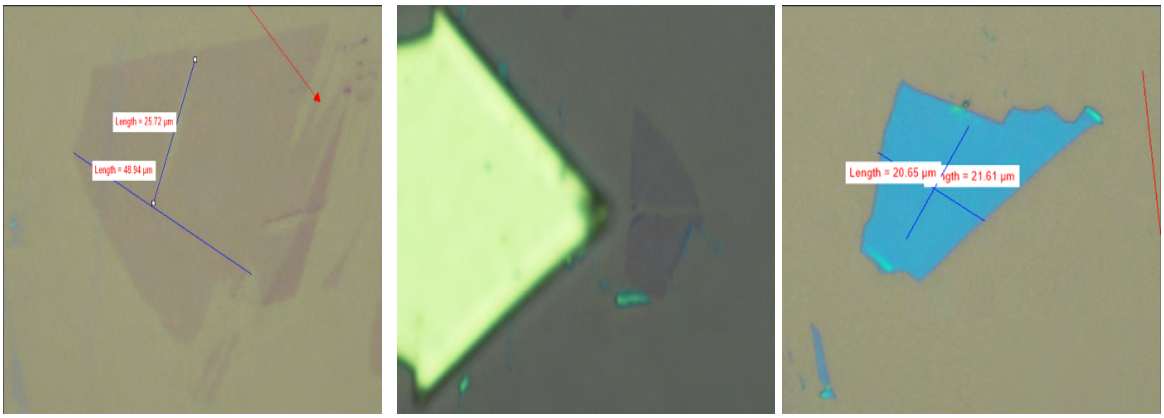

(a) Monolayer graphene (b) seperated pieces (c) hBN

(PDMS) stack on a glass slide mounted on a custom-made micro-positioning stage to pick up an hBN flake at 100°C and then used the vdW force between hBN and graphene to tear the graphene flake at the same temperature. The separated graphene pieces were rotated manually by a twist angle of about 1.2°–1.3° with the help of the Venier scale and stacked together again, which resulted in a controlled TBG structure. The stack was encapsulated with another hexagonal boron nitride flake on the bottom and picked up a bottom graphene gate. Finally, we heated the transfer stage to 220°C to melt the PC film, removed the remaining PC with chemicals, and transferred the stack onto the substrate2(d).

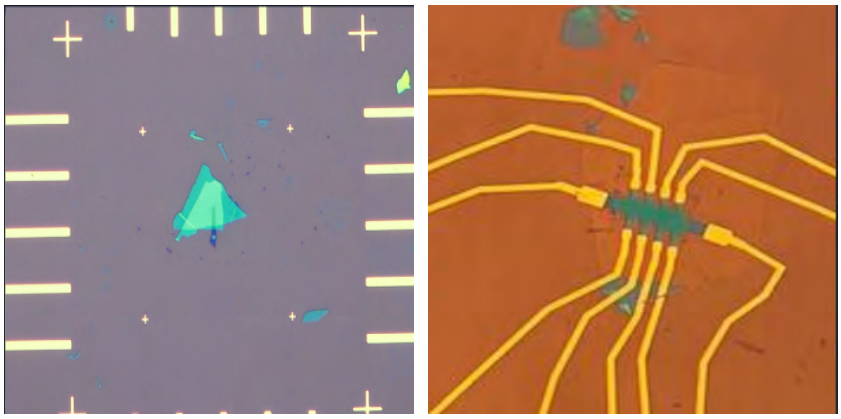

(d) stack (e) device

4 Results

After other group members etched the stack, transport measurements were performed in a dilution refrigerator. We used standard low-frequency lock-in techniques. The current flowing through the sample was amplified by a current pre-amplifier and measured by the lock-in amplifier. The four-probe voltage was amplified by a voltage pre-amplifier and measured by another lock-in amplifier. And we got the resistivity-voltage relation at different low temperatures2.

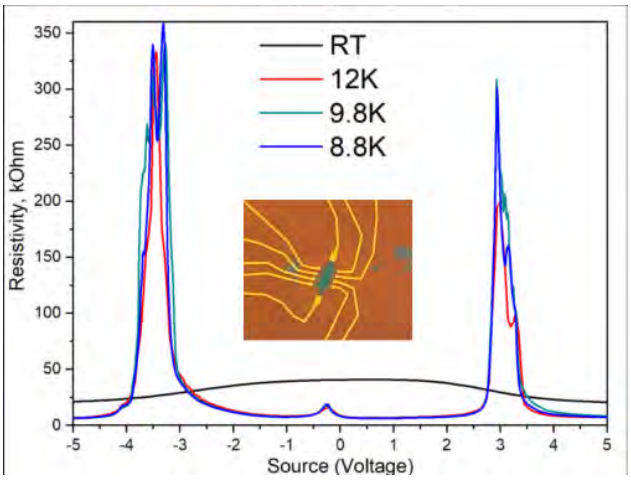

Figure 2: Resistivity-Voltage relation of device

5 Conclusion

This report starts with introducing the 2D vdW heterostructure and then goes back to the band structure theory of MATBG revealing the physics behind the exotic phenomena. The author accomplished the preparation of the encapsulated TBG device and measured the current-voltage relation of the device, which confirms the quality of this device. With the device, we can process further exploration of properties of MATBG and 2D vdW heterostructure.

References

[1] Y. Cao, V. Fatemi, and e. a. Deminar, Nature **556**, 80 (2018).

[2] Y. Cao and e. a. Fatemi, Nature **556**, 43 (2018).

[3] R. Bistritzer and A. MacDonald, Proceedings of the National Academy of Sciences **108**, 30 (2011).

Areal Thickness of HIPPO Calculated Using Beam Energy Differences in St. George

KATIE WHIPPLE

2024 NSF/REU Program
Department of Physics and Astronomy
University of Notre Dame

ADVISOR(S): Prof. Manoel Couder

Abstract

HIgh Pressure Point like gas target (HIPPO) is the helium gas target of Strong Gradient Electromagnetic Online Recoil separator for capture Gamma Ray Experiments (St. George). A conflict has arisen between two methods of determining HIPPO's areal thickness: injection pressure and energy differences of the beam. An accurate understanding of the areal thickness of the helium jet in HIPPO is needed to correctly characterize the reactions studied with St. George. Energy differences of the beam were measured before and after hitting the target. The areal thickness of the jet in HIPPO was then calculated. The thickness calculations showed no change in thickness with changing pressure. This suggests that the beam may have missed the helium jet. The next step is to determine why the jet was missed, but an exact route to this goal has yet to be determined.

1 Background

The Strong Gradient Electromagnetic Online Recoil separator for capture Gamma Ray Experiments (St. George) is a recoil separator used to study low energy (α, γ) reactions[1]. Recoil separators use electric and magnetic fields to separate out recoils. Recoils are the products of nuclear reactions happening in the target, from the beam headed toward the device's detector.

St. George uses inverse kinematics to facilitate these nuclear reactions. Inverse kinematics for St. George is defined as "high intensity heavy ion beams on hydrogen or helium gas targets"[1]. In simpler terms, a beam of larger particles is accelerated and directed at smaller particles which make up the target.

The target system of St. George is High Pressure POint like gas target (HIPPO). HIPPO is a system of recirculating helium that pressurizes the gas and passes it through a nozzle into a vacuum chamber where the particle beam of interest can pass through helium jet and react with the helium, leading to a radiative alpha capture [2].

Areal thickness is an important condition to know, especially in a system like HIPPO and St. George. Areal thickness is defined by the equation

$$\Delta x = \rho L \tag{1}$$

and has units of $\frac{kg}{m^2}$. Areal thickness, also referred to as simply just "thickness", is the volume density of a material when reduced to two dimensions.

2 Introduction

Having an understanding of what is going on inside scientific equipment is essential to the scientific process. This understanding enables scientists to better draw conclusions by eliminating unknowns and creating specific conditions. This idea is important to St. George and the target areal thickness in its target system, HIPPO.

In the past, the areal thickness of the jet of helium in HIPPO has been determined using the injection pressure of the gas in the nozzle, as discussed in Kontos et. al[2]. Recent calculations done using energy differences of the beam before and after passing through the target have sparked controversy as to how thick the helium target of HIPPO actually is at a given pressure.[3] It is important to know what the areal thickness of HIPPO is at a given pressure in order to correctly characterize the reactions that St. George studies.

3 Methods

I started by creating a Python code that took known before and after energies, E_{in} and E_{out}, to calculate the areal thickness of a given target using target information and linear stopping power values generated in a table created by the computer program SRIM[4]. This Python code used two methods to calculate the areal thickness–the range method and an iterative method–and compared the two.

The range method found the range of the beam at E_{in} and the range of the beam at the final energy after it passed through the target, E_{out}, interpolating when necessary. It then found the change in range (L), and multiplied it by the target density to calculate the areal thickness, as defined in Equation 1.

The iterative method started at E_{in}, calculated the energy after a small amount of areal thickness,

interpolating when necessary, and saved that thickness. The code would then take more and more steps until it reached the given E_{out}, adding up the small amounts of areal thickness to calculate the total thickness over the energy range. Comparing the two thickness calculations using the different methods yielded no significant difference between the two. This enabled me to use the iterative method in future calculations.

The next step in preparing for calculating the thickness of HIPPO using collected measurements was to calibrate the new focal plane silicon strip detector that was installed at the end of St. George. This was achieved by collecting counts of two materials of known peak energies. The three main peaks of ^{241}Am and the singular peak of ^{148}Gd were used to calculate a calibration slope for each of the 16 strips of the detector.

After calibration was completed, we took measurements using St. George at varying injection pressures of HIPPO and with three different beam types: $^{15}N^{4+}$, $^{20}Ne^{5+}$, and $^{16}O^{4+}$. Measures were taken to ensure we hit the helium jet of HIPPO using collimators to focus the beam where we wanted.

Once the data was collected, the subsequent analysis required the compilation of the Python code I had written previously, such as the iterative method of calculating areal thickness and the calibration slopes that were calculated, in addition to some new functions. New code needed to be written to account for the loss of energy in the detector due to a $50nm$ dead layer of silicon on the focal plane detector. The code that was written calculated the energy of the beam before the dead layer, and used that energy as E_{out} for the thickness calculations of the HIPPO target. The helium target's thickness was calculated for each run, unless there was no gas in HIPPO or the run was not included in the set due to errors in collecting the data or they did not contain information relevant to the HIPPO thickness issue being investigated.

4 Results

The areal thicknesses of each run, when plotted as a function of injection pressure of the helium jet in HIPPO did not yield what was expected. The results show that the thickness of HIPPO did

not change with increasing pressure (see Figure 1). It was expected that the thickness would follow a positive linear trend as a function of pressure, as was indicated in Kontos[2]. In Figure 1, it is evident across all three beam types that the thickness was unchanging with pressure.

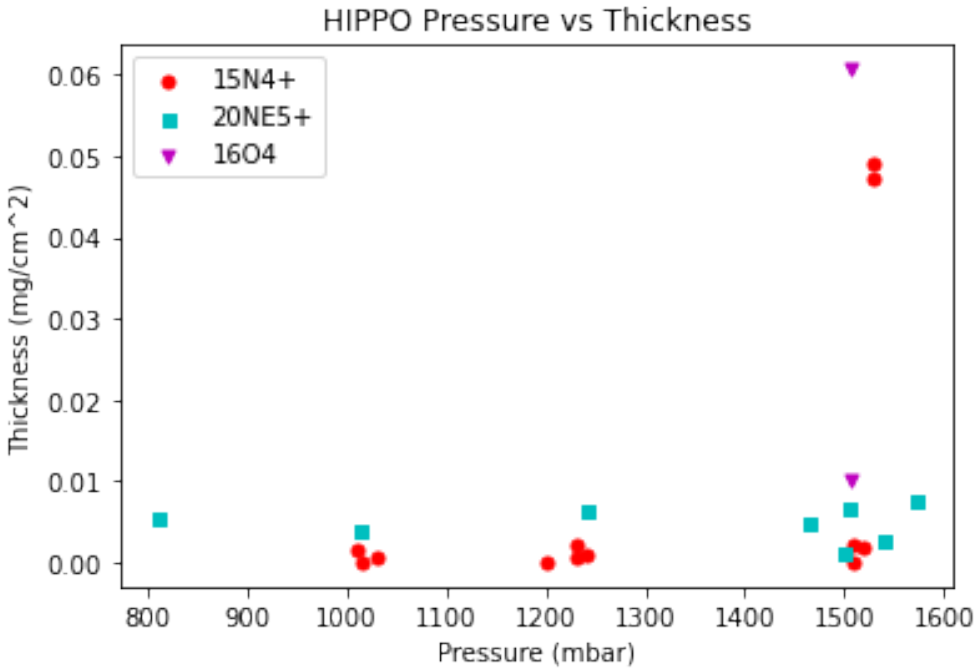

Figure 1: A plot of the runs of varying pressures plotted against the calculated thicknesses shows little to no change in thickness.

These results indicate that the beam is most likely not hitting the jet. This leads us to suspect that the collimator used to focus the beam in HIPPO may be pointed in the wrong place, and is therefore causing the beam to miss the jet entirely. There are a few statistical anomalies, as seen in one of the $^{16}O^{4+}$ runs and two of the $^{15}N^{4+}$ runs, that resulted in a higher thickness. This is suspected to be due to scattering from the collimators causing parts of the beam to hit the jet.

Another possible reason these results may have occurred would be due to the fact that the energy distribution of the ions reaching the focal plane silicon detector is significantly broader than what is expected. The reasoning for this is not fully understood at this time, but it may be due to the use of slits in the beam line to reduce the beam intensity in order to protect the detector. The slits may be causing unwanted scattering of the beam that the detector is picking up instead of the ions of the main beam. This possible scattering due to the slits may impact the issue of the beam missing

the jet and would explain why the average energy of the ions reaching the focal plane detector is presenting the way it is.

5 Conclusion

In conclusion, the conflict between the injection pressure method and the energy difference method of calculating the areal thickness of the helium jet in HIPPO has not been conclusively resolved. The current calculations using the energy difference method indicate that there is no change in the areal thickness of the jet, regardless of the pressure. The first step moving forward toward solving this conflict would be to determine why the beam is missing the jet target and to remedy the issue. There has yet to be found an effective method for correcting this at this time. However, once the issue of the beam missing the jet can be resolved, then repeating the measurements and performing the areal thickness calculations for said measurements will hopefully yield conclusive results toward resolving the conflict regarding the thickness of the helium jet of HIPPO.

References

[1] M. Couder, G. Berg, J. Gorres, P. LeBlanca, L. Lamma, E. Stecha, M. Wieschera, and J. Hinnefeld, Nuclear Instruments and Methods in Physics Research A (2007).

[2] A. Kontos, D. Schurmann, C. Akers, M. Couder, J. Gorres, D. Robertson, E. Stech, R. Talwar, and M. Wiescher, Nuclear Instruments and Methods in Physics Research A (2011).

[3] M. Couder, private interview (2024).

[4] J. F. Zeigler and J. P. Biersack, Srim.

Ink-Jet Printing of CeO_2 Thin Film Targets

VICTOR WILLIAMS

2024 NSF/REU Program
Department of Physics and Astronomy
University of Notre Dame

ADVISOR(S): Prof. Khachatur Manukyan

Abstract

Thin film targets are an essential component for nuclear experiments and are challenging to produce with high uniformity and a controllable thickness. Ink-jet printing coupled with solution combustion synthesis is a novel development with high material efficiency that reduces costs and synthesizes thin films with materials that are otherwise difficult to handle. The printer deposits picoliter-sized droplets of combustible solutions composed of metal nitrates and fuel onto aluminum substrates, which then are heat-treated for combustion synthesis to turn the deposited solutions into thin films of metal oxides. This experiment used cerium nitrate (oxidizer) and acetylacetone (fuel) dissolved in 1-butanol, ethanol, or 2-methoxyethanol to synthesize CeO_2 thin films. These thin films can be used as targets for nuclear measurements and as surrogates for synthesizing actinide thin films. This work will cover a parametric study (solvent type, droplet deposition step size, heating conditions) to investigate the effects on the uniformity and thickness of thin films.

1 Introduction

During a nuclear physics experiment, a particle accelerator or neutron source will subject targets to bombardment from various beams of particles. The success of such experiments depends upon the quality of the target used. These targets come in the form of a thin (10s to 100s of nanometers thick) film that is deposited onto a substrate, generally aluminum, carbon, or silicon. Of primary importance is the thickness of thin films, as experiments require precision thickness to improve the accuracy of measurements. In addition, targets must also be robust, ensuring they do not breakdown under irradiation, and uniform to ensure accuracy. Thickness, durability, and uniformity, determine the quality and usability of a thin film target, and are dependent on the process used to make the target. A variety of thin film deposition techniques are employed today for actinide targets. Predominately, vapor deposition and molecular plating are used for thin film synthesis. However, vapor deposition films of expensive radioisotopes have a low material collection and high radioactivity, and molecular plating has low-control over the chemical composition of targets [3].

An ink-jet printer is a device that deposits thousands of 10-100 picoliter droplets of solution onto a substrate. Once the printer has deposited a thin layer of combustible solution, the solution requires a small amount of heat to undergo a solution combustion synthesis (SCS) reaction, producing a metal oxide thin film. Coupling ink jet printing with SCS represents a novel development in thin

film target making due to the high material collection efficiency and the ability to reduce costs, as well as the potential to produce thin films with materials that are otherwise difficult to handle due to radioactivity or limited quantities. The goal of this project is to carry out a parametric investigation (solvent type, droplet deposition step size, heating conditions) into the printing and combustion process to optimize the synthesis of thin films for eventual use with radioactive materials such as thorium and uranium.

2 Background

2.1 Ink-Jet Printer

The ink jet printer is a Jetlab® 4 manufactured by MicroFab Technologies Inc. The primary component of the printer is the droplet dispenser, which consists of a syringe to hold the solution, a glass tube for the droplets to pass through, and a piezoelectric crystal with electrodes on both ends to generate the droplets [2]. Piezoelectricity is a feature of certain materials in which applying an electric field through the material causes the material to experience mechanical stress. The piezoelectric material in the printer, when no electric field is present, does not allow any fluid to flow through the glass tube. However, when a voltage differential is applied across the crystal from the two electrodes, an electric field is created, which causes a deformation in the crystal that allows fluid to flow (Figure 1). By making the voltage differential time dependent in the form of a wave, the electric field will fluctuate through time from its maximum value to zero and create droplets rather than a continuous stream of solution. These droplets are then dispensed onto the substrate.

The quality of deposition is influenced by a variety of factors, such as the size of the droplets, the velocity of droplets, and the step size in between droplets, which is the distance the printer tip moves in between dispensing. These factors can be controlled by changing the values of the components of the voltage wave through the piezoelectric crystal. For example, increasing the dwell voltage will lead to larger droplets that fall with a faster speed.

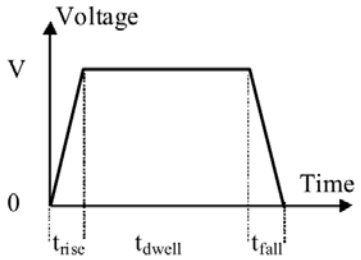

Figure 1: Plot of one for a basic voltage waveform [2, p. 4]. t_{rise} is the time (ns) for the voltage to reach the maximum voltage desired (dwell voltage), t_{dwell} is the time (ns) how long the desired voltage lasts for, and t_{fall} is the time (ns) for the voltage to return to 0.

2.2 Combustion Synthesis and CeO_2

Solution combustion synthesis is the process of a self-sustaining exothermic reaction between an oxidizer (metal nitrates) and a fuel (organic reducing agent) that produces nanoscale oxide materials [1]. This process converts the metal nitrate to its corresponding metal oxide, and it is a low cost and energy-efficient method of material synthesis. In these reactions, a solution of metal nitrate and fuel is heated up, evaporating solvent, until the combustion reaction initiates, which generates heat, the desired metal oxide and various gaseous byproducts. Metal oxide thin films can be created using combustion synthesis by depositing a small layer of combustible solution onto a substrate, in this case using ink-jet printing, and then combusting the sample to convert the thin layer of liquid to a film.

In this experiment, cerium oxide (CO_2) was used as the material for thin films. Cerium, a lanthanide element with atomic number 55, can serve as a surrogate for actinides, such as uranium and plutonium, which are of interest for nuclear physics studies. CeO_2 can be made through combustion synthesis from cerium nitrate, $Ce(NO_3)_2$ and acetylacetone ($C_5H_8O_2$). The general combustion reaction of cerium nitrate with acetylacetone to make cerium oxide is: $3Ce(NO_3)_2 + C_5H_8O_2 \rightarrow 3CeO_2 + 5CO_2 + 4H_2O + 3N_2 +$ heat. Depositing solutions of cerium nitrate and acetylacetone dissolved in a solvent (1-butanol, ethanol, or 2-methoxyethanol) and combusting it will create the very thin layer of CeO_2 needed for a thin film target.

3 Methods

SCS solutions were prepared by dissolving Ce(NO3)4 (98%, Sigmda-Alridch) * 6H2O + ($C_5H_8O_2$)(99%, TCI) in either 1-butanol (99%, TCI), ethanol (Koptec 100%), or 2-methoxeythanol (99%, TCI) to produce a 0.125M or 0.0625M solution.

For deposition, 10 x 10 mm polished aluminum substrates were utilized. Before use, the substrates were annealed in a preheated 350°C furnace for 20 minutes, to remove adhesive residue and to ensure surface uniformity. Prior to solution deposition, the printer was flushed using the respective solution solvent to clean any residual particles and improve droplet consistency. Next the combustible solution was put in printer head, and the printer was primed by optimizing the voltage wave and pressure to get the desired droplet size. For this experiment, droplets of approximately 60-70 pL in volume were used. Droplet size before a run was determined using the printers drop analysis feature, which determines the volume by calculating an average based off of 3 consecutive images of droplets as well as the speed and angle that droplets are falling. The maximum voltage and the dwell time were adjusted to maintain the desired droplet size.

The substrate was placed onto the mechanical stage and moved into position, ensuring the area for deposition would only cover the substrate. The area used for each sample in this experiment was kept constant as a 2.0 mm by 2.0 mm square on the substrate. The electronically controlled stage is able to position itself to within 25 μm of the intended droplet position during deposition. After deposition, the samples were placed in a preheated furnace or a room temperature furnace following a ramp-rate for heating to undergo combustion. After combustion, Scanning Electron Microscopy (SEM) was used to image thin film surfaces, and backscattered electrons (BSE) were used to distinguish areas of the thin-film based on elemental mass to determine CeO_2 (light) and aluminum substrate (dark), which shows the distribution of deposited material to evaluate uniformity.

4 Results

Samples were analyzed post combustion to examine areas for CeO_2 thin film. Figure 2 displays results of Energy Dispersive X-Ray Spectroscopy (EDS) analysis of a darker area and the center of a

deposited droplet on a sample. The EDS of the dark area shows peaks corresponding to aluminum, carbon, and oxygen. The large aluminum and oxygen peak is due to the substrate. The presence of carbon is most likely left over from trace organic residues. As expected from the darker area of only substrate, only a minor amount of cerium was detected. The EDS of the center of the droplet shows peaks corresponding to cerium, oxygen, aluminum, and carbon. The aluminum and carbon are most likely from the substrate and organic residues, while the more intense cerium and oxygen peak show that there is a CeO_2 thin film.

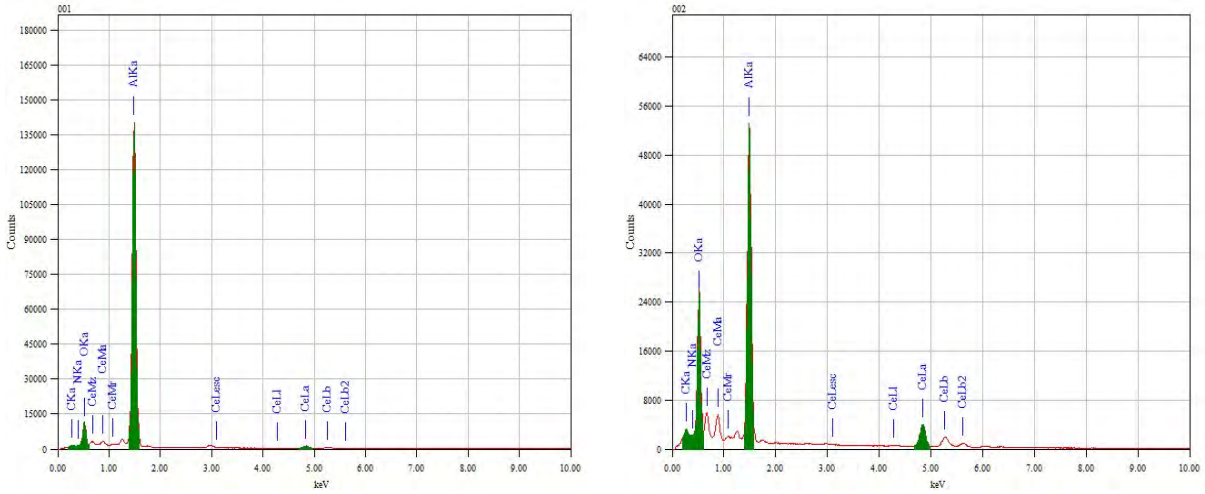

(a) darker area (b) center

Figure 2: EDS analysis of (a dark area and (b center of deposited droplet for $Ce(NO_3)_3 + C_5H_8O_2$ in 1-Butanol heated at 350°C for 20 min.

4.1 Solvent

Three different types of solvent: ethanol, 1-butanol, and 2-methoxyethanol were explored, while maintaining a concentration of 0.125 M for the $Ce(NO_3)_3 + C_5H_8O_2$ system, a step size of 50 μm step size, and were heated at 350°C for 20 min.

Figure 3 shows the SEM images of samples made with each respective solvent. In the ethanol system, the material has a limited spread post-combustion, due to the high rate of evaporation, limiting the formation of thin-films (Figure 3a). In the 1-butanol system, small islands of CeO_2 form throughout the material (Figure 3b). While 1-butanol has a slower evaporation rate than ethanol and 2-methoxyethanol, the solution may be filtered differently during printing. Finally,

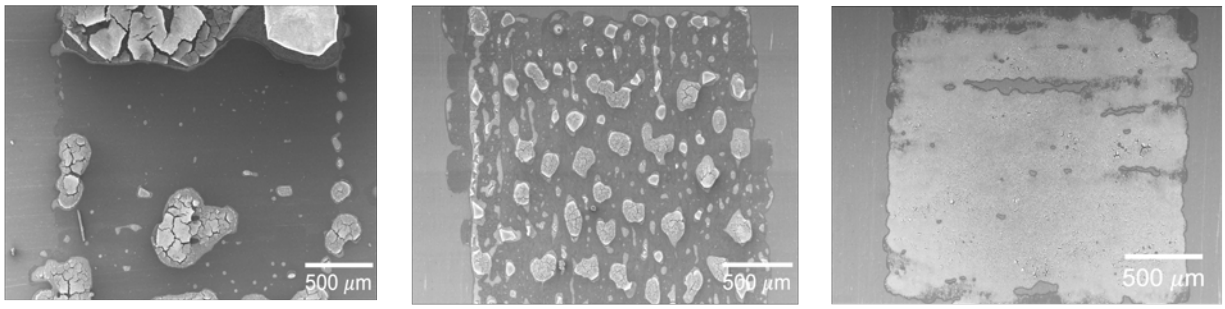

(a) ethanol (b) 1-butanol (c) 2-methoxyethanol

Figure 3: The deposition of three different solvent systems (a ethanol, (b 1-butanol and (c 2-methoxyethanol all printed using a 0.125 M $Ce(NO_3)_3$ + $C_5H_8O_2$ system dissolved in each respective solvent, 50 μm step size, and were heated at 350°C for 20 min.

the 2-methoxyethanol system shows a semi-uniform deposition producing a cracked CeO_2 material (Figure 3c).

4.2 Step Size

Different step sizes were explored, as increasing or decreasing the step size in a set area can likewise affect the concentration of material deposited, which ultimately can impact the thin-film produced. For each solvent, prints were made using the following step sizes: 25 μm, 40 μm, 50 μm, 60 μm, and 80 μm.

Each of these step sizes were tested with 0.125 M solutions of each of the three solvents heated at 350°C for 20 min. following deposition. For ethanol and 1-butanol solvents, the same film formation occurs as in Figure 3a and in Figure 3b, and was found regardless of the step size (not shown). None of the samples made with 1-butanol or ethanol resulted in thin films for any of the step sizes tested.

Figure 4 shows the films synthesized using 2-methoxyethanol for 5 different steps sizes. The 25 μm and 40 μm step size films both experience severe cracking. This is most likely due to too much material being deposited, and the subsequent buildup of byproduct gases created during the combustion synthesis reaction. These gases lead to cracks in the film as where they have burst out and released. For the 60 μm and 80 μm step sizes, thin films did not form over the entire surface because there was not enough material present. For 50 μm, minor cracking occurs, but the overall

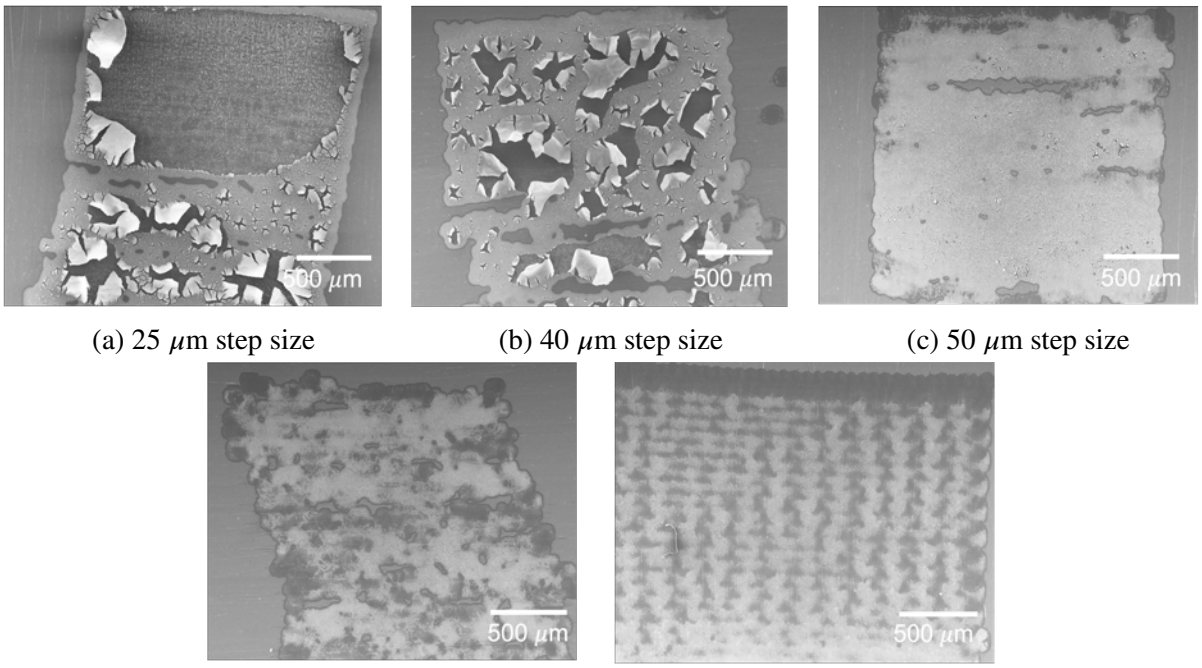

(a) 25 μm step size (b) 40 μm step size (c) 50 μm step size

(d) 60 μm step size (e) 80 μm step size

Figure 4: SEM of thin films of varying step sizes for 0.125 M $Ce(NO_3)_3$ + $C_5H_8O_2$ + 2-methoxyethanol, and were heated at 350°C for 20 min.

deposition is the most uniform, meaning that the 50 μm step size is the optimal step size.

4.3 Heating Rates

The reaction of cerium nitrate with acetylacetone can ignite after the solvent evaporates (below 350°C).The rapid heating in the preheated furnace potentially led to bubbling of the solvent and therefore cracking and breaking of the film. This bubbling cracks the film and so different heating rates to buildup from 30°C to 350°C to slow the rate of evaporation. Rates of 10°C per min. and 20°C per min. were used with solutions of 0.125 M $Ce(NO_3)_3$ + $C_5H_8O_2$ system in 1-butanol and 0.0625 M $Ce(NO_3)_3$ + $C_5H_8O_2$ system in 2-methoxyethanol. The concentration of CeO_2 was lowered from 0.125 M to 0.0625 M after cracking occurred in 0.0625 M solutions with 2-methoxyethanol using the original heating parameters of 350°C for 20 min. as well.

Figure 5 shows the SEM and BSE images of post combustion films for 1-butanol and 2-methoxyethanol. For the 1-butanol samples, the conglomoration of material into islands persisted, and in the BSE images the islands of CeO_2 (light areas) are evident for both the 10°C/min. and

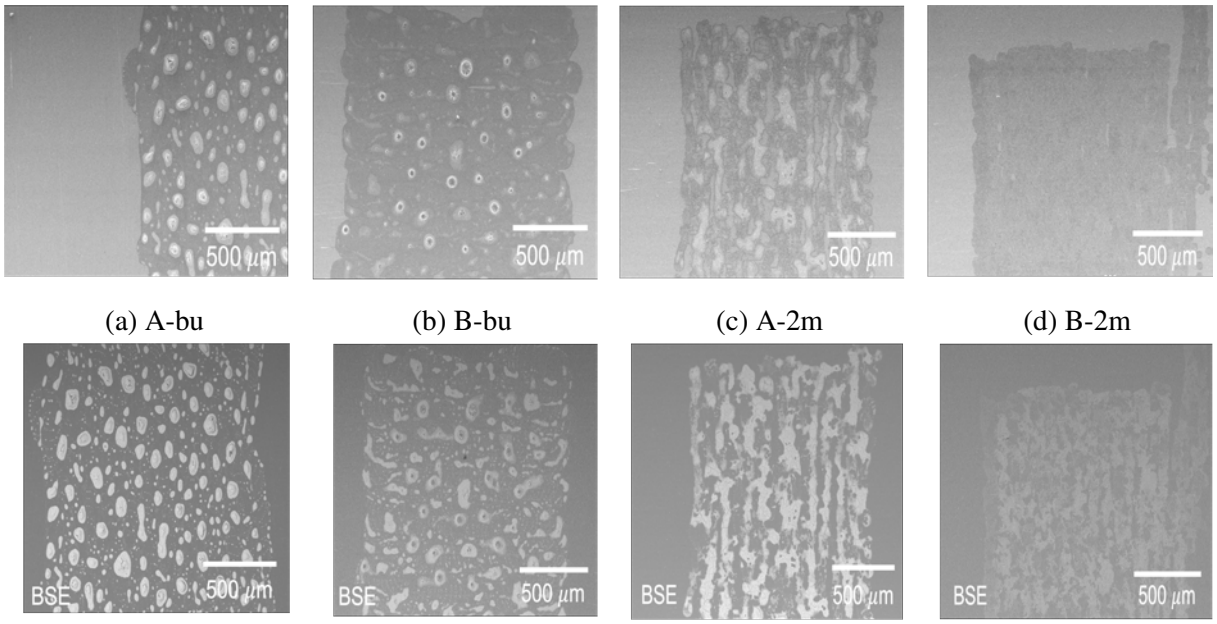

(a) A-bu (b) B-bu (c) A-2m (d) B-2m

(e) C-bu (f) D-bu (g) C-2m (h) D-2m

Figure 5: post-combustion films made by 0.125 M $Ce(NO_3)_3$ + $C_5H_8O_2$ system with 1-butanol (-bu) and 0.0625 M $Ce(NO_3)_3$ + $C_5H_8O_2$ system with 2-methoxyethanol (-2m), 50 μm step size, heated from 30 to 350°C at (A 10°C/min, (B 20°C/min, (C BSE of area A and (D BSE of area B. CeO_2 islands emerged for 1-butanol whereas 2-methoxyethanol had areas of CeO2 film.

20°C/min. samples. For the 2-methoxyethanol samples, the 20°C/min. for 2-methoxyethanol shows isolated thin-films and no evidence of cracking, significantly better than any other print. This sample did have a large area of thin film, and as shown in the BSE image (D-2m), the CeO_2 distribution is fairly uniform.

5 Conclusion and Discussion

In this work, we found that ink-jet printing is a viable method of producing uniform thin films, and the optimal parameters to make thin films were determined. 2-methoxyethanol preformed the best of the 3 solvents tested, and unlike ethanol or 1-butanol, thin films could be created with 2-methoxyethanol. 50 μm step size is the optimal step size, since below 50 μm too much material was deposited and cracking occurred, while above 50 μm too little material was deposited and the print had empty spaces. Using a heating rate of 20°C/min was most successful at producing thin films in the 2-methoxyethanol system at a lower concentration (0.0625 M).

Based on the study's results, there are numerous next steps to pursue. The first will be to investigation of the thickness of printed films. Now that the conditions for uniformity have been found, focused ion-beam milling and atomic force microscopy can be used to measure the thicknesses of printed targets. Furthermore, uniformity can potentially be improved by printing multiple layers sequentially on one substrate, prior to heat treament. The most uniform thin films produced in this study (Figure 5: B-2m) did not have perfectly distributed CeO_2 (as shown through BSE images), and so multiple depositions of a lower concentration could improve the distribution of CeO_2. Finally, the ultimate goal of this project is to transition from printing CeO_2 thin films to printing thin films made out of actinides. Next, thorium oxide (ThO_2) thin films targets will be studied based on results with printing CeO_2 for use in nuclear measurements irradiation studies.

6 Acknowledgments

Research opportunity and funding provided by the Vincent P. Slatt Fellowship for Undergraduate Research in Energy Systems and Processes, administered through the Center for Sustainable Energy at Notre Dame (ND Energy). The National Nuclear Security Administration (NNSA) of the United States Department of Energy (DOE) provided financial support for the work through Grant # DE-NA0004093.

References

[1] Arvind Varma, Alexander S. Mukasyan, Alexander S. Rogachev, and Khachatur V. Manukyan Chemical Reviews 2016 116 (23), 14493-14586 DOI: 10.1021/acs.chemrev.6b00279

[2] Ink-Jet Microdispensing Basic Set-up. Microfab Technologies, Inc.

[3] J.B. Roberto et. al, Actinide targets for the synthesis of super-heavy elements, Nuclear Physics A, Volume 944, 2015, Pages 99-116, ISSN 0375-9474, https://doi.org/10.1016/j.nuclphysa.2015.06.009

Search for rare processes in paired dimuon events in CMS scouting data

CONNIE YANG

2024 NSF/REU Program
Department of Physics and Astronomy
University of Notre Dame

ADVISOR: Prof. Marc Osherson

Abstract

This paper presents a search for rare processes in paired dimuon events using CMS scouting data. We search for exotic Higgs bosons Φ associated with the $pp \to \Phi \to \phi\phi \to 4\mu$ process by comparing the four-muon mass $m_{4\mu}$ spectrum to estimated background. No new particles are observed. As a proof of principle, we also measure the asymmetry in pseudorapidity η and the charge-parity violation (CPV) sensitive angle $\Delta\Phi$ in a known resonance of J/ψ pair production events. We show that background events in the scouting dataset can be well-modeled, and our analysis is sensitive to signs of new physics.

1 Introduction

The Standard Model (SM) is the most successful theory of subatomic constituents and their interactions, but it describes only 15% of mass in the universe. To account for the remaining mass, many theories propose the existence of dark matter particles that can interact with the SM sector. Much like electrons and other SM particles obtain their mass through interactions with the Higgs field, dark matter particles could also receive mass from exotic Higgs fields. The exotic Higgs bosons associated with such fields may be produced in high energy particle collisions at the Large Hadron Collider (LHC) and observed at the Compact Muon Solenoid (CMS) detector. In searches for rare processes such as the production of exotic Higgs bosons, CMS scouting datasets may prove useful. Compared to the normal trigger system, the scouting algorithm saves events at a rate 5 times greater but recovers information at lower quality. In this work, we investigate the sensitivity of muon scouting data to signatures of rare processes. A search for exotic Higgs bosons in the four-muon mass $m_{4\mu}$ spectrum is presented, and a known J/ψ resonance is further analyzed as a proof of principle to show that background estimation and tests for new physics are feasible.

2 Background

2.1 Exotic Higgs bosons

The Standard Model provides a successful explanation for three of the four fundamental forces: electromagnetism, the strong force, and the weak force. The last particle in the model, the Higgs

boson, was discovered by the ATLAS and CMS collaborations at CERN in 2012. This particle is associated with a spin-0 scalar field, known as the Higgs field, which gives mass to other SM particles via the Brout-Englert-Higgs mechanism.

The Higgs boson may also be relevant to understanding dark matter, which comprises 27% of the energy content and 85% of the mass in the universe. This form of matter has yet to be detected experimentally, but its gravitational attraction has been observed in many cosmological phenomena, including gravitational lensing and the observed orbital velocities of stars. Many theories hypothesize the existence of exotic Higgs fields from which dark matter particles obtain their mass. According to these theories, the associated exotic Higgs bosons Φ could potentially be produced in high energy proton-proton (pp) collisions at the LHC. In this analysis, we focus on the theoretical $pp \to \Phi \to \phi\phi \to 4\mu$ production and decay channel, shown in Figure 1. After being produced, Φ decays into a pair of spin-0, charge-neutral particles ϕ. Each ϕ then decays into a muon-antimuon pair $\mu^-\mu^+$, which may be detected at CMS.

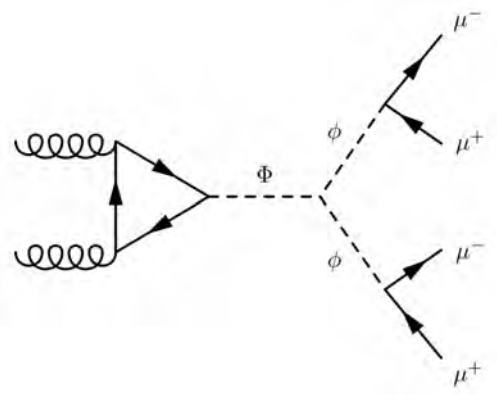

Figure 1: Feynman diagram of the $pp \to \Phi \to \phi\phi \to 4\mu$ process. An exotic Higgs boson Φ is produced through gluon-gluon fusion, via a fermion loop, then decays into a pair of spin-0, charge-neutral particles ϕ. Each ϕ then decays into a muon-antimuon pair $\mu^-\mu^+$.

2.2 Data scouting at CMS

The LHC collides protons at a rate of 40 MHz, but only 1 kHz of data can normally be stored to disk. At CMS, event selection is provided by a two-step trigger algorithm [1], outlined in Figure 2. The Level 1 (L1) trigger uses custom hardware to reduce the initial rate to 100 kHz. Then using a farm

of commercial processors, the High Level Trigger (HLT) performs a series of online reconstruction and filtering processes to further reduce the rate to 1 kHz. Reconstruction involves combining the signals from each CMS subdetector to recover information about an event, and threshold requirements are subsequently applied to select for the events of interest. For events that pass the HLT selections, the full detector readout is stored for later offline reconstruction at 1 MB per event. Altogether, this process requires a trigger bandwidth of 1 kHz x 1MB = 1 GB/s [2].

To expand the rate of data collection, scouting was introduced in 2011 to run alongside the HLT algorithm. The scouting algorithm imposes looser restrictions, which allows more events to pass and results in a higher rate of 5 kHz. The selected events undergo additional online reconstruction and are stored in a compact form at 1.5 kB per event. This reduces the required trigger bandwidth to 5 kHz x 1.5 kB = 7.5 MB/s [2]. Scouting datasets do not contain the full raw data, which makes analysis more difficult. Nonetheless, the inclusion of more events can be advantageous for searches of exotic physics. For example, scouting datasets include events with low transverse momenta p_T, which may be excluded from normal datasets. This is particularly useful in the search for $pp \to \Phi \to \phi\phi \to 4\mu$ processes, in which we expect the production of Φ to be rare and the final 4μ state to exhibit low p_T.

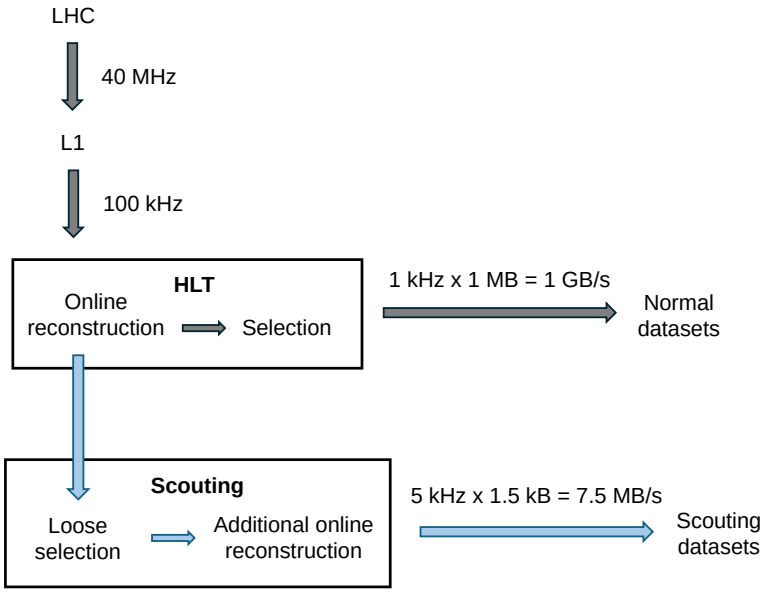

Figure 2: Process for generating normal and scouting datasets. Collision events at the Large Hadron Collider (LHC) are normally selected in a two-step process (dark grey arrows) using the Level 1 (L1) and High Level Trigger (HLT) algorithms. The event rate is reduced from 40 MHz to 1 kHz, and a trigger bandwidth of 1 GB/s is required. The scouting algorithm (light blue arrows) applies looser selection criteria and compactifies the data stored, increasing the event rate to 5 kHz and decreasing the trigger bandwidth to 7.5 MB/s.

3 Methods

Using CMS muon scouting data, a search for exotic Higgs bosons is performed in the four-muon mass $m_{4\mu}$ distributions for various average dimuon masses $\hat{m}_{\mu\mu}$. A known J/ψ resonance, corresponding to $3.05 < \hat{m}_{\mu\mu} < 3.15$ GeV$/c^2$, is further analyzed for angular production asymmetry. All plots are produced using PyROOT.

3.1 Background estimation using the ABCD method

To distinguish signals from background events, estimates of the background are performed using the ABCD method [3]. Events with 4 or more muons and at least 1 pair of opposite charges are selected for analysis. The selected events are categorized into the signal region A and three control

regions B, C, and D according to mass asymmetry m_{asym} and four-muon charge $q_{4\mu}$. These are defined

$$m_{asym} = \frac{|m_{\mu\mu} - m'_{\mu\mu}|}{m_{\mu\mu} + m'_{\mu\mu}}, \qquad q_{4\mu} = |q_{\mu\mu}| + |q'_{\mu\mu}|, \tag{1}$$

where $m_{\mu\mu}$, $m'_{\mu\mu}$ are the two dimuon masses, and $q_{\mu\mu}$, $q'_{\mu\mu}$ are the two dimuon charges. In each event, the dimuon pair is identified as the combination with lowest m_{asym}.

The distributions of m_{asym} and $q_{4\mu}$ are each divided into a signal region and sideband. Since the expected $\Phi \to \phi\phi$ process involves the production of identical charge-neutral particles, we define the signal regions to be $m_{asym} < 0.05$ and $q_{4\mu} = 0$, with sidebands $0.075 < m_{asym} < 0.5$ and $q_{4\mu} \neq 0$. Region A consists of events in the intersection of both signal regions, $\{m_{asym} < 0.05 \cap q_{4\mu} = 0\}$. Region B consists of $\{m_{asym} < 0.05 \cap q_{4\mu} \neq 0\}$, while region C consists of $\{0.075 < m_{asym} < 0.5 \cap q_{4\mu} = 0\}$. Region D consists of events in the intersection of both sidebands, $\{0.075 < m_{asym} < 0.5 \cap q_{4\mu} \neq 0\}$. The ABCD selection criteria are listed in Table 1. We expect the control regions to contain negligible amounts of signal and assume the relationship

$$N_A^{bkg} = N_B \frac{N_C}{N_D} \tag{2}$$

between the number N_A^{bkg} of background events in region A and the total number of events N_B, N_C, and N_D in each of the control regions.

Table 1: Selection criteria for signal region A and control regions B, C, and D.

Region	m_{asym}	$q_{4\mu}$
A	< 0.05	$= 0$
B	< 0.05	$\neq 0$
C	$(0.075,\ 0.5)$	$= 0$
D	$(0.075,\ 0.5)$	$\neq 0$

In a given window of $\hat{m}_{\mu\mu}$ values, the $m_{4\mu}$ distribution is analyzed for possible resonances corresponding to exotic Higgs bosons. In each $m_{4\mu}$ distribution, the number of background events is estimated using equation 2 on a bin-by-bin basis. Due to correlations between $m_{4\mu}$ and $\hat{m}_{\mu\mu}$, the ratio N_C/N_D is plotted with respect to $\alpha = \hat{m}_{\mu\mu}/m_{4\mu}$. A second-degree polynomial function $R_{C/D}$

is fitted to the α distribution. For each bin of $m_{4\mu}$, the estimated background $N_A^{bkg}(m_{4\mu}, \alpha)$ is then plotted by weighting each event in region B by $R_{C/D}(\alpha)$.

3.2 Measurements of angular production distributions

Angular production distributions of η asymmetry and the CPV sensitive angle $\Delta\Phi$ are measured for J/ψ pair production events. The pseudorapidity $\eta = -\ln[\tan(\theta/2)]$ is related to the angle θ of a particle's trajectory with respect to the beam axis. The η asymmetry $A^{\eta}_{2J/\psi}$ is a measure of directional bias in the J/ψ pair production and is plotted as a function of the average pseudorapidity $|\hat{\eta}_{J/\psi}|$ of each J/ψ pair. For each bin of $|\hat{\eta}_{J/\psi}|$,

$$A^{\eta}_{2J/\psi} = \frac{N(\Delta\eta > 0) - N(\Delta\eta < 0)}{N(\Delta\eta > 0) + N(\Delta\eta < 0)}, \tag{3}$$

where $\Delta\eta$ is the difference in η between the higher-p_T and lower-p_T J/ψ mesons, and $N(\Delta\eta > 0)$, $N(\Delta\eta < 0)$ are the number of events with positive and negative $\Delta\eta$.

$\Delta\Phi$ is the angle between the two J/ψ planes [4], defined in the four-muon rest frame as

$$\Delta\Phi = a \arccos(\hat{n}_1 \cdot \hat{n}_2), \tag{4}$$

where $\hat{n}_1$, $\hat{n}_2$ are the unit vectors normal to the higher-p_T and lower-p_T J/ψ planes, and $a = \pm 1$ determines the positive/negative direction of $\Delta\Phi$. These are defined

$$\hat{n} = \frac{\vec{p}_{\mu^-} \times \vec{p}_{\mu^+}}{|\vec{p}_{\mu^-} \times \vec{p}_{\mu^+}|}, \qquad a = \frac{\vec{p}_1 \cdot (\hat{n}_1 \times \hat{n}_2)}{|\vec{p}_1 \cdot (\hat{n}_1 \times \hat{n}_2)|}, \tag{5}$$

where $\vec{p}_{\mu^-}$, $\vec{p}_{\mu^+}$ are the momentum vectors of the $\mu^-\mu^+$ pair associated with a J/ψ meson, and $\vec{p}_1$ is the momentum vector of the higher-p_T J/ψ.

4 Results

The search for exotic Higgs bosons is performed by analyzing the $m_{4\mu}$ distribution of various $\hat{m}_{\mu\mu}$ windows. A few examples are presented in Figure 3.

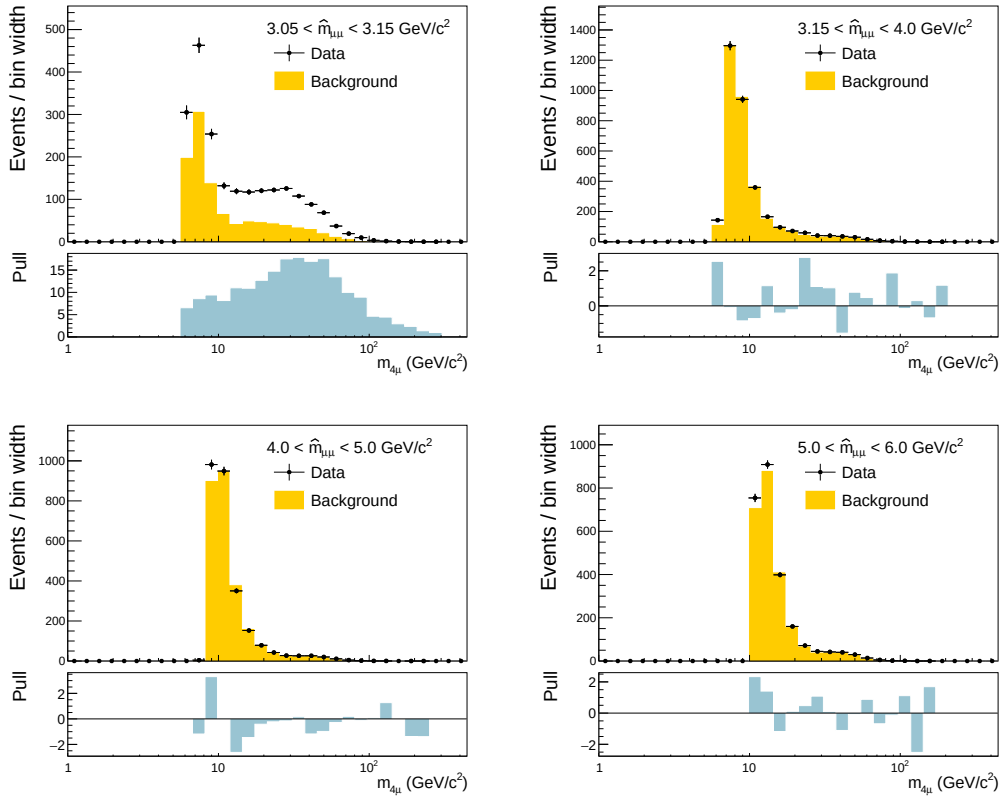

Figure 3: Distributions of $m_{4\mu}$ for events in the J/ψ pair production window $3.05 < \hat{m}_{\mu\mu} < 3.15$ GeV$/c^2$ (top left) and in windows $3.15 < \hat{m}_{\mu\mu} < 4.0$ GeV$/c^2$ (top right), $4.0 < \hat{m}_{\mu\mu} < 5.0$ GeV$/c^2$ (bottom left), and $5.0 < \hat{m}_{\mu\mu} < 6.0$ GeV$/c^2$ (bottom right). In the upper panels, black points indicate the number $N_A(m_{4\mu})$ of events in the $\hat{m}_{\mu\mu}$ window, with vertical error bars indicating statistical uncertainty. Yellow shaded regions indicate background estimates $N_A^{bkg} = N_B(m_{4\mu})R_{C/D}(\alpha)$ for the same $\hat{m}_{\mu\mu}$ window. In the lower panels, blue shaded regions indicate the pull values $(N_A - N_A^{bkg})/\sqrt{N_A}$.

The J/ψ window, corresponding to $3.05 < \hat{m}_{\mu\mu} < 3.15$ GeV$/c^2$, shows data well above the expected background. This indicates that the analysis is sensitive to J/ψ pair production, which has been previously observed in paired dimuon events [5]. The pull plots of other $m_{4\mu}$ distributions show small deviations from 0 due to statistical fluctuations. There is close agreement between the data points and expected background, which indicates a well-fitted background estimation. No

peaks in the $m_{4\mu}$ distributions are observed to indicate a four-muon particle.

Measurements of η asymmetry and $\Delta\Phi$ produce results consistent with SM expectations (Figure 4). The plot of $A^{\eta}_{2J/\psi}$ vs $|\hat{\eta}_{J/\psi}|$ is randomly distributed about 0, and the $\Delta\Phi$ distribution is symmetric. Signs of new physics would be indicated by significant deviations from the shapes of these distributions presented.

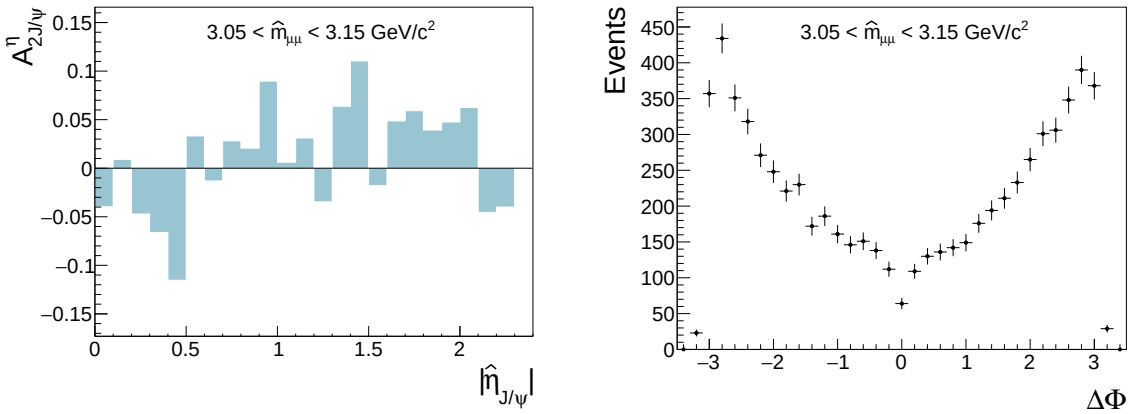

Figure 4: Plot of $A^{\eta}_{2J/\psi}$ as a function of $|\hat{\eta}_{J/\psi}|$ (left) and the distribution of $\Delta\Phi$ (right) for J/ψ pair production events. Vertical error bars in the $\Delta\Phi$ distribution indicate statistical uncertainty. Both plots show results consistent with the Standard Model.

5 Conclusion

A search for rare processes is performed in paired dimuon events in CMS scouting data. The $m_{4\mu}$ spectrum is analyzed for signs of exotic Higgs bosons associated with the $pp \to \Phi \to \phi\phi \to 4\mu$ process, and no resonances corresponding to Φ are observed. As a proof of principle, additional measurements of η asymmetry and $\Delta\Phi$ are performed for a known J/ψ resonance, and results are consistent with the Standard Model. This work shows that the background in muon scouting datasets can be well-modeled, and searches for new physics are feasible.

6 Acknowledgements

This work was made possible by the Physics and Astronomy REU program at the University of Notre Dame, the NSF, and the CMS collaboration. I would especially like to thank Prof. Marc Osherson for guiding me through this project, as well as Prof. Umesh Garg and Ms. Kristen Amsler for organizing the REU program.

References

[1] A. M. Sirunyan *et al.*, JINST **13** (P06015), DOI: 10.1088/1748-0221/13/06/P06015.

[2] S. Mukherjee, in *LLC Workshop* (Amsterdam Science Park, 2018).

[3] W. Buttinger, Background Estimation with the ABCD Method Featuring the TRooFit Toolkit (2018).

[4] T. Agatonovic-Jovin *et al.*, in *PoS(EPS-HEP2021)*, Vol. 398 (2022) p. 495.

[5] The CMS collaboration, J. High Energ. Phys. **94**, DOI: 10.1007/JHEP09(2014)094.

Making and Testing Microwave Filters for Low Temperature Quantum Computing System

ZHUHAO YE

2023 NSF/REU Program

Department of Physics and Astronomy

University of Notre Dame

ADVISOR: Prof. Dafei Jin

Abstract

Quantum computing is a computing method that exploits quantum mechanical phenomena, which have the potential capacity to perform calculations exponentially faster than any modern "classical" computing method. Superconducting-circuit -based quantum computing system which is adapted by Google and IBM, is one of the strong competitors for future quantum computing, where low temperature is essential for preservation of the superconducting state, minimize thermal disturbances, and optimize quantum coherence. In this case, some thermal noise from the room temperature will enter the low-temperature core of the system along the microwave transmission line. Therefore, microwave filters are needed to cut off this thermal noise. Here I report my work in learning, making, calculating and measuring eccosorb-filled microwave filters and their performance from room temperature down to the nitrogen temperature about 4 Kelvin. The result shows that in room temperature the pass rate of microwave signals with frequencies above 5GHz is less than -15dB; in nitrogen temperature about 4 Kelvin, this number raise to -12dB, which reach the expectation to cut off the noise.

1. Introduction

Quantum computing is a computing method that exploits quantum mechanical phenomena differing a lot from the classic computing method. The qubit is the basic unit of a quantum computer, performing the same function as the bit in classic computer. However, unlike the classic bit which can be in one of two state, a qubit can exist in a superposition of its two or more basis states. Therefore, once the quantum computer can operate the qubit the a particular way, they have the potential capacity to carry out faster computing than that classic computer does.

However, existing experiments have shown the difficulty of making a qubit. A ideal qubit should be equipped with long coherence time, fast operation, high fidelity and large connectivity. The possible quantum computing platforms include superconducting quantum circuits, which Google and IBM adopt, semiconductor

quantum bots, which Intel and Microsoft adopt, optically trapped atoms and electromagnetically trapped lons.

In the summer 2024 I joined the REU program in the Department of Physics and Astronomy at the Notre Dame University. I work with Professor Dafei Jin in his Emergent Quantum System Lab. This lab is equipped with two 10 millikelvin dilution refrigerators dedicated to quantum material based new qubit development. Our general project is to control a single electron on the surface of solid neon as a qubit under a low temperature superconducting system. And my job is to make microwave filters filling with a kind of special material called Eccosorb, which can absorb microwave, for the reduction of microwave noise.

2. Background

2.1 The Necessity of Low Temperature Condition

Our project aims to use a single electron trapped on an ultraclean solid neon surface in vacuum to make a single qubit. The whole system is based on the superconducting microwave circuit placed in a dilution refrigerator that can provide us the temperature down to 10 millikelvin. The low temperature is needed for several reasons. Firstly, the circuit is driven by microwave and the test of electron is based on resonators, therefore a superconducting circuit is required to reduce the losses in circuit and provide high quality factor in resonators, where low temperature is essential for the preservation of superconductivity of the material. Secondly, the thermal noise is one of the biggest factors for the reduction of qubit's coherence time. Low temperatures reduce thermal fluctuations and other sources of noise that can disturb the fragile quantum states of qubits, thereby extending coherence times and improving the reliability of quantum operations.

2.2 Microwave Filters

Although the system is placed in a low temperature environment, there is still noise from room temperature that may transmit into the system along the transmission line.

Aside of this, the superconductor itself would produce some high frequency noise that may contribute to the reduction of the qubit's coherence time.[1] Therefore, microwave filters are required to reduce all kinds of noise in our target frequency band, which is about 5Ghz. The filters I made in summer are low pass filters removing the high frequency noise.

The design of the filter is coaxial filter using cooper as the outer container and beryllium cooper for the inner conductor, then filled with Eccosorb CR-124, which I will introduce below.

2.3 Eccosorb

Eccosorb is a brand name for a family of electromagnetic interference (EMI) absorption materials. These materials are designed to absorb electromagnetic radiation across a wide range of frequencies, typically from radio frequencies up to microwave frequencies. Specially, Eccosorb CR is a series of castable epoxy resins which can be used to mold waveguide terminations, attenuators, loads and other custom parts to finished size [2] for the absorption of microwave frequency over 1Ghz. The type of eccosorb we adopt is Eccosorb CR-124, which is recommended for the filters whose passing frequency is under 5Ghz.

There are some advantages for adopting eccosorb. Firstly, eccosorb has a thermal expansion coefficient compare to that of copper, a little bit higher than copper's. However, most plastics and epoxies contract much more when cooling down. This makes eccosorb low-temperature compatible while other material would crack upon cooling process. Moreover, eccosorb is vacuum compatible since it does not outgas much, while in general plastics tend to outgas, making them not compatible for the vacuum.

2.4 Vector Network Analyzer (VNA):

Vector network analyzer is a testing device for electromagnetic wave energy, which

can use its own signal source to measure scattering parameters of RF microwave devices, cables, connectors, etc. It combines various technologies such as spectrum analysis, signal generation, and signal separation, and is commonly used in the research, development, testing, and production of basic industries and fields such as microwave devices, materials science, and electronic communication. The vector network analyzer can measure various parameter amplitudes and phases of single port or two port networks, and can display test data using Smith charts. More convenient for engineering applications and debugging. It has many functions and is known as the "king of instruments".

3. Methods

3.1 The Transmission Line Theory [3, p.50]

As shown in figure, the transmission line is often represented as a two-wire line, since the transmission lines for TEM wave propagation always have at least two conductors. When the below quantities are defined as below:

R=series resistance per unit length, for both conductors, in Ω/m

L=series inductance per unit length, for conductors, in H/m

G=shunt conductance per unit length, in S/m

C=shunt capacitance per unit length, in F/m

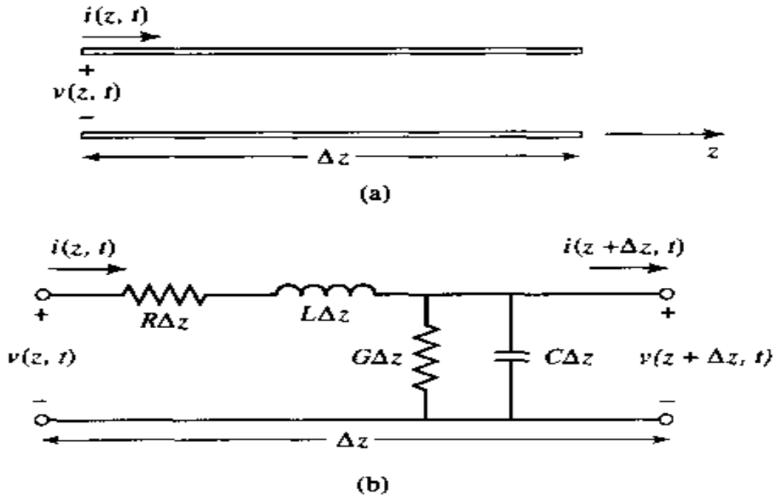

The piece of line of infinitesimal length Δz can be modeled as a lumped element circuit as shown in figure. the Kirchhoff's voltage law and current law can lead to the result that the characteristic impedance Z of the unit line can be defined as below:

$$Z = \sqrt{\frac{R + j\omega L}{G + j\omega C}}$$

Where j is the imaginary unit and ω is the angular frequency.

And the complex propagation constant can be defined as below:

$$\gamma = \sqrt{(R + j\omega L)(G + j\omega C)}$$

In this case the current on the line can be written as:

$$I(z) = \frac{1}{Z}(V^{+}e^{-\gamma z} - V^{-}e^{\gamma z})$$

For a coaxial line with complex permittivity $\epsilon = \varepsilon_0(\varepsilon' - j\varepsilon'')$, permeability μ, surface resistance Rs, and an outer conductor of inner radius b and inner conductor with an outer radius of a, the parameters are :[3, p.54]

$$R = \frac{Rs}{2\pi}\left(\frac{1}{a} + \frac{1}{b}\right) \qquad L = \frac{\mu}{2\pi}(\ln(b) - \ln(a))$$

$$G = \frac{2\pi\omega\varepsilon''}{\ln(b) - \ln(a)} \qquad C = \frac{2\pi\varepsilon'}{\ln(b) - \ln(a)}$$

Simplified under high frequency limit, where R is small compared to $j\omega L$, and with a possible complex permeability $\mu = \mu_0(\mu' - j\mu'')$, characteristic impedance Z can be moreover written as :

$$Z = \frac{\sqrt{\mu_0/\varepsilon_0}}{2\pi}\sqrt{\frac{\mu' - j\mu''}{\varepsilon' - j\varepsilon''}}\ln\left(\frac{a}{b}\right)$$

All the data can be found in the guide Laird published as a function of frequency.[4] When mark Zc as the characteristic impedance of the feed transmission line. We can calculate the voltage reflection coefficient Γ and transmission coefficient T. The simplified model is shown below, a filter with impedance Z, complex propagation constant γ and length, connected by transmission line.

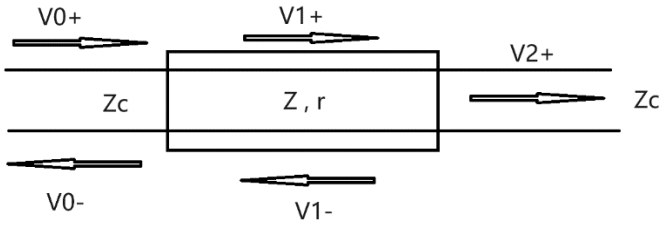

The equation of voltage and current:

$$V_0^{+} + V_0^{-} = V_1^{+} + V_1^{-}$$

$$V_1^{+}e^{-\gamma d} + V_1^{-}e^{\gamma d} = V_2^{+}$$

$$\frac{1}{Zc}\left(V_0{}^{+} - V_0{}^{-}\right) = \frac{1}{Z}\left(V_1{}^{+} - V_1{}^{-}\right)$$

$$\frac{1}{Z}\left(V_1{}^{+}e^{-\gamma d} - V_1{}^{-}e^{\gamma d}\right) = \frac{1}{Zc}V_2{}^{+}$$

Then we can have the voltage reflection coefficient Γ and transmission coefficient T:

$$\Gamma = \frac{V_0{}^{-}}{V_0{}^{+}} = \frac{Z(1+k) - Zc(1-k)}{Z(1+k) + Zc(1-k)} \qquad T = \frac{V_2{}^{+}}{V_0{}^{+}} = \frac{2Z(e^{-\gamma d} + ke^{\gamma d})}{Z(1+k) + Zc(1-k)}$$

Where $k = \frac{Zc-Z}{Zc+Z}e^{-2\gamma d}$.

In the result part , I will show the table of theoretical result of reflectivity and transmittance, and compare with the experimental result.

3.2 Filter Production

The production process generally composed with modeling, cutting the outer container, install connecters and filling with eccosorb.

The modeling is completed by Autodesk Fusion. The body part is shown as brown volume, and the golden part are the two connecters in each side. The body part is composed by a cuboid with a all through hole and a side hole for the filling of eccosorb.

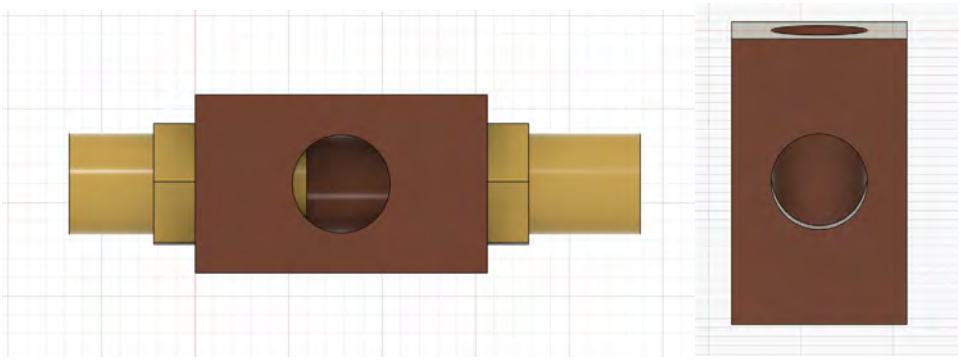

The size of cuboid is set as 15.621mm*9.525mm*9.525mm, and the diameter of the holes is 5.232mm. The depth of connector threads is 5.425mm; therefore the length of the eccosorb is calculated to be 4.771mm.

The cutting process is carried out by a desktop CNC machine tool with 1/8 inch flat mill. After cutting the body, we install the connecter and the inner conductor. The

inner conductor is made by baryllium copper, which is a standard material for pins in coaxail connectors, with the diameter of 0.508mm.

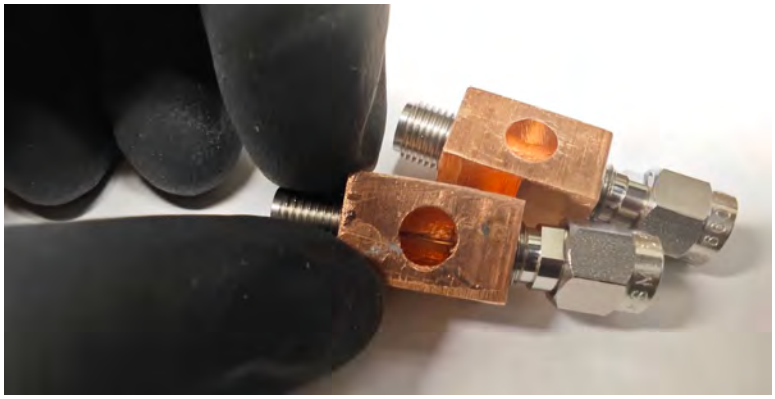

The last step before testing is to fill in the eccosorb. The eccosorb CR-124 is mixed by two parts. According to the instruction by Laird, the eccosorb CR-124 requires 100 weight of part A and 2.6 weight of part B. After mixing them up, heat them up to 150℃. Quickly use a small stick to move melted eccosorb into the filter until it's full. Keep the temperature of 150℃ for 1hours to remove the air inside the eccosorb. Then the eccosorb will become hard and the filter completed.

Mix ratios and recommended frequency range are given in the table below:

Series	Range (Ghz)	Part A	Part B
CR-110	26+	100	16.5
CR-112	12-18	100	11.3
CR-114	10-14	100	6.5
CR-116	6-12	100	4.3
CR-117	4-8	100	3.2
CR-124	<5	100	2.6

3.3 Filter Testing

Use the vector network analyzer to test the transmittance and reflectivity for frequency range from 0.3Ghz to 20Ghz under the room temperature about 293 Kelvin and liquid nitrogen temperature of 4 Kelvin.

4. Result

4.1Room Temperature Result

As shown in the figure, the theoretical value differs significantly from the

experimental value. The jitter of the reflectance curve is caused by impedance mismatch. The theoretical transmittance is closely linear, which goes along the experimental result. However, the actual attenuation raises faster as the frequency increase than the theoretical attenuation.

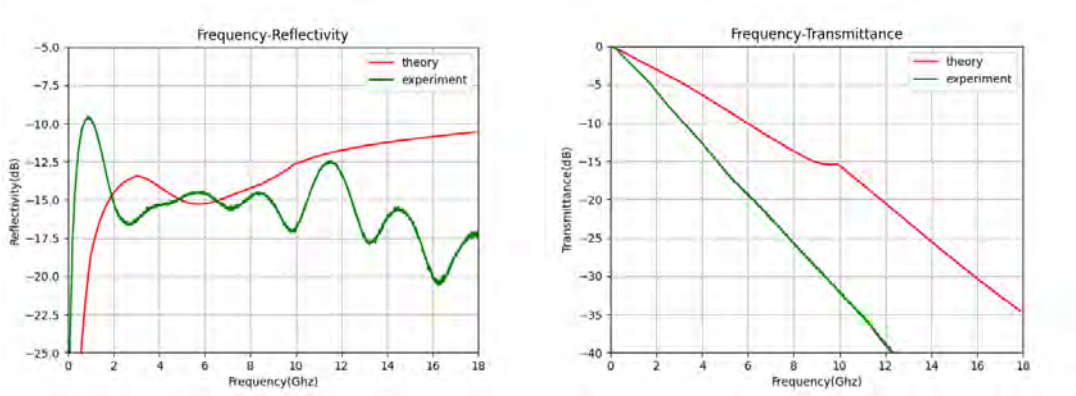

Possible reasons for the difference may be that the connectors in the side of filters may introduce extra impedance into the calculation, which is assumed to be ignored; or the characteristic impedance of the feed transmission line would differ from 50Ω or significantly change with frequency.

Back to the filter itself, the attenuation at 5Ghz is over 15dB, which reach the expectation to remove the noise in target frequency band. The maximum of reflectivity shows up at about 1Ghz, after that the maximum value of reflectivity is no more than -12.5dB, which reach the expectation for the low loss (reflection) of the signal.

4.3 Liquid Nitrogen Temperature Result

The result is shown below. In nitrogen temperature, the transmittance raises a little bit. However, the filter still reaches our expectation for the less then -15dB attenuation at 5Ghz. The transmission graph seems to be messy. However, this is because when using two longer transmission line for the nitrogen testing, the line itself bended and therefore introduced some new scattering to the signal. Generally, the reflectivity and transmittance raise when temperature goes down. Possible reason is that the eccosorb crack when cooling down because of the different thermal expansion coefficient between copper and eccosorb. Also, the change of permittivity and permeability under different temperature would also affect the result.

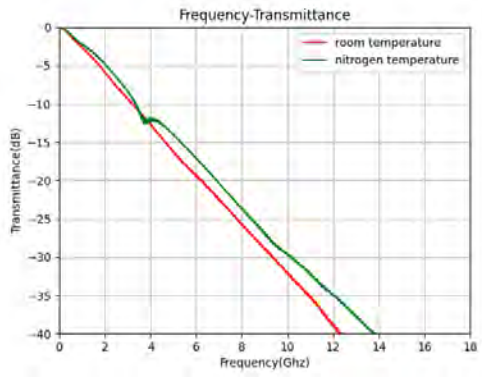

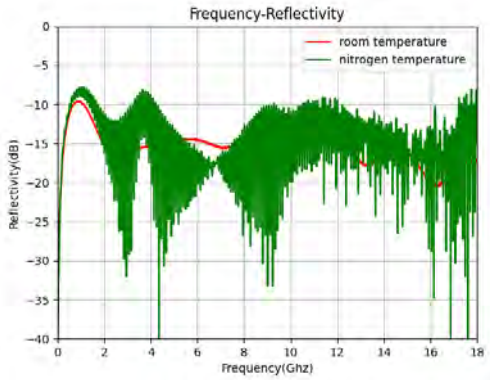

5. Conclusion

From a practical perspective, the production of filters is successful. The filter has low reflectivity in the target frequency band and sufficient attenuation in the high-frequency part. This makes it very suitable for the overall project requirements, filtering out unwanted thermal noise.

However, from a theoretical perspective, the analysis of filters is relatively unsuccessful. Aside of impedance mismatch, connecters would introduce additional impedance or some other effect that I haven't made it clear. Theoretical transmittance and experimental transmittance both exhibit roughly linear characteristics when expressed in decibels, but the theoretical transmittance is slightly higher than the experimental transmittance, perhaps due to flaws in the theoretical derivation. This is worth further exploration in future studies.

6. Acknowledgement

I would like to express my gratitude to Professor Dafei Jin for his planning guidance, Professor Sergei Sheludiakov for teaching me all the practical knowledge, and Senior Yutian Wen and Senior Shan Zou for their help in my theoretical studies, as well as for their assistance with language and daily life issues in the United States. I would also like to express my sincere gratitude to Ms. Kristen Amsler and Professor Umesh Garg for their contributions to the REU project, which have provided me with a wonderful learning experience.

7. References

[1] Norris, G. J. (2017). *Improving infrared-blocking microwave filters* (Doctoral dissertation, MS thesis, ETH Zurich).

[2] *Eccosorb CR Two-Part Castable Load Absorber Series.* Technical Bulletin. Laird Technologies, Inc. url: https://www.laird.com/sites/default/files/2021-01/RFP-DS-CR%2018062020.pdf (visited on July. 30,2024)

[3] Polar, D. M. (2006). *Microwave engineering (3rd ed.)*. J. Wiley & Sons.

[4] *Eccosorb MF. Lossy, Magnetically Loaded, Machinable Stock.* Technical Bulletin. Laird Technologies, Inc. url: https://ece.co.jp/assets/pdf/products/ECCOSORB%20MF_en.pdf (visited on July. 30, 2017)